Université de Provence
3 place Victor Hugo
13331 Marseille Cedex 3, France

IRFM, Association Euratom-CEA
Centre de Cadarache
13108 Saint Paul-Lez-Durance, France

THESE

pour obtenir le grade de

DOCTEUR DE L'UNIVERSITÉ DE PROVENCE

Ecole Doctorale: Physique et Sciences de la Matière

ETUDE DU TRANSPORT DE LA CHALEUR ET DES PARTICULES DANS LES TOKAMAKS TORE SUPRA ET HL-2A

Présentée et soutenue publiquement

par

Shaodong SONG

le 14 Décembre 2011

Rapporteurs :	
Marco de BAAR	Professeur à l'Eindhoven University of Technology, Pays-Bas
Xuantong DING	Physicien au Southwestern Institute of Physics, Chengdu, Chine
Membres du jury :	
Gerardo GIRUZZI[1]	Ingénieur au Commissariat à l'Energie Atomique, Cadarache
Xiaolan ZOU	Ingénieur au Commissariat à l'Energie Atomique, Cadarache
Fabrice DOVEIL	Directeur de Recherches au CNRS, Marseille
Peter BEYER	Professeur a l'Université de Provence, Aix-Marseille I
Gia-Tuong HOANG	Ingénieur au Commissariat a l'Energie Atomique, Cadarache
Michel TALVARD	Ingénieur au Commissariat a l'Energie Atomique, Saclay

[1] Directeur de thèse au CEA et à l'Université

Etude du transport de la chaleur et des particules dans les tokamaks Tore Supra et HL-2A - Résumé

Résumé

Introduction

Le transport de la chaleur et des particules est un des sujets de recherche fondamentaux de la physique des plasmas chauds confinés par des champs magnétiques, systèmes physiques qui sont étudiés dans le cadre des recherches sur la fusion thermonucléaire contrôlée. L'analyse du transport a pour but de trouver la relation entre les flux et les gradients des quantités macroscopiques, telles que la densité et la température. Les diffusivités de densité et de température, avec la dimension de (longueur)^2/temps, sont les coefficients habituellement utilisés pour caractériser les processus de transport. Ces diffusivités dépendent des paramètres du plasma, tels que la densité, la température, la densité de courant, la quantité de mouvement, le taux d'impuretés, etc., ainsi que de leurs gradients. Dans les expériences, il a été constaté depuis longtemps que les processus de transport radial des électrons sont beaucoup plus importants que les estimations théoriques basées sur les collisions Coulombiennes entre particules, prenant aussi en compte l'effet géométrique de la configuration magnétique. En contrepartie de ce transport, que l'on appelle néo-classique, le transport observé expérimentalement est souvent appelé anormal. Ces phénomènes de transport anormal sont essentiellement liés à la turbulence électrostatique ou électromagnétique et ils sont donc extrêmement difficiles à modéliser par la théorie. Des expériences spécifiques sont alors réalisées sur des machines expérimentales, telles que les tokamaks ou les stellarators, afin d'améliorer la connaissance de ces phénomènes.

Expérimentalement, le transport peut être étudié en régime stationnaire, grâce à l'équation du bilan de la quantité considérée. Le point faible de cette méthode est la non séparation entre phénomènes de diffusion et de convection. Comme un complément nécessaire, l'approche dite perturbative, ou du transport transitoire, a comme but d'étudier la réponse d'un système à une petite perturbation autour de l'équilibre, ce qui s'est avéré très fructueux pour l'étude du transport dans les plasmas de fusion. Dans ce cadre, les expériences utilisant la modulation des sources (de chaleur, de matière, de rotation ou d'impuretés) sont considérées comme un outil direct et puissant de recherche sur les phénomènes de transport. La modulation temporelle des sources permet de réduire les erreurs expérimentales, en faisant la moyenne de la réponse à une série de perturbations indépendantes et identiques et en utilisant l'analyse de Fourier afin d'extraire des informations sur les coefficients de transport.

Dans ce travail de thèse, trois phénomènes de transport sont étudiés avec la technique des modulations des sources:

1) la convection de la chaleur vers l'intérieur (aussi appelée "pincement de chaleur"),

2) le "pump-out" ou expulsion des particules causée par le chauffage des électrons,

3) le transport dit "non-local".

Cette thèse décrit des études expérimentales de ces trois phénomènes réalisées sur deux tokamaks de grande dimension: Tore Supra (machine basée au CEA/Cadarache) et HL-2A (basée au Southwestern Institute of Physics, Chengdu, Chine). Dans ces expériences, un chauffage modulé par ondes à la résonance cyclotronique électronique (ECRH) est utilisé pour étudier le pincement de chaleur et le pump-out de la densité, tandis que les expériences de transport non-local utilisent l'injection de matière, par un faisceau supersonique moléculaire (SMBI), comme source de modulation.

Outils numériques d'analyse

L'outil de base qui a été utilisée dans ce travail de thèse pour l'analyse du transport à l'équilibre est le code CRONOS. C'est une suite de codes numériques pour la simulation prédictive et /ou interprétative de la décharge plasma d'un tokamak.

Pour l'analyse perturbative, le code ANALYTIQUE a été développé afin d'obtenir les coefficients de transport par une méthode d'approximations successives. Ce code s'appuie sur la solution analytique de l'équation de transport de la chaleur ou des particules à coefficients constants. Un code d'utilisation conviviale nommé GSONIQUE a été développé pour fournir une solution de la même équation pour des coefficients quelconques. Dans ce code, les coefficients de transport peuvent être soit constants dans le temps, soit dépendants des paramètres du plasma, ou tout simplement définis par l'utilisateur. Le code REMA fournit le profil de puissance ECRH absorbée par le plasma, calculé en résolvant les équations de propagation des ondes dans l'approximation de l'optique géométrique, et utilisant le tenseur diélectrique relativiste.

Expériences sur le pincement de chaleur

Dans le transport des particules, l'état stationnaire du profil de densité est généralement un profil piqué, bien que la source de particules soit fortement localisée à la périphérie du plasma: il s'agit là d'un phénomène typique de pincement, ou convection vers l'intérieur. Le cas du transport de la chaleur est différent: le phénomène dominant est bien la diffusion, malgré le fait que la plupart des théories du transport turbulent comportent aussi de la convection.

Le pincement de chaleur a été observé, par exemple, dans les tokamaks DIII-D [1], RTP [2], ASDEX-U [3]. Par définition, le flux de chaleur diffusif est proportionnel au gradient de la température électronique T_e, tandis que la partie convective est proportionnelle à la température elle-même. Le flux de chaleur q_e est donc une combinaison des deux termes, qui peut s'écrire comme

$$q_e = - (n_e \chi_e \nabla T_e + n_e V_e T_e)$$

où n_e est la densité électronique, χ_e le coefficient de diffusion et V_e est la vitesse de convection. Le transport de la chaleur vers l'intérieur peut être dû à la convection, mais aussi au terme de diffusion, si χ_e dépend de la variable spatiale, et à plus forte raison s'il dépend de la température et/ou de son gradient. Quelle partie du flux joue un rôle dans le pincement de chaleur observé est un point clé pour la compréhension des mécanismes de transport de la chaleur.

Le chauffage cyclotronique électronique (ECRH) constitue l'un des meilleurs choix de source de chaleur pour l'étude du transport de la chaleur des électrons. Par cette méthode de chauffage, les ions sont peu perturbés, le profil de dépôt de puissance est très localisé dans l'espace, et il peut être parfaitement contrôlé en utilisant des miroirs mobiles pour injecter les ondes. Ces propriétés permettent d'éviter l'effet de la source de chaleur elle-même dans le processus d'analyse des phénomènes de transport. Le système ECRH de Tore Supra se compose de deux gyrotrons, chacun capable d'injecter environ 300 kW dans le plasma, avec une largeur de dépôt de 3 à 5 cm et un réglage précis de l'angle d'injection. Les ondes injectées sont à 118 GHz, c'est à dire à une fréquence proche de la fréquence cyclotronique des électrons pour la valeur nominale du champ magnétique de Tore Supra. La puissance est injectée dans le mode ordinaire (O-mode) par le côté faible champ, perpendiculairement au champ magnétique. Les expériences de modulation ECRH ont été réalisées avec un courant du plasma variant de 0,6 MA à 1 MA, le champ magnétique sur l'axe 3,73 T et 3,53 T, correspondant à des positions de dépôt de ρ = 0,5 et 0,6; la densité linéaire moyenne était de 1,4 ~ 5,4 × 10^{19} m^{-3}, la température centrale 2 ~ 5 keV. Avec ces conditions, une bonne absorption de puissance est obtenue: même aux plus faibles densités utilisées dans les expériences, l'absorption au premier passage était supérieure à 80%. Un schéma de modulation carré a été utilisé avec un rapport cyclique de 0,5. Nous avons également réglé la fréquence de modulation à exactement 1Hz, 3Hz, 5Hz, 7 Hz et 9 Hz, bien que la plupart des résultats ait été obtenus pour 1 Hz.

Le profil de température électronique a été mesuré par l’émission cyclotronique électronique (ECE), détectée grâce à un radiomètre hétérodyne à 32 canaux, avec une résolution spatiale d'environ 2,5 cm. La précision de calibration relative entre les canaux est meilleure que 3%, ce qui permet des mesures du profil de température de haute qualité et une détermination assez bonne du gradient de température. La résolution temporelle était de 1 ms pour nos expériences. Le profil de densité a été mesuré par deux ensembles de réflectomètres hétérodyne en mode X, travaillant à des fréquences allant de 50 à 110 GHz et de 105 à 155 GHz, respectivement. Le temps du balayage de la fréquence était de 20 ms, et l'incertitude du profil radial inférieure à 1cm. Un interféromètre infrarouge à 9 canaux, qui a une résolution spatiale d'environ 7 cm, a été également utilisé pour la mesure du profil de densité dans les cas où les réflectomètres ne pouvaient pas couvrir toute la gamme des rayons du plasma.

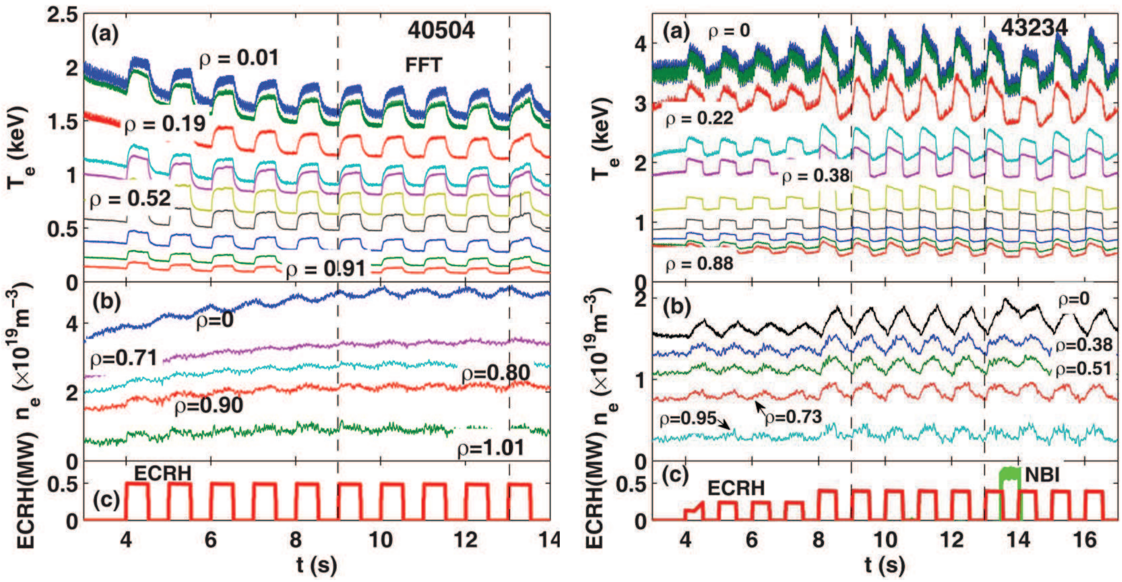

Figure 1: Evolution temporelle de (a) la température électronique (mesurée par l'ECE), (b) la densité (mesurée par la réflectométrie) et (c) la puissance ECRH, pour une décharge plasma à haute densité (TS#40504, gauche) et une à faible densité (TS#43234, droite)

Différents types de comportements ont été observés en fonction de la densité du plasma, avec deux régimes distincts pour la densité centrale $n_{e0} = 3 \sim 5 \times 10^{19}$ m^{-3} (haute densité) et $n_{e0} = 1 \sim 3 \times 10^{19}$ m^{-3} (faible densité). Pour le cas de haute densité, nous avons sélectionné une décharge avec les principaux paramètres plasma suivants: champ magnétique B_T = 3,73 T, courant plasma I_p = 700 kA, densité centrale $n_{e0} = 4 \sim 5{,}4 \times 10^{19}$ m^{-3}, facteur de sécurité au bord du plasma q_{edge} = 6,3. Dans l'intervalle de temps analysé, la perturbation de T_e est de l'ordre de 10% de la T_e moyenne, ce qui reste raisonnable pour une analyse des perturbations. Pour le cas de faible densité, nous avons choisi une décharge avec les principaux paramètres du plasma comme: B_T = 3,72 T, I_p = 700 kA, n_{e0} = 1.5 à 1.8 × 10^{19} m^{-3}, q_{edge} = 6,6. Pour l'intervalle de temps considéré, le niveau de perturbation de la température est compris entre 7 et 12%. La modulation ECRH est essentiellement la même que dans le cas de haute densité. L'évolution typique de la densité et de la température électronique pendant les modulations de puissance pour les deux cas considérés est montrée en Fig. 1. Plusieurs techniques d'analyse et de simulation ont été appliquées à ces deux décharges, afin de comprendre leur comportement différent vis-à-vis du transport de la chaleur.

Pincement de chaleur: simulations

Des simulations basées sur deux modèles différents ont été réalisées. Le premier modèle est appelé Modèle de Pincement Linéaire (LPM). Il utilise des coefficients de transport constants dans le temps et ayant une structure spatiale en marche d'escalier. Dans ce modèle, les trois coefficients de transport de la chaleur sont les suivants: la diffusivité χ_e, la vitesse de convection V_e et un temps d'amortissement τ, qui représente tous les autres phénomènes de perte d'énergie des électrons (transfert aux ions, rayonnement, réduction du chauffage ohmique due à l'augmentation de la température, etc.). La détermination de leurs valeurs est basée sur la sensibilité de ces coefficients aux variations de l'amplitude et de la phase des différentes harmoniques de Fourier. En bref, la pente du profil de phase est surtout sensible à la diffusivité χ_e, la forme de l'amplitude de l'harmonique fondamentale est sensible à la vitesse de convection V_e, tandis que la valeur absolue du minimum de la phase et le niveau global de l'amplitude de toutes les harmoniques sont plutôt sensibles au temps d'amortissement τ.

Dans ces simulations, les conditions aux limites sont les suivantes: $\partial T_e/\partial r|_{\rho=0} = 0$ and $T_e|_{\rho=1} = T_{edge}(t)$, où $\rho = r/a$ est la coordonnée radiale normalisée au petit rayon du plasma, et la température au bord du plasma $T_{edge}(t)$ est obtenue par extrapolation des données ECE combinées avec les mesures de température par diffusion Thomson. La technique utilisée est de reproduire d'abord par la simulation une harmonique, et de comparer ensuite les autres afin de confirmer la validité des coefficients obtenus.

Pour reproduire les profils de l'amplitude et de la phase de la décharge de haute densité, un modèle purement diffusif est suffisant, sauf dans la région de $\rho < 0,25$, où une vitesse de convection vers l'intérieur de 3,5 m/s doit être utilisée. En revanche, pour le cas de faible densité, fort pincement de chaleur (environ 8 m/s) est nécessaire pour reproduire le déplacement vers l'intérieur du point maximum de l'amplitude par rapport au point minimale du profil de phase, comme montré en Fig. 2.

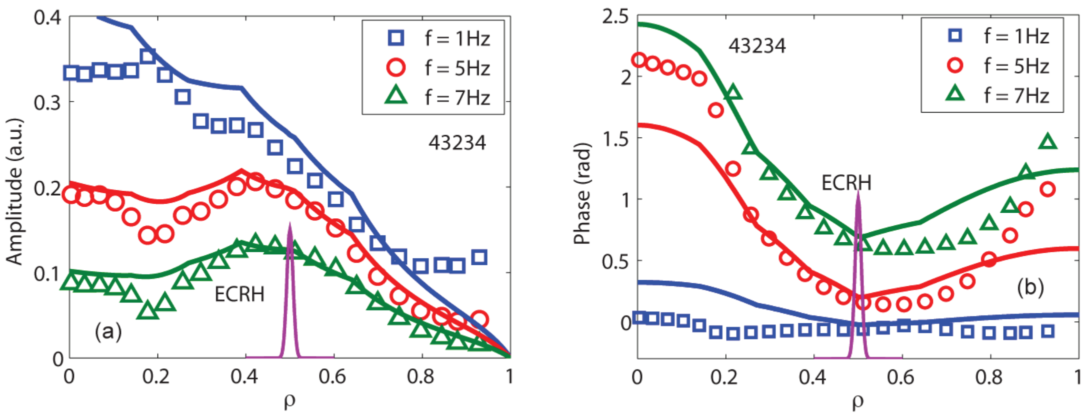

Figure 2: Simulation avec le modèle LPM pour une décharge à faible densité (TS#43234). Les différents symboles sont les valeurs expérimentales; les lignes représentent la simulation. Amplitude (a) et phase (b) des harmoniques 1, 5 et 7.

Un autre modèle a été utilisé dans cette thèse pour essayer de reproduire les mêmes décharges. Il s'agit du modèle à gradient critique (CGM), qui a été appliquée avec succès à diverses expériences, dans les tokamaks ASDEX Upgrade [4,5], DIII-D [6], JET [7], FTU [8]. Dans ce modèle, la diffusivité de la chaleur est donnée par [9,10]

$$\chi_s = \chi_{gB} [\chi_s (-R\partial_r T/T - \kappa) H(-R\partial_r T/T - \kappa) + \chi_0]$$

où $\chi_{gB} = q^{\nu}(T_e/eB)\rho_s/R$. Ici q est le facteur de sécurité, κ la valeur seuil du gradient de température normalisé $(-R\partial_r T_e/T_e)_{crit}$, H est la fonction de Heaviside qui décrit l'effet seuil: si $-R\partial_r T_e/T_e < \kappa$, $H = 0$ alors que si $-R\partial_r T_e/T_e \geq \kappa$, H = 1 et le transport augmente fortement. $\chi_{gB}\chi_0$ est la diffusivité résiduelle qui décrit le transport en dessous du seuil κ, χ_s est appelé facteur de rigidité et caractérise la force de la transition critique. Dans cette étude, le modèle CGM est utilisé comme un paradigme des modèles basés sur une température critique, indépendamment de toute considération sur le régime de turbulence qui gouverne effectivement ces décharges, et qu'en tout cas il est difficile de déterminer avec précision.

Pour le cas de haute densité, avec un profil de diffusivité homogène dans l'espace, la simulation des profils de température, de l'amplitude et de la phase est en plutôt bon accord avec les données expérimentales. Cependant, pour le cas de faible densité, il est plus difficile de reproduire l'amplitude et la phase simultanément avec le modèle CGM. Afin d'obtenir de meilleurs résultats, un terme de pincement additionnel doit être introduit, avec une vitesse de convection de l'ordre de 1,5 m/s.

En comparant les résultats de l'analyse du bilan de puissance (obtenus en utilisant le code CRONOS) et ceux des deux modèles (LPM et CGM), on arrive à avoir une assez bonne compréhension des caractéristiques du transport de la chaleur pour ces décharges. La valeur de la diffusivité obtenue par le bilan de puissance est similaire à celle du CGM, ce qui démontre la validité globale de ce modèle. L'accord entre la diffusivité effective obtenue par les modèles CGM et LPM, ainsi que l'accord entre leurs vitesses de convection, montrent la cohérence des deux méthodes. Néanmoins, le terme de pincement se révèle nécessaire pour bien simuler la dynamique du système soumis au chauffage modulé. Ceci montre que la technique des modulations permet d'accéder à des caractéristiques plus fines des mécanismes de transport de la chaleur.

Le phénomène d'expulsion de la densité (pump-out)

Un système de chauffage ECRH a été spécifié pour accomplir de multiples fonctions dans ITER: chauffage localisé, génération localisée de courant, contrôle en temps réel des instabilités MHD, assistance au démarrage de la décharge ainsi qu'à la montée du courant et conditionnement de la paroi. En conséquence, le transport des particules pendant le chauffage ECRH devient un enjeu important. Il a été observé que le chauffage ECRH peut fortement affecter le profil de densité du plasma, en particulier à de faibles densités. Cet effet, pas encore complètement compris, peut être un outil de contrôle intéressant dans les réacteurs à fusion et il est déjà largement utilisé dans les stellarators.

L'expulsion (ou pump-out) des particules se manifeste par l'aplatissement du profil de densité et par une perte accrue de particules pendant le chauffage ECRH.

Ceci a été observé, entre autres, dans le tokamak HL-2A. Pour l'état stationnaire, le piquage de la densité peut être lié au rapport de la vitesse de convection des particules V et de leur coefficient de diffusion D, i.e., $\nabla n / n = V / D$. La vitesse de convection peut être écrite comme la somme d'un terme néoclassique et d'un terme anormal, ou turbulent : $V = V_{\text{neo}} + V_{\text{an}}$. V_{neo} inclut le pincement dit de Ware, qui est proportionnel au champ électrique toroïdal, ainsi que les contributions des gradients de la température des ions et de la densité d'impuretés. L'existence d'une vitesse de convection anormale est prédite par les théories turbulentes sur la base des micro-instabilités ITG (liées au gradient de la température des ions) et TEM (liées aux électrons piégés dans les inhomogénéités du champ magnétique) et a été mis en évidence, entre autres, dans les décharges complètement non-inductives réalisées dans Tore Supra [11]. Le flux de particules Γ peut donc être exprimé comme [12]

$$\Gamma = -D\,[\nabla n_e + (C_q \nabla q/q - C_T \nabla T_e/T_e) n_e\,] + V_{\text{neo}} n_e$$

où C_q, C_T ne dépendent pas des gradients. Il est donc clair que le phénomène d'expulsion des particules peut apporter des informations précieuses sur les propriétés du transport turbulent des particules.

Les expériences de pump-out de densité décrites dans cette thèse ont été réalisées sur le tokamak HL-2A, (grand rayon R = 1,65 m, petit rayon a = 0,40 m, B_T = 1,3 T, I_p = 160 kA). Le plasma est circulaire avec configuration limiteur ou divertor. Le système ECRH dans HL-2A est composé de 3 gyrotrons à 68 GHz, avec une puissance totale maximale de 1,5 MW et une durée d'impulsion de 1 s.

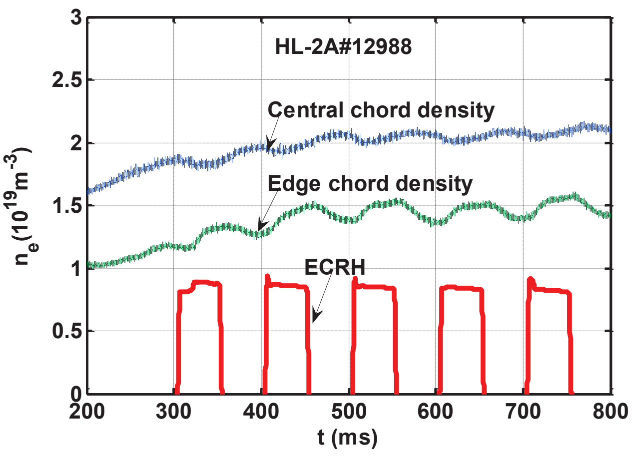

Figure 3: Evolution temporelle de la densité moyenne au bord (vert) et au centre (bleu) du

plasma pendant les modulations de la puissance ECRH (rouge). .

Pour le cas de la configuration limiteur, une perturbation de densité négative (c'est-à-dire un pump-out) dans la région centrale a été observé, et aussi une perturbation de densité positive dans la région périphérique, comme montré par la Fig. 3. L'augmentation de la densité de bord est probablement due au dégazage causé par l'ECRH sur les composants face au plasma. Une forte asymétrie de la propagation des deux perturbations de densité, négative et positive, a été observée sur les profils de l'amplitude et de la phase des harmoniques obtenues par transformée de Fourier, un phénomène qui est très similaire à celui observée lors de la propagation d'impulsions de chaleur. Une corrélation entre l'augmentation de la turbulence et le phénomène de pump-out a été trouvée.

Contrairement au cas de la configuration limiteur, en configuration divertor à la fois les densités de centre et de bord sont modulées en opposition de phase par rapport à l'impulsion ECRH. Cependant, la perturbation de densité positive (dégazage) est fortement réduite : la perturbation de densité est largement dominée par le phénomène de pump-out. Par ailleurs, la diminution de la densité est plus rapide dans la partie centrale que dans la partie périphérique, lors de l'application de l'ECRH. A partir du profil de la phase, la source de la perturbation de densité négative (pump-out) a été localisée dans la région centrale, de toute évidence proche de la région de déposition de la puissance ECRH.

En utilisant le code ANALITYQUE, nous constatons que les valeurs de la diffusivité D et de la vitesse de convection V sont beaucoup plus grandes pour la perturbation de densité négative que pour celle positive, à savoir, la perturbation de densité négative se propage beaucoup plus rapidement que celle positive. Par analogie, cette différence peut être expliquée par le fait que la perturbation de densité positive est due à la propagation de particules, tandis que la perturbation de densité négative pourrait être due plutôt à la propagation de la turbulence. Etant donné que la turbulence associée au modes de type TEM peut conduire à une convection vers l'extérieur via thermo-diffusion [13], le phénomène d'expulsion des particules pourrait résulter de la combinaison de deux effets: une forte convection de particules vers l'extérieur (-4 m/s), probablement causée par les modes TEM, et, plus important encore, un phénomène de propagation de la turbulence associé à une forte convection vers l’extérieur (-10 m/s).

Phénomènes de transport non-local

Des réponses transitoires, apparemment non-diffusives et de longue portée au refroidissement du bord du plasma ont été observées depuis longtemps dans les expériences. L’ensemble de ces phénomène est souvent appelé « transport non-local ». Le phénomène de transport non-local le plus célèbre est constitué par une inversion de polarité, c'est-à-dire un chauffage du centre du plasma presque simultané au refroidissement induit par une perturbation du bord (par exemple, une injection de matière). Ce chauffage central associé à un refroidissement du bord (CHEC, central heating edge cooling), est couramment observé dans les tokamaks aux faibles densités, alors qu’à plus forte densité la phénoménologie observée est celle d’une simple propagation d’impulsion froide (CP, cold pulse). Cependant, les mécanismes responsables ne sont pas encore tout-à-fait clairs, ce qui donne une forte motivation aux études expérimentales spécifiques de ces effets.

Des expériences avec injection modulée de matière à une vitesse supersonique (SMBI) ont été réalisées à la fois dans Tore Supra et dans HL-2A dans ce but. Le SMBI est une méthode d’alimentation du plasma intermédiaire entre l’injection de gaz et l'injection de glaçons. Dans Tore Supra, les impulsions supersoniques sont injectées à partir du côté fort champ du tokamak, avec un nombre de Mach ~4 et une durée d'impulsion de 2 ms. Ces expériences ont montré que le phénomène appelé CHEC est observé seulement lorsque la température centrale T_{e0} est supérieure à 3 keV et l’intégrale de la densité sur une corde traversant le centre du plasma n_{el} est inférieure à $2{,}5 \times 10^{19}$ m^{-2}. Ces limites peuvent être considérées comme des seuils pour l’existence du phénomène. L’évolution de la température électronique en présence de CHEC, avec propagation d’une impulsion chaude et d’une froide, est montrée dans la Fig. 4.

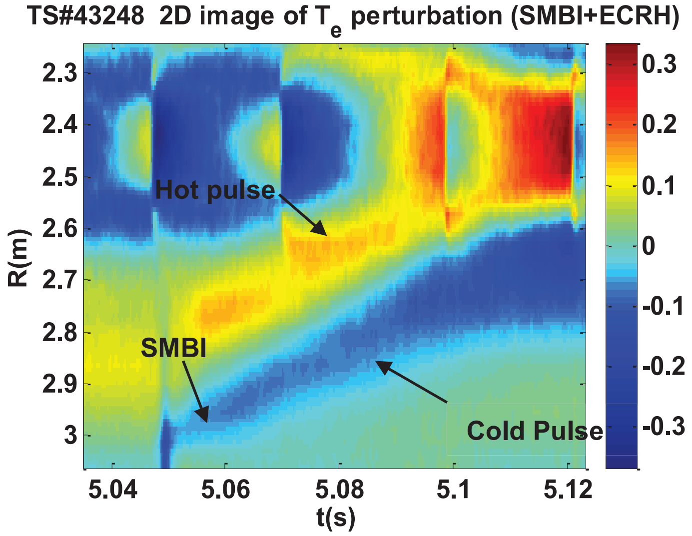

Figure 4: evolution spatio-temporelle de la perturbation de T_e lors d'une injection SMBI et en présence de chauffage ECRH.

Des tendances intéressantes ont été observées en utilisant une représentation synthétique des résultats expérimentaux par des diagrammes comme celui présenté en Fig. 5. Dans ce type de diagrammes, les états de la décharge à des intervalles de temps réguliers sont représentés par des points dans un plan (R/L_{ne}, R/L_{Te}), où L_{ne}, L_{Te} sont les longueurs de gradient de la densité et de la température au milieu du profil radial et R est le grand rayon du plasma. Lorsqu'on observe le phénomène de chauffage central accompagnant le refroidissement du bord (CHEC), la rotation des points dans cet espace après l'injection SMBI est toujours dans le sens des aiguilles d'une montre, tandis que dans le cas sans CHEC, avec une pure propagation d'impulsion froide (CP) la rotation est dans le sens inverse des aiguilles d'une montre ou en forme de 8, comme dans la Fig. 5.

Une autre différence fondamentale entre les régimes de type CHEC et ceux de type CP est associée au confinement de l'énergie. Dans les expériences avec CHEC, une amélioration du confinement de l'énergie, qui peut transitoirement atteindre jusqu'à 30%, a été observée lors de la perturbation de température. D'autre part, aucune amélioration n'a été observée pour le cas CP. La vitesse de rotation poloïdale mesurée par la réflectométrie Doppler montre que dans le régime CHEC des changements significatifs du niveau de rotation sont observés, alors que presque aucun changement n'est constaté dans les cas sans CHEC. Cela indique un lien possible entre la formation d'une barrière interne de transport (ITB) et le cisaillement de rotation du plasma.

Des expériences avec modulation SMBI ont également été effectuées sur le tokamak HL-2A, avec une phénoménologie essentiellement similaire.

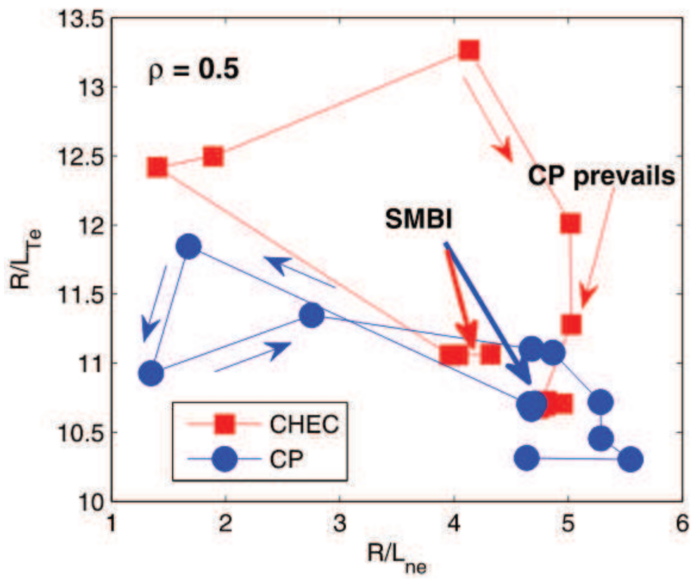

Figure 5: Diagramme des gradients normalisés de température et de densité à ρ = 0.5 pendant SMBI pour la décharge 42509. Les carrés rouges correspondent à une phase CHEC, les cercles bleus à une phase de pure propagation d'une impulsion froide (CP).

Transport couplé de densité et température

Nous avons observé que dans les expériences de modulation de SMBI et d'ECRH décrites dans cette thèse, les perturbations de densité et de température ont une ampleur similaire. Par conséquent, le couplage entre les équations de transport de la chaleur et des particules doit être pris en compte. Pour simplifier, ici on ne traite que le couplage entre la densité et la température, tout en omettant l'influence possible d'autres grandeurs physiques, telles que la température ionique, la densité de courant, etc.

L'interaction entre la densité et la température peut être analysée en utilisant la matrice de transport générale décrite dans la référence [14]. S'appuyant sur cette formulation, une étude systématique des équations couplées pour le transport de la densité et de la température a été effectuée, en utilisant une matrice de transport très simple et purement diffusive, mais non-diagonale. Les caractéristiques générales de la réponse de la densité et de la température aux sources externes de chaleur et de matière ont été étudiées. Dans certains cas, la densité oscille en présence d'une source de chaleur externe, montrant le phénomène de pump-out comme dans les expériences. En présence d'une source de matière, qui provoque un refroidissement au bord, le phénomène de type CHEC est aussi reproduit, au moins qualitativement. De toute évidence, un accord meilleur pourrait être obtenu en utilisant une matrice de transport non-linéaire, c'est-à-dire, dépendant des gradients.

Conclusions

Ce travail de thèse contient trois parties principales, à savoir, le pincement de chaleur, l'effet d'expulsion de la densité, et le transport non-local. Ces trois sujets ont été étudiés à l'aide d'expériences spécifiques, réalisées sur les tokamaks Tore Supra et HL-2A. Les expériences de modulation de la puissance de chauffage sur Tore Supra ont mis en évidence une convection de la chaleur vers l'intérieur du plasma (un phénomène dont l'existence est toujours controversée). La comparaison avec des simulations faites à l'aide de différents modèles a joué un rôle essentiel dans cette démonstration.

L'injection d'ondes ECRH peut conduire à une perte accrue ou à une redistribution radiale des particules, comme cela a été observé dans plusieurs expériences. Au cours des expériences avec modulation du chauffage ECRH (à la fois sur Tore Supra et sur HL-2A), et dans des conditions de faible densité, nous avons également observé une telle réduction de la densité, aussi appelé phénomène de pump-out. En fait, deux régions différentes ont été identifiées, une centrale dominée par le pump-out, et une périphérique dominée par le dégazage (c'est à dire, augmentation de la densité). Le comportement des deux régions a été caractérisé par l'analyse de Fourier.

Le phénomène dit de transport non-local a été observé dans différentes configurations expérimentales. L'effet est une réponse anormalement rapide à une stimulation extérieure, loin de la position de la source de perturbation. Une caractéristique importante de ce phénomène est la polarité inversée, c'est à dire, quand une impulsion froide est injectée au bord du plasma, le cœur du plasma se réchauffe quasiment au même moment. Nous avons effectué une injection de gaz à vitesse supersonique (SMBI) modulée au cours d'expériences sur les deux tokamaks, et ce phénomène de polarité inversée a été observé dans des conditions de faible densité. Une tentative pour expliquer ces phénomènes en utilisant une matrice de transport non-diagonal a été effectuée avec des résultats qualitativement en bon accord avec les expériences.

[1] T.C. Luce, C.C. Petty and J.C.M. de Haas 1992 *Phys. Rev. Lett.* **68** 52

[2] P. Mantica, G. Gorini, G.M.D. Hogeweij, N.J. Lopes Cardozo and A.M. R. Schilham 2000 *Phys. Rev. Lett.* **85** 4534

[3] P. Mantica *et al* 2006 *Plasma Phys. Control. Fusion* **48** 385

[4] F. Ryter *et al* 2003 *Nucl. Fusion* **43** 1396

[5] F. Ryter *et al* 2005 *Phys. Rev. Lett.* **95** 085001

[6] J.C. DeBoo *et al* 2005 *Nucl. Fusion* **45** 494

[7] P. Mantica *et al* 2008 *Fusion Sci. Technol.* **53** 1152

[8] A. Jacchia *et al* 2002 *Nucl. Fusion* **42** 1116

[9] F. Imbeaux *et al* 2001 *Plasma Phys. Control. Fusion* **43** 1503

[10] X. Garbet *et al* 2004 *Plasma Phys. Control. Fusion* **46** B557

[11] G.T. Hoang, C. Bourdelle, X. Garbet *et al* 2003 *Phys. Rev. Lett*. **90** 155002

[12] C. Angioni *et al* 2004 *Nucl. Fusion* **44** 827

[13] X. Garbet, L. Garzotti, P. Mantica *et al*. 2003 *Phys. Rev. Lett*. **91** 035001

[14] N.J. Lopes Cardozo 1995 *Plasma Phys. Control. Fusion* **37** 799

Heat and Particle Transport Studies in the Tore Supra and HL-2A Tokamaks

Abstract

Heat and particle transport is one of the fundamental subjects of research in controlled thermonuclear fusion devices such as tokamaks. These transport processes are anomalous and mainly driven by electrostatic or electromagnetic turbulence. Transport perturbation experiments with modulation of sources are considered as a direct and powerful tool for the transport investigation. In this work, three transport phenomena are investigated with the modulation technique: inward heat pinch, density pump-out and non-locality. This thesis reports on experimental studies performed on two large tokamaks: Tore Supra (IRFM, CEA/Cadarache, France) and HL-2A (South-Western Institute of Physics, Chengdu, China). The modulated source is the Electon Cylotron Resonance Heating (ECRH) for the heat pinch and density pump-out studies, while the non-local transport experiments use the Supersonic Molecular Beam Injection (SMBI) as source of modulation. The emphasis is put on the inward heat pinch.

The profile analysis or power balance in plasma steady-state is the most common investigation method for transport phenomena. The weak point of this method is the lack of separation of the diffusion and convection terms. The modulation technique allows for the separation of the transport process by analyzing the amplitude and phase of the Fourier transform of the harmonics of the perturbation.

Inward heat pinch is not always observed in tokamaks. Its existence remains controversial[29, 31]. In the off-axis ECRH modulation experiments on Tore Supra with low frequency (1 Hz), strong heat inward transport has been observed, in particular for low density. The maximum point of the first harmonic amplitude profile is found to be shifted towards the plasma center relative to the heating position, which can be considered as the signature of the heat pinch. Two transport models have been applied in order to analyze the experimental behavior. The first one is the Linear Pinch Model (LPM), *i.e.* a simple diffusive/convective model with piecewise constant coefficients. The second one is an empirical model based on micro-instabilities theory,

purely diffusive and non-linear, named Critical Gradient Model (CGM). Good agreement has been found for all harmonics between the experimental data and the simulation using the LPM, which includes time constant diffusivity and convection velocity profiles. It should be emphasized that the heat diffusivity, the heat convection velocity, and the damping time can be independently determined in LPM by using the sensitivity of the phase and amplitude of the modulated electron temperature relative to these three parameters. On the other hand, good agreement has not been achieved using the CGM. An additional heat pinch is needed for CGM in order to reproduce both experimental amplitude and phase. Micro-instability analysis by Weiland Model (WM) shows agreement on diffusivity, while it produces a much smaller inward pinch compared to the LPM and CGM results.

The density pump-out with large particle and energy losses during ECRH is commonly observed in the tokamak[1]. The phenomenology which was first reported in the T-10 tokamak in 1976 [2] is that the application of ECH or ECCD may cause the density to redistribute radially, usually from the center toward the edge, appearing as a decrease in the line averaged density of 30% or more, or even for the total number of electrons in the plasma to decrease. However, this phenomenon is thought to be governed by transport processes[3,4], but it is not completely understood at present. This effect can be an interesting control tool in the next fusion reactors as ITER for the removal of the alpha particles produced by fusion reactions from the center, for the density peaking reduction to increase β limit, and for the core impurity evacuation. A new dynamic approach using the modulation technique has been used in HL-2A for analyzing the transient phase of the density pump-out. Negative density perturbation (density pump-out) in the central region has been observed, and also a positive density perturbation in the peripheral region. The edge density increase is likely due to the out-gassing caused by ECRH on the plasma facing components[1]. Strong asymmetry for the negative and positive density perturbation propagation has been observed, which is very similar to that observed in cold and hot pulse heat transport. The outward convection (negative velocity) has been observed during the pump-out transient phase. Correlation between the turbulence increase and the density pump-out has been found. Turbulence reduction has been observed during the pump-out/pinch transition.

The "non-local" transport phenomenon[74], characterized by a fast transient process compared to the normal diffusive response to the perturbation, is observed but the mechanism remains unclear. In low density cases, the edge cold pulse provokes central temperature increment, which is commonly observed in tokamaks. Experiments with modulated SMBI have been performed in Tore Supra and HL-2A for the investigation of the non-local effect. The density threshold under which this effect appears is found to be around 2.5×10^{19} m^{-2} (line integrated density) in Tore Supra. Before and after the injection of cold pulse, the time evolution of two thermodynamic forces, temperature and density gradient, are shown in one diagram. For different observations, that is, with or without the appearance of hot pulse in the central plasma, the patterns of the diagram are different.

Both phenomena, i.e., pump-out and non-locality, show a simultaneous variation on density and temperature. This can be an inspiration for the usage of *transport matrix* which considers the density and temperature evolution together. Simulations with a simple transport matrix, with non-diagonal terms coupling temperature and density, qualitatively reproduce the non-local and pump-out effects qualitatively. However, the physical process of this model is local and diffusive, hence the evolution of density and temperature is slower than the experimental observation. The combination of nonlinear process together with the transport matrix could be a good alternative compared to the independent formulation of heat and particle transport equations. In this case, some effects such as turbulence spreading, the transition between turbulence modes, and the formation of an internal transport barrier (ITB) driven by plasma rotation, can be introduced as the possible interpretations of these experiments.

Acknowledgement

Finally the thesis marathon comes to an end. The spectrum of the feeling ranges widely from far-infra to maybe gamma-ray. As a sensitive person defined by some friends of mine, I should apologized here for the incompleteness of the thesis work. This work covers from heat to particle transport of plasma, referring to two tokamaks in two countries, although being just a specific narrow point in the variety of physical world. I am honored to be given the chance to engage myself and also my four years' youth in this mission. Secondly I should immediately start the long list of acknowledgement.

I should pay my homage to my supervisor, Gerardo Giruzzi, the handsome and erudite Italian. It is he who chose and helped me to promote the profession level by learning and working in France. After the years of training, I noticed that white hairs are climbing up his head, which doesn't mean the autumn has come but hints how much energy he has devoted to this lazy student's career. His sincere attitude towards his students affected me a lot and almost every time after a discussion with him I can find myself energized and have positive viewpoints on everything. Unfortunately I am a person lacking of ability to handle the relationship between people, as a result, I lost too many opportunities to communicate with him. Thank you!! I couldn't find a single word or phrase to conclude my complex feeling towards this respectful teacher. So I just stop here.

I should give my endless thanks to Xiaolan Zou, my associated tutor, although he has rejected from time to time to be connected with this title. Anyhow, it is Xiaolan who has helped to draw me abroad and trained me in his subjects. With his help I learned different aspects of French life, like the bank, telephone, network, education, assurance and places of interest etc. And also he introduced me to the Chinese communities, which absolutely prevent me from going crazy due to loneliness. With respect to the work, following his instructions, I learned the basic knowledge of transport (not public but plasma physics) and knew how to deal with the experimental data and simulation curves. Almost all the CEA staff I know is because of Xiaolan's help. Thank you!

I should also thank Dr. Alain Bécoulet who had approved the register of a student from China. I also thank Xavier Litaudon for his warm welcome and timely concern for my study. I should also thank Tuong Hoang for his always appearance when I am in need. And I should also thank the original decision maker, Yong Liu (Director of SWIP, my master's supervisor) and Xuru Duan (Deputy Director of SWIP), who started my French travel and accelerated the accomplishment of this voyage.

I should give my thanks to Morten Lennholm. I have spent half a year working with him without perceiving he was in fact one of my bosses. Whenever I devaluate my English level he defended by demonstrating that he was not working on well in speaking French. Francesca Turco, my first officemate, a pretty popular nice Italian girl, has favored me a lot in handling CRONOS etc. At that time when she was still in office, it is amazing to find the room always full of people, joking and laughing. Anne, the post-doc of L.-G. Eriksson, also the officemate introduced me a lot in the western culture. Jean-François Artaud, thank you for your patient introduction and interpretation to the CRONOS code, with CRONOS I find an easy way to understand the composite system of plasma physics. Vincent Basiuk, an intelligent guy and also expert on the CRONOS code, helped me a lot in dealing with numerous problems. Thierry Aniel, thank you for doing me a favor on TPROF staff, its elaborated design has attracted me for a long period. Philippe Huynh who I misunderstand as a Chinese guy for the first eye, helped me a lot to install the CRONOS code on my computer. I should thank Clarisse Bourdelle for her generous assistance in analyzing the CRONOS simulation. Her strict attitude towards the experimental data left me strong impression and her instruction to find corresponding persons in charge of the diagnostics brought me wider view sight to IRFM. Frédéric Imbeaux, an expertise on transport modelling, helped me in understanding the necessity of building empirical model on heat transport and also helped me apply the CGM model, which is an important part in the thesis. Xavier Garbet, a hardworking cool professor and comprehensive theoretician, left me with pieces of splendid comments and viewpoints in our limited conversations. He himself absolutely is one of my examples in the future working life. I thank Patrick Maget for the arrangement of my experiments on Tore Supra. Thank you, Marc Goniche, for the always concerns to my thesis status and also for your arrangement of visiting the tokamak. Thank you, Didier Moreau, for the warm greetings from the beginning and the invitation to your Paque home party. Your reasonable separation between working time and spare time suits my taste. Laurent Colas, an expert on ICRH with a frank personality…I am sorry for disturbing you with ambiguous questions from time to time. Gloria Falchetto, thank you for your encouragement in time. Maurizio Ottaviani, thank you for your concern always there. Mireille Schneider, I admire your ability of suffering two cups of coffee in the morning and concentrating to the work. Jéronimo Garcia, I will never forget your big laugh for the jokes we talked about.

Benoit Lacroix, Jean-Louis Marechal, Sylvie Nicollet, thank you for your care always there. Jean-François Mahieu, thank you for installing the computers and giving me the LINUX accounts, I also thank you for the sharing of your family stories. Sylvain Brémond, I should say sorry that I failed to give some push to the cooperation between the two institute on some specific topics, and I should thank you for your confidence on me. Patrick Hertout, an energetic guy, I should have got more knowledge on French idioms through discussion with you. Nicolas Silvestrie, Karine

Vincente, Valérie Icard, Stéphanie Villechavrolle, Karine Ruiz, Anne Bigand, thank you for the staff you have helped me on the secretary affairs; with your aide, I can wander inside Cadarache, breathing the free academic air.

Thank all the staff on their necessary works on various diagnostics and heating systems, they are, Jean-Luc Ségui, Didier Elbèze, Frédéric Clairet, Christel Fenzi, François Bouquey, Roland Sabot, Roland Magne, Elodie Corbel etc. Without your work not a single word could be possible in this thesis.

Gaël Selig, I share the office for almost two and half a year with him. There are a lot of warm memories from talking about Chinese and French culture, political and philosophy topics to family and jobs. I thank you for the help to train my French and I should say sorry for I failed to promote it quickly so that now my French level is still lower than pupils. Romain Futtersack, although I have joked on you about your romantic name, I found that you are rather gentle and sometimes sweet instead. Feng Liu, I thank you very very much for dragging me back to the normal life!! You are one of the key persons who helped me turn over some old view of points towards the world. Guillaume Jiolat, thank you for all the encouragement during the three years we know each other. Nicolas Cypres, your optimism deeply affected me, and I should also thank you lifting me to Cadarache from time to time. Timo Dittmar, always smart and curious towards science, thank you, I may tell you I finish it now; I wish we meet in various meetings my friend. Özgur Gürcan, finally I am at the last stage, I should have given you the news. Stanislas Pamela, you have shown your working ability by study and breeding two children at the same time, thank you for your warm encouragement and your thesis which helped me at the last moment. Patrick Tamain, I knew you before but did not speak to you, good job for your thesis and you are also an example for me. Thanks to Alessandro Casati, your question about what model I used three years ago still hovers there. Thank you, Daniel Villegas, although you didn't have time in explaining the usage of QuaLiKiz code, thank you for your generous sharing of your thesis. Thank you, the young guys I got to know (some of whom I knew in my fourth year) at Cadarache, Farah Hariri (pretty and sportive girl), Thomas Cartier-Michaud (gentleman), Jonathan Jacquot (shy and intelligent), Timothée Nicolas (handsome and cute), François (active tall guy), David Zarzoso (unbelievable fluent French), Antoine Merle (cool guy), Dmytro Meschcheriakov (optimistic and modest), François-Xavier Duthoit (nobleman), Jérémie Abitboul (sophisticated at your age), Didier Vezinet (strong and humble), Gregoire Hornung (special voice) etc…Joking and laughing with you I found myself as young as five years ago.

I should say thank you to my entire Chinese colleagues working at ITER site: Caipin Zhou, very generous to the young people, helped me to visit some nice places. Talking to him always help you promote your eyesight. Youkun Fu, hardworking expertise on mechanics design, also helped me travel some places since I have no car (and driving license). Fu Zhang, thank you for your encouragement during the four years. Xiaoyu Wang, at similar age to me but has made more fruitful progresses. Yu Yang, thank you very much for your consistent kindness and also for your criticism to some of my wrong behaviors. I should give my acknowledgements to Shaoqi Wang, Peide Weng, Songtao Wu, Jie Yu, Damao Yang, Jun Tao, Fan Li, Huayan Che, Hang Wang, Mingxing Su and so on. Without you I cannot imagine if I still have the sense of belonging. I thank Doshi Bharat for his confidence on me. Thank you, Shimpei Futatani, for your sharing of the thesis and experience. Thank you, Valerie Bouquet, I won't forget your kindness bringing me to the nice scenery of the Mediterranean.

I also want to give my thanks to Weiwen Xiao, a guy who comes from SWIP and spent one year in Cadarache. We have shared a lot on various points ranging from politics to academic views. This guy is quite active enterprising, which is definitely in need on my side. I should thank Bojiang Ding, who comes from CIPP (Hefei): he shared a lot of experience abroad, which helped me a lot.

I should say thank you, Jacques Alexandre, I really regret to know you so late. Cécile, Roxane and Cyril, the time spent with you is unforgettable (if I forget it should be unforgivable).

Thank you, Audrée Daumas, the honorable landlady, thank you very much for the regarding letter per month, training my French. Yan Fei, a hardworking and experienced Chinese student, taught me basic knowledge on how to live in France. Liao Liao, a brilliant sociology student, shared a lot of information in different spheres. Mengchu Fu, making progresses in her high school career, helped me a lot in learning French.

Four years have passed. My wife acquired her doctor's degree and has already spent two years in Chengdu after getting a research job. From time to time I want to quit due to the difficulty but it's her devotion that let me hold on up to now. During these four years, two relatives passed away, my mother and grandma. The suffering of losing relatives seems to be just yesterday. Thank you, my great father; it's you who have upheld the family at this juncture. I should also thank my brother and sister-in-law; your persistence helped me work in France without too much anxiety.

Contents

Résumé 1
Abstract 16
Acknowledgement 19
Contents 23
Chapter 1 Introduction 26
1.1 Energy 26
1.2 Fusion 27
1.3 Tokamak 28
1.4 ITER 30
1.5 Motivations and outline of the thesis 32
Chapter 2 Heat and particle transport theory 34
2.1 Tokamak magnetic topology 35
2.2 Classical and neoclassical transport 36
2.3 Anomalous transport 38
2.4 Drift wave instabilities 39
Chapter 3 Methodology and numerical tools 42
3.1 Steady-state and perturbative transport analysis 42
3.2 Numerical tools 45
3.2.1 CRONOS 45
3.2.2 ANALYTIQUE 47
3.2.3 Inverse Fourier Hamonic Method 51
3.2.4 GSONIQUE 55
3.2.5 REMA 58
Chapter 4 Heat pinch investigation and experimental results 61
4.1 Earlier experiments and analyses on the heat pinch phenomenon 61
4.2 Experimental setup on Tore Supra 62
4.3 Experimental results 64
4.3.1 High density discharges 65
4.3.2 Low density case 68
4.4 FFT analysis 72
4.5 Sawteeth effect 74
4.6 Density effect 77

4.7 Conclusion 80
Chapter 5 Simulation of heat pinch experiments.. 82
5.1 ECRH deposition determination by REMA 82
5.2 CRONOS simulation 84
5.3 Simulation with the Linear Pinch Model 86
5.3.1 Sensitivity analysis.. 87
5.3.2 High density case 91
5.3.3 Low density case... 94
5.4 Simulation with the Critical Gradient Model... 98
5.4.1 High density case 99
5.4.2 Low density case... 100
5.4.3 Summary 103
5.5 Simulation with a simplified Weiland Model 104
5.6 Conclusion 106
Chapter 6 Density Pump-out experiments.. 108
6.1 Experimental setups on HL-2A 109
6.2 ECRH modulation analysis in limiter configuration 112
6.3 ECRH modulation analysis in divertor configuration 115
6.4 Discussion and Interpretation 118
6.5 Conclusions... 120
Chapter 7 Non-local experiments 121
7.1 Experimental setup on Tore Supra 121
7.2 Fourier analysis.. 137
7.3 Energy confinement and turbulence rotation 140
7.4 SMBI experiments on HL-2A.. 143
7.5 Conclusions... 147
Chapter 8 Coupled heat and particle transport simulation 148
8.1 The paradigm model 148
8.2 Qualitative simulation for the non-local phenomenon... 151
8.3 Qualitative simulation for the pump-out phenomenon 159
8.4 Comparison with experiments 164
8.5 Discussion and interpretation.. 166
Chapter 9 Conclusions... 168
Publications and conferences 172
Bibliography 174

Chapter 1 Introduction

1.1 Energy

Energy is one of the basic elements in the human society, in some sense the "lifeblood" of industrial society. One of the most important discoveries of the 20th century is the use of nuclear energy. The energy released by nuclear reactions per nucleon is approximately a million times that of the more conventional chemical reactions. The enormous energy release of nuclear reactions can be explained through the binding energy of the atomic nuclei. One of the fundamental concepts of nuclear energy is the concept of the equivalence of energy and mass, which was first introduced by Albert Einstein in 1905 as a conclusion of his special theory of relativity. Energy can be obtained from a reaction between nuclei that decreases the mass of the system.

Figure 1.1 shows the measured values of the packing fraction for various isotopes, which means the energy per nucleon. The value of the packing faction is defined as $P = (M\text{-}A)/A$, where M is the isotopic mass, A is the mass number. This fraction can have positive or negative sign: a positive fraction describes a tendency towards instability, while a negative one means that the isotopic mass is less than the actual mass number. By examining the graph for packing fractions, it is seen that energy can be released by either of the two methods: production of heavier elements out of light elements, or breakdown of an extremely heavy element into medium heavy elements. We call the first type of nuclear reaction fusion, and the second one fission. Although from Figure 1.1 we could find that nuclear fusion could produce far more energy per unit, the pace of development of nuclear fission energy was much faster than that of nuclear fusion.

Since the build-up of the first nuclear power stations in the 50's, nuclear fission plays a more and more important role in energy production. According to IAEA (International Atomic Energy Agency), in 2009, 13-14% of the world's electricity came from nuclear power. However, nuclear fission faces three main challenges: limited Uranium resources; safety and security issues; radioactive waste. The long-lasting industrial development and safe human life calls for new alternatives. Nuclear fusion is one of them.

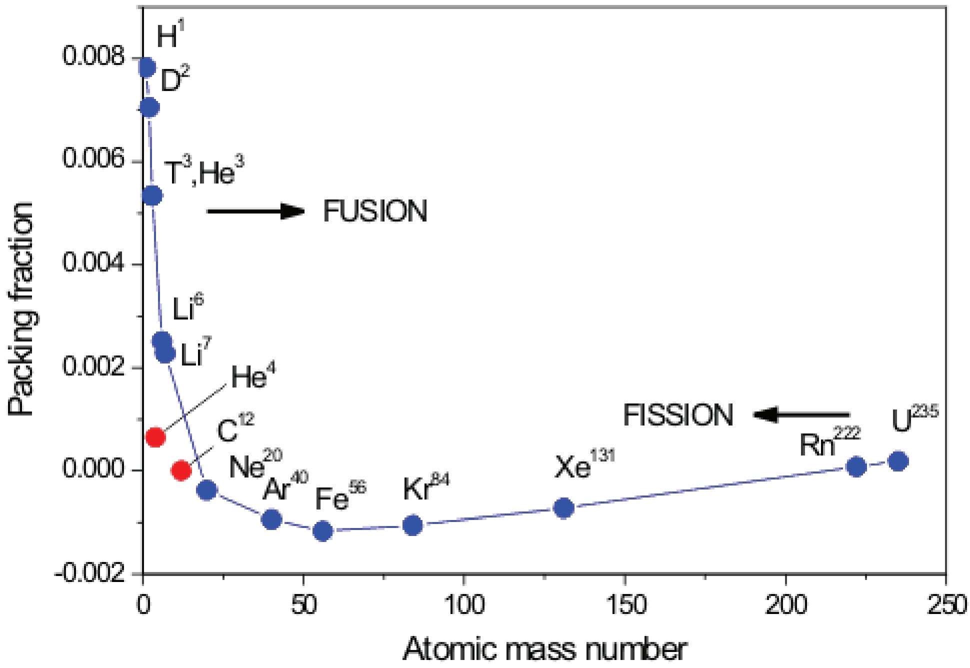

Figure 1.1 Packing fraction $P = (M\text{-}A)/A$ as a function of mass number A, where M is the actual mass of the nucleus

1.2 Fusion

Deuterium and tritium are the most often investigated elements for nuclear fusion applications. The energy released per nucleon for Deuterium is about 8 times higher than that of Uranium. 1 liter of sea water contains only 0.033g Deuterium, however, through fusion reactions the energy released is equivalent to that of 300 liters of oil. Taking into account Lithium availability (since Lithium is the material used to produce Tritium) on earth, fusion energy can produce at least thousands of years for human being.

The most accessible reaction for fusion applications is the one between Deuterium and Tritium. The related reaction equation is:

$$D + T \rightarrow He^4(3.52MeV) + n(14.06MeV) \qquad (1.1)$$

where T is triton, He^4 is helium-4 (also known as α particle) and n is neutron. In order to bring the two nuclei together, the Coulomb barrier has to be overcome, which requires very high temperatures. In order to make fusion happen, the ions need overcome the electrostatic repulsion between each other, considering the energy distribution and tunneling effect, the necessary temperature for fusion is around

10keV (i.e. approximately 10^8 K). The working substance for fusion is hot plasma, i.e., a highly ionized and globally neutral gas, usually known as the fourth state of matter. The difficulty for fusion research is to confine the ionized plasma at very high temperature in special containers.

In order to realize a sustainable fusion process, the kinetic energy carried by α particles should replace the external heating source and sustain the necessary high temperature. This condition is called ignition condition. In the temperature range of 10-20 keV, the ignition condition is approximately equivalent to the following condition:

$$nT\tau_E > 3\times10^{21}\mathrm{m}^{-3}\mathrm{keVs} \tag{1.2}$$

where n is the density, T is temperature and τ_E stands for the energy confinement time. This triple product is a major figure of merit evaluating the performance of fusion plasmas and also the top level requirement for a fusion reactor.

Different kinds of approaches have been investigated to confine the hot plasma, and they can be classified into magnetic confinement and inertial confinement. Inertial confinement uses high power lasers or accelerated particle beams to implode a pellet of D-T fuel to form the very high pressure that makes fusion occur. The magnetic confinement methods include toroidal and open end configurations. Open end configurations are limited by end loss of particles and the confinement time cannot be improved by increasing size or intensity of magnetic field. The most promising approaches for toroidal configurations are tokamaks and stellarators. The stellarator is a kind of device which has helical rather than axially symmetric magnetic field [5]. The poloidal fields necessary for confinement are produced by external coils rather than by plasma current. It has the merit of avoiding thermal and mechanical cycling, current drive and disruptions as tokamaks have. However the most promising research line nowadays is still focused on the tokamaks.

1.3 Tokamak

Tokamak is the most successful device yet found for magnetic confinement of hot plasmas. The name comes from a Russian acronym for toroidal magnetic chamber. It was first proposed by Lev Artsimovich in 1956. In its early days, it quickly produced much higher performance parameters than other configurations, which attracted much attention of the international scientific community, and motivated the construction of several tokamaks. The shape of the tokamak plasma is like a ring, confined by the strong magnetic field which includes two parts: toroidal (i.e. along the ring) and poloidal (i.e. the direction cycling around the ring). For pure toroidal field configurations, the charge separation induced electric field can lead to outward drift which causes particle loss. The presence of a poloidal field connects the upper and lower parts of the plasmas by magnetic field lines, and overcomes the drawback of the purely toroidal field configuration. The poloidal magnetic field is mainly produced by an electrical current flowing in the plasma, which is a good conductor. Figure 1.2 shows the structure of a typical tokamak, in which the plasma current is produced by a magnetic circuit playing the role of a transformer.

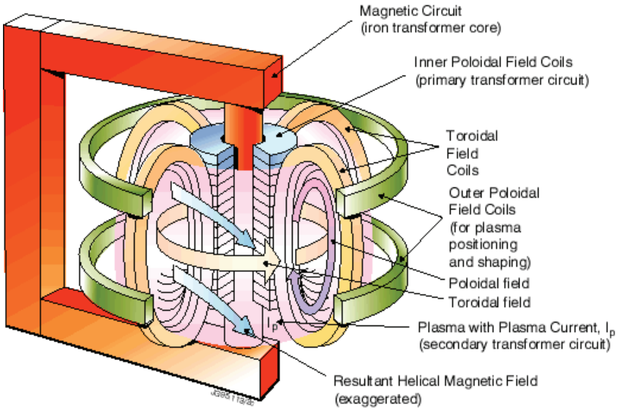

Figure 1.2 Tokamak approach for fusion reactor

Once the plasma is confined, it is necessary to heat it up to thermonuclear temperatures. The plasma heating is obtained by Ohmic heating, radio frequency wave heating and beam heating. Pure Ohmic heating by the plasma current can heat the plasma to temperatures of a few keVs. However, owing to the simultaneous decrease of plasma resistance the efficiency of Ohmic heating deteriorates quickly. Additional heating is then needed either by particle beams or radio frequency waves. After research efforts of several years, the record was obtained for fusion power production in the European tokamak JET of 16 MW and a Q factor (which stands for the ratio between generated and injected power) of 0.7.

One of the methods to predict the future tokamaks is through empirical scaling, which is to accumulate data from a number of tokamaks and to use statistical methods to determine the dependence of the confinement on the parameters involved [6]. The scaling therefore allows extrapolation to the projected tokamaks within some error for prediction purpose. Figure 1.3 shows a scheme of the evolution of confinement during the past decades [7]. In this figure, the progress is illustrated by the triple product $n_i T_i \tau_E$, where n_i and T_i are ion density and temperature respectively, and τ_E is the energy confinement time. τ_E is defined in terms of steady state plasma as the ratio between plasma energy content and the necessary input power. This triple product represents a figure of merit for plasma performance. Steady improvement of tokamak performance leads to the interest and necessity of constructing a much larger tokamak aiming at the commercial use of fusion energy.

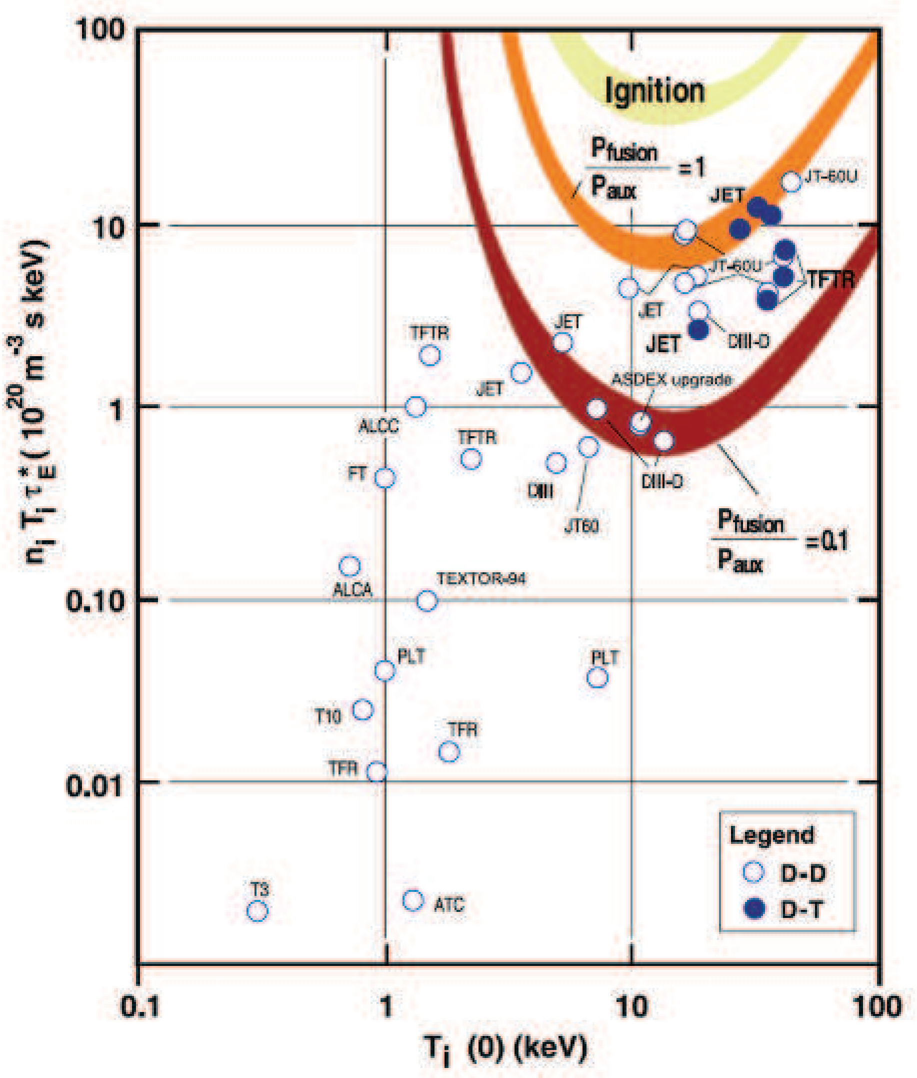

Figure 1.3 Confinement improvement scheme. (After Ref. [7])

1.4 ITER

ITER (International Thermonuclear Experimental Reactor) is an international tokamak research project that will make the transition from today's studies of plasma physics to future electricity-producing fusion power plants. The construction of ITER can help build further knowledge on the burning plasma physics, and also integrate technology with physics. Furthermore it will demonstrate and test some fusion power plant technologies. The main physics goals of ITER are: to produce plasmas dominated by α-particle heating; to produce a significant fusion power amplification factor (Q = 10) in long-pulse operation; to achieve steady-state operation (Q = 5); and also to retain the possibility of exploring controlled ignition (Q = 30). The technology goals are: to demonstrate integrated operation of technologies for a fusion power plant; to test components required for a fusion power plant; and to test concepts for a tritium breeding module [8].

Already balanced between ambitious physical goals and economic restrictions, the cost of constructing the ITER tokamak still exceeds 10 billion euros. For a project which does not bring in direct economic profit, the cost is prohibitive for a single country, therefore it is now shared among 7 international partners (EU, USA, Japan, Russia, Korea, India and China). For now, ITER is the largest energy research project worldwide and also an important example of global scientific and technical collaboration. It will be a test bed for many of the components needed for a practical fusion power station. The constructive work has already been started at Cadarache, France, and the first plasma is scheduled to be generated in 2019, which will definitely pave the way for further improvement of the knowledge on both physical and engineering needs for reactor size tokamaks. Here we give the main parameters of the future ITER experiment in Table 1.1 [9].

Table 1.1 ITER experiment – representative parameters

Parameter	Units	Value
Minor radius (a)	m	2.0
Major radius (R_0)	m	6.2
Inverse aspect ratio ($a/R_0 = \varepsilon$)	-	0.32
Plasma elongation (κ)	-	1.85
Toroidal magnetic field at R_0 from the central axis of the machine (B_T)	T	5.3
Nominal plasma current (I_p)	MA	15
Initially-installed additional plasma heating	MW	73
Plasma pulse length (inductive drive / steady-state operation)	s	400 / 3000
Average electron density ($\langle n_e \rangle$)	m^{-3}	1.1×10^{20}
Average electron temperature ($\langle T_e \rangle$)	keV	8.9
Peak fusion power	MW	500

1.5 Motivations and outline of the thesis

Transport of heat and particles is a central problem of tokamak plasma physics, in the framework of controlled thermonuclear fusion research. In order to improve our knowledge of both particle and heat transport phenomena, studies of transport using perturbations of an equilibrium state, have been carried out on the two tokamaks: Tore Supra (IRFM, CEA/Cadarache, France) and HL-2A (South-Western Institute of Physics, Chengdu, China). With this basic methodology we have investigated three different transport phenomena: *inward heat pinch*, *density pump-out*, and *non-locality*.

For a typical tokamak plasma, the temperature profile is peaked in the core and minimum at the edge. This peaked profile leads to a consistent heat flux directed outwards due to the diffusion effect. However, inward heat convection has been observed in some experiments and it is thought to be favorable for the improvement of plasma energy confinement[26,27]. In this thesis, the phenomenon of inward heat pinch has been experimentally investigated, by means of dedicated power modulation experiments. This programme has been carried out through low frequency modulation of Electron Cyclotron Resonant Heating, diagnosing the response on the temperature profile.

Generally, a peaking factor $n_0/\langle n\rangle$ defined as the ratio between the central density and line averaged density is introduced to denote the shape of the density profile. Peaked profile is one of the desired properties of tokamak plasma as it produces higher fusion gain [10]. Early limiter L-mode plasmas in tokamaks had peaked density profile; while in H-mode operation, a density pedestal appeared and profiles become flatter. It is recognized that the peaked density seems to be dependent on the turbulence-driven particle pinch [72]. An interesting phenomenon is the density flattening effect after the injection of ECRH power, which is called the *density pump-out effect* [1]. The thesis also focuses on the ECRH induced pump-out effect, by experimental studies carried out on the HL-2A tokamak.

In the modeling of perturbative transport experiments, transport is assumed to be a locally determined process. However, in some experiments, the rapid response to perturbations is much faster than allowed by a purely local process. The third focus of this thesis is on the so-called *non-local transport effect* [74]. The experimental tool is the Supersonic Molecular Beam Injection (SMBI). Accompanying the fast transient response, a phenomenon of opposite polarity on the temperature perturbation is observed, i.e., a heating of the core while the edge is cooled. The condition of appearance of this opposite polarity has been investigated, in particular by analysing the effects of a non-diagonal transport matrix.

The outline of this thesis work is the following. In chapter 2, the framework of the tokamak configuration and the flux coordinate description will be introduced. The two main approaches, i.e., fluid and kinetic description of the plasma will be addressed. The main equations of the heat and particle transport will be given, as well as a brief introduction of the main aspects of the heat and particle transport dealt with in this thesis. Main concepts are: diffusive and convective transport, neoclassical and anomalous transport, diagonal term contribution and nonlinear driven pinch. The physics of non-local and pump-out effects will be also discussed in this chapter. Chapter 3 mainly deals with the experimental and numerical tools of investigation, which include the power balance, perturbation and modulation methods, transport codes, ray-tracing codes and Fourier analysis. Chapter 4 describes the heat pinch experiment setup and basic results. Chapter 5 presents the two models used in the simulation of the heat pinch experiments and discusses the comparison between modelling and experimental data. Chapter 6 introduces the SMBI modulation experiments and related results, and also deals with the pump-out effect, investigated by means of modulated Electron Cyclotron Heating. Chapter 7 describes the experiments on non-local transport effects, carried out both on Tore Supra and on HL-2A. Chapter 8 presents systematic numerical simulations of coupled heat and particle transport equations, in particular to investigate the impact of a non-diagonal transport matrix. Finally, the main conclusions of this thesis work are presented in Chapter 9.

Chapter 2 Heat and particle transport theory

The basic problem of confining the plasma can be considered as a transport problem. In engineering and physics, transport is a subject which concerns the exchange of mass, energy or momentum within physical systems. It is a fundamental component of disciplines involving fluid mechanics, thermodynamics, kinetics, mechanics, electromagnetism etc.

In physics, transport phenomena refer to all irreversible processes of statistical nature stemming from the random motion of particles, mostly observed in fluids. They involve a net macroscopic transfer of matter, energy or momentum in thermodynamic systems that are not in statistical equilibrium. The main quantities of transport family include momentum, energy, and mass, which share similar mechanisms carrying out the exchange process and can be treated in a similar mathematical framework.

The theory of transport phenomena in hot plasmas is not isolated, and it starts from the transport theory developed in the fluids, including in particular neutral gas. However, due to the specific properties of the plasma, mainly related to particle ionization and the role of electro-magnetic fields, the transport theory in plasma has its own characteristics. Plasma transport theory can be characterized as a truly interdisciplinary domain. It refers to theoretical physics, kinetic theory, thermodynamics etc.

Nowadays, the transport theory of plasmas can be classified into two groups, one is classical and neoclassical transport theory, the other is anomalous transport theory.

The classical transport theory is more or less similar to the traditional theory in neutral gas. Classical theory applies to plasmas in which the transport of matter, momentum and energy is governed by the interaction of the particles through binary collisions. The external magnetic field is assumed to be straight, homogeneous and stationary.

Neoclassical theory applies to plasmas in curved, inhomogeneous magnetic fields. The neoclassical theory can be considered as an extension of classical theory to the real magnetic confinement cases. It is found that the global geometry of the field plays a dominant role even in the limit of very weak collisions.

Anomalous transport theory arises from the phenomenon that the experimentally measured transport coefficient is quite often larger than the neoclassical predictions, where the word anomalous refers to this inexplicable fact at that time. Turbulence is thought to play a major role and its physical regime is connected with the plasma wave instabilities; therefore, the anomalous transport is usually called turbulent transport. Nowadays, turbulent transport is a quite active area of research, which is in accordance with the large interest in turbulence studies for neutral fluids.

The following sections are arranged as follows: section 2.1 describes the geometry of the tokamak plasma, section 2.2 introduces the basic concepts of classical and neoclassical transport, and section 2.3 gives a general description of anomalous transport.

2.1 Tokamak magnetic topology

The tokamak magnetic topology is to a good approximation axis-symmetrical, and it can be treated as a series of nested magnetic surfaces, as shown in Figure 2.1. The magnetic field is produced by external coils and by the plasma current. The resultant magnetic equilibrium field can be computed using the Grad-Shafranov equation, which in cylindrical coordinates (r, φ, z) writes

$$L(\psi)+\mu_0 r^2\frac{\partial p(\psi)}{\partial\psi}+\frac{\mu_0^2}{8\pi^2}\frac{\partial I^2(\psi)}{\partial\psi}=0 \tag{2.1}$$

where $L(\psi)=\left(r\frac{\partial}{\partial r}\frac{1}{r}\frac{\partial}{\partial r}+\frac{\partial^2}{\partial z^2}\right)\psi$, $\psi= rA_\varphi(r,z)$, and A is the magnetic vector potential. This equation is usually solved numerically by equilibrium codes, such as EFIT, HELENA, CEDRES. However, for circular plasmas, the case for Tore Supra, simplified form for magnetic force is normally given as,

$$B=B_\theta\hat{e}_\theta+B_\varphi\hat{e}_\varphi \tag{2.2}$$

$$B_\varphi=B_0\left(1-\frac{r}{R_0}\cos\theta\right) \tag{2.3}$$

Here, r is the minor radius; R_0 is the major radius on the magnetic axis.

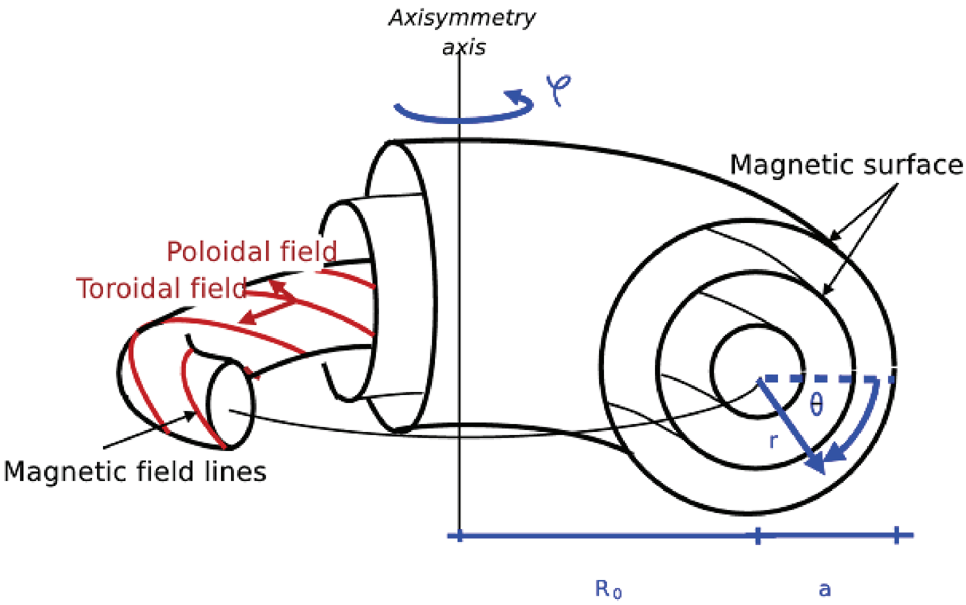

Figure 2.1 The tokamak core magnetic configuration and its traditional toroidal coordinates (After Ref.[11])

2.2 Classical and neoclassical transport

One of the most notable features of plasma is its ability to maintain a state of charge neutrality due to the low electron inertia. The field due to any charge imbalance is shielded, and therefore its influence is effectively restricted to within a finite range, which is called Debye length. For classical tokamak plasmas nowadays, the approximate value is $\lambda_D \sim 7\times10^{-5}$m.

The transport process can be characterized, for simplicity, by diffusion coefficients, with dimension of (length)^2/time. In non-magnetised plasmas, the diffusion coefficient of particles can be estimated using random walk theory, as

$$D = \lambda_c^2 / \tau_c \tag{2.4}$$

Where λ_c is the *mean free path*, and τ_c is the collision time. For uniform magnetized plasma, the transport is anisotropic, i.e., it can be described by two different components, one is parallel, and the other is perpendicular to the magnetic field lines. The parallel diffusion is not affected by the magnetic effect,

$$D_{||} = \lambda_c^2 / \tau_c \tag{2.5}$$

While for strong field case, $|\Omega| >> \nu_c$, i.e. the cyclotron or Larmor frequency much larger than the collision frequency (which is generally true for tokamak plasmas), we have

$$D_\perp = r_L^2 / \tau_c \tag{2.6}$$

where r_L is the Larmor radius, i.e., the charged particle rotation radius around the magnetic field line. Therefore the ratio between the parallel and perpendicular diffusion coefficient is $(\lambda_c/r_L)^2$, which is always >> 1. In other words, the diffusion process in the parallel direction is much faster than in the perpendicular direction. Strong magnetic fields lead to strong decrease of diffusion across the magnetic lines, and this is the original basis of the magnetic confinement concept. Once temperature or density gradients form in the parallel direction, they can be quickly restored to flat profiles, and hence in the parallel direction, the plasma can be treated as uniform in density and temperature.

However, the dynamical behaviour in the perpendicular direction is more complex. In magnetized plasma, the motion of charged particles can be treated as the superposition of a relatively fast gyration motion around a point called guiding center and a relatively slow *drift* of this point. For the tokamak configuration, the gradient and curvature of the magnetic field can lead to a drift of the guiding center, which enhances the diffusion by

$$D_\perp^{col} = q^2 r_L^2/\tau_c \tag{2.7}$$

where q is the safety factor, which stands for the ratio between the toroidal and poloidal angle variations along the magnetic field line.

In toroidal configurations, another process happens. Particles with small enough parallel velocity $v_\parallel$, may be reflected and trapped in the high field side to form banana-shaped orbits. The portion of trapped particles is approximately $\varepsilon^{1/2}$, where $\varepsilon = r/R_0$ is the inverse aspect ratio. Although this value is small, it plays an important role in the determination of the diffusion coefficient, since these particles have slower average parallel velocity and therefore longer time staying in the orbits. Considering the trapped particles effect, we have

$$D_\perp^{ban} = (q^2/\varepsilon^{3/2}) r_L^2/\tau_c \tag{2.8}$$

which is a factor $1/\varepsilon^{3/2}$ larger than for the passing particles. This regime is crucial in the case of low collision frequency $\nu_c < \varepsilon^{3/2}/\tau_B$, where τ_B is the bounce time the particle takes to experience a complete banana orbit before being scattered out of the orbit by collisions.

The resultant dependence of the diffusion coefficient on the collision frequency is shown in Figure 2.2. Three regimes are shown schematically, characterized by different collision frequencies. The corresponding transport coefficients are called *neoclassical transport coefficients* compared to those of *classical transport*.

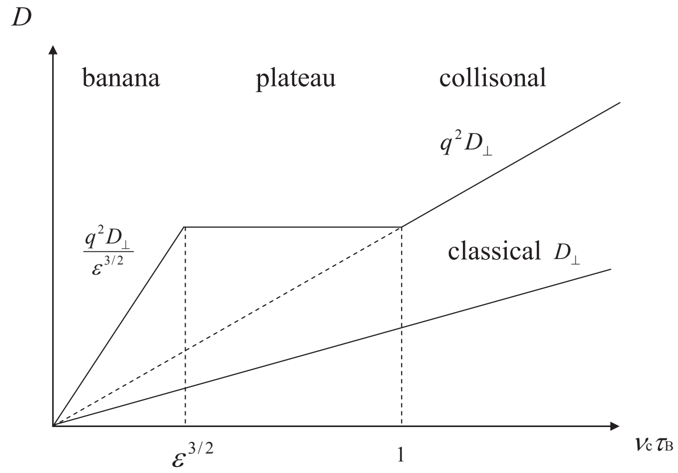

Figure 2.2 Dependence of perpendicular diffusion coefficient on collision frequency

2.3 Anomalous transport

The previous section describes transport caused by *binary collisions*, which gives the confinement time for the most ideal case. With classical and neoclassical transport coefficients only, the losses of particles and energy would be low enough for fusion to be demonstrated in tokamaks of modest size. However, the actual transport diffusion coefficient observed in experiments was much higher than the prediction using neoclassical theory, especially for electrons, usually about two orders of magnitude or more. The name of *anomalous transport* was therefore given to this process. At present, it is one of the major obstacles for the realization of controlled thermonuclear fusion.

The anomalous transport of particles is usually related to the turbulent character of the plasma behavior. Turbulence is a state characterized by a certain level of fluctuations. In fluid, characteristic macroscopic quantities, such as density, temperature, and sometimes magnetic field, are not in a quiescent state. Once the fluctuations get stronger, they evolve into coherent structures, and then in the macroscopic scale the fluid can show a chaotic behavior. The counterpart of turbulent flow is laminar or stratified flow. It has been demonstrated that hot plasmas in most magnetic confinement devices are in a turbulent state. Ever since the close connection between turbulence and transport was discovered, the investigation of turbulence transport in plasma has become a very important subject of research.

Under specific assumptions, fluid motion can be decomposed into two parts: one is the large scale, mean flow, and the other is some small scale, randomly fluctuating component. For density and fluid velocity, we have

$$n = n_0 + \tilde{n} \tag{2.9}$$

$$v = v_0 + \tilde{v} \tag{2.10}$$

If we substitute them into the equation of continuity,

$$\frac{\partial n}{\partial t} + \nabla \cdot (nv) = 0 \tag{2.11}$$

We can get the variation due to fluctuations, assuming the time variation of n_0 is a second order quantity, i.e.,

$$\frac{\partial n_0}{\partial t} = -\nabla \cdot (\tilde{n}\tilde{v}) \tag{2.12}$$

Under the framework of Fourier analysis, if the phase between the fluctuation of density and velocity is not synchronous, a particle flux is induced. Turbulent diffusion can also be described using diffusion coefficients. With so called mixing length estimate, the diffusivity can be expressed as:

$$D = L^2/\tau_c = \gamma/k^2 \tag{2.13}$$

Here L is the characteristic length (radial mode correlation length), τ_c is the autocorrelation time (eddy turnover time), γ and k are the growth rate and wave number of the maximum turbulent mode, respectively. For small scale turbulence with $L \sim \rho_s$, which is the gyro-radius of ions, we get the gyro-Bohm scaling; for larger scale turbulence with $L \sim (a\rho_s)^{1/2}$, where a is the minor radius, we have the Bohm scaling, which corresponds to the maximum diffusion coefficient. However one should remember that these coefficients are only phenomenological estimates, to be compared to classical and neoclassical transport coefficients.

2.4 Drift wave instabilities

One major phenomena leading to fine scale plasma turbulence is microinstabilities. These instabilities have wavelengths comparable to the ion Larmor radius.

Drift waves are the prominent member in the family of microinstabilities. Drift refers to the motion of the guiding center with respect to the magnetic field. In homogenous plasmas, drifts can be divided into four groups according to their mechanisms, that is,

The $\boldsymbol{E}\times\boldsymbol{B}$ drift:

$$\mathbf{v}_{\mathbf{E}} = \frac{\mathbf{E}\times\mathbf{B}}{B^2} \tag{2.14}$$

The ∇B drift:

$$\mathbf{v}_{\nabla B} = \frac{1}{2}\rho_j \frac{\mathbf{B}\times\nabla B}{B^2} v_\perp, \quad \rho_j = \frac{m_j v_\perp}{e_j B} \tag{2.15}$$

The curvature drift:

$$\mathbf{v}_c = \frac{v_\parallel^2 + \frac{1}{2}v_\perp^2}{\omega_{cj}} \frac{\mathbf{B}\times\nabla B}{B^2}, \quad \omega_{cj} = \frac{e_j B}{m_j} \tag{2.16}$$

The polarization drift:

$$\mathbf{v}_p = -\frac{1}{\omega_{cj} B}\frac{\mathrm{d}\mathbf{E}}{\mathrm{d}t} \tag{2.17}$$

In homogeneous plasmas, the combination of $\boldsymbol{E}\times\boldsymbol{B}$ drift, polarization drift and parallel motion of electrons produce ion acoustic waves. Once the pressure gradients are induced, the drift waves are formed. The corresponding frequency is called diamagnetic frequency. For electrons, we have

$$\omega_{*e} = -\frac{k_y T_e}{eBn}\frac{\mathrm{d}n}{\mathrm{d}r} \tag{2.18}$$

Both potential and density fluctuations travel along the direction which is orthogonal to B and ∇n. Without resistivity, there is no phase shift between the two, and the propagation of drift wave is just like that of a water wave; no radial transport is produced. However, with resistivity, the decay of the electron response leads to a phase lag with respect to density fluctuations, hence the wave gets “energy” from the density gradient and radial transport happens. Besides, other major mechanisms responsible for the phase shift are the Landau damping and breaking of the hypothesis of electrons adiabadicity. Similarly, temperature gradient can also be a source for drift instabilities.

Considering the gradient of magnetic force, in the region where density gradient and magnetic gradient are in the same direction, charge separation can be induced, arising from the initial density perturbation, which may enhance the wave. This is called *interchange* instability, the mechanism of which is analogous to the Reyleigh-Taylor instability. The magnetic geometry is then divided into “unfavorable” and “favorable” curvature regions, which are located in the low-field side and the high-field side, respectively. For passing particles, they experience both regions. The amplification of the instability could be suppressed partly when travelling in the favorable region. The situation for trapped particles is different, because they spend more time in the unfavorable region.

The main instabilities responsible for the anomalous transport in core plasmas are ITG, TEM and ETG modes. ITG (Ion Temperature Gradient) mode is often referred to as η_i mode, since the most relevant parameter for the turbulent drive is the ratio $\eta_i = d(\log T_i)/d(\log n)$. The TEM (Trapped Electron Modes) are electrostatic modes due to trapped electrons active at the ion spatial scales. The free energy source can be ∇T_e as well as ∇n_e and they are usually classified into (1) collisional and (2) dissipative (CTEM and DTEM) trapped electron modes. The DTEM is more dangerous since it is related to collisionalities which exist no matter the magnetic curvature is good or bad. The ETG (Electron Temperature Gradient) mode is the electron counterpart of the ITG mode, the energy forces are ∇T_e as well as ∇n_e, and the relevant parameter is $\eta_e = d(\log T_e)/d(\log n)$. Figure 2.3 shows the wavelength spectrum of the three major instability schemes [12]. Beyond the above-mentioned three modes, other instabilities, such as micro-tearing and current diffusive ballooning modes, in which dissipative processes such as collisional resisitvity or anomalous current diffusion plays essential roles, may be important at some specific circumstances. The drift-Alfven mode and the pressure (or resistivity and current) gradient driven modes may become more important at the edge.

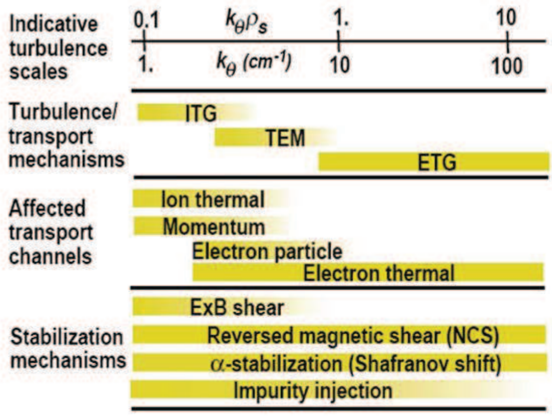

Figure 2.3 An schematic summary of drift wave turbulence scales, with corresponding turbulence mechanisms, affected transport channels and stabilization mechanisms. (After Ref.[12])

Chapter 3 Methodology and numerical tools

3.1 Steady-state and perturbative transport analysis

Experimentally, transport can be investigated at equilibrium under steady-state conditions through the balance equation of the considered quantity [13]. The so-called *perturbative transport* or *transient transport* approach, investigate the response of a system to a small perturbation around equilibrium yields further information, which is proven very fruitful to study transport in fusion plasmas.

Transport of physical quantity y is governed by its continuity equation,

$$\frac{\partial y}{\partial t} = -\nabla\Gamma_y + S_y \tag{3.1}$$

where Γ_y is the flux of y and S_y are the sources and/or sinks. The aim of transport studies is to find the relation between the fluxes and the thermodynamic forces (∇n_e, ∇T_i, ∇T_e and E_ϕ). Often these relationships are written in matrix notation [14]

$$\begin{pmatrix} \Gamma \\ q_e \\ q_i \\ j \end{pmatrix} = \begin{pmatrix} D & a_{12} & a_{13} & W \\ a_{21} & \chi_e & a_{23} & a_{24} \\ a_{31} & a_{32} & \chi_i & a_{33} \\ B & a_{42} & a_{43} & \sigma \end{pmatrix} \begin{pmatrix} \nabla n_e \\ \nabla T_e \\ \nabla T_i \\ E_\phi \end{pmatrix} \tag{3.2}$$

The fluxes are due to both diagonal and off-diagonal matrix elements. The fluxes due to the diagonal elements are often referred to as diffusive. The fluxes due to the off-diagonal components are often referred to as convective. The best-known examples of fluxes due to the off-diagonal components are the Ware-pinch (associated with W) and the bootstrap-current (associated with B). In neoclassical theory, the off-diagonal elements are non-zero generally. For simplicity, the considered flux can be written as

$$\Gamma_y = -D_y \nabla y + V_y y \tag{3.3}$$

D_y and V_y are diffusion and convection coefficients. All the off-diagonal terms can be transformed into the V_y terms. However, in steady-state, the two coefficients cannot be separated, and the flux is written in an effective diffusivity,

$$\Gamma_y = -\chi_y^{eff} \nabla y \tag{3.4}$$

In transient transport experiments, a perturbation of Γ_y is induced with an adequate actuator to which the system responds with variations of y and ∇y. This yields the relation between flux and the gradient around the equilibrium point.

For steady-state analysis of particle transport, especially for the electron particle transport, the particle source is mainly located at the edge (e.g., $\rho > 0.95$), hence at the steady-state, the particle flux is zero in the bulk plasma (e.g., $\rho < 0.95$), as a result the ratio of the diffusive and convective transport coefficients can be derived, as

$$\frac{V_e}{D_e} = \frac{\nabla n_e}{n_e} \tag{3.5}$$

This formula gives the ratio of the two coefficients; however, the value of each coefficient remains unknown.

For steady-state analysis of heat transport, both the source and sink are not localized as is in the particle case. The usual way to treat this is to find the effective diffusivity as shown in Equation (3.4). We define this quantity as χ_e^{PB}, as deduced from the power balance analysis.

$$\chi_e^{PB} = -q_e / n_e \nabla T_e \tag{3.6}$$

The first application of the perturbative method to investigate electron heat transport was carried out in 1974 with a pulse of electron heating in the FM-1 Spherator [15]. Three years later, the electron heat diffusivity deduced from the propagation of heat pulses induced by sawtooth crashes has been reported to be much faster than assuming χ_e from power balance [16]. Since then, numerous experiments and analyses have yielded the same conclusion. The results until 1995 were reviewed in [39]. An essential step in understanding perturbative experiments is the demonstration of the dependence of χ_e on ∇T_e in 1987 [17]. Defining χ_e^{PB} = $-q_e/(n_e \nabla T_e)$ the heat diffusivity from power balance, and χ_e^{HP} the heat diffusivity from the propagation of the perturbation, it is shown that,

$$\chi_e^{HP} = \chi_e^{PB} + \frac{\partial \chi_e}{\partial (\nabla T_e)} \nabla T_{e,0} \tag{3.7}$$

$T_{e,0}$ being the equilibrium temperature, assuming that χ_e depends on ∇T_e only and neglecting convection. This explains the observation $\chi_e^{HP} > \chi_e^{PB}$. Figure 3.1 is a sketch showing the relation between the power balance and perturbative analysis on diffusivities.

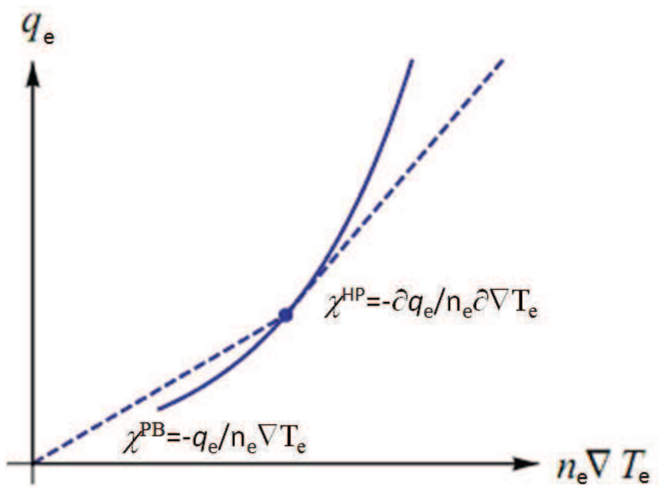

Figure 3.1 A sketch for the diffusivity deduced from power balance analysis and perturbative analysis

The actuators of perturbation vary in many forms. The main types of actuators used to excite the perturbation for electron heat transport are electron heating, 'cold pulse' induced by impurity injection, naturally occurring sawtooth crashes in tokamaks only. Sawtooth crashes have been widely used in the past, but it should be underlined that they are often not a small perturbation and 'ballistic effect', for instance, can affect the transport interpretation [18]. Indeed, χ_e^{HP} deduced from sawtooth pulse propagation can yield significantly larger values than those yielded by more controlled modulation [19].

One should take care in the use of perturbation analysis: the perturbation induced by external sources should be large enough to overcome the background noise, but also be small enough in order to avoid breaking the background parameters. For modulation experiments, a good choice of modulation frequency is important: too high would yield low modulation signals and also wipe out the pinch effect, but if it is too low, the characteristics of the radial propagation cannot be resolved [13].

Modulation method is an often used for perturbation analysis. It can reduce the experimental errors in the single perturbation case, by averaging the response to a series of independent and similar perturbations. Fourier transform of signals have been widely used in the modulation experiments, and some useful and simplified formulas have been derived [20,21]. Here we given the most often used one for the heat transport [21],

$$\chi_e^{HP} = \frac{3\omega}{4\phi'(A'/A)} \tag{3.8}$$

where A, ϕ and ω are the amplitude, phase and angle frequency of the Fourier harmonic respectively, and the primes denote radial gradient.

3.2 Numerical tools

In this thesis, the CRONOS code is used for the purpose of power balance analysis, the ANALYTIQUE code is used for perturbative analysis, under the assumption of transport coefficients constant in time; the GSONIQUE code is used to provide solution of the heat transport equation considering the effect of density variation and also the nonlinear effect of diffusivity dependence on the temperature gradient. The Inverse Fourier Harmonic Method is also introduced in order to analyse some specific cases (smooth amplitude and phase profiles). The REMA code provides the ECRH power deposition profile, computed by solving the ray propagation equations. These numerical tools are described in this Section.

3.2.1 CRONOS

The basic tool for power balance analysis that was used in this thesis work is the CRONOS code [22,23]. It is a suite of numerical codes for the predictive and/or interpretative simulation of a full tokamak discharge. It integrates, in a modular structure, a 1D transport solver with general 2D magnetic equilibra, radiation and particle losses, several heat, particle and impurities transport models, as well as heat, particle and momentum source modules. It also includes the essential ingredient for reactor simulations, i.e., the kinetic description of alpha particles generated by the fusion reactions. The CRONOS code includes the functions of direct access to the experimental databases of various tokamaks, using experimental profiles of various fluid quantities to deduce the transport coefficients, post-processing tools for evaluation and comparison with predicted output of several diagnostics. As a simulator, it is capable of predicting the full time evolution of a tokamak discharge, having as input the same control and feedback parameters that are used to pilot the machine itself. The strong point for CRONOS is that it offers a quite comprehensive suite of state-of-the-art modules for the heating and current drive schemes used on tokamaks, of which the major ones are shown in Figure 3.2.

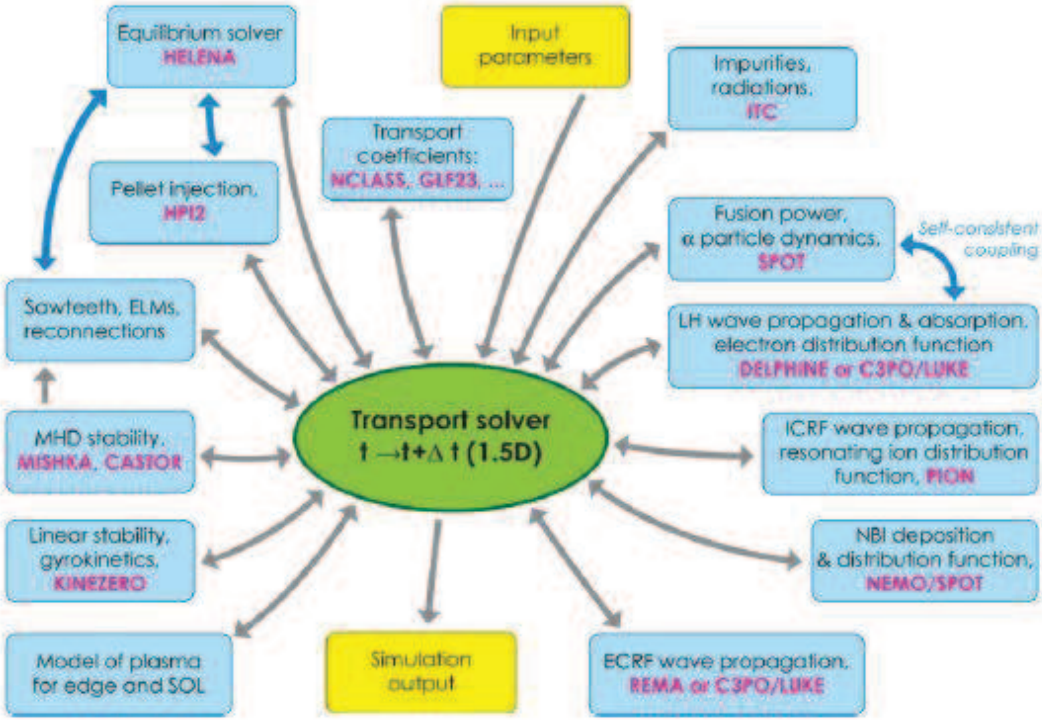

Figure 3.2 Global CRONOS workflow with the main sophisticated physics modules and the core transport equation solver. (Adapted from [23])

CRONOS includes an integrated graphical environment allowing setting up all simulation parameters, preparing input profiles from experimental data, post-processing (including synthetic diagnostics) and the specific visualization tools for the comparison of simulation results with experimental data.

The transport equations deal with radial transport only and most variables in CRONOS are time dependent 1D radial profiles, corresponding to the average values of physical quantities over an infinitesimal volume around a flux surface at given radial position. The radial grid is equally spaced in the normalized toroidal flux coordinate $x = \rho/\rho_m$, with $\rho = \sqrt{\Phi / \pi B_0}$, where Φ is the toroidal magnetic flux, B_0 is the vacuum magnetic field at a given major radius R_0 and ρ_m is the value of ρ at the last closed flux surface.

The equilibrium is calculated consistently with the evolution of the plasma profiles, thus the transport equations are solved based on the self-consistent equilibrium.

Here we give the basic transport equations for current diffusion, electron heat transport and particle transport as examples. The current diffusion equation is solved in terms of the poloidal flux Ψ, as,

$$\left.\frac{\partial\Psi}{\partial t}\right|_x = \frac{\left\langle|\nabla\rho|^2/R^2\right\rangle}{\mu_0\sigma_\parallel\rho_m^2\left\langle 1/R^2\right\rangle}\frac{\partial^2\Psi}{\partial x^2} + \left\{\frac{\left\langle|\nabla\rho|^2/R^2\right\rangle}{\mu_0\sigma_\parallel\rho_m^2\left\langle 1/R^2\right\rangle}\frac{\partial}{\partial x}\left[\ln\left(\frac{V'\left\langle|\nabla\rho|^2/R^2\right\rangle}{F}\right)\right.\right.$$
$$\left.\left. + \frac{x}{\rho_m}\frac{\mathrm{d}\rho_m}{\mathrm{d}t}\right]\right\}\frac{\partial\Psi}{\partial x} + \frac{B_0}{\sigma_\parallel F\left\langle 1/R^2\right\rangle}j_{\mathrm{ni}} \tag{3.9}$$

where $\sigma_\parallel$ is the parallel conductivity, F is the diamagnetic function, j_{ni} is the current density driven by non-inductive sources, R the major radius and m0 the magnetic permeability of free space. The notation < > is the magnetic flux surface average, defined as follows,

$$\begin{aligned}\left\langle A\right\rangle &= \frac{1}{\mathrm{d}V}\int_V A\mathrm{d}V = \frac{1}{dV}\int_\rho^{\rho+d\rho} d\rho\int_0^{2\pi} d\varphi\int_0^{2\pi} AJd\theta \\ &= 2\pi\frac{\mathrm{d}\rho}{\mathrm{d}V}\int_0^{2\pi} AJd\theta = \frac{2\pi}{V'}\int_0^{2\pi} AJd\theta\end{aligned} \tag{3.10}$$

The equation describing the conservation of electron thermal energy is,

$$\frac{3}{2}\frac{\partial}{\partial t}\left(P_e V'^{5/3}\right) + V'^{2/3}\frac{\partial}{\partial\rho}\left[V'\left\langle|\nabla\rho|^2\right\rangle\left(q_e + \lambda T_e\Gamma_e\right)\right] = V'^{5/3}Q_e \tag{3.11}$$

and its counterpart in ion channel,

$$\frac{3}{2}\frac{\partial}{\partial t}\left(P_i V'^{5/3}\right) + V'^{2/3}\frac{\partial}{\partial\rho}\left[V'\left\langle|\nabla\rho|^2\right\rangle\left(q_i + \lambda T_i\Gamma_i\right)\right] = V'^{5/3}Q_i \tag{3.12}$$

where P, T, q, Γ and Q represent the pressure, temperature, heat flux, particle flux and heat sources, and the subscripts e and i denote the electron and ion channels respectively. For the particle transport, the CRNOS only deal with the electron channel in the present status. The solution to the other ion species is acquired by specific ‘impurity’ modules.

$$\frac{\partial}{\partial t}\left(V'n_e\right) + \frac{\partial}{\partial\rho}\left(V'\left\langle|\nabla\rho|^2\right\rangle\Gamma_e\right) = V'S_{ne} \tag{3.13}$$

where S_{ne} denotes the particle source term. The sources or sinks for the heat and particle transport equation are from calculation in specific modules, which is not detailed here.

3.2.2 ANALYTIQUE

In this thesis work, the ANALYTIQUE code is used to obtain the solution of the linearized perturbative transport equation for both heat and particles. In the transport equation, the transport coefficients, i.e., diffusivity and convection velocity, are assumed to be constant in time. Equation (3.14) is an example for the heat transport,

$$\frac{\partial T_e}{\partial t} = \frac{1}{r}\frac{\partial}{\partial r}\left(r\kappa \frac{\partial T_e}{\partial r} + rvT_e \right) - bT_e + S(r,t) \tag{3.14}$$

where $\kappa = \frac{2}{3}\chi_e$, $v = \frac{2}{3}V_e$, $b = \frac{1}{\tau_d}$, $S = \frac{2}{3}\frac{P}{n_e}$.

The χ_e, V_e are the heat diffusivity and convection velocity, τ_d is the damping time representing the power loss rate due to various effects, and the use of κ, v and b are for the purpose of simplification. The source/sink term S has the dimensions of power. P is the heating power density, which is a function of space and time, depending on the shape of the heat source, e.g., the Ohmic power and heat deposition profile of radio frequency waves. The following initial and boundary conditions are chosen,

$$T_e(r,t=0) = 0,\ T_e(r=a,t) = 0,\ \frac{\partial T_e}{\partial r}(r=0,t) = 0 \tag{3.15}$$

The solution is obtained by the standard Green's function procedure involving the following steps:

(i) Start from the equation for the Green's function $G(r,r',t,t')$ associated with Equation (3.14), i.e., the same equation with a Dirac source term $S = \delta(r-r')\delta(t)$.

(ii) Solve the Laplace transform of the Green's function equation.

(iii) Find the singularities of the Laplace transform of G (eigenvalues).

(iv) Inverse-Laplace transform the solution back to the time domain.

(v) Space-time convolve the Green's function and the source to obtain the solution $T_e(r,t)$, i.e.,

$$T_e(r,t) = \int_0^t dt' \int_0^a dr' 2\pi r' G(r,r',t,t') S(r',t') \tag{3.16}$$

For nonzero initial and/or boundary conditions of the type

$$T_e(r,t=0) = T_0(r),\ T_e(r=a,t) = T_a(t) \tag{3.17}$$

It is straightforward to show that the solution can be expressed in terms of the same Green's function as

$$
\begin{aligned}
T_e(r,t) = & \int_0^t dt' \int_0^a dr' r' G(r,r',t,t') S(r',t') \\
& + \int_0^a dr' r' T_0(r') G(r,r',t,t'=0) \\
& - \int_0^t dt' T_a(t') \left[\kappa(r') r' \frac{\partial G}{\partial r} \right]_{r'=a}
\end{aligned}
\tag{3.18}
$$

The case of more general inhomogeneous boundary conditions, of the type

$$
h_1 T_e(a,t) + h_2 \left. \frac{\partial T_e}{\partial r} \right|_{r=a} = f(t) \tag{3.19}
$$

can also be treated as a generalization of the previous ones.

User friendly GUI interfaces have been developed and Figure 3.3 an example for the heat transport simulation case is given. The spatial profile of κ, v, and b are given piecewise, in our case five segments defined by setting up 4 separating points between the center and the edge, $x1$, $x2$, $x3$ and $x4$ as shown in the figure. The corresponding coefficients are defined by $\{k1, k2, k3, k4, k5\}$, $\{v1, v2, v3, v4, v5\}$, and $\{b1, b2, b3, b4, b5\}$. A sketch of the profiles is shown instantly after varying any parameters, which helps the user to have an initial idea of what was their effect on the profile. The perturbation source is defined by three parameters, the power, width and deposition point, assuming a Gaussian profile. The modulation frequency is defined and the number of numerical points is given, too. This interface allows the user to simulate the FFT components quite easily and makes the comparison with experimental data convenient. An example of simulation of the experimental data is shown in Figure 3.4.

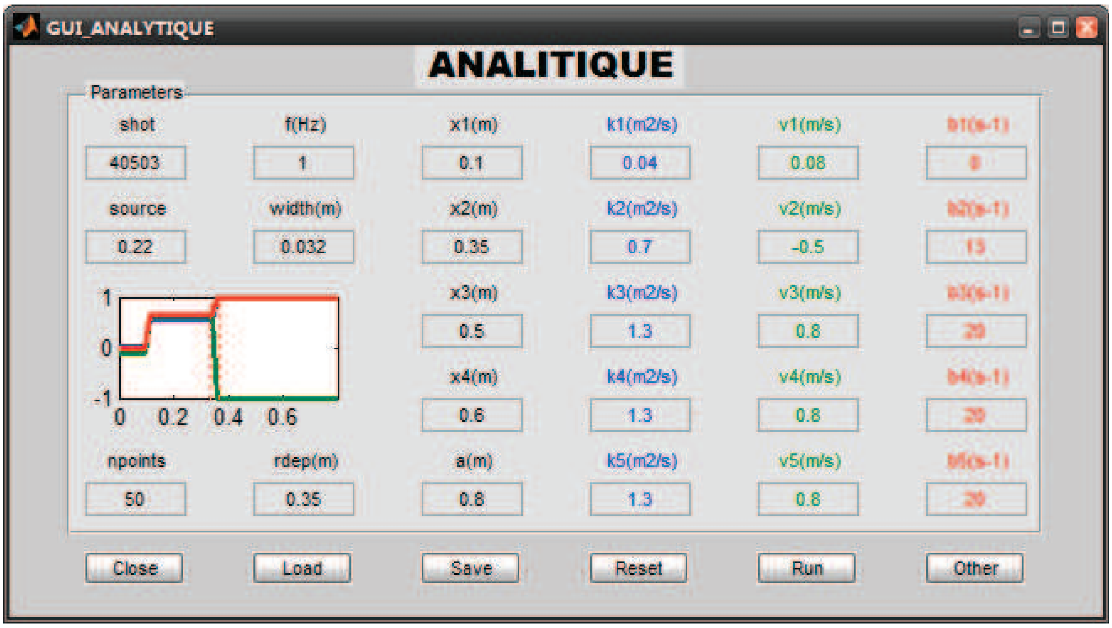

Figure 3.3 The interface of the ANALYTIQUE code

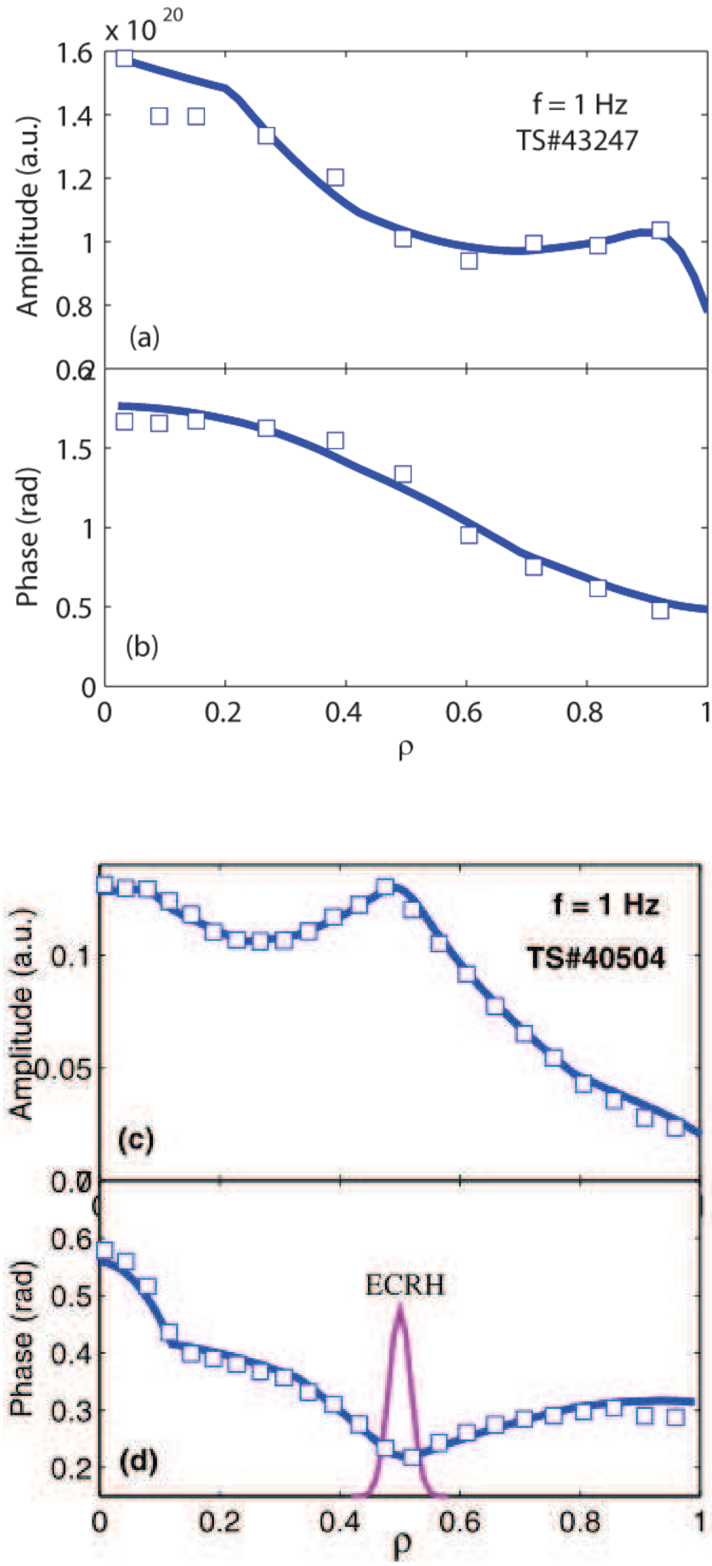

Figure 3.4 Comparison between experimental data and ANALYTIQUE simulation. Amplitude (*a*) and phase (*b*) profiles of density perturbation and their simulation results. Amplitude (*c*) and phase (*d*) profiles of the temperature perturbation and their simulation results. The discrete points stand for experimental data, while the solid lines represent the simulated results.

3.2.3 Inverse Fourier Harmonic Method

The Inverse Fourier Harmonic Method (IFHM) is developed in order to check the results obtained in the simulation with ANALYTIQUE. For the analysis of modulated particle and heat transport experiments, a method based on FFT analysis results can be used for the simplified transport equation. Once we treat the problem in the Frequency domain, we can find a direct way to determine the transport coefficients, in the case the coefficients are spatially constant or their variations can be neglected.

Firstly we give the derivation of some formulas used in this method:

Particle transport:

For particle transport, we have the form of

$$\frac{\partial n}{\partial t}+\frac{1}{r}\frac{\partial}{\partial r}\left[r\left(-D\frac{\partial n}{\partial r}+Vn\right)\right]=S \tag{3.20}$$

In the Frequency domain, the equation can be written as follows,

$$i\omega n_\omega+\frac{1}{r}\frac{\partial}{\partial r}\left[r\left(-D\frac{\partial n_\omega}{\partial r}+Vn_\omega\right)\right]=S_\omega \tag{3.21}$$

where $n_\omega(r)=\frac{1}{\sqrt{2\pi}}\int_0^T n(r,t)e^{-i\omega t}dt$, $S_\omega(r)=\frac{1}{\sqrt{2\pi}}\int_0^T S(r,t)e^{-i\omega t}dt$

taking the integral of Equation (3.16), one could get, assuming $\Gamma|_{r=0}=0$,

$$D\frac{\partial n_\omega}{\partial r}-Vn_\omega=\frac{1}{r}\int_0^r\left(i\omega r'n_\omega-r'S_\omega\right)dr' \tag{3.22}$$

For the case where particle source is localized in the edge, the formulas can be written as,

$$D\frac{\partial n_\omega}{\partial r}-Vn_\omega=\frac{1}{r}\int_0^r i\omega r'n_\omega dr' \tag{3.23}$$

Assuming $n_\omega(r)=A(r)e^{-i\phi(r)}$, then the solution of the above equation is obtained by solving,

$$D\frac{\partial A}{\partial r}-VA=\mathrm{Re}\left[\frac{e^{i\phi}}{r}\int_0^r i\omega r'Ae^{-i\phi}dr'\right] \tag{3.24}$$

$$DA\frac{\partial \phi}{\partial r}=-\mathrm{Im}\left[\frac{e^{i\phi}}{r}\int_0^r i\omega r'Ae^{-i\phi}dr'\right] \tag{3.25}$$

Heat transport:

Similarly, the heat transport coefficient can also be obtained by rewriting the transport equation in the frequency domain,

$$\frac{3}{2}\left(i\omega+\frac{1}{\tau}\right)nT_{\omega}+\frac{1}{r}\frac{\partial}{\partial r}\left[r\left(-n\chi\frac{\partial T_{\omega}}{\partial r}+nVT_{\omega}\right)\right]=P_{\omega} \tag{3.26}$$

$$T_{\omega}=\frac{1}{\sqrt{2\pi T}}\int_{0}^{T}T_{e}e^{-i\omega t}dt \tag{3.27}$$

$$P_{\omega}=\frac{1}{\sqrt{2\pi T}}\int_{0}^{T}P(r,t)e^{-i\omega t}dt \tag{3.28}$$

Assuming $T_{\omega}=Ae^{-i\phi}$ and $P_{\omega}=A_{0}e^{-i\phi_{0}}$, one could find the solution by integrating the following equations,

$$\chi\frac{\partial A}{\partial r}-VA=\frac{1}{nr}\mathrm{Re}\left\{e^{i\phi}\int_{0}^{r}r'\left[\left(\frac{3}{2}i\omega+\frac{3}{2\tau}\right)nAe^{-i\phi}+S_{\omega}\right]dr'\right\} \tag{3.29}$$

$$\chi A\frac{\partial \phi}{\partial r}=-\frac{1}{nr}\mathrm{Im}\left\{e^{i\phi}\int_{0}^{r}r'\left[\left(\frac{3}{2}i\omega+\frac{3}{2\tau}\right)nAe^{-i\phi}+S_{\omega}\right]dr'\right\} \tag{3.30}$$

The above formulas are derived by assuming a constant density profile $n(r)$ and zero heat flux in the center. In fact, if we transform Equation (3.14) into the frequency domain, i.e. making Fourier transform to both sides, then we obtain Equation (3.26). Note that the phase profile in Figure 3.4 is the phase difference between the source and the temperature, i.e. $\varphi = \phi - \phi_0$.

In cylindrical coordinates, the integral form of Equation (3.26) can be written as

$$\begin{aligned} nr\left(\chi_{e}\frac{\partial T_{\omega}}{\partial r}-V_{e}T_{\omega}\right)=\int_{\xi}^{r}r'\left[\frac{3}{2}\left(i\omega+\frac{1}{\tau}\right)nT_{\omega}-P_{\omega}\right]dr' \\ +\left[nr\left(\chi_{e}\frac{\partial T_{\omega}}{\partial r}-V_{e}T_{\omega}\right)\right]\Bigg|_{r=\xi} \end{aligned} \tag{3.31}$$

$$\forall \xi\in[0,a]$$

The solution of this complex equation is

$$\chi_{e}=-\frac{1}{nrA\frac{\partial\varphi}{\partial r}}\mathrm{Im}\,M \tag{3.32}$$

$$V_e = \frac{\chi_e}{A}\frac{\partial A}{\partial r} - \frac{1}{nrA}\mathrm{Re}\,M \tag{3.33}$$

$$M = e^{i\varphi}\left\{\int_\xi^r r'\left[\frac{3}{2}\left(i\omega + \frac{1}{\tau}\right)nAe^{-i\varphi} - P_0\right]dr' + N\right\} \tag{3.34}$$

$$N = e^{-i\phi_0}\left[nr\left(\chi_e \frac{\partial T_\omega}{\partial r} - V_e T_\omega\right)\right]\Bigg|_{r=\xi} \tag{3.35}$$

In principle, if the damping factor is given, and the values of diffusivity and convection velocity at a specific point are given, then the profiles of diffusivity and convection velocity can be derived using Equation (3.32) uniquely. However, due to the derivative terms in the expression of the solution, in practice the error could be large. Owing to the error in the derivative of experimentally measured phase, if the value of the derivative is around zero, the local diffusivity may be widely overestimated, since the derivative term is in the dominator, as shown in Equation (3.32). As a result, the solution could be helpful for the understanding of the transport process, but not applicable for evaluation of the transport coefficients.

Coupling of density variation to temperature:

As seen in our experiments and described in the following chapters, if the density profile is not constant in time, in order to determine the heat transport coefficient, we have to deal with the Fourier harmonics of the density at the same time. That is, we have to investigate the influence of the density on the temperature perturbation.

If the density oscillation is included, the Equation (3.26) can be rewritten as:

$$\frac{\partial}{\partial t}n_e = -\nabla \cdot \Gamma + S_p \tag{3.36}$$

$$\begin{aligned}&\frac{3}{2}\left(i\omega + \frac{1}{\tau}\right)\left(n_0 T_\omega + n_\omega T_0\right) \\ &+ \nabla \cdot \left(-\chi_e\left(n_0 \nabla T_\omega + n_\omega \nabla T_0\right) + V_e\left(n_0 T_\omega + n_\omega T_0\right)\right) = P_\omega\end{aligned} \tag{3.37}$$

After a similar procedure, the solution for the diffusivity and convection velocity is obtained from the complex equation as follows:

$$p(r)\chi + q(r)V = w(r) \tag{3.38}$$

Where

$$p(r) = r\left[n_0 \nabla\left(Ae^{-i\varphi}\right) + A_n e^{-i\psi}\nabla T_0\right] \tag{3.39}$$

$$q(r) = -r\left(n_0 A e^{-i\varphi} + A_n e^{-i\psi} T_0\right) \quad (3.40)$$

$$w(r) = \int_0^r r'\left[\frac{3}{2}\left(i\omega + \frac{1}{\tau}\right)\left(n_0 \nabla\left(A e^{-i\varphi}\right) + A_n e^{-i\psi} \nabla T_0\right) - P_0\right] dr' \quad (3.41)$$

$$T_\omega = A e^{i\phi}, \quad n_\omega = A_n e^{i\phi_n}, \quad P_\omega = P_0 e^{i\phi_0} \quad (3.42)$$

and let,

$$\varphi = \phi_0 - \phi, \quad \psi = \phi_0 - \phi_n \quad (3.43)$$

And the solution is in the form of,

$$\begin{bmatrix} \chi \\ V \end{bmatrix} = B^{-1} \cdot b \quad (3.44)$$

Where

$$B = \begin{bmatrix} \mathrm{Re}[p(r)] & \mathrm{Re}[q(r)] \\ \mathrm{Im}[p(r)] & \mathrm{Im}[q(r)] \end{bmatrix}$$
$$b = \begin{bmatrix} \mathrm{Re}[w(r)] \\ \mathrm{Im}[w(r)] \end{bmatrix} \quad (3.45)$$

It is clear that when density oscillation decreases to zero, the solution will degenerated into the Equation (3.32).

Figure 3.5 shows an example of the IFHM solution for particle transport. The diffusivity and convective velocity profiles shown in (*c*) and (*d*) are limited to the region inside r = 0.65 m, where the particle source can be omitted. The solution is based on the polynomial fit of the discrete harmonic points. To get the profiles of coefficients, an additional assumption is used here, i.e., the value of D and V on the axis are assumed to be 0.

The advantage of this method is that it provides a straightforward way to determine the perturbative transport coefficients; the disadvantage is that it depends greatly on the resolution of measurements, and large errors will appear when using derivatives or second order derivatives. However, it is a tool to estimate the errors of transport coefficients derived from trial-and-error technique.

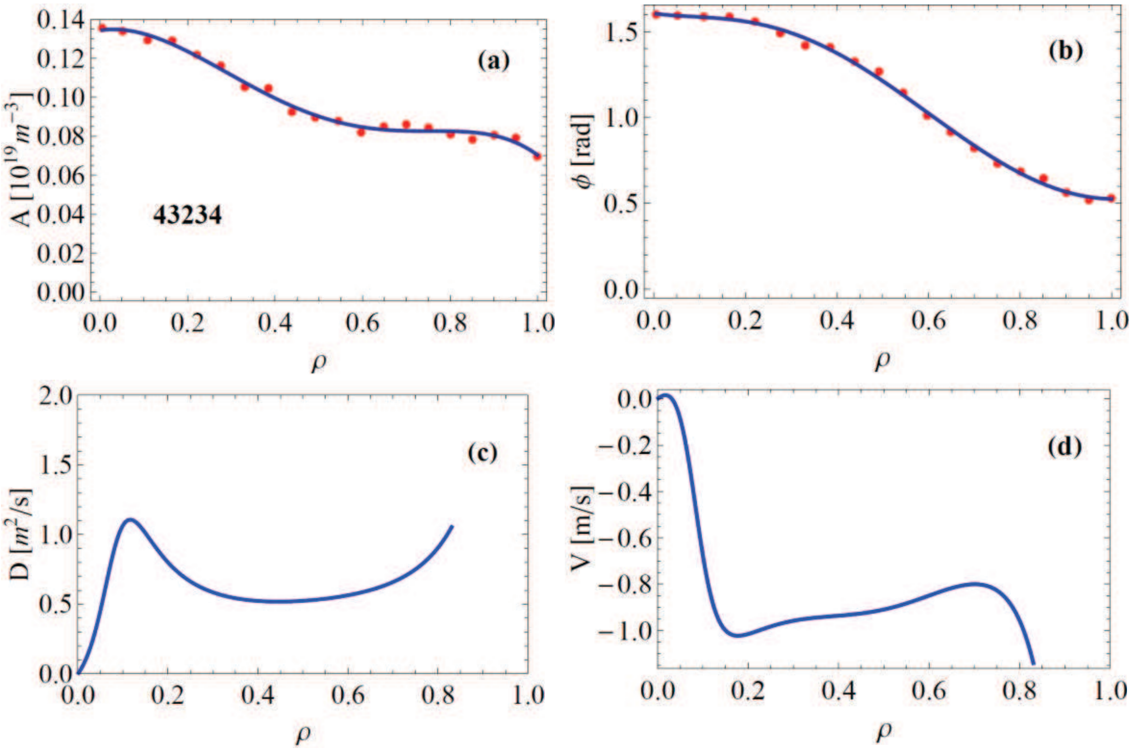

Figure 3.5 An example of IFHM method for particle transport. Amplitude and phase profiles of density perturbation for shot 43234 and its corresponding diffusivity and convective velocity. The discrete points in (*a*) and (*b*) are experimental data, while the solid lines are polynomial fits to them.

3.2.4 GSONIQUE

In order to check the numerical stability and find out the weak points (such as limited segmental definition of transport coefficient) of ANALYTIQUE, and also utilize the data from the power balance analysis for the purpose of perturbative analysis, we have developed a numerical tool called GSONIQUE, in order to compute the temperature profile for more general transport models.

The code GSONIQUE realizes predictive simulations of heat transport, based on simple transport models; the transport coefficient can be constant or defined by the user, which helps to get intuition of the effect on the electron temperature. The core of the GSONIQUE transport solver is the PDE tool in Matlab. The initial condition is the temperature profile given, and the boundary condition can be varied by writing scripts. The source term includes Ohmic and ECRH, which in some cases can be negative power, in order to simulate cold pulse propagation. The ECRH can be constant in time or modulated, by defining the period and duty factor, as shown in the interface. The transport coefficient can also be defined as temperature or density dependent. The loss term is defined by means of a damping factor, as in Equation (3.14). The main interface of GSONIQUE is shown in Figure 3.6.

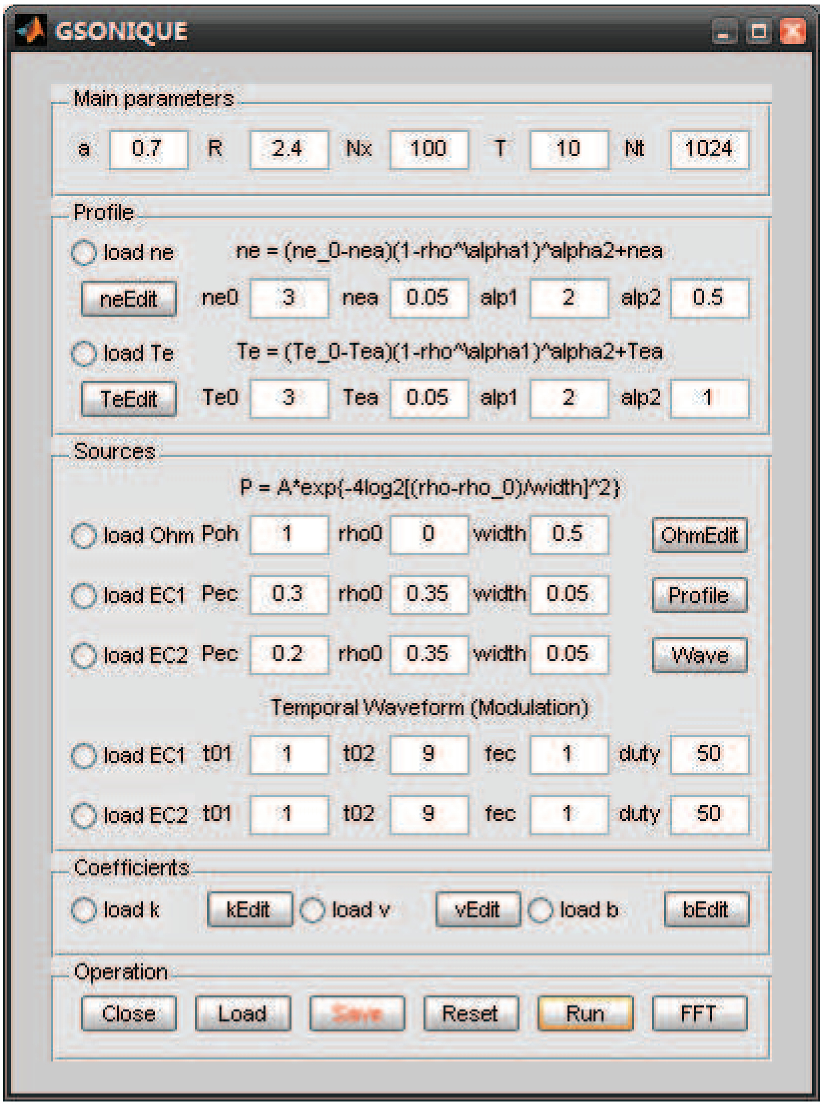

Figure 3.6 The interface of the simple numerical tool for heat transport analysis GSONIQUE

The profiles of density, temperature and source can be defined with several parameters, in which Ohmic and EC wave deposition profiles are Gaussian by default. It can also be modified by a user interactive interface as shown in Figure 3.7. The main method used to modify the profile is interpolation and extrapolation of discrete points, for which linear, piecewise, cubic spline methods are employed.

The transport coefficient temporal-spatial profile can also be modified manually with the interface like Figure 3.8. The basic principle is SVD decomposition. By changing the dominant components of the decomposition, the main temporal-spatial feature is modified. The basic drawback of this method is that once the spatial component is modified, the temporal structure is also modified, although the effect is smaller.

Since the GSONIQUE code is mainly used to investigate the features of the modulation experiment, a FFT module is added to do Fourier analysis, which aims at comparing simulation results with the experiments. This module defines the start and ending times and also the number of points for the FFT analysis, and hereafter allows the comparison with experimental data by giving the shot number and loading the data from storage. One example for the simulation results is shown in Figure 3.9.

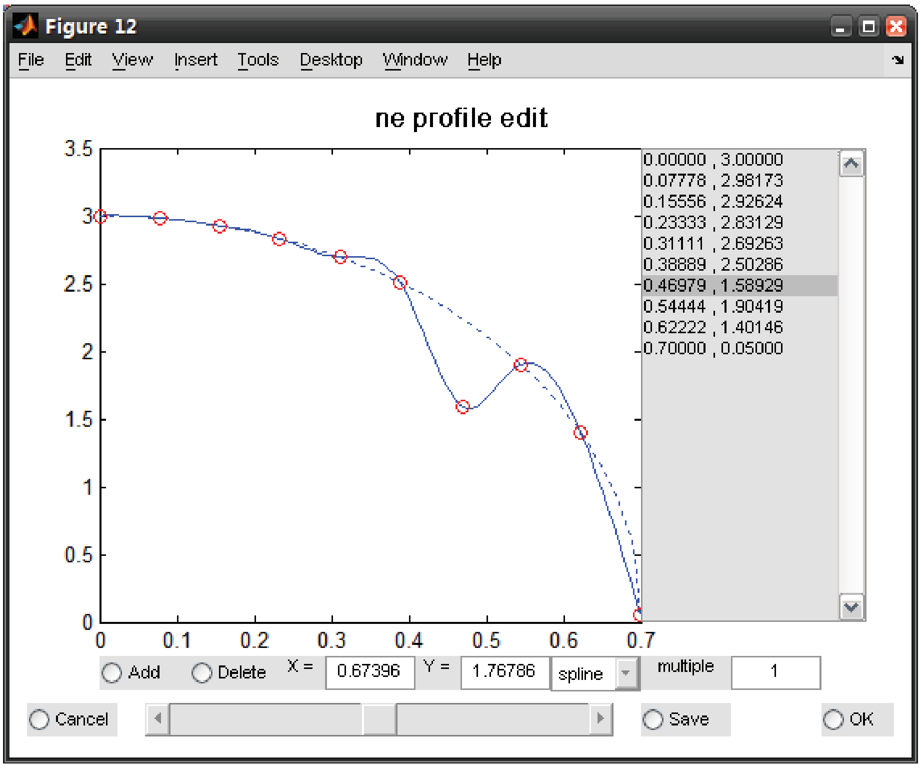

Figure 3.7 Spatial profile modification user interactive interface

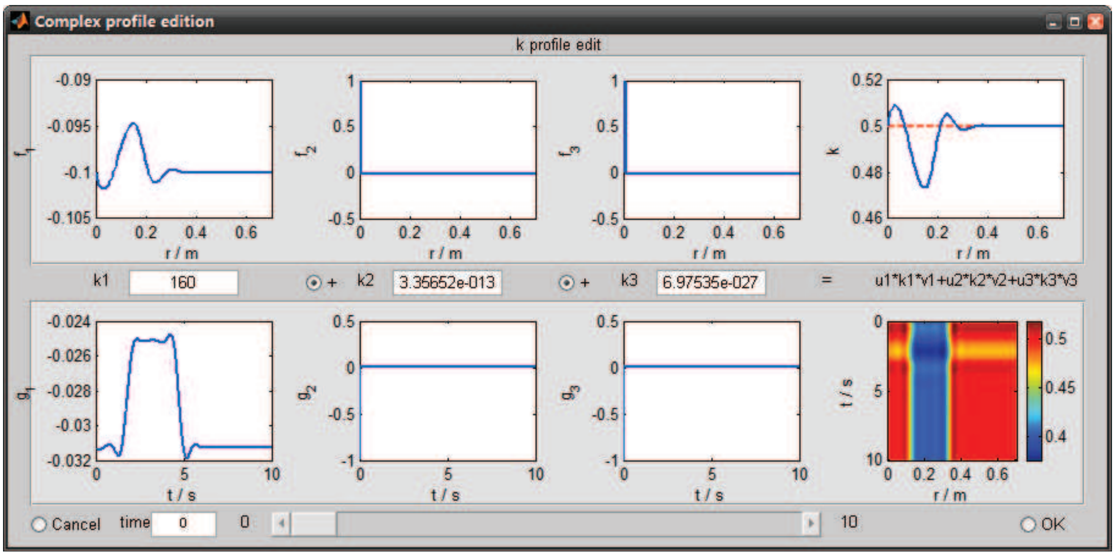

Figure 3.8 User interactive interface for modification of temporal-spatial profile of transport coefficients

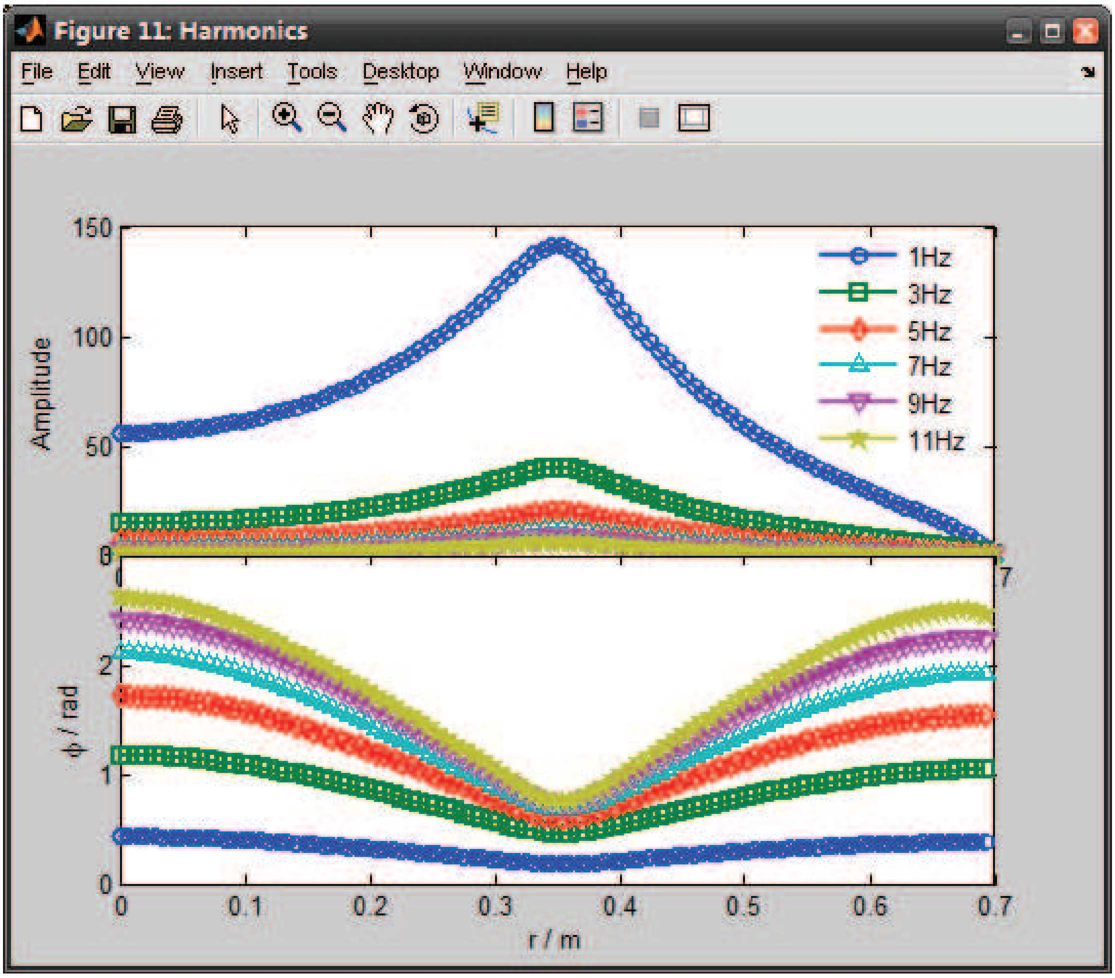

Figure 3.9 Amplitude and phase profiles of the harmonics obtained by FFT analysis

3.2.5 REMA

The REMA code is a toroidal ray tracing code for ECRH, which can calculate the propagation, absorption and the non-inductive current generated by the EC waves. It was firstly written by V. Krivenski [24] in 1980s, and modified by G. Giruzzi and R. Dumont. It is written in Fortran and it has a user interface under Matlab, including the function of inputting data, executing calculation and drawing curves. The magnetic structure is described by an analytical circular equilibrium with the measured Shafranov shift. The ray tracing calculation is based on the assumption of cold plasma approximation; the absorption is calculated with complete relativistic dielectric tensor, for both O mode and X mode; the generation of current by waves is calculated from a linear formula including the effect of trapped electrons [25].The interface of REMA code is shown in Figure 3.10, which includes the typical values of the input parameters for Tore Supra.

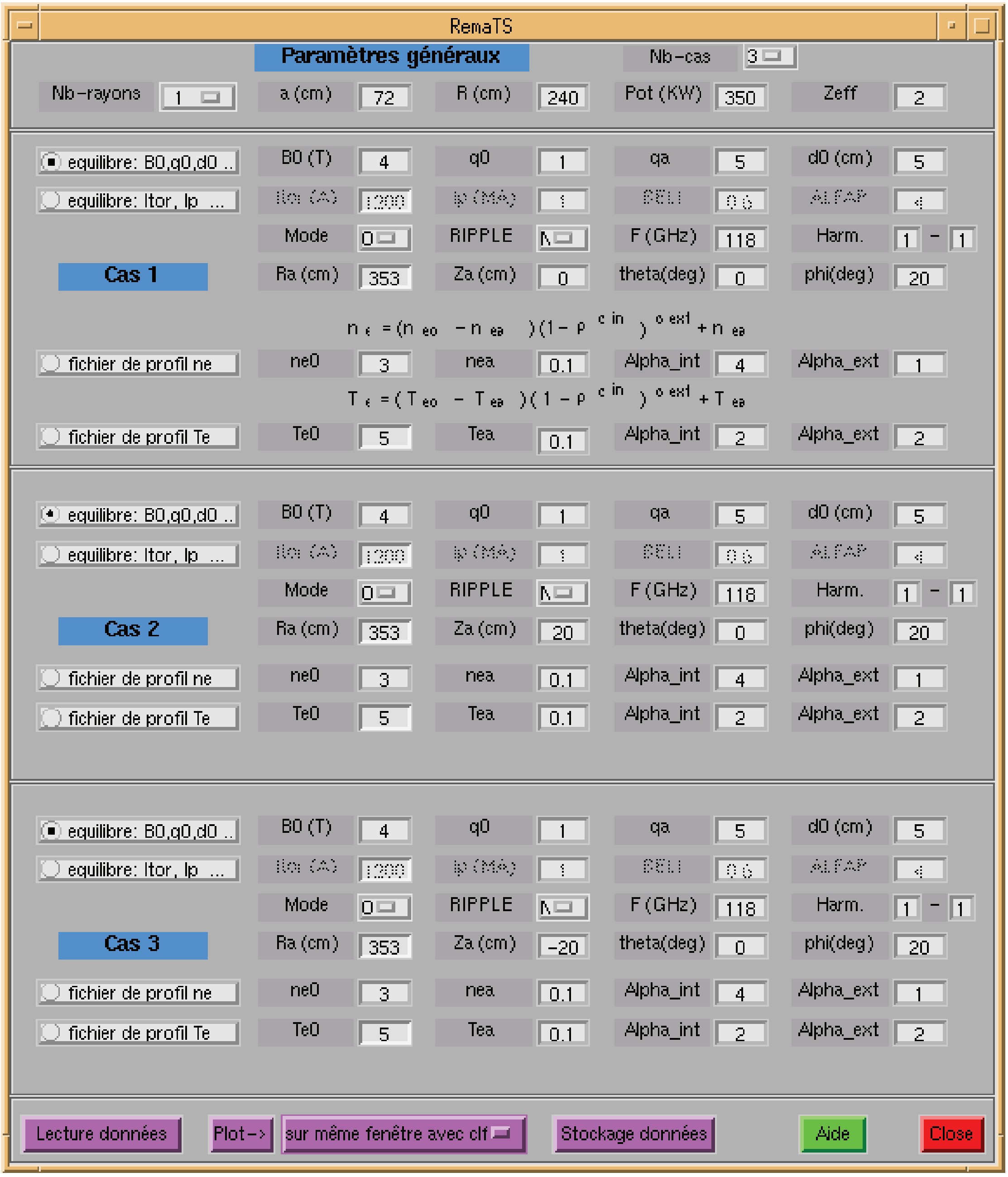

Figure 3.10 The interface of the REMA code

The interface allows calculation of up to three EC wave beams, up to 500 rays are calculated for each beam; it allows the user to choose the equilibrium, either defining the central magnetic field B_0, central and edge safety factor, q_0 and q_a, and also the Shafranov shift; or by providing the plasma current I_p, the current flowing in the toroidal magnetic field coils I_{tor}, $\beta_p + l_i/2$ and the peaking factor α of the plasma current density profile. An example for three beams of EC waves which could be launched by the three mirrors of the Tore Supra antenna is shown in Figure 3.11. It permits the view of the poloidal and toroidal projections of the rays. The fraction of absorbed power and the profile of power deposition are also shown in terms of ρ. Other quantities like the parallel refractive index $N_{\|}$, profile of density and temperature etc. can be found by clicking the 'Otherplots' button in the figure.

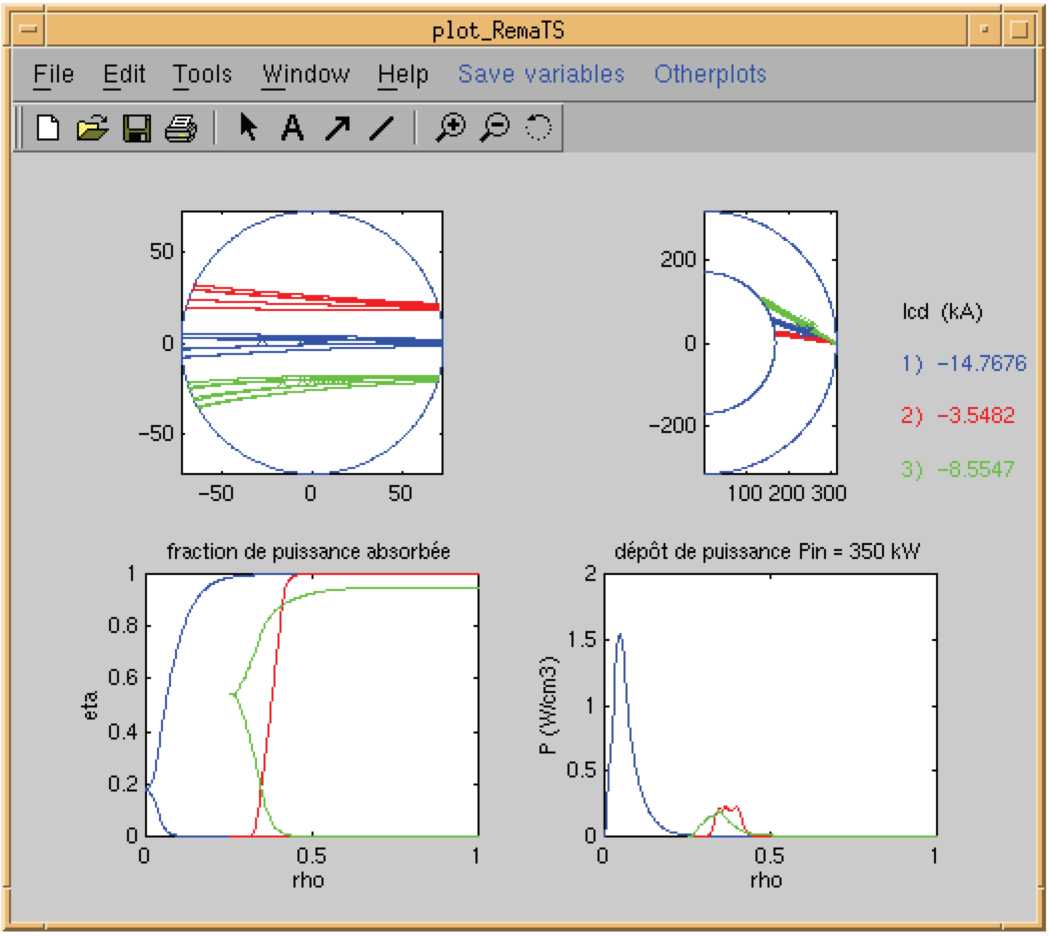

Figure 3.11 The calculation results for three EC wave beams

Chapter 4 Heat pinch investigation and experimental results

In order to gain further knowledge on the controversial inward heat convection phenomenon, dedicated ECRH modulation experiments have been carried out on Tore Supra in the 2008 and 2009 campaigns. Clear signatures of inward heat transport have been observed in several low density discharges. In this chapter, these experiments will be described.

4.1 Earlier experiments and analyses on the heat pinch phenomenon

Diffusive heat transport is detrimental for plasma confinement, because it tends to transfer energy and particles towards the plasma edge, where they are lost. Conversely, inward convective heat transport is thought to be favorable for the improvement of plasma energy confinement, and it has been observed in some tokamak experiments [26,27]. In the interpretation of these experiments, some controversies remain. One of them is whether the inward heat flux is purely diffusive or partly convective. By definition, the diffusive heat flux is proportional to the temperature gradient, while the convective part is proportional to the temperature itself. For the convective part, the word "pinch" is used here to denote the inward convection. Naturally the heat flux q_e should be a combination of the two terms, which basically can be written as follows,

$$q_e = -\left(n_e \chi_e \nabla T_e + n_e V_e T_e\right) \tag{4.1}$$

Which part plays a role in the observed inward heat transport is the key point in the debate. In [26,28], strong off-axis Electron Cyclotron Resonance Heating (ECRH) in which 80% of the total energy is deposited outside of ρ = 0.5 (ρ is the normalized radius of magnetic surfaces) produced a peaked electron temperature profile, and the power balance analysis, under purely diffusive assumption, yielded a negative diffusivity inside ρ = 0.5, which indicates the existence of a heat pinch. In the experiments in RTP [27, 29], FFT analysis for ECRH experiments with modulation frequency of 310Hz and duty cycle of about 85% produced peculiar fundamental harmonic amplitude profiles, in which the peak is shifted inwards compared to the minimum phase delay, a feature that is different from the usual "diffusive" behavior.

In the ECRH modulation experiments in ASDEX-Upgrade [30], evidence of the combined effect of electron transport regulated by a critical gradient and an electron heat pinch term was given. Note that any radial dependence of the heat diffusivity would give a term in the transport equation that is mathematically equivalent to a convection term. In particular, the widely documented Critical Gradient Model (CGM), which includes a strong dependence of diffusivity on the temperature gradient [31], naturally yields a pseudo-pinch, only affecting the modulation amplitude.

With the purpose of gaining further knowledge of the inward heat transport, dedicated ECRH modulation experiments have been recently done on Tore Supra. Under low density conditions, features corresponding to inward heat transport are observed with off-axis ECRH. Modulations are carried out in order to provide the perturbation transport coefficients and hence FFT analysis is used. In these experiments, a low modulation frequency (as low as 1 Hz) is chosen, which has not yet been done previously, in order to acquire more measurable harmonics, which is particularly useful for studies of inward heat transport phenomena. In fact, a different behavior of lower and higher harmonics is known to be a distinctive feature of heat convection.

4.2 Experimental setup on Tore Supra

In the heat transport experiments, ECRH modulation is used as a tool of investigation. As a result of the pure electron heating, ECRH is always one of the best choices for the electron heat transport; with well designed antenna systems, well localized power deposition profile can be obtained, which helps avoid the effect of the heat source itself in the process of transport analysis. For the perturbed transport analysis, Fourier analysis is a good and often used tool. Normally modulation of power source is demanded, in order to concentrate the power spectrum (frequency domain) to separate harmonics, which helps to improve the Signal-to-Noise ratio. In our case, quite low modulation frequency for the ECRH pulse is used, i.e., as low as 1 Hz. This regime demands stationary operation of plasma discharges for several modulation cycles, which is well within the Tore Supra tokamak capabilities.

The Tore Supra ECRH system [32] consists of two gyrotrons each capable of injecting ~300 kW into the plasma, with a deposition width as low as 3 cm, and precise adjustment of the injection angle. The ECRH system works at 118 GHz, i.e., close to the fundamental harmonic of the electron cyclotron frequency for the nominal

Tore Supra magnetic field (3.8 T). The power is injected in the ordinary mode (O-mode polarisation) from the low field side, perpendicularly to the magnetic field for this specific experiment. The ECRH modulation experiments have been carried out with major radius of R = 2.43 m and minor radius of a = 0.72 m, plasma current varying from 0.6 MA to 1 MA, magnetic field on axis 3.73 T and 3.53 T, corresponding to deposition positions of ρ = 0.5 and 0.6, line-averaged density $1.4\sim5.4\times10^{19}$ m^{-3}, central electron temperature 2~5 keV. With the conditions above, good first-pass power absorption is obtained in all the cases considered (lower in the lower density case, when the least first-pass absorption is still more than 80%) (calculated with REMA [24]).

Square wave modulations have been performed with a duty cycle of 50%. In previous ECRH modulation experiments in other tokamaks, the modulation frequency range is from 30 Hz to 300 Hz. In our experiments the modulation frequency is chosen to be as low as 1 Hz. The advantages of using low frequency modulation in the perturbation transport analysis are: 1) a large perturbation amplitude with high signal to noise ratio; 2) having many measurable harmonics (1^{st} to 11^{th}); 3) to be less affected by sawteeth and other perturbations; 4) the most important: to be more sensitive to the convection effect compared to the convection (heat pinch) effect. Indeed the higher the modulation frequency, the smaller the convection effect compared to the diffusion effect. Of course there are also disadvantages for the low frequency modulation: 1) the transport coefficients varying along with the heat pulses; 2) more requirements for plasma control; 3) an additional parameter should be taken into account with the damping time which characterizes the loss term (see discussion in the next chapter); 4) the influence of the edge boundary condition on the propagation characteristics of the perturbation and in the modeling should also be taken into consideration; 5) at very low modulation frequency, the FFT results might be influenced by the slow evolution of the parameters, the choice of the time interval is therefore important.

The electron temperature profile was measured by a 32-channel heterodyne ECE radiometer, with a spatial resolution of about 2.5 cm [33]. The cross-calibration precision between channels is better than 3%, which allows high-quality temperature profile measurements and fairly good determination of the temperature gradient. The time resolution is 1 ms for our experiments. The ion temperature was measured by charge exchange recombination spectroscopy [34]. The density profile is measured by two sets of X mode heterodyne reflectometers, working at frequencies ranging from

50 to 110 GHz and from 105 to 155 GHz, respectively. The frequency sweeping time is up to 20 μs, and the radial profile uncertainty is less than 1cm. [35,36]. A 9 channel infrared interferometer, which has a spatial resolution of ~7 cm, is also used for the measurement of density profile in case the reflectometers cannot cover the whole range of plasma radii [34].

Out of 23 shots, two classical ones are selected; the basic parameters are shown in Table 4.1. The scenario of the plasma discharge for shot 43234 is shown as an example in Figure 4.1.

Table 4.1 Summary of the experimental conditions of the analyzed discharges

shot	40504	43234
Central electron temperature (keV)	1.8	4
Line-averaged electron density ($\times 10^{19} m^{-3}$)	5.4	1.6
ECRH modulation frequency (Hz)	1	1
Plasma current (MA)	0.71	0.7
Toroidal Magnetic field (T)	3.73	3.72

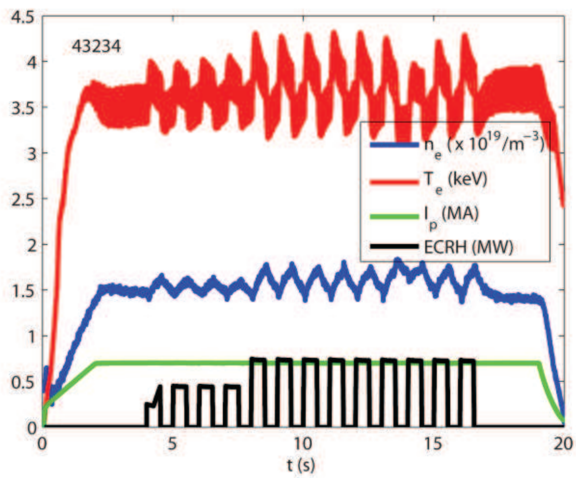

Figure 4.1 43234 discharge scenario; Note: the density and temperature are central values.

4.3 Experimental results

Experimental results are now reported. Different types of transport behaviors have been observed depending on the plasma density, with two distinct regimes for central density n_{e0} = 3~5×10^{19} m^{-3} (high density) and n_{e0} = 1~3×10^{19} m^{-3} (low density).

These two cases are illustrated in the next two sub-Sections.

4.3.1 High density

Figure 4.2 presents the time evolution of the electron temperature and density, for a deuterium discharge in which the ECRH power was deposited at $\rho_{dep} = 0.5$ on the equatorial plane. The main plasma parameters are: magnetic field $B_T = 3.73$ T, plasma current $I_p = 700$ kA, central density $n_{e0} = 4\sim5.4\times10^{19}$ m^{-3}, edge safety factor $q_{edge} = 6.3$. Other discharges with high density (i.e. roughly $3\sim5\times10^{19}$ m^{-3}) and half-radius ECRH deposition display similar effects. The ECRH modulation is carried out at a frequency of 1 Hz with 100% amplitude rise and fall, square waveform and duty cycle factor of 50%. The ECRH power (~600 kW) is applied between 4 s and 14 s. During the time interval from 4 s to 8 s the density increases, while the temperature decreases. For the time interval from 8 s to 14 s, the perturbation of T_e is ~10% of the average T_e, which remains reasonable for a perturbation analysis. In this case, it should be noted that the density is moderately modulated by ECRH. Figure 4.3 shows the T_e and n_e profiles at $t = 9.9$ s (Ohmic phase) and $t = 10.4$ s (ECRH phase).

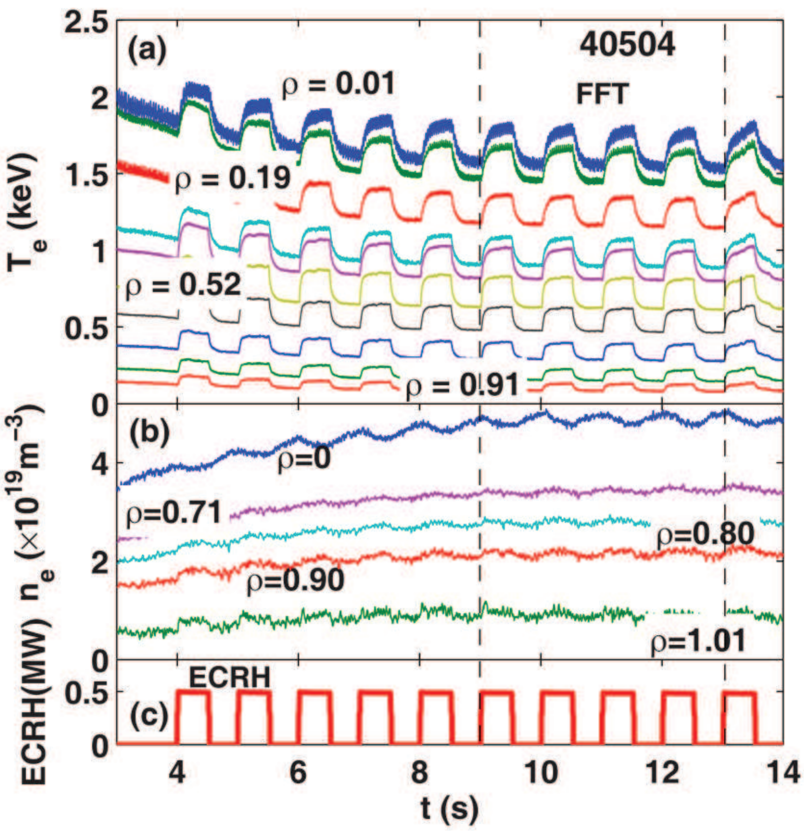

Figure 4.2 Temporal evolution of (*a*) the electron temperature (ECE), (*b*) density (from reflectometry) and (*c*) the ECRH power (TS#40504). The density in (*b*) at $\rho = 0$ is taken from the interferometry (lacking data from the reflectometry at this point). The FFT time window is shown

between the two dashed lines.

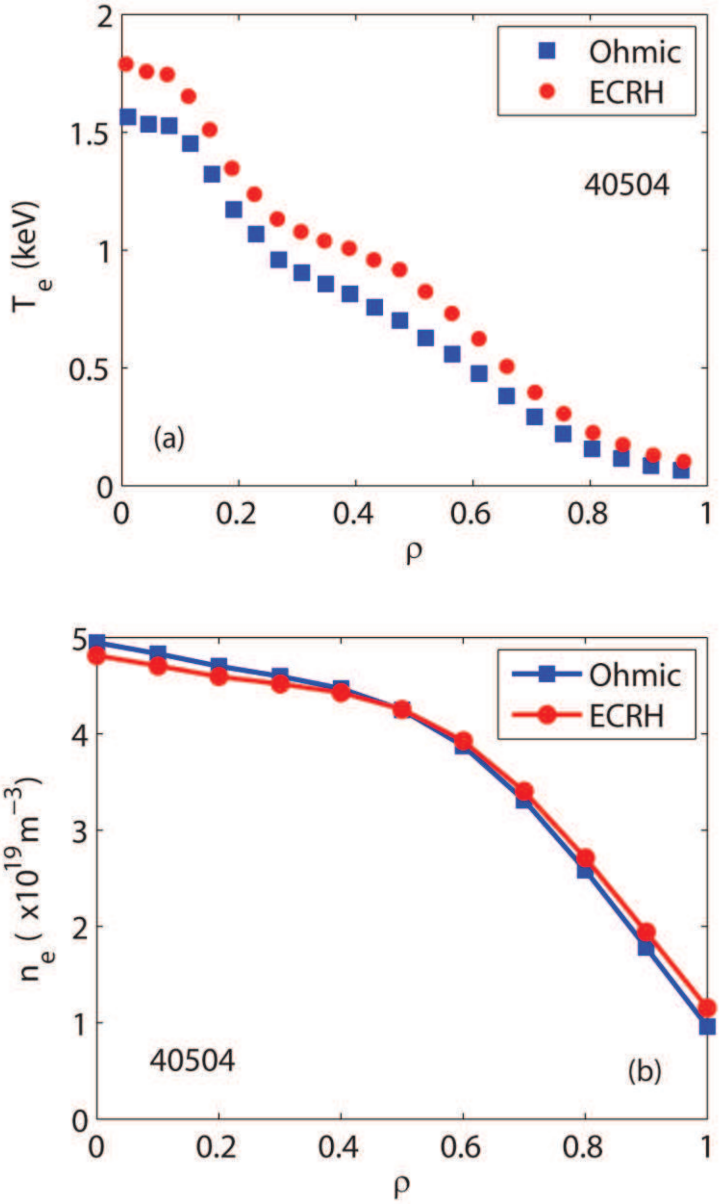

Figure 4.3 Electron temperature (ECE channels) (*a*) and density (Abel-inverted interferometry data) (*b*) profiles for shot 40504. The Ohmic phase corresponds to t = 9.9 s, and the ECRH phase corresponds to t = 10.4 s.

Figure 4.4 shows the T_e incremental variation profile during one ECRH pulse. The ΔT_e is defined as the difference between the electron temperature in the ECRH phase and in the Ohmic phase, where the T_e profile in the Ohmic phase is taken from t_0 = 10.02 s, which corresponds to a time just before the injection of ECRH power. The time $t = t_0$ + 300 ms corresponds to the 'saturation' phase of the ECRH regime. From this figure, we can observe that during the ECRH phase the heat starts to increase from the ECRH deposition layer, and then spreads inside and outside of this layer due to transport processes. Here the maximum of the temperature perturbation remains unchanged at the ECRH deposition. This indicates that in this case the dominant transport process is the diffusion, while the heat convection, if it exists, should be small. A secondary local maximum of the temperature perturbation is located at ρ = 0.15 just outside the q = 1 surface, where the sawteeth inversion radius locates between ρ = 0.08 and ρ = 0.11. As the region inside the q = 1 surface is affected by sawtooth activity, it is also possible that the secondary local maximum is not due to a transport process.

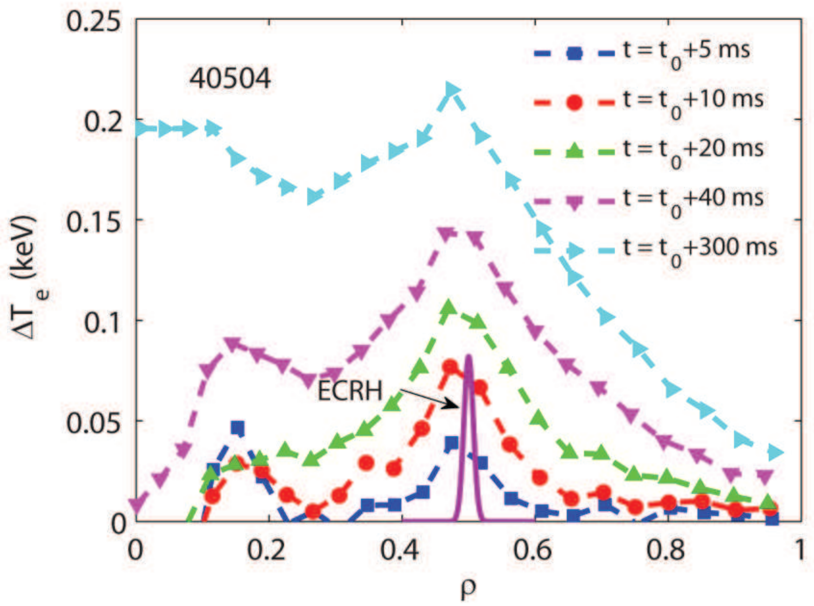

Figure 4.4 Time evolution of the electron temperature perturbation profile during an ECRH modulation pulse for shot TS#40504 (t_0 = 10.02 s).

A useful representation of the heat transport process is the time-space evolution of the temperature perturbation, which is shown in Figure 4.5. The heating position corresponds to the starting point of the temperature perturbation, which is located around R = 2.8 m or ρ = 0.5. In this case, the most heated part remains peaked at the predicted maximum of the EC wave absorption, which means that the diffusion effect is dominant.

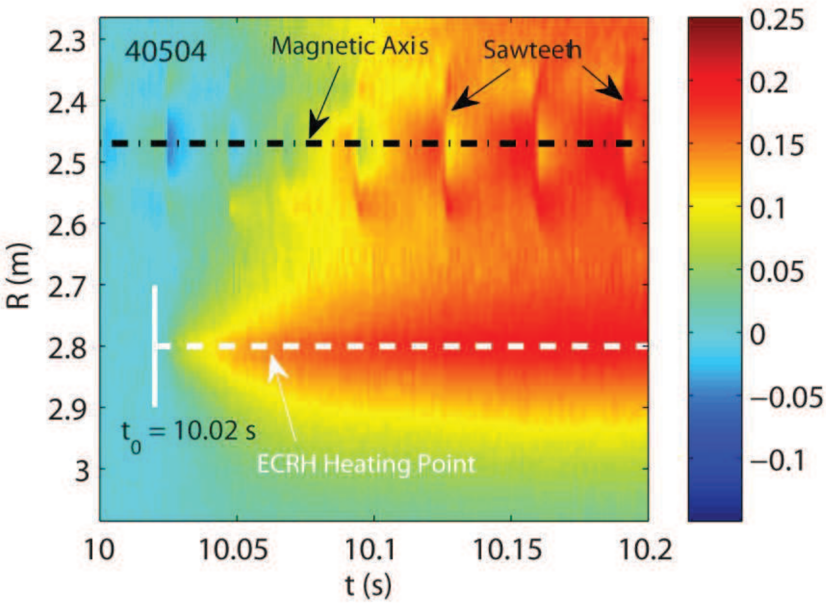

Figure 4.5 2D temporal-spatial image of the T_e perturbation during ECRH for shot TS#40504.

4.3.2 Low density

Experiments with ECRH performed in low density plasmas (i.e. n_{e0} = 1-2×10^{19} m^{-3}) show different behaviors for the temperature perturbation with respect to the high density ones. Figure 4.6 shows the time evolution of electron temperature and density for shot TS#43234. In this shot, the two gyrotrons are switched on subsequently (t = 4 s for the first gyrotron, then t = 8 s for the second one), which produces temperature perturbations of different levels. The main parameters for this shot are B_T = 3.72 T, I_p = 700 kA, n_{e0} = 1.5-1.8×10^{19} m^{-3}, q_{edge} = 6.6. The modulation frequency is 1 Hz, and the injected ECRH power is about 300 kW from 4 s to 8 s and 600 kW from 8 s to 17 s. At t = 13.485 s, the diagnostic neutral beam is injected into the plasma in order to measure the ion temperature T_i profile by charge exchange spectroscopy. The power of the Neutral Beam is ~350 kW, hydrogen is injected at energy of 50 keV, for 600 ms. Note that measurements of the ion temperature are only available at this time of the discharge, when the beam power is applied. The ion temperature is therefore computed by means of the CRONOS code using the measurement as a constraint and taking into account the perturbation of the density by the Neutral Beam. In the modulation analysis this simulated ion temperature is used. Owing to the low electron-ion coupling in this low density discharge, the sensitivity to the exact shape of T_i is limited. This has been checked by a sensitivity analysis.

In this shot, the waveforms of the electron temperature and density perturbations are quite different from shot TS#40504, especially for the central channels. The temperature evolution in one ECRH modulation period can be divided into four phases as described in the following: a drastic temperature increase for 100 ms, then a slow temperature decrease for 400 ms, when ECRH is switched on; a drastic temperature decrease for 100 ms, then a slow temperature increase for 400 ms, when ECRH is switched off. For this discharge the electron density is as low as the natural density of the vacuum vessel, i.e., without gas injection. From 4 s to 8 s, the density perturbation level at ρ = 0.5 is 3% of its mean value, while the temperature perturbation level at the same position is 7%. From 8 s to 13 s, the density perturbation level is 6%, while the temperature perturbation level is 12%. It should be noted that at low density, the density is modulated in phase with the ECRH power (i.e., it increases during the power pulse), while at high density, outside ρ = 0.75 the density is modulated in phase while inside ρ = 0.75 it is in opposition of phase (i.e., it decreases when the EC power is applied.)

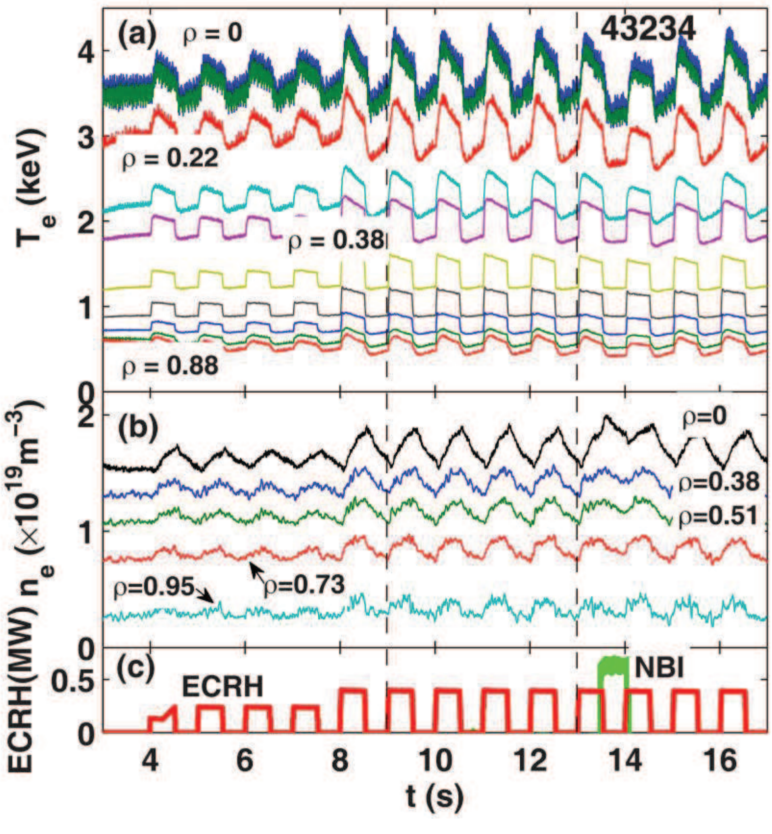

Figure 4.6 Temporal evolution of (*a*) the electron temperature (ECE), (*b*) the electron density (reflectometry) and (*c*) ECRH power, the injection of neutral beam (NBI) is also shown in (*c*). (shot TS#43234)

Figure 4.7 shows the T_e and n_e profiles measured at t = 9.9 s (Ohmic phase) and t =

10.4 s (ECRH phase) for shot TS#43234, the ion temperature T_i measured at t = 13.9 s is also shown. The electron temperature profile measured by ECE outside $\rho \sim 0.6$ is relatively high compared to shot TS#40504, since the optical depth for the EC wave is less than 2 there. The ECE data in this part includes wall reflection effects, leading to an overestimation of the electron temperature. However, it is difficult to quantify the overestimation of the electron temperature in regions of low optical depth and low density, because in the same region the temperature measurements by Thomson scattering are also affected by a significant error. Comparison with Thomson scattering data suggests that the overestimation increases with minor radius, from ~ 10% at $\rho = 0.6$, to 20-30% at $\rho = 0.7$, up to > 50% at $\rho > 0.8$.

Figure 4.8 shows the electron temperature profile evolution during ECRH. The temperature perturbation profile is broader compared with that of the high density case (TS#40504), and manifestly asymmetric from 10 ms after ECRH is turned on, i.e., the temperature increment inside the ECRH power deposition layer is relatively larger. It should be noted that the maximum of the temperature perturbation at t = 300 ms is now shifted towards the center. The little secondary maximum inside $\rho = 0.2$ (also shown on Figure 4.4) is probably due to sawteeth. This effect is more visible on the Figure 4.9, which displays the 2D temporal-spatial image of the electron temperature perturbation. Indeed, from this figure we can see that the ECRH driven heat, represented by the red color, propagates inward from the ECRH deposition to the center, as shown in Figure 4.9 by an arrow. This behavior may be due to either the existence of inward heat pinch or lower diffusivity inside. For the latter there should be a transport barrier, around which low diffusivity value exists, preventing outward heat transport. In the next chapter Fourier analysis and simulation with transport model will be done in order to determine the actual mechanism responsible for this observation.

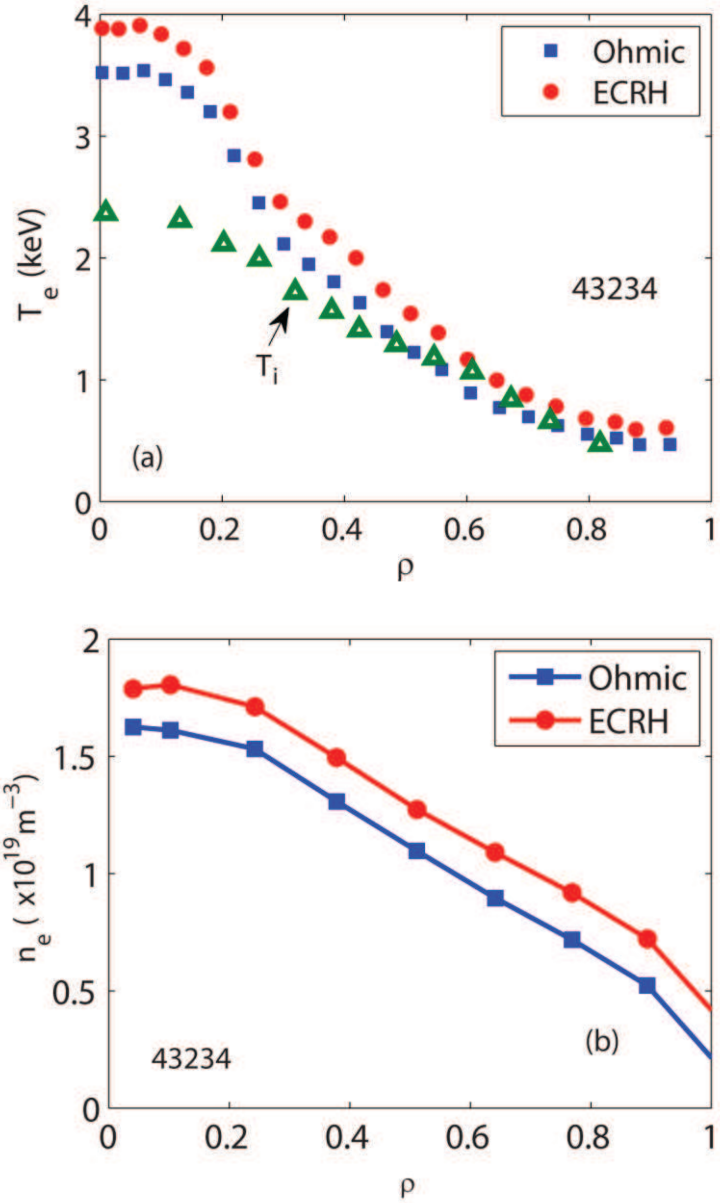

Figure 4.7 The electron temperature (ECE) (*a*) and density (reflectometry) (*b*) profiles for shot 43234. Ohmic phase corresponds to t = 9.9 s; ECRH phase corresponds to t = 10.4 s. The measured T_i profile at t = 13.9 s is also presented in (*a*).

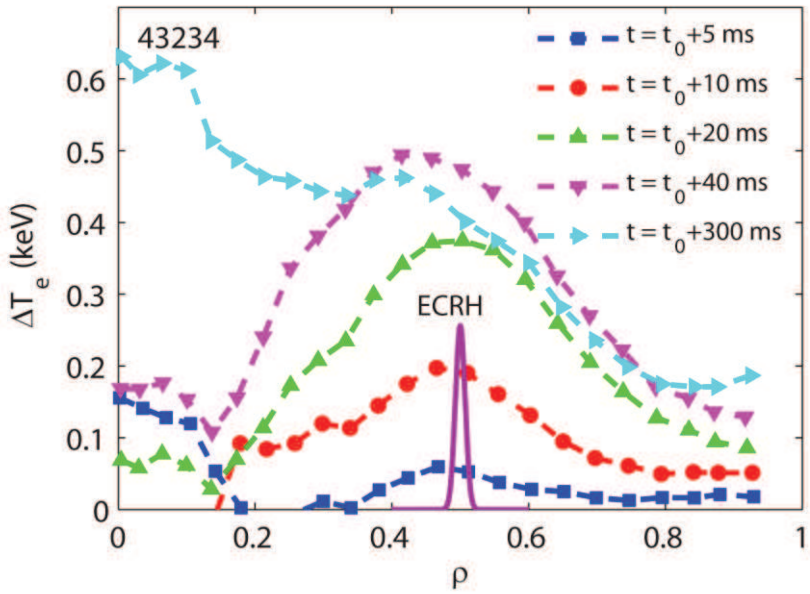

Figure 4.8 The perturbed electron temperature profiles at various times during an ECRH pulse. T_e profile at t_0 = 11.015 s is selected as the reference profile.

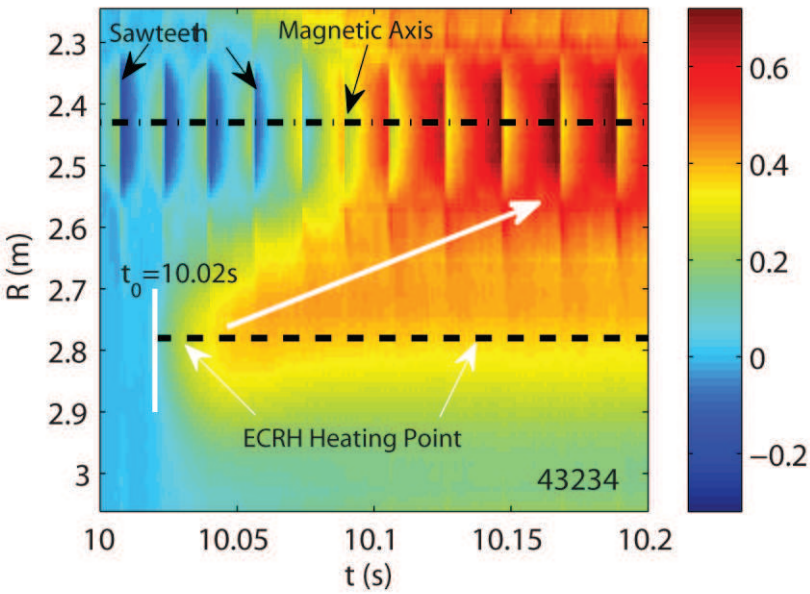

Figure 4.9 2D temporal-spatial image of the electron temperature perturbation (ECE) for shot TS#43234.

4.4 FFT analysis

Low frequency modulation of ECRH at 1 Hz provides accurate measurements of the plasma response at several harmonics. For purely square-modulated wave and a duty factor of 50%, the even harmonics are absent, as seen in the experimental data where the odd harmonics are dominant. At first the signal quality in the frequency domain is qualified by the signal-to-noise ratio. In the power spectrum, the signal-to-noise ratio of each ECE channel is defined as the value of the peak divided by the mean value of the shoulders [31]. In Figure 4.10, the signal-to-noise ratio for different harmonics for shots TS#40504 and TS#43234 is shown. Note that in the region $\rho \geq 0.2$, the value is higher than 5 (a reasonable limit for good detection) for harmonics from 1 to 7. However, the density oscillation may couple to the temperature oscillation, i.e. the amplitude and phase profiles of the temperature may contain the contribution from density oscillation. Due to the pure ECRH heating, the density oscillation should be a by-product compared to temperature variation. The variation of n_e should be slower than the T_e, so that the main component of n_e is associated to the fundamental harmonic, rather than to the higher ones. In the case of stronger n_e oscillations, we use higher harmonics instead; while for weaker n_e oscillations, we use lower harmonics, because of their higher signal-to-noise ratio.

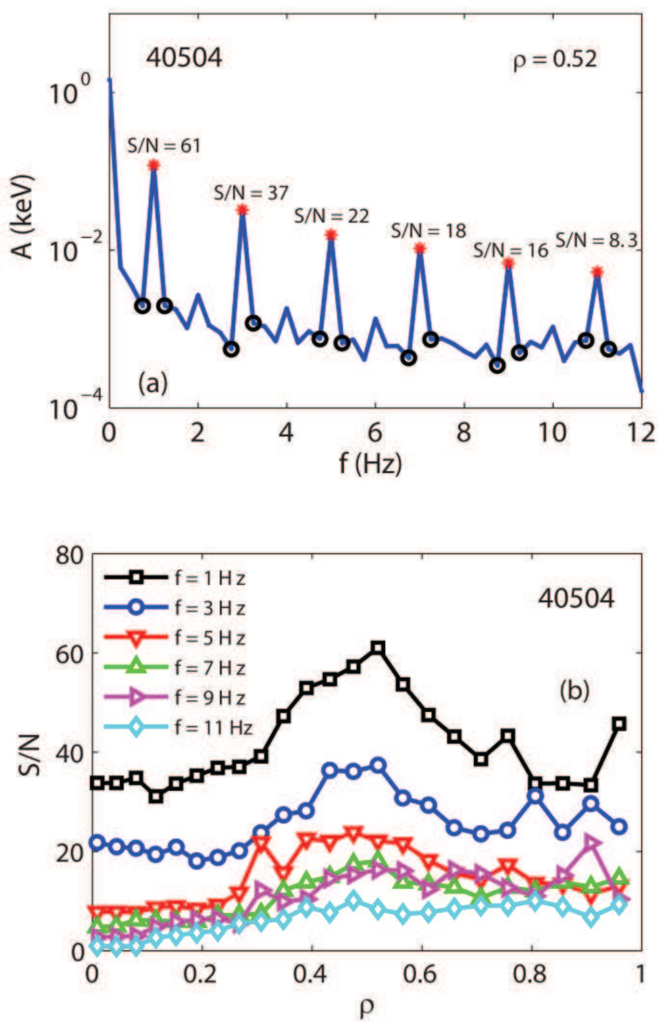

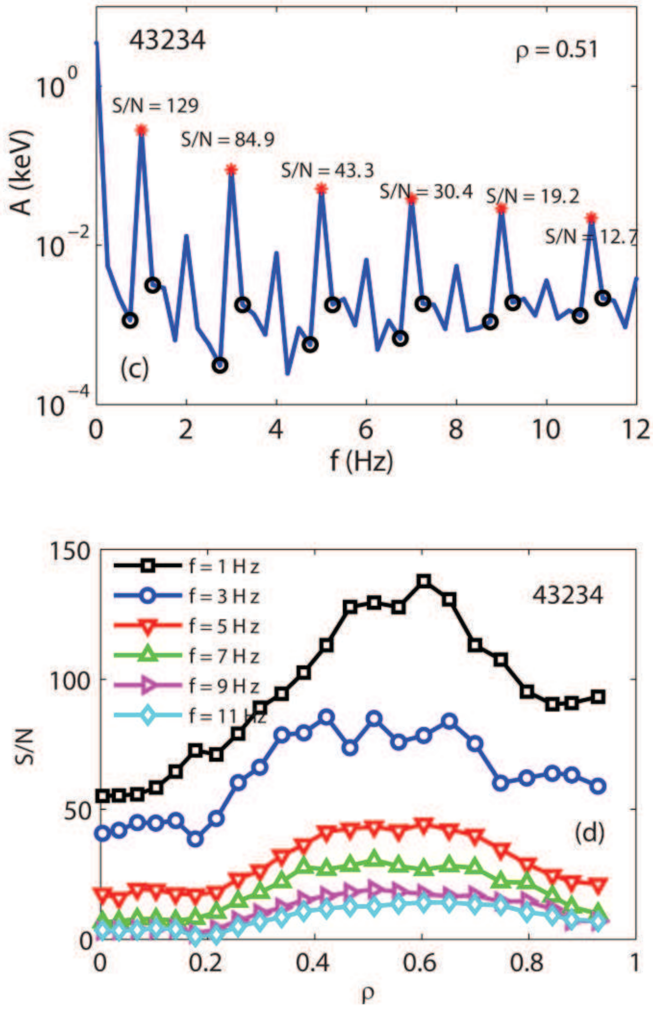

Figure 4.10 Signal-to-noise ratio (SNR) of the harmonics of Te in the time interval (9-13 s). SNR around the ECRH heating position for TS#40504 (*a*) and TS#43234 (*c*). SNR profiles of harmonics from 1st to 11th for TS#40504 (*b*) and TS#43234 (*d*).

4.5 Sawteeth effect

Sawteeth oscillations are cyclic recurring phenomenon in which plasma temperature, density and other plasma parameters in the central region rise slowly (the sawtooth ramp) and is followed by a sudden drop (the sawtooth crash) [37]. This phenomenon was first observed in 1974 on the ST tokamak [38]. The sawtooth crash happens in the region $r < r_s$, which is called inversion radius, while flat profiles for density and temperature extending to $r = r_{mix}$, which is called mixing radius. Sawteeth are one of the first perturbation actuators for perturbative transport analysis. However, from the experimental data, we find that usually the coefficients from sawteeth perturbation are larger than from other sources, such as ECRH. Due to the limited region of applicability (usually limited in the region between $q = 1$ and $q = 2$), little information on the profiles of transport coefficients is obtainable.

Figure 4.11 shows the temporal evolution of the electron temperature in the presence of sawteeth. The temperature profiles before and after the sawtooth crash are shown in (*b*). The sawtooth period is around 30 ms in the ECRH phase and 25 ms in the Ohmic phase, and the sawteeth amplitude increases slightly in the core region $r < r_s$ while it almost keeps invariant outside $r = r_s$ in the ECRH phase compared to the Ohmic phase, as shown in (*c*). Note that the use of ECRH at mid-radius has a stabilization effect on the sawteeth. ECRH is a well-known tool for stabilization of sawteeth effect, i.e., increase of the sawteeth period and magnitude.

The frequency of sawteeth is much larger than the modulation frequency, which minimizes the modulated data pollution from sawteeth. However, the sawteeth dominant area extends from the center to r_{mix}, which is approximately at $\rho = 0.1$.

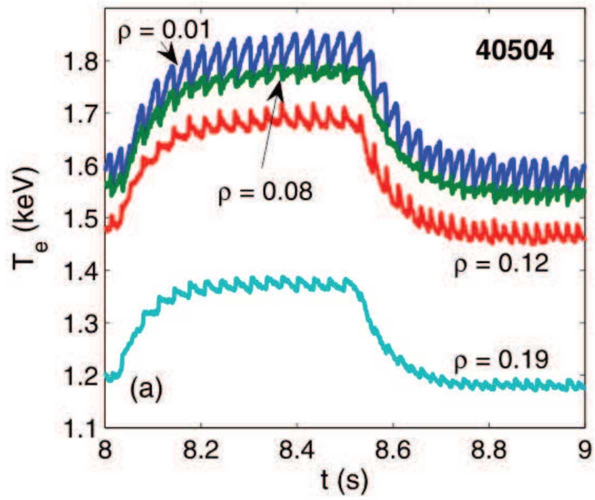

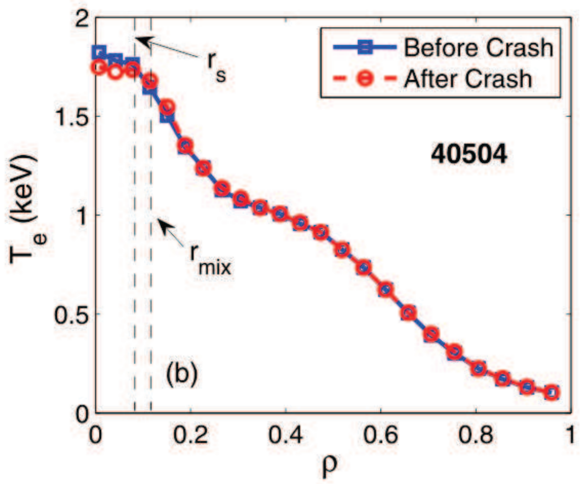

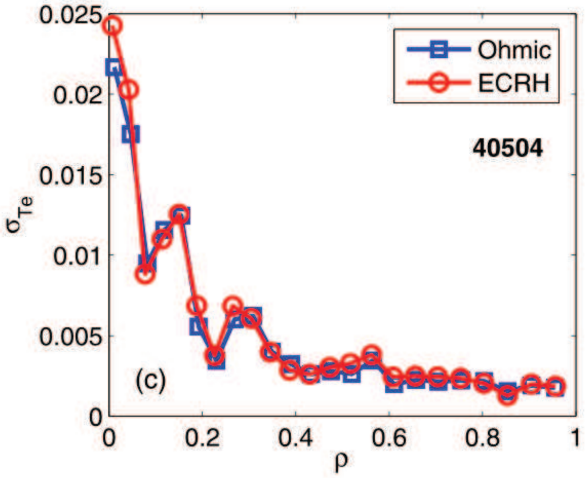

Figure 4.11 Sawteeth at various radii for shot 40504. (*a*) is the temperature evolution, (*b*) is the temperature profile before (solid) and after (dashed) a sawtooth crash for the ECRH phase, and (*c*) is the standard deviation of temperature during the Ohmic phase and ECRH phase.

Previous work on transport induced by sawteeth has shown a transport barrier around $q = 1$ radius. [39] However, in our case, the temperature gradient is not sharp enough to exhibit the existence of a transport barrier. The FFT analysis of sawtooth perturbation is shown in Figure 4.12. The flat part of the phase profile in the core region shows the rapid homogenization of energy due to the magnetic reconnection after the sawtooth crash; the phase difference between the mixing radius and the core is around π, which means that they have opposite phase, corresponding to the temperature instantaneous increase after the crash. The amplitude is peaked inside $r = r_s$, while at the sawtooth inversion radius, the amplitude shows a dip. In the so called *confinement region*, i.e., outside $r = r_{mix}$, the amplitude and phase profile show a diffusive behaviour. The corresponding diffusivity in the confinement region can be derived using Equation (3.8). For $R = 2.6$ m (corresponding to $\rho = 0.2$ on the low field side), $\chi_e^{HP} = 0.18$ m^2/s for the Ohmic phase and $\chi_e^{HP} = 0.24$ m^2/s for ECRH phase. For $R = 2.31$ m (corresponding to $\rho = 0.21$ on the high field side), $\chi_e^{HP} = 0.11$ m^2/s for the Ohmic phase and $\chi_e^{HP} = 0.38$ m^2/s for ECRH phase. It is clear that during the ECRH phase, the heat diffusivity increases on both sides of the magnetic axis.

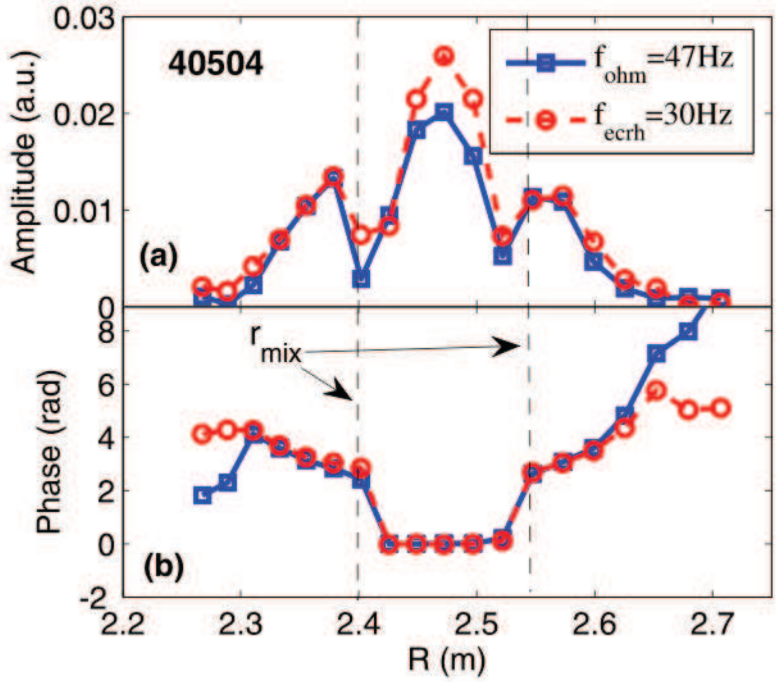

Figure 4.12 The fundamental harmonic amplitude (*a*) and phase (*b*) of the temperature perturbation due to sawtooth oscillation in the Ohmic and ECRH phases.

4.6 Density effect

The influence of density on the temperature evolution can be intuitively seen from the comparison of the temperature evolution at various radii between shot TS#40504 and shot TS#43234. Figure 4.13 shows the spatial-temporal density profiles and their relative variations for shot 40504 and 43234 (Note: the so-called relative variation here is the ratio of the perturbation to the mean value). From this figure we can find that for both high density and low density cases, the density varies when the ECRH is switched on/off. However, in the region $\rho < 0.8$, the relative variation of density is quite low for shot 40504, the absolute magnitude is 2~4%; and for shot 43234, it is about 10%.

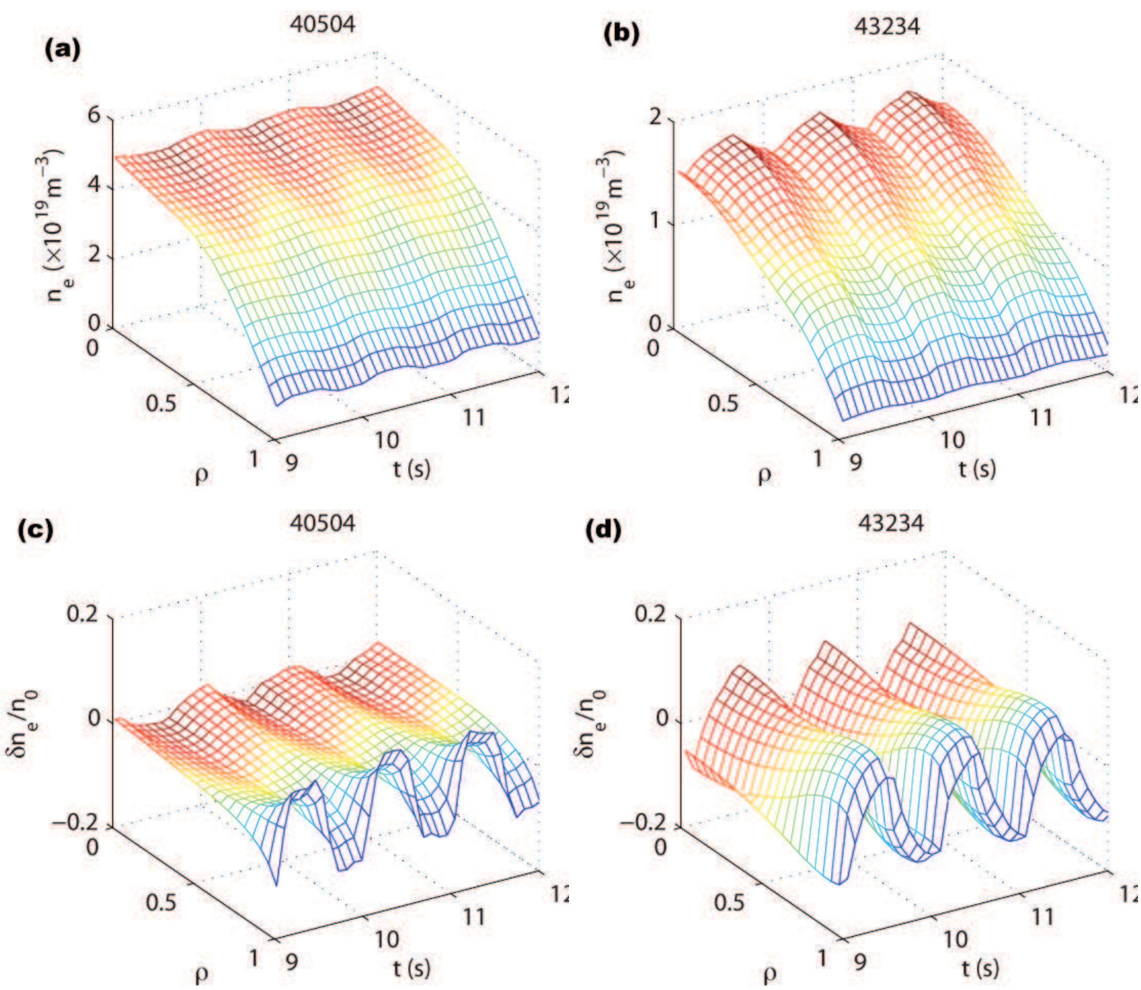

Figure 4.13 (*a*) and (*b*) Electron density spatial-temporal profiles for shot 40504 and 43234; (*c*) and (*d*) the corresponding relative variations of density. The smoothed data come from the Abel inversion of the interferometer signal.

Figure 4.14 shows the density and electron temperature evolution for high density and low density cases. It appears that in the high density case the density varies little during the EC heating pulse, whereas in the low density case a clear density response to the heating pulse can be identified, especially in the region $\rho < 0.8$. Since the time scale of transport of the ECRH heat pulse is different from that of the density oscillation, we can try to isolate the density effect on the temperature oscillation in a simple way. Since for constant volume and internal energy, the product of temperature and density is constant, one can correct the effect of density by multiplying $T_e(r, t)$ by $n_e(r, t)/\langle n_e(r, t)\rangle_t$, where $\langle n_e(r, t)\rangle_t$ is a time average, neglecting the heat transport process. In this way, we can get approximate temperature evolution curves, as shown in Figure 4.15(*b*), which shows 'normal' behaviors as seen in the high density case; the original data is also shown in Figure 4.15(*a*).

The corresponding influence on the amplitude and phase profile for the 1st and 3rd harmonics are shown in Figure 4.15(*c*) ~ (*f*), from which we could draw the conclusion that the density oscillation have a stronger influence on the fundamental amplitude and phase profiles than on those of the third harmonic. For the low density case, the third harmonic is used to determine the best fit for the transport coefficients for the simulation in the following chapters; however, the corrected 1st harmonic data could also be used with similar results.

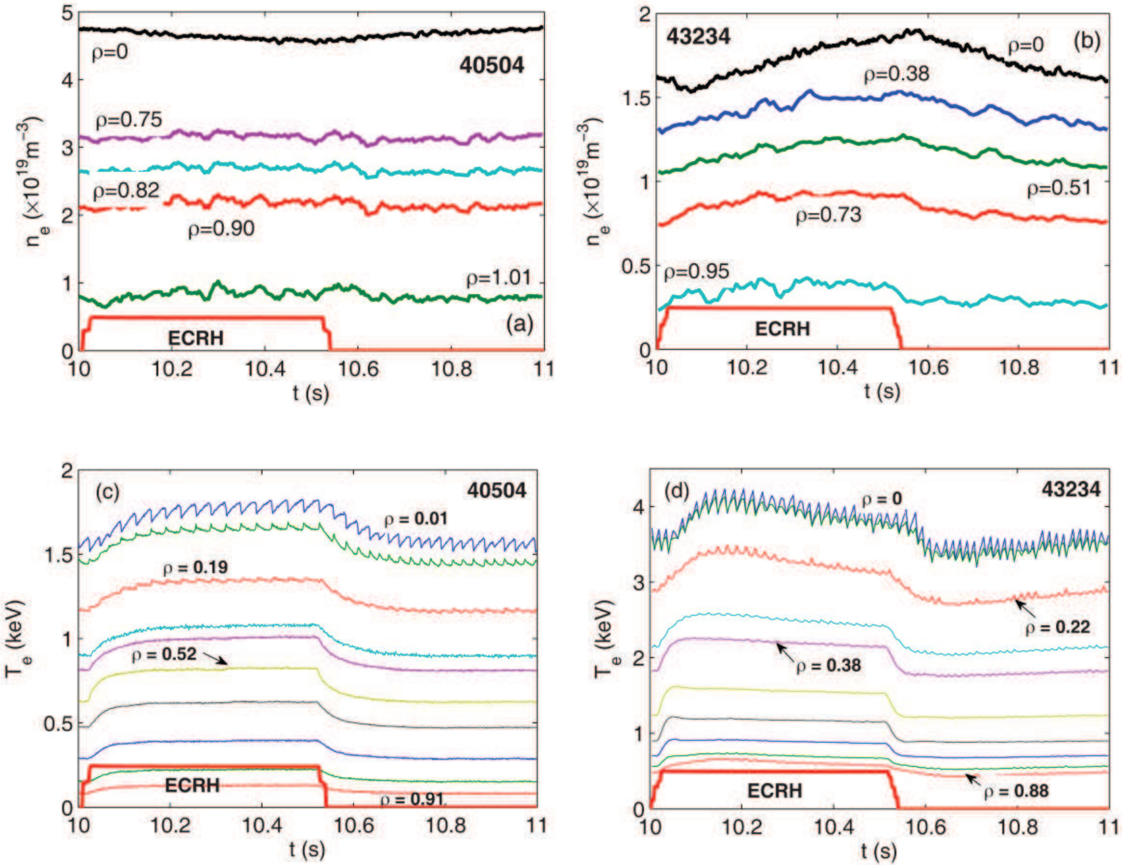

Figure 4.14 (*a*) and (*b*) are density evolution curves at high (*a*) and low (*b*) density cases respectively, during one ECRH modulation period. (*c*) and (*d*) are analogous curves for the electron temperature

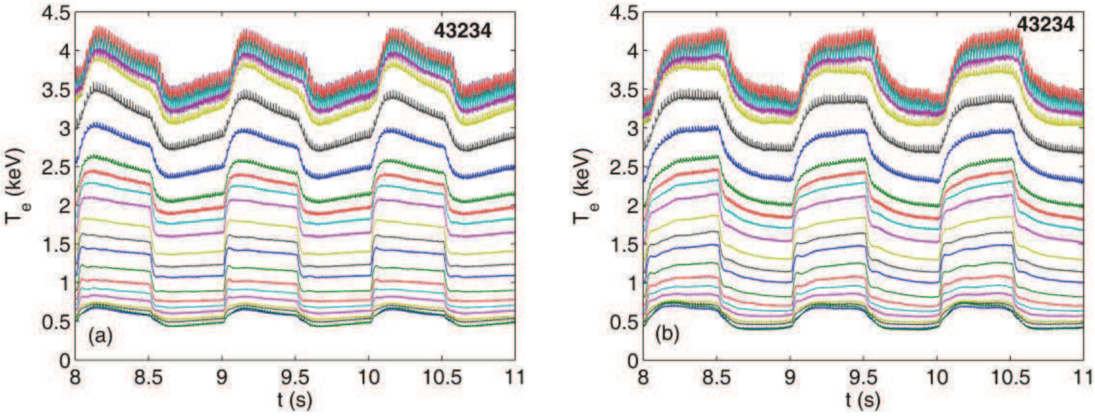

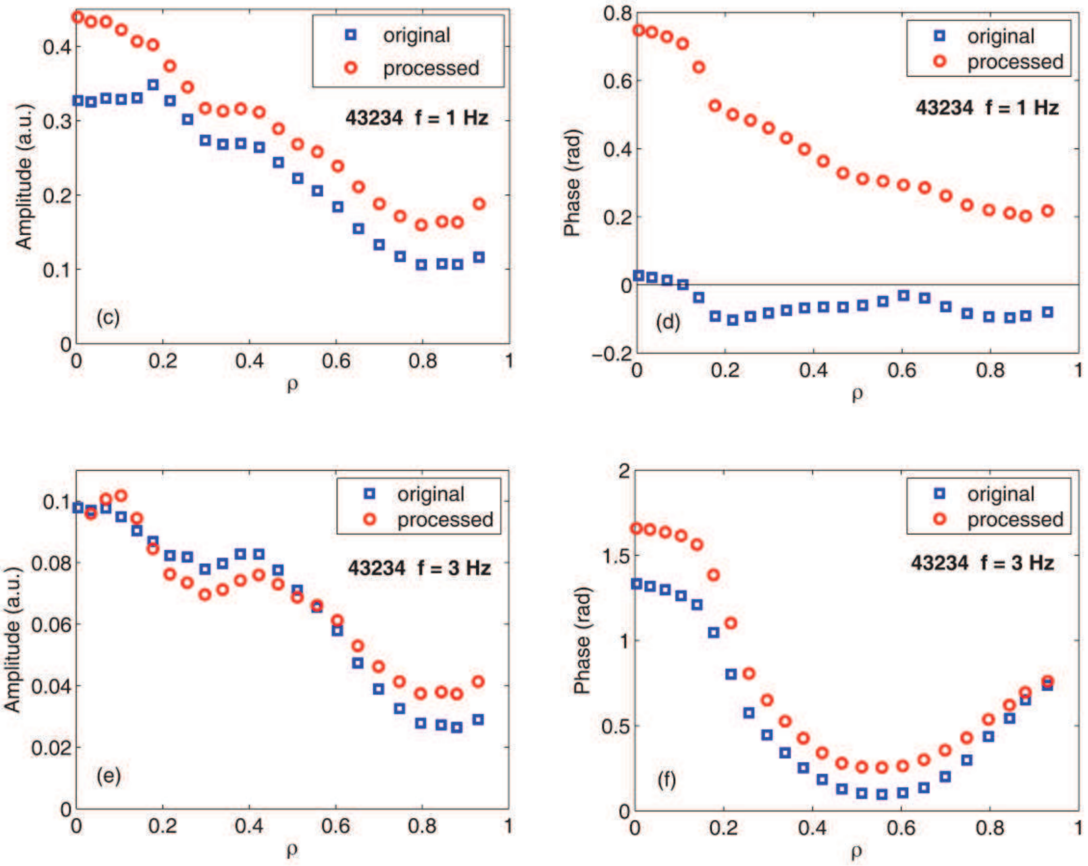

Figure 4.15 (*a*) shows the temperature evolution curves at different radii where higher values are from central measurements, and (*b*) is the modified version of T_e after correction of the density modulation effect. The amplitude and phase profiles for the 1st and 3rd harmonics are shown in (*c*) ~ (*f*) respectively, showing the different extent of influence from density correction, where the blue squares are experimental data and the red circles are processed data. (shot TS#43234)

4.7 Conclusion

Low frequency modulated ECRH experiments have been carried out on the Tore Supra tokamak. The heat pulse propagation has been investigated by the Fourier analysis method. The experimental results are classified into two groups, i.e., high density case (n_{el} = 3~5×10^{19} m^{-3}) and low density case (n_{el} = 1~2×10^{19} m^{-3}). In both cases, inside ρ = 0.3, the amplitude profile has a peak centered at the magnetic axis. The difference between the two is the maximum point shift relative to the minimum point of the phase (which is normally associated with the heating position). In the high density case, the inward shift is not obvious, i.e., it is at most the same ECE channel on the fundamental harmonic; while in the low density case, the shift is three to four channels, which corresponds to a distance of about 10 cm. This is referred as the inward heat pinch effect. The peak inside ρ = 0.3 may be related to the sawteeth, while the strange behavior on the fundamental phase profile is found to be due to the simultaneous oscillations of the density.

Chapter 5 Simulation of heat pinch experiments

The analysis of the heat transport experiments is carried out by both power balance and perturbative methods. In Section 5.1, the ECRH power deposition profile is carefully verified with the ray-tracing code REMA. In Section 5.2, the power balance analysis is done with CRONOS. However, power balance analysis can only find the heat flux, while for heat pinch determination, it is helpless. To find the convective contribution to the heat flux, the easy and direct way is to assume fixed transport coefficients, i.e., not time dependent ones. In this background, the heat flux is divided into two parts, the diffusive one and the convective one. Section 5.3 describes the simulation results using the ANALYTIQUE code. However, the drawback of the direct method is obvious, since the diffusivity can depend on the temperature and/or on its gradients, i.e., it will change according to time. Furthermore, the explanation using fixed diffusivity and convective velocity could be criticized as lacking of physical consideration. Based on these considerations, an often used empirical Critical Gradient Model [31,40] is introduced to replace the fixed diffusivity, together with additional pinch term as a complement. Section 5.4 deals with the CGM model where simulation using GSONIQUE is carried out. However, in order to make further understanding of the physics, turbulence analysis is in need. Section 5.5 deals with the turbulence analysis with Weiland model. A summary is then given at Section 5.6.

5.1 ECRH deposition determination by REMA

The EC wave absorption has been computed with the help of the fully relativistic ray-tracing code REMA, using the global experimental parameters of the discharge (major and minor radius, magnetic equilibrium) and the measured electron density and temperature profiles. The total fraction of absorbed power is found to be 93% for discharge 40504 and 86% for discharge 43234 (rays and absorptions of the two beams for shot 43234 are shown in the first set of figures below). Figure 5.1 shows the power deposition profile for shot 43234.

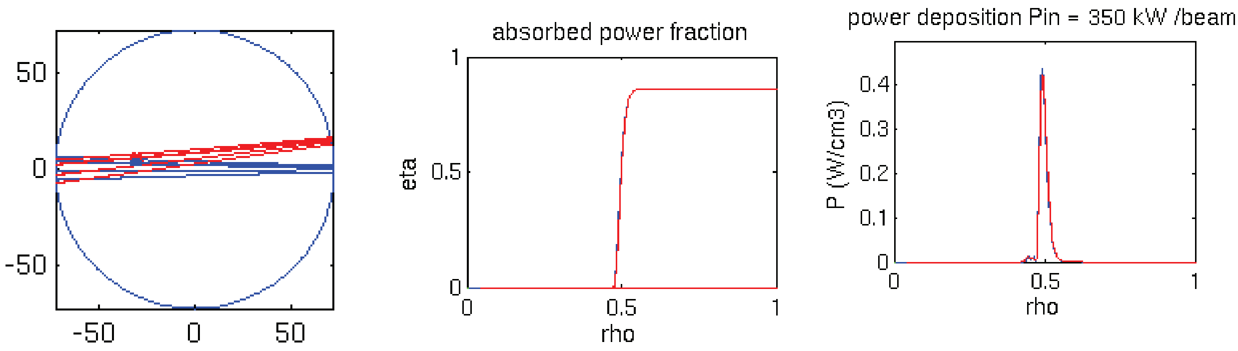

Figure 5.1 The ray traces and power deposition profiles of the two EC waves for shot 43234.

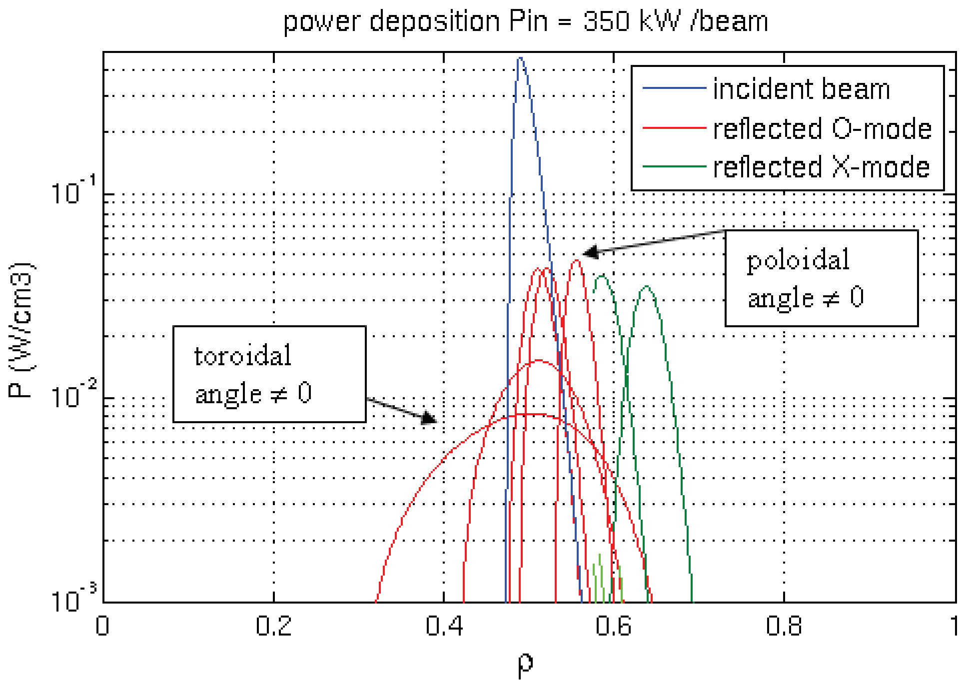

Figure 5.2 Possible spurious power deposition profiles due to reflection from the wall

In order to determine the influence of possible spurious power deposition, especially in the low optical depth case, further calculations with pseudo spurious wave are carried out. Figure 5.2 is an example for the worse case (43234). We assume that the 14% of the power that is not absorbed is reflected on the wall, possibly changing polarisation, poloidal and toroidal angles. In the Figure 5.2, the power deposition profiles of incident and reflected waves are shown in logarithmic scale, for the two polarisations, and various poloidal and toroidal angles of the reflected wave beams. It is found that variation of the toroidal angle leads to a broadened power absorption, whereas variation of the poloidal angles leads to further off-axis power absorption. In summary, this figure shows that:

1) the reflected power absorbed inside $\rho = 0.5$ is typically at least a factor >50 lower than the incident absorbed power, therefore always negligible. Note that this is the plasma region important for the study of the heat pinch.
2) even if the reflected beam were completely polarised and reflected at a single angle, which is of course unlikely, the power deposited would be always at least 10 times smaller than that of the incident beam, and in any case located outside $\rho = 0.5$.
3) if the beam is mainly reflected in the O-mode polarisation and also perpendicularly, it will be absorbed at the same location as the incident beam.
4) it is more likely that reflected beam is polarised partly in the two modes and angularly spread. In this case, the power deposition will be also spread radially and therefore *a fortiori* negligible.

5.2 CRONOS simulation

The goals of the applying the CRONOS suite in this simulation are as follows:

(i) To calculate the magnetic equilibrium and connect physical quantities with the magnetic flux geometry;

(ii) To evaluate the heat source and loss terms, in our case, the sources are Ohmic and ECRH heating; and the loss terms refer to the ion-electron energy exchange, line, bremsstrahlung, and synchrotron radiation;

(iii) To determine an effective diffusivity as reference for the following transport analysis.

In fact, in order to get good power balance analysis, good profiles for density, temperature (both ion and electron channels) and also magnetic equilibrium are necessary. Hereafter, the treatment of the data attracts much attention. In our simulation, the electron temperature profiles are taken from TPROF, which is an experimental data processing tool used on Tore Supra in order to reconstruct smooth profiles, and which is coupled to CRONOS.

The simulation of CRONOS for the two cases (i.e., shot TS#40504 and TS#43234) is performed in the interpretative mode, in which only the current diffusion equation is solved in the predictive mode to keep the consistency between the poloidal flux and the plasma equilibrium. Since the Ohmic and ECRH phases of the modulations last 500 ms and the energy confinement time is of the order of 200 ms, the final times of each phase can be reasonably used for power balance analysis. Using the measured electron density and temperature profiles, heat diffusivity can be determined, in the final 100 ms before the end of each modulation phase, where the stationarity requirement is better fulfilled. Both the power balance and the FFT analyses have been performed in the last few modulations, where temperature, density and current profiles have almost stopped their slow evolutions ($t > 5$ s).

Figure 5.3 shows the effective transport coefficients assuming purely diffusive transport, (*a*) for the shot TS#40504, and (*b*) for the shot TS#43234. It appears that ECRH produces a marked change in the profile of the heat diffusivity, around the absorption location: the diffusivity increases outside and decreases just inside the ECRH peak ($0.4 < \rho < 0.5$). This asymmetry or jump in the heat diffusivity in the presence of ECRH around the power deposition could be explained by the existence of a critical temperature gradient [41]. Furthermore this change in diffusivity profile is much larger for low density than for high density. The global confinement of course decreases in the presence of ECRH, where the plasma is in L-mode. The peak at $\rho \sim 0.3$ in Figure 5.3(*a*) is probably an artifact associated with sawteeth. Note that from this power balance analysis negative diffusivity is not found, therefore inward pinch is not strictly necessary to explain the stationary behaviour. However, it will be shown in the following that inward convection is a good candidate to explain the response to power modulations of low density discharges of this type.

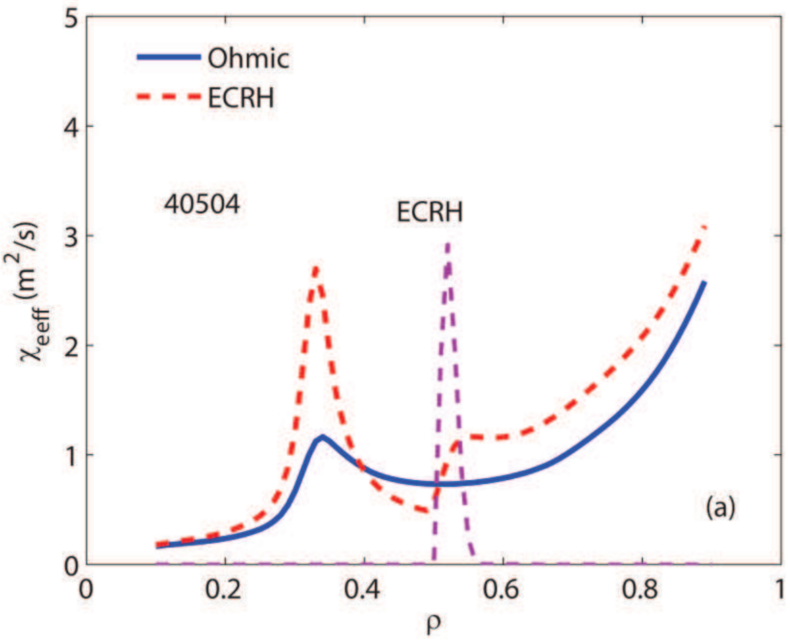

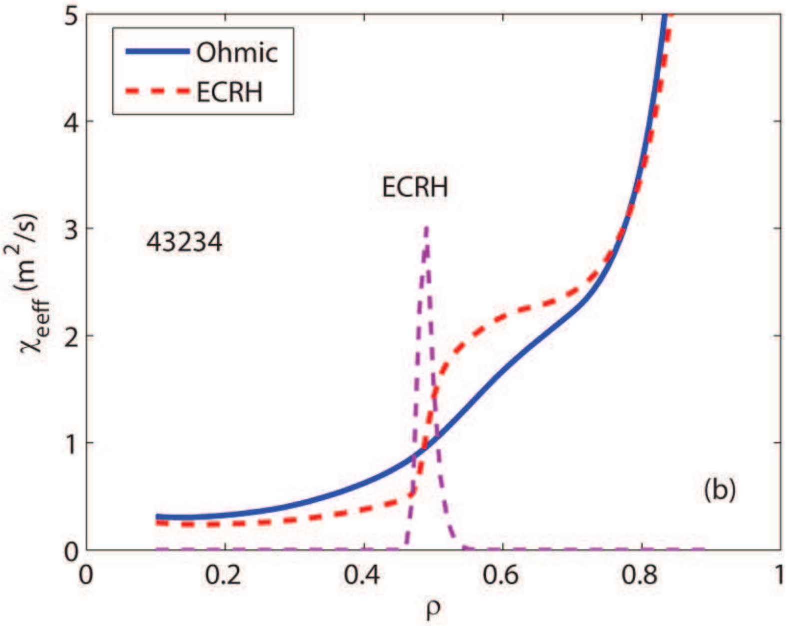

Figure 5.3 Heat diffusivity χ_{eff} from power balance analysis with CRONOS. (*a*) is for shot TS#40504 and (*b*) is for shot TS#43234.

5.3 Simulation with the Linear Pinch Model

The Linear Pinch Model (LPM) is based on a simple description of the perturbed heat flux. As known in the transport analysis, perturbation methods can distinguish the different contributions of diffusive and convective terms, which power balance analysis cannot discriminate. In the so-called LPM, we used constant, i.e., time independent diffusivity and convective velocity profiles. *Linear* refers to the Partial Derivative Equations of the heat transport problem, i.e., the coefficients do not depend on the temperature or its gradients. The *pinch* refers to the convective, mainly inward, term in the heat flux.

In LPM, the transport equation for the temperature perturbation $\widetilde{Te}$ is cast in the following form:

$$\frac{3}{2}\frac{\partial n_e \widetilde{T}_e}{\partial t} - \nabla \cdot \left(n_e \chi_e \nabla \widetilde{T}_e + n_e V_e \widetilde{T}_e\right) + \frac{3}{2}\frac{n_e \widetilde{T}_e}{\tau} = \widetilde{S}_h \tag{5.1}$$

where τ is the damping time which represents all the heat loss terms, including radiation, energy transfer to the ions, decrease of the electron channel, respectively. Note that here positive V_e means inward transport. The values of these parameters are assumed to be constant in time and have spatial profiles. The $\widetilde{S}_h$ term is the modulated ECRH heating source.

Its counterpart in the particle channel has the form of,

$$\frac{3}{2}\frac{\partial \widetilde{n}_e}{\partial t} - \nabla \cdot \left(D\nabla \widetilde{n}_e + V\widetilde{n}_e \right) = \widetilde{S}_p \tag{5.2}$$

where the diffusivity D and particle convection velocity V are also assumed to be constant in time. $\widetilde{S}_p$ is the perturbation of the particle source.

5.3.1 Sensitivity analysis

In practice, the crucial point is how to determine the three relevant parameters, i.e., diffusion coefficient χ_e, convection velocity V_e and damping time τ with a set of experimental data. As for particle perturbation transport experiments [31], the three parameters could be determined by using the different sensitivities of the phase and amplitude to these parameters. Compared to the particle transport, the problem is more complex for the heat transport since the damping time should be taken into account, while this parameter is not involved in particle transport where the loss is negligible in the core of the plasma. In this section, we mainly focus on the heat transport channel.

To determine the transport coefficients with LPM, we use a trial-and-error procedure. This procedure is based on the basic dependence of amplitude and phase profiles on the χ_e, V_e and τ profiles. Figure 5.4 shows the sensitivity of the amplitude and phase of electron temperature Fourier components to the three major parameters. In these figures, constant (in space) χ_e, V_e and τ profiles are assumed, and the boundary conditions at the plasma centre and edge, respectively, are assumed to be $\partial \widetilde{Te} / \partial\rho|_{\rho=0} = 0$and $\partial \widetilde{Te} / \partial\rho|_{\rho=1} = 0$. The n_e profile is assumed to be $n_e(\rho) = 1.2(1-\rho^2)^{0.5}+0.3$; the ECRH power profile is assumed to be Gaussian in space centered at ρ□ = 0.5 with a width of w = 5 cm at the half height, and P_{ecrh} = 0.5 MW ($\widetilde{S}_h = P/2n_0$). The EC power has a square waveform with f_{mod} = 1 Hz and a duty factor of 50% in time. From Figure 5.4(*b*), (*d*) and (*f*), we can see that the phase gradient is only sensitive to the diffusivity χ_e, but much less sensitive to the convection velocity V_e and the damping time τ. Specifically, the phase gradient (in absolute value) decreases when the diffusion coefficient increases and vice versa. In slab geometry, the diffusivity is simply inversely proportional to the square of the gradient of the phase [39]. Unlike the phase, the amplitude is highly sensitive to the convection velocity. For small values of V_e, only the slope of the amplitude profile is changed, while the point of the maximum of the amplitude is always located at the source position. However, for large values of V_e, the position of the maximum of the amplitude moves from the source position. If V_e is positive (inward or pinch), the maximum is shifted towards the plasma centre, if V_e is negative (outward), the maximum is shifted towards the plasma edge.

As for the damping time τ, it changes the overall value of the amplitude and phase, but it has little effect on their slopes. Mathematically, it has similar effect on the phase as the modulation frequency. The effect of the edge boundary condition is shown in figure 11, where amplitude and phase of the first harmonics are compared for $T_e(\rho = 0) = 0$ and $\partial T_e/\partial \rho|_{\rho=1} = 0$. It appears that the region inside the ECRH deposition is hardly affected and that the effect of the edge boundary condition decreases for increasing harmonic number. More generally, using different harmonics improves the determination of the three transport parameters by best fit or trial and error procedures.

However, the description above is just a simplified one, where the transport coefficients are assumed to be constant in radius. Since both the diffusivity and convection velocity have profiles, the real behavior is generally more complex. In practice, when the phase or amplitude presents obvious changes in their gradients, we choose corresponding areas relative to this feature, and assume that inside each area the transport coefficients vary little. By this treatment, LPM can be applied to the whole region.

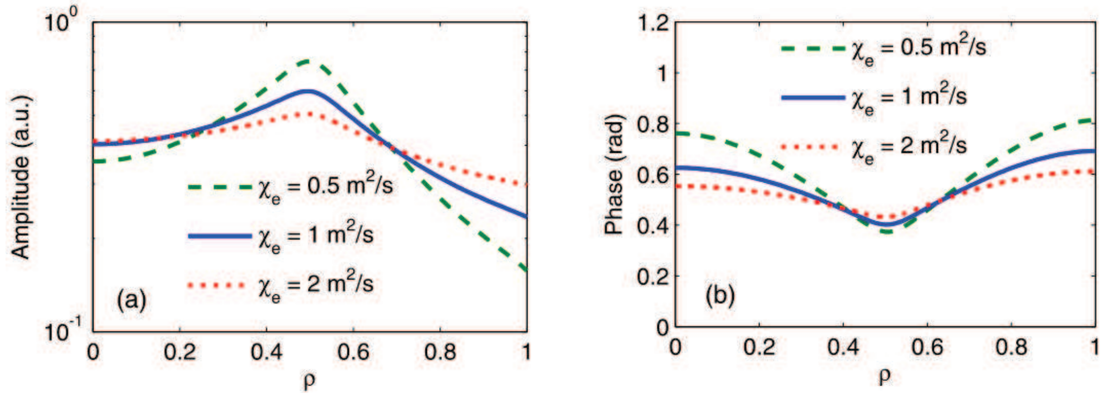

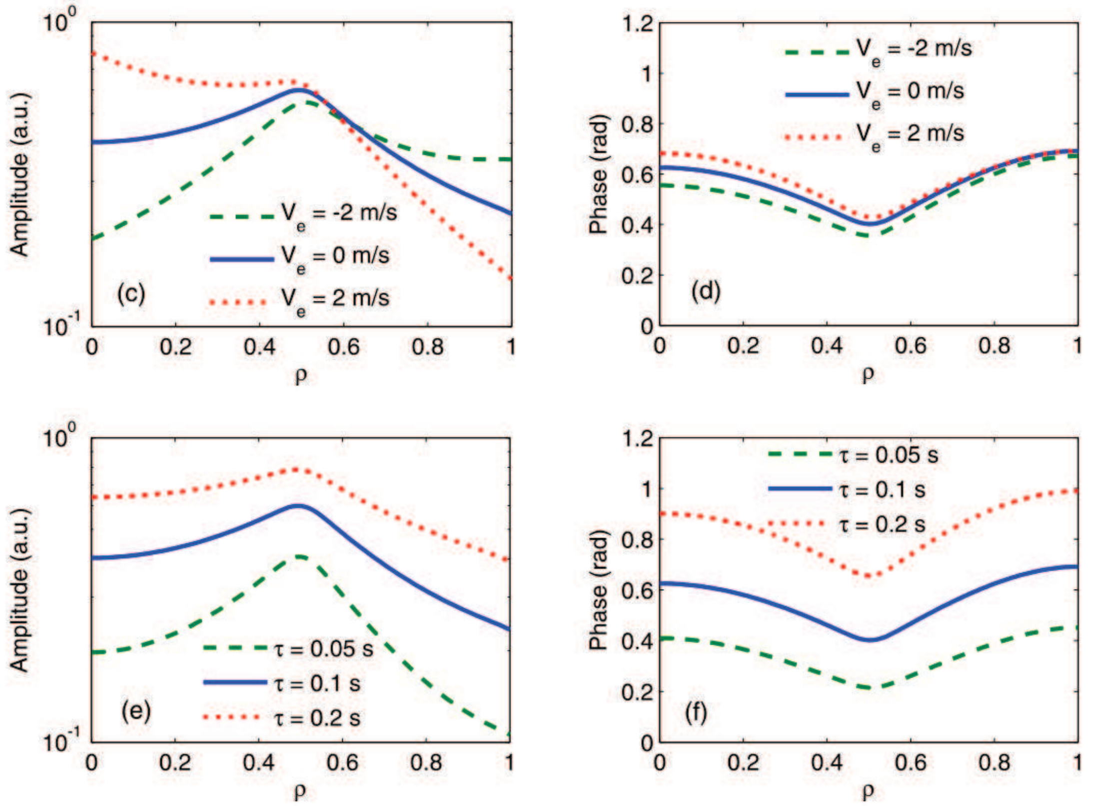

Figure 5.4 Influence of electron diffusivity χ_e, convection velocity V_e (here positive value means inward) and damping time τ to the amplitude and phase profiles of T_e. (*a*) and (*b*) show the influence of τ; (*c*) and (*d*) that of χ_e ; (*e*) and (*f*) that of V_e. The solid lines correspond to the same transport coefficients.

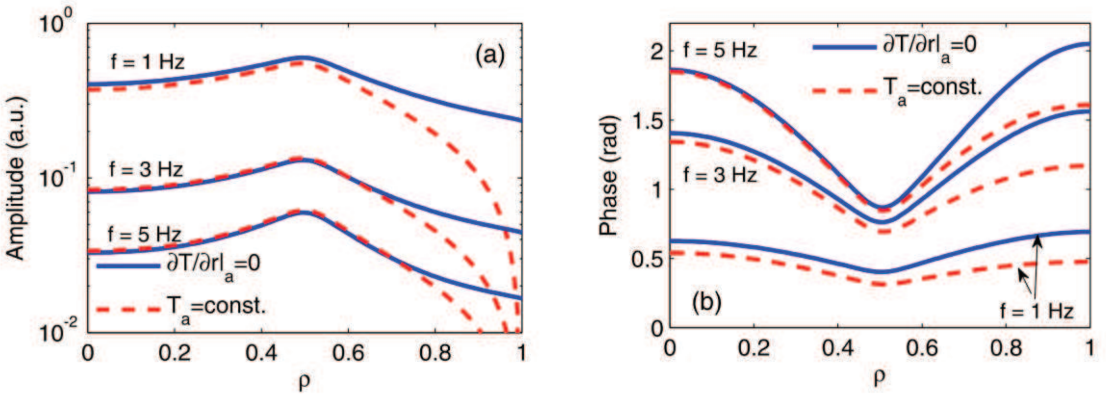

Figure 5.5 Influence of boundary conditions on the amplitude (*a*) and phase (*b*) profiles for the first three harmonics. (χ_e = 1 m^2/s, V_e = 0 m/s and τ = 0.1 s).

For the determination of the damping time τ, we plot the phase as a function of the harmonic frequency, then comparing with the simulation allows us to determine the damping time. Figure 5.6 Shows an example for the determination of τ at the position of the phase minimum. The red circle points represent the experimental points. It appears that the experimental points are very close to the simulation line with τ = 0.02

s. The same method is valid for the determination of τ at other positions.

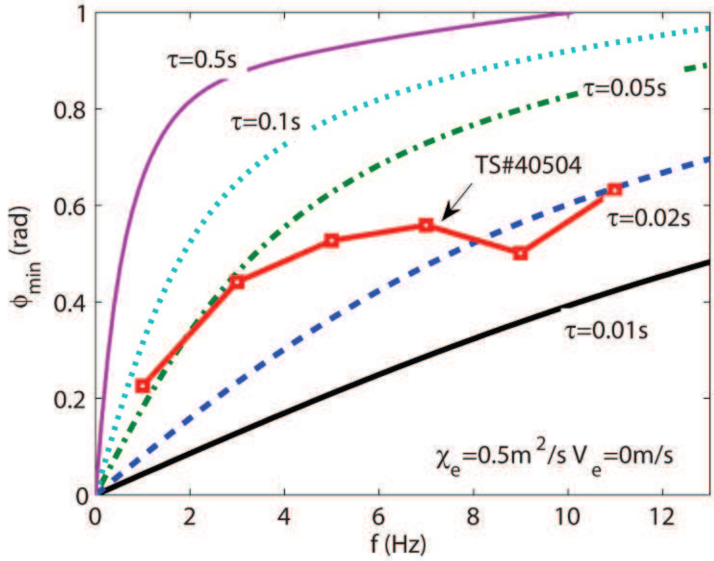

Figure 5.6 Minimum of the phase as a function of the harmonic frequency for various values of τ. χ_e = 0.5 m^2/s, and V_e = 0 m/s for these simulations. The red squares represent the experimental points.

However, an optional solution of the determination of the damping time comes from power balance analysis. Since we are able to compute all the damping terms, what we need to do is just to write them in the form of $3n_eT_e/2\tau$. However there are some differences between the equilibrium values and perturbative ones in the damping term. For the case of the ion-electron exchange term, the energy loss in equilibrium and perturbative case are shown below,

$$Q_{e,i} = \frac{3}{2}\frac{T_e - T_i}{\tau_{ie}} \tag{5.3}$$

$$\tau_{ie} = \frac{m_i}{2m_e}\tau_e = \frac{12\pi^{3/2}}{\sqrt{2}}\frac{\varepsilon_0^2 m_e^{1/2} T_e^{3/2}}{n_i Z^2 e^4 \ln\Lambda} \tag{5.4}$$

$$\tau_{pert} = \left(\frac{\partial Q_{ei}}{n_e \partial T_e}\right)^{-1} = \frac{4}{3}\frac{T_e}{3T_i - T_e}\tau_{ie} \tag{5.5}$$

For the Ohmic power, the effect of ECRH heating, for example, will induce a power sink due to the increment of the electrical conductance of the plasma. Therefore, the damping coefficient for the perturbative term can be derived in the form of,

$$\eta = 1.65\times10^{-9}\ln\Lambda / T_e^{3/2}\ \mathrm{ohm\,m} \tag{5.6}$$

$$\tau_{pert}^{ohm} = \frac{\partial S_{\Omega}}{n\partial T_e} = \frac{3}{2}\frac{S_{\Omega}}{nT_e} \tag{5.7}$$

The above two terms normally play the dominant role in the fraction of total energy loss in the central plasma, with respect to radiative losses.

5.3.2 High density case

The simulations are carried out in the whole plasma region. The boundary condition is set to be $\partial_\rho \widetilde{T}_e|_{\rho=0} = 0$ and $\widetilde{T}_e|_{\rho=1} = \widetilde{T}_{e\,\mathrm{edge}}(t)$, where the edge temperature $\widetilde{T}_{e\,\mathrm{edge}}$ is taken from extrapolation of the experimental ECE data combined with Thomson scattering data. Here we call the harmonic with their orders, which stand for the multiple of the modulation frequency (e.g., the 3rd harmonic means its frequency is 3 times the modulation frequency).

Figure 5.7 shows the results of the simulation with LPM in the high density regime (TS#40504): amplitude and phase determined from Fourier transform for the various harmonics and also the temperature profile in the Ohmic phase. The transport coefficients of this simulation are shown in Figure 5.8, as well as the effective electron heat diffusivity calculated with CRONOS. To improve the simulation, an iterative method is used in which $\chi_e = 1\ \mathrm{m^2/s}$, $V_e = 0$ m/s and $\tau = 0.2$ s are taken as initial values for shot 40504. The ion temperature is assumed to be equal to the electron temperature in the Ohmic phase. For the 1st harmonic, the fit is good for both amplitude and phase in the whole region; for higher harmonics (3rd, 5th, 7th), the results of the simulation are also rather good. From Figure 5.8(*a*), we can see that on one hand, the heat diffusivity obtained with CRONOS (power balance) in the ECRH regime (red dotted line) is larger than that in the Ohmic regime (green dashed line), except for the region just inside the ECRH power deposition layer ($0.4 < \rho < 0.5$). On the other hand, the transient heat diffusivity determined with LPM (blue solid line) is slightly larger than that obtained with CRONOS. This just confirms the results previously obtained on other tokamaks for the perturbation transport analysis [50]. Note that, as extensively discussed in [39] (Sec. 2.6), steady-state and perturbative analyses are expected to yield the same transport coefficients only in the ideal case of a diagonal transport matrix with constant coefficients. As shown in Figure 5.8(*b*), the convection velocity is zero, except in the region $\rho < 0.25$; this means a diffusive propagation phenomenon of heat transport in the region $0.25 < \rho < 0.5$. From Figure 5.7(*a*), we can also see that inside $\rho = 0.25$ the amplitude of the inner part is higher than the outer part for the 1st harmonic. In order to reproduce this in the transport analysis, an inward convection velocity (pinch) of 3.5 m/s (Figure 5.8(*b*)) was needed in order to match the experimental points. As this area coincides with the region inside $q = 1$ surface, it is not excluded that this effect is due to the sawteeth activity.

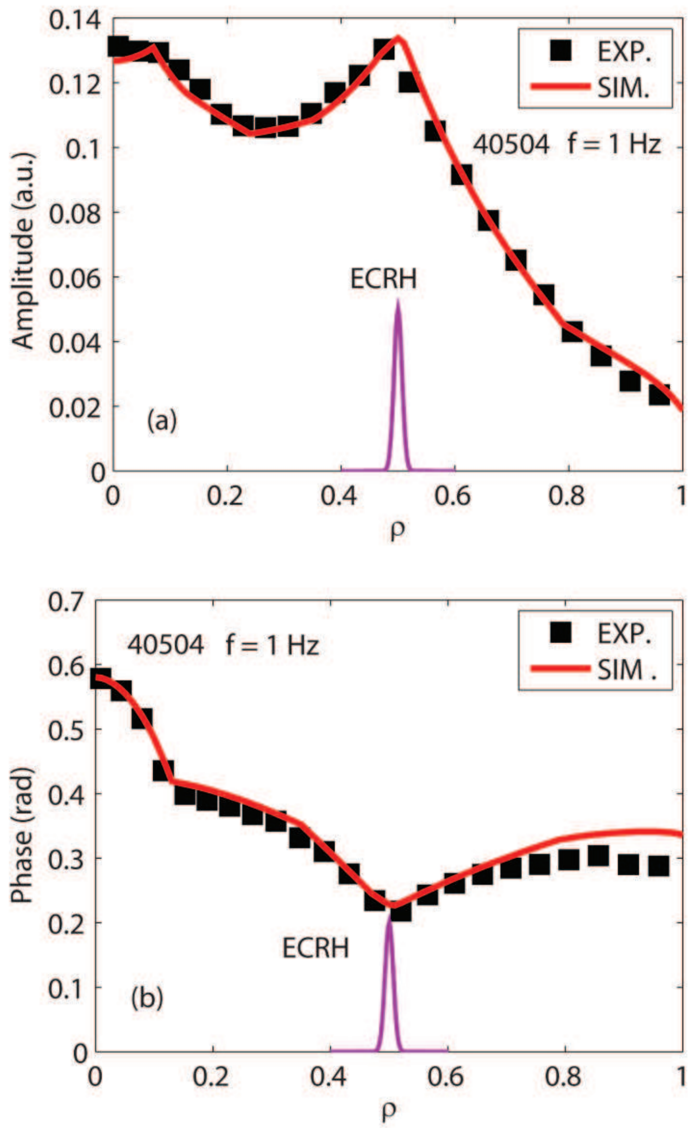

Figure 5.7 Simulation using LPM for high density (TS#40504). The discrete points are experimental values of the fundamental harmonic, and the solid lines represent the corresponding simulation. Amplitude (*a*) and Phase (*b*) of the fundamental harmonic.

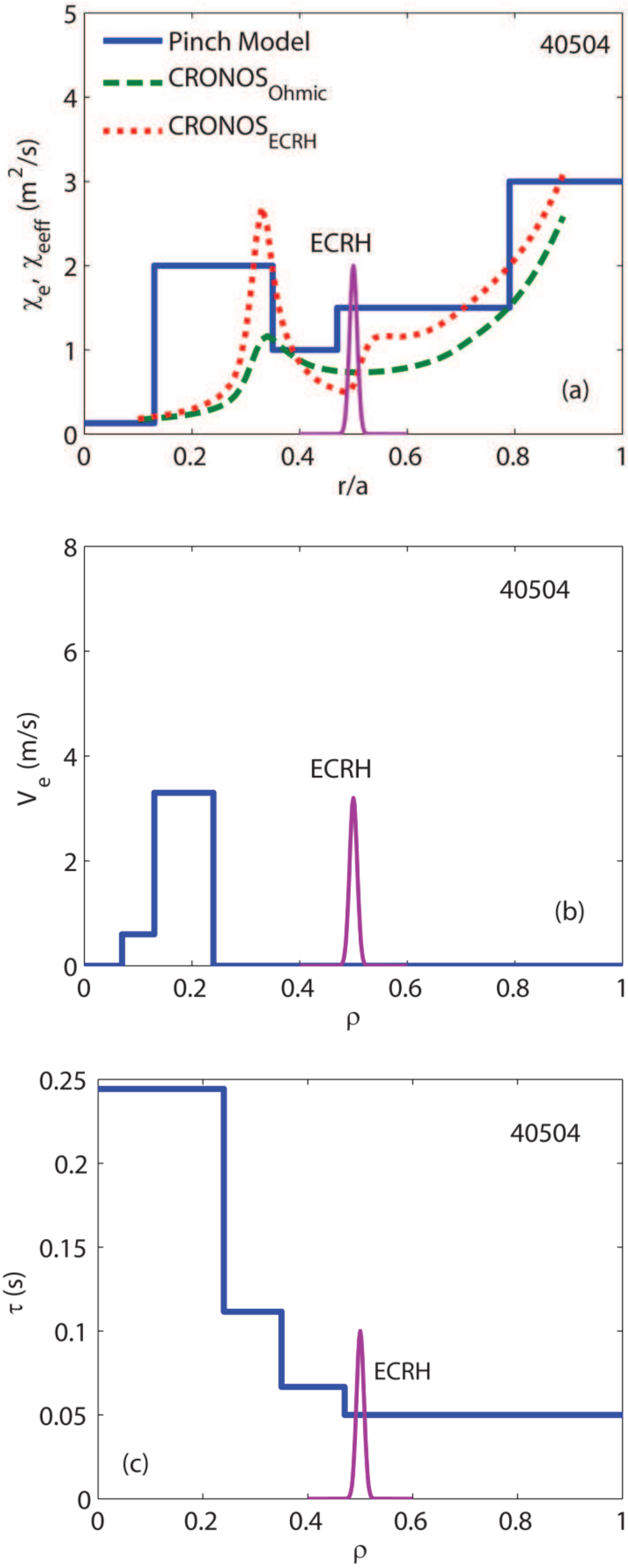

Figure 5.8 Parameters used for the simulation with LPM shown in Figure 5.7(*a*) Diffusivity obtained by LPM (solid line), by CRONOS in the ECRH regime (dotted line) and in the Ohmic

regime (dashed line). (*b*)Pinch velocity (positive for inward). (*c*) Damping time.

The other harmonics are also shown in Figure 5.9. For the 1st harmonic, agreement is found for both amplitude and phase in the whole region; for higher harmonics (3rd, 5th, 7th), the results of the simulation are also rather good.

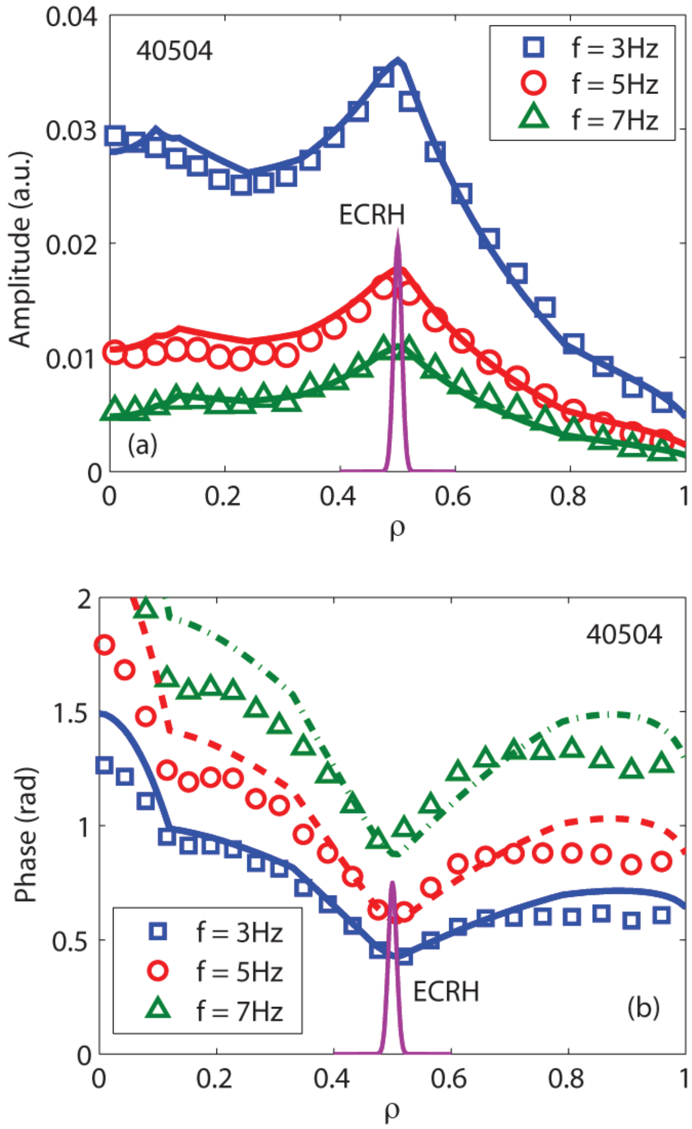

Figure 5.9 Simulation using LPM for high density (TS#40504). The discrete points are experimental values, and the solid lines represent the simulation. Amplitude (*a*) and phase (*b*) of the 3rd, 5th, and 7th harmonics.

5.3.3 Low density case

For shot 43234, the third harmonic is chosen to be the goal for simulation, as discussed in section 4.6. The results of the simulation for the 3rd harmonic using LPM are shown in Figure 5.10(*a*) and (*b*). The experimental data is marked with discrete squares, and the solid curves are fits using LPM with boundary condition of constant edge temperature, while the dashed curves are fits with time varying edge temperature boundary condition. From these figures, we could see that rather good agreement with the experimental data is found for $\rho < 0.8$. In the region $\rho > 0.8$, the two boundary conditions yield different results, and the time-varying boundary condition is always in better agreement, in particular for the phase. The corresponding transport parameters in this simulation are shown in Figure 5.12.

As expected, a large pinch velocity over a broad area ($0 < \rho < 0.7$) has been found with LPM. This pinch velocity can reach values of order of 8 m/s near the ECRH power deposition region. This large heat pinch velocity is essential to reproduce the inward shift of the maximum of the amplitude. Now the transient heat diffusivity determined with LPM (blue solid line) is much larger (2 or 3 times) than that obtained with CRONOS. This dependence on density of the ratio between the transient and the steady-state diffusivities confirms the observations of ASDEX Upgrade and the related interpretation work [50]. In Ref. [50], the decrease of this ratio with the density has been interpreted as a transition from the turbulence driven by trapped electron modes (TEM) to that driven by the ion temperature gradient (ITG) via the change in collisionality.

Figure 5.12 shows the simulation results for the other harmonics, i.e., the 1^{st}, 5^{th} and 7^{th}. For the purpose of clarity, only the simulation results with constant edge temperature are then shown. The results of simulation for higher harmonics (5^{th}, 7^{th}) are also acceptable, while for the 1^{st} harmonic amplitudes show qualitative agreement and phases are quite different, due to the density effect as expected and discussed in Sec. 4.6.

In summary, this modelling exercise has shown that reproducing the behaviour of several harmonics without an inward pinch would be difficult, in particular in the low density case.

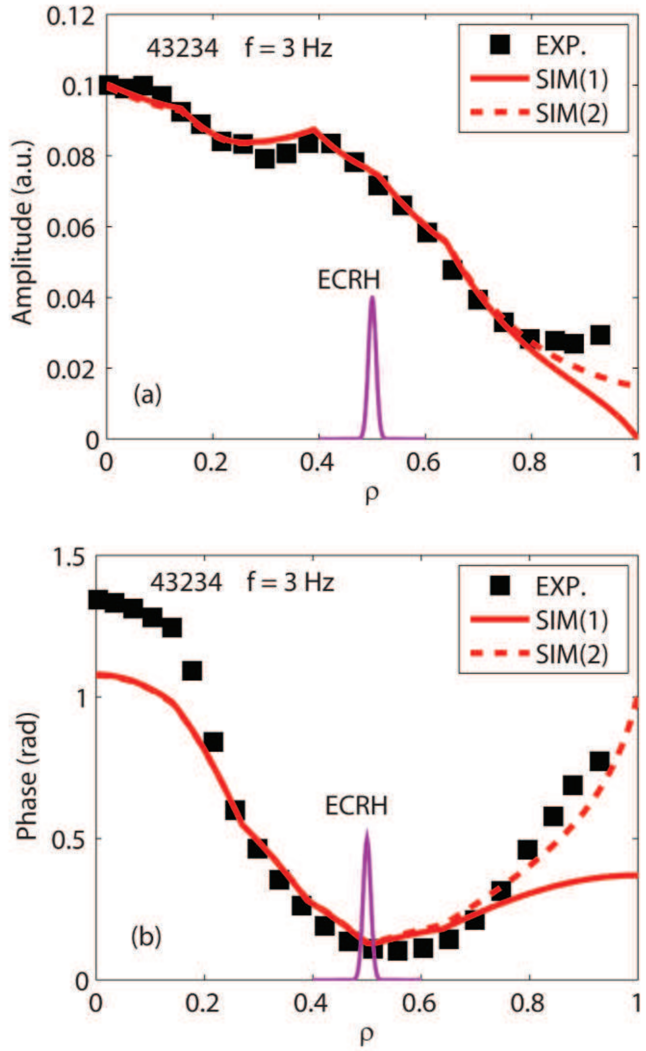

Figure 5.10 Simulation using LPM for low density (TS#43234). The discrete points are experimental values, the solid lines marked by SIM(1) represent the simulation with fixed boundary condition (T_{edge} = const.), and the dashed lines marked by SIM(2) represent the simulation with time varying edge temperature as boundary condition. Amplitude (*a*) and phase (*b*) of the 3rd harmonic.

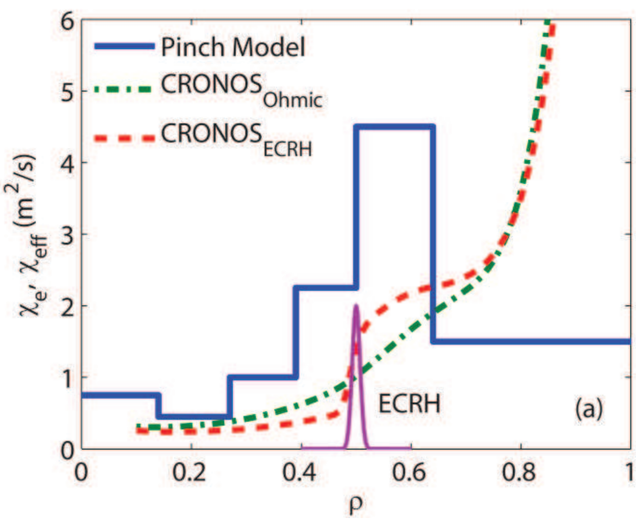

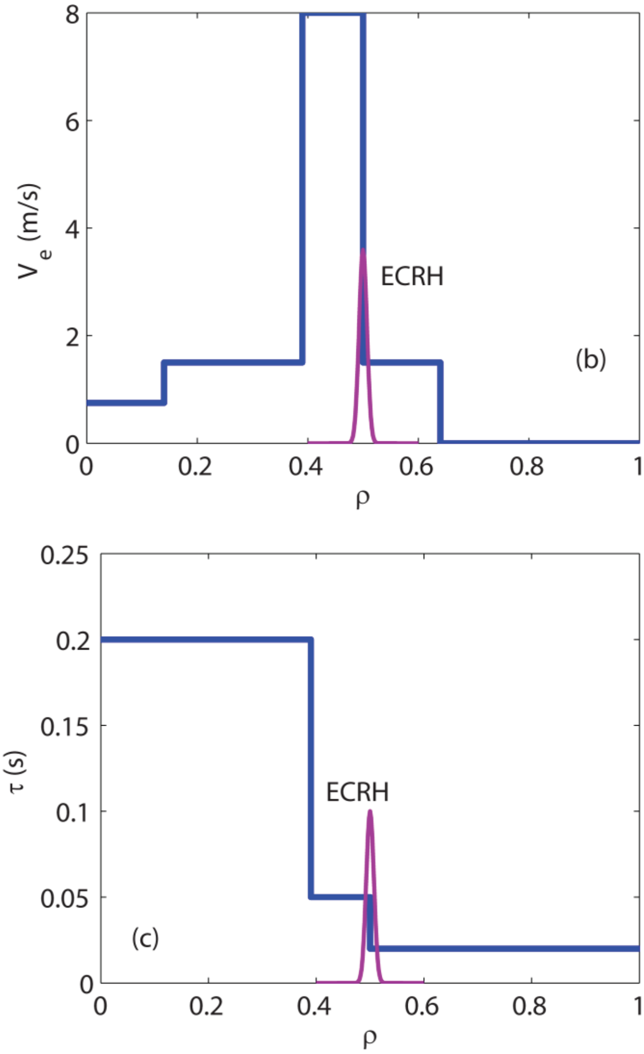

Figure 5.11 Parameters used for the simulation with LPM shown in Figure 5.10(*a*) Diffusivity obtained by LPM (blue solid line), by CRONOS in the ECRH regime (red dotted line) and in the Ohmic regime (green dashed line). (*b*) Pinch velocity (positive for inward convection). (*c*) Damping time.

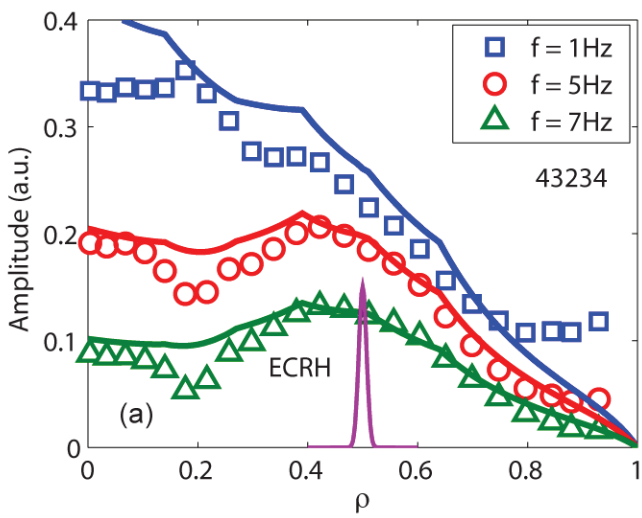

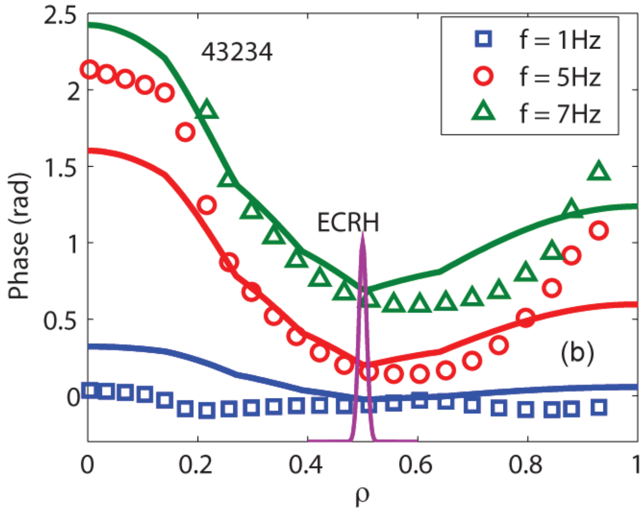

Figure 5.12 Simulation using LPM for low density (TS#43234). The discrete points are experimental values; the solid lines represent the simulation. Amplitude (*a*) and phase (*b*) of the 1st, 5th and 7th harmonics.

5.4 Simulation with the Critical Gradient Model

It is commonly accepted that turbulence contributes to the main part of electron heat transport. Turbulent transport is generally induced by the growth of instabilities, in which two kinds of electrostatic drift-wave instabilities ITG (Ion Temperature Gradient) and TEM (Trapped Electron Modes) are considered to be the most likely causes of electron heat transport for low β regimes [50], where $\beta = p/(B^2/2\mu_0)$, p is the pressure, and B the magnetic field. In the majority of transport models such as RLW [42], IFS-PPPL [43], GLF23 [44], OHE [45], Multi-Mode [46] and Weiland model [47], a threshold exists in the temperature gradient at which the transport switches from a low residual level to highly turbulent. A review of these models is available in [48]. This threshold behaviour is illustrated by an empirical transport model called Critial Gradient Model (CGM) [31,40], in which the heat diffusivity has the form

$$\chi_e = \chi_{gB}\chi_s\left(-R\partial_r T/T-\kappa\right)H\left(-R\partial_r T/T-\kappa\right)+\chi_0 \tag{5.8}$$

where $\chi_{gB} = q^{\nu}(T_e/eB)\rho_s/R$. Here κ is the threshold of the normalized temperature gradient $(-R\partial_r T_e/T_e)_{crit}$, H is the Heaviside function which produces the threshold effect: for $-R\partial_r T_e/T_e < \kappa$, $H = 0$ and for $-R\partial_r T_e/T_e \geq \kappa$, H = 1. $\chi_{gB}\chi_0$ is the residual diffusivity which is responsible for heat transport whenever $-R\partial_r T_e/T_e$ is lower than the threshold κ, χ_s is called stiffness factor and characterizes the strength of the critical gradient transition. In the following, $\nu = 3/2$ is chosen, as suggested in [40]. The CGM was successfully applied to various experiments in ASDEX Upgrade [49,50], DIII-D [51], JET [52], FTU [53] and in comparisons between devices [40,54].

In this study, the CGM model is used as a paradigm of critical temperature based models, independently of any considerations on the turbulence regime that effectively governs these discharges, and that in any case is difficult to determine with precision.

5.4.1 High density case

Best fit CGM parameters for the experimental data of the high density case (shot 40504) is shown in Figure 5.13, where $\kappa = 6$, $\chi_s = 0.8$ and $\chi_0 = 0.4$ (constant values). The ion temperature profile is reconstructed by means of the CRONOS code, using measurements constraints whenever available. Sensitivity to the ion temperature profile has been found to be little. The boundary condition is assumed to be the time-varying temperature which derives from extrapolation of experimental measurements (ECE and Thomson scattering).

The temperature, amplitude and phase profiles agree rather well with experimental data. For the fundamental and third harmonics, the amplitudes inside $\rho = 0.1$ are too low compared to experimental ones, owing to the fact that the temperature gradient inevitably goes below the threshold close to the plasma centre. This probably indicates that a little inward pinch could improve the agreement here; however, such a term would make the agreement on the phase worse. Note that in the LPM analysis a pinch had been added for $0.1 < \rho < 0.25$ in order to simulate this feature.

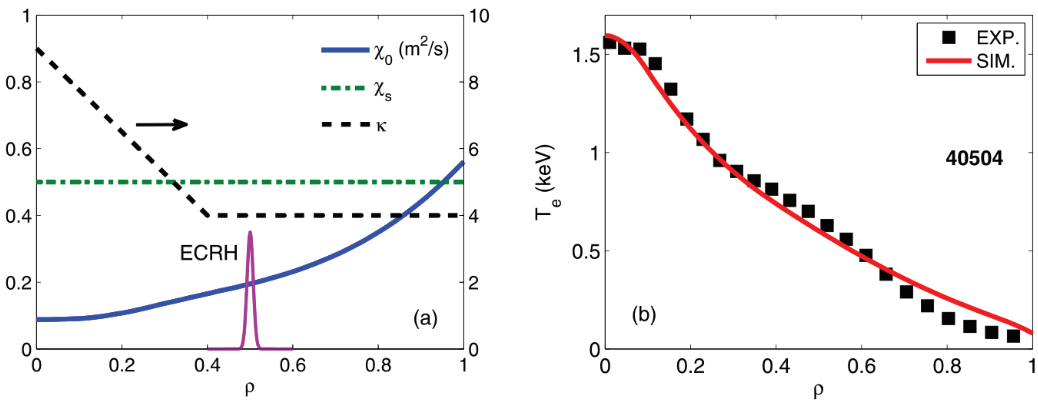

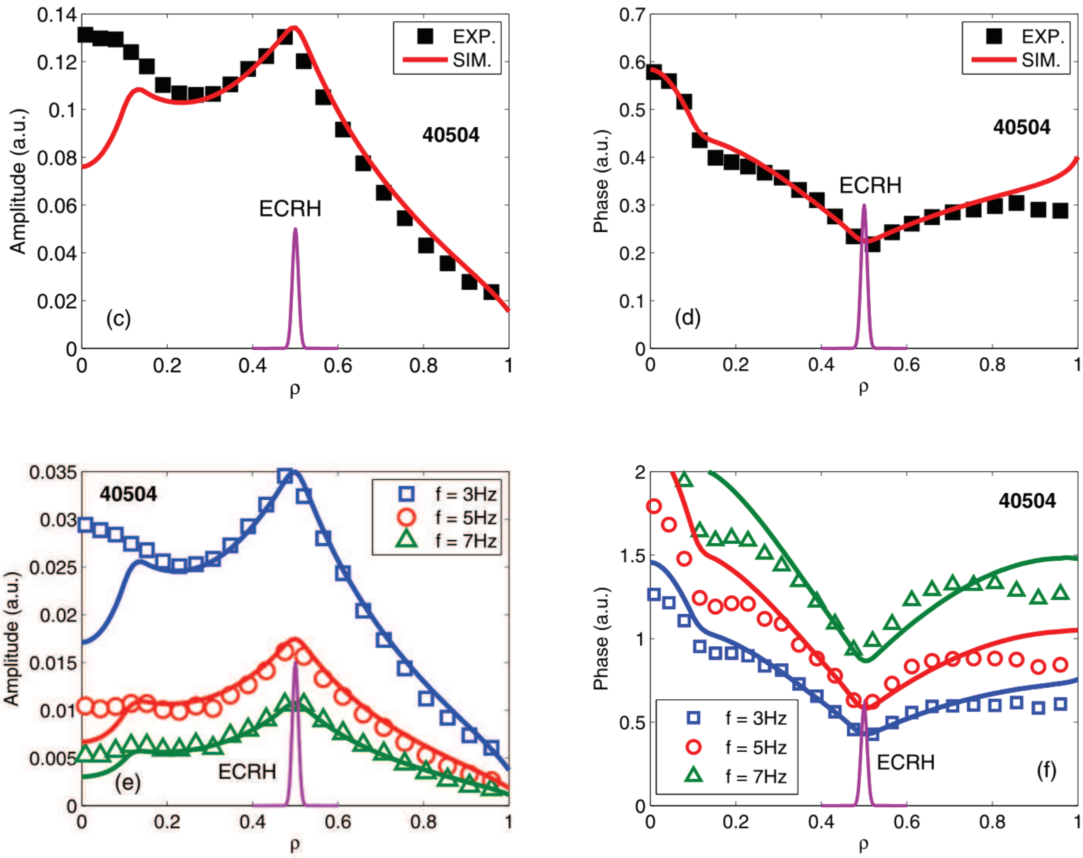

Figure 5.13 Simulation for shot TS#40504 using purely diffusive CGM. (*a*) Parameters used in CGM, κ = 6, ν = 3/2. (*b*) Electron temperature profile. (*c*) Amplitude and (*d*) phase of the fundamental harmonic. (*e*) Amplitude and (*f*) phase of the 3rd, 5th and 7th harmonic. For (*b*) ~ (*f*), the discrete points represent the experimental data, and the solid curves represent the simulation results.

5.4.2 Low density case

For the discharge showing an inward heat transport trend, i.e. shot 43234, the simulations with CGM have also been performed trying to reproduce the experimental data. The best simulation is shown in Figure 5.14, in which ν = 1.5 (constant values) and the threshold value κ increases towards the centre. The main parameters used in the simulation are shown in Figure 5.14(*a*), and in Figure 5.14(*b*) ~ (*f*), the dashed curves are simulations without pinch term, and the solid curves are simulations with pinch. As seen in Figure 5.14(*c*), the amplitude is lower than the experimental data in the absence of a pinch term. This suggests the necessity of adding a heat pinch to the CGM coefficients. By using a simple constant value for the pinch velocity inside $\rho <$ 0.3, much better agreement on both amplitude and phase could be reached; this could of course be optimized by finely tuning the shapes of all the transport coefficients used in this simulation. Note that there is a delicate interplay between the effect of this additional pinch and the non-linearity of the CGM model, in particular close to the threshold, since the heat convection modifies the temperature gradient. A more comprehensive non-linear model including heat convection should be developed for this type of comparisons.

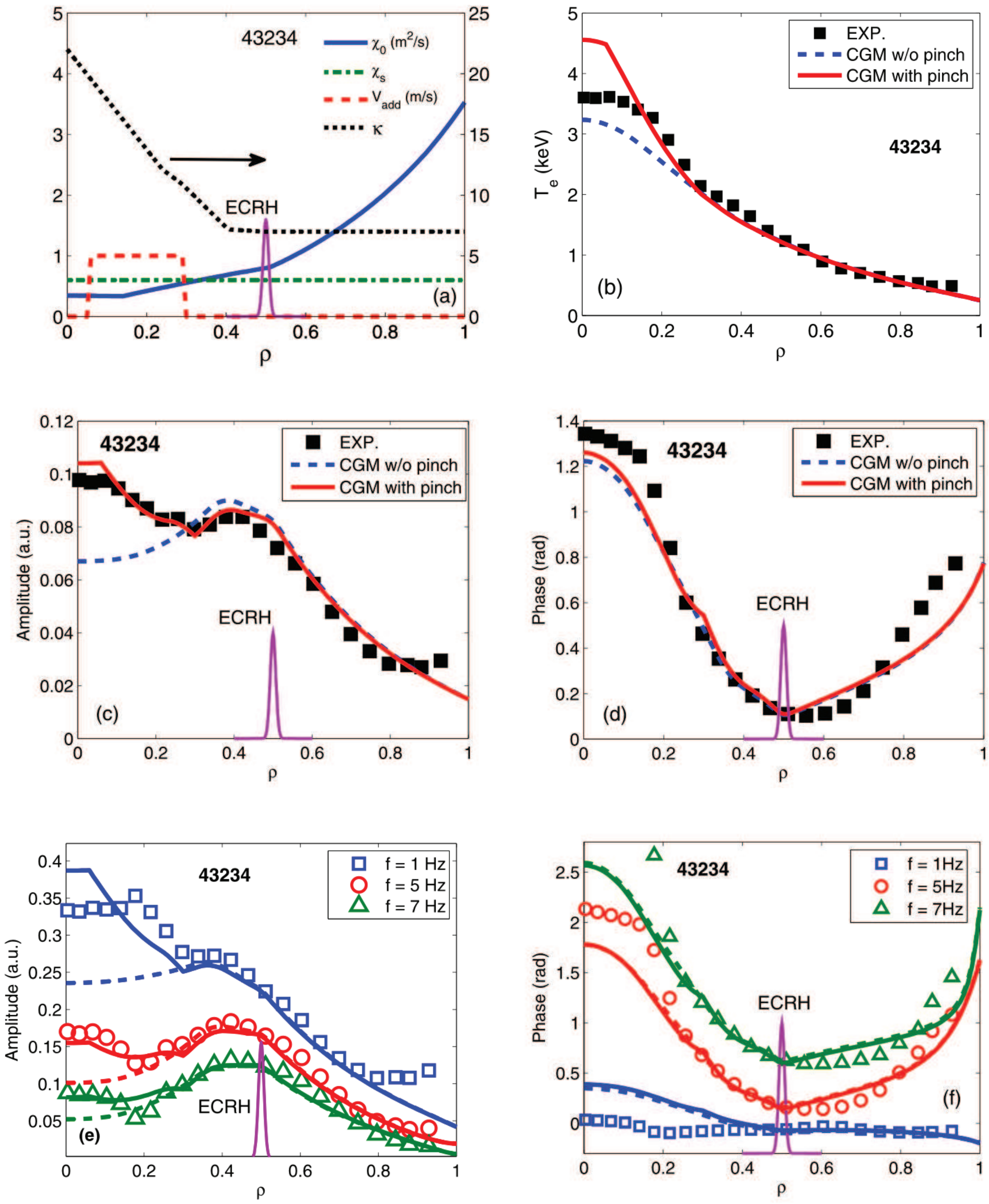

Figure 5.14 Simulation for shot TS#43234 using purely diffusive CGM and with a pinch term, where $\kappa = 7$, $\nu = 3/2$. (*a*) Parameters used in CGM, (*b*) Electron temperature profiles in the Ohmic phase. (*c*) Amplitude and (*d*) phase of the 3rd harmonic. (*e*) Amplitude and (*f*) phase of the 1st, 5th and 7th harmonics. In these figures, the solid lines are simulations with pinch term, while the dashed lines are simulations without pinch. For (*b*) ~ (*f*), the discrete points represent the experimental data, and the solid curves represent the simulation results.

The simulations using the CGM model can be used to illustrate the role of the density variations during the ECRH modulations. To this end, the temperature evolution at $\rho = 0.34$ with time varying density profile is shown in Figure 5.15, where other parameters are those used in the simulation with pinch term of Figure 5.14. The four phases of the temperature evolution described in Section 4.3.2 are well reproduced by the simulation, when the density variation is included.

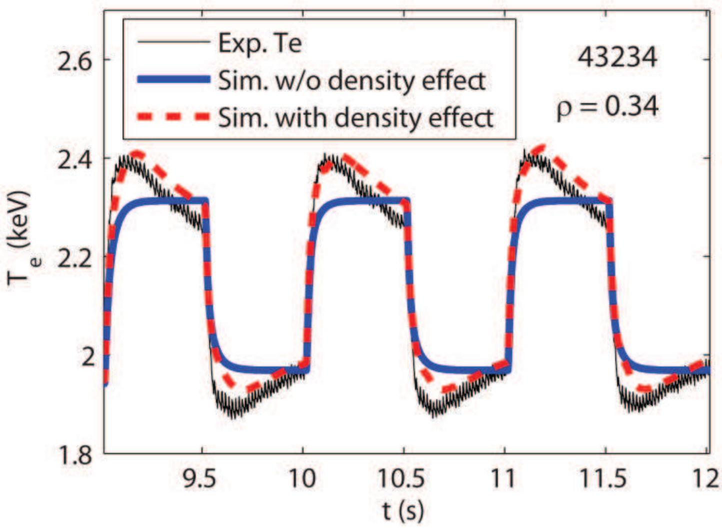

Figure 5.15 Comparison between the experimental data and the simulation with and without the consideration of density oscillation effect (at $\rho = 0.34$).

The empirical CGM model has been used in order to explain both the steady state and perturbation properties of the modulated discharges. The perturbative heat transport equation can be obtained by linearizing the CGM model in the form of [88]

$$\frac{3}{2} n_{e0} \frac{\partial \tilde{T}_e}{\partial t} - \chi_e^{HP} n_{e0} \nabla^2 \tilde{T}_e + V_{eff} \nabla \tilde{T}_e + \frac{n_{e0} \tilde{T}_e}{\tau} = \tilde{Q}_e \tag{5.9}$$

here the coefficients of χ^{HP} and V_{eff} represent the effective diffusion and convection part for the propagation of the perturbation. The damping term τ has similar meaning as in the LPM model. The effective coefficients can be written as:

$$\begin{aligned} \chi_e^{HP} &= \chi_e + \frac{\partial \chi_e}{\partial (\nabla T_e)} \nabla T_e \\ &= \chi_{gB} \chi_s (-2R\partial_r T_e / T_e - \kappa) H(-R\partial_r T_e / T_e - \kappa) + \chi_0 \end{aligned} \tag{5.10}$$

$$\begin{aligned} V_{eff} &= -\frac{\partial \chi_e}{\partial T_e} \nabla T_e^{PB} \\ &= -\frac{1}{2} \frac{\partial_r T_e}{T_e} \chi_{gB} \chi_s (-R\partial_r T_e / T_e - 3\kappa) H(-R\partial_r T_e / T_e - \kappa) \end{aligned} \tag{5.11}$$

where $V_{\mathrm{eff}} > 0$ corresponds to an inward velocity. In this equation, for peaked profile (i.e., $\partial_r T_e < 0$), the contribution from the gradient difference is positive when $-R\partial_r T_e/T_e < 3\kappa$. In our simulation, in the region $\rho < 0.3$, the normalized gradient is below the threshold, which leads to a consant diffusivity and hence makes the effective pinch effect to vanish.

These two effective transport coefficients are compared with the ones we used for the LPM in Figure 5.16. In panel (*a*), the diffusivities in ECRH and Ohmic phases of CGM and CRONOS simulations are shown. A qualitative agreement with the LPM in the region $\rho < 0.6$ is found. Panel (*b*) shows the effective pinch together with that of the LPM case. In the simulation, at the region $\rho < 0.3$, constant diffusivity is assumed, which makes the effective pinch effect to vanish. However, if we had used a pure CGM model, in the region where $-R\partial_r T_e/T_e < \kappa$ (i.e., $\rho < 0.3$ in our case), an outward pinch would have been found.

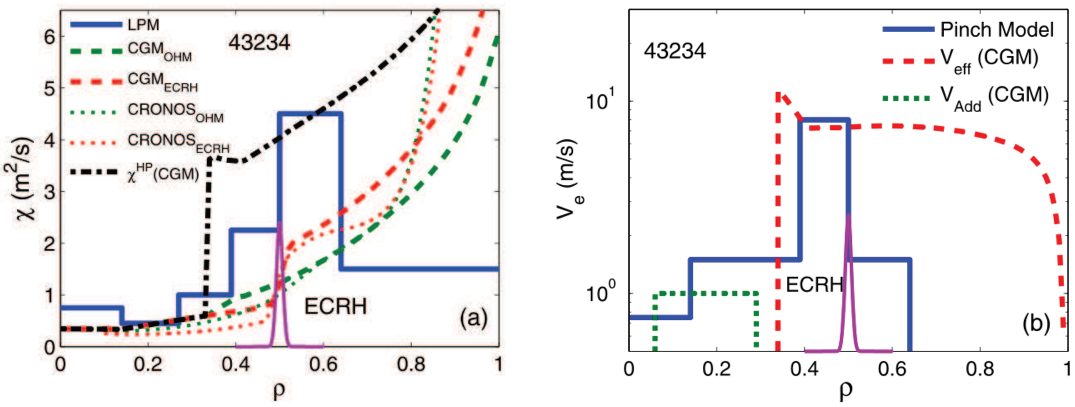

Figure 5.16 (*a*) Comparison of the diffusivity profiles from different models. The solid line is the diffusivity from LPM, the thin dashed line and dotted line are ECRH and Ohmic data from CRONOS simulation, and the thick dashed line and dotted line are ECRH and Ohmic data from CGM simulation. (*b*) Comparison between the value of pinch (solid line) in LPM, effective pinch (dashed line) introduced by CGM, and the additional pinch (dotted line) to CGM.

In summary, the inward heat transport features observed in Tore Supra in low density regimes with off-axis ECRH modulation are likely due to the combination of two effects: a large pseudo pinch due to the non-linearity in the heat diffusivity in the region $0.3 < \rho < 0.5$ (close to the ECRH power deposition), and a non-diffusive heat pinch in the region $\rho < 0.3$. The added pinch term has been determined by a trial and error procedure.

5.4.3 Summary

To summarize, for high density case, with pure CGM model, the experimental data can be recovered with simple constant transport parameters. However, even with complex profiles of CGM, good agreement cannot be reached for the low density case. Owing to the non-linearity of the CGM model, a pseudo-pinch naturally exists, coming from the derivative of the diffusivity with respect to ∇T_e. Nevertheless, this pseudo-pinch is not sufficient to reproduce the experimental results, in particular the amplitude in the modulation experiments, and an additional heat pinch is required. .

5.5 Simulation with a simplified Weiland Model

In this section, micro-instability analysis carried out on the basis of the Weiland model is described. The reactive drift modes of the Weiland model are interchange modes arising from the pressure inhomogeneity, with gravity replaced by the ∇B force, including temperature perturbations, and the centrifugal force experienced by the particles as they follow the twisted magnetic field lines. Reactive drift modes arise if particle trapping inhibits quasi-neutrality or if a temperature gradient causes a competition between convection and thermalization [55]. In this model, the stability of TEM and ITG modes is considered; the impurity ITG modes and electromagnetic effects are omitted here, that is why we called it the simplified version. The dispersion relation is given by [47],

$$\begin{aligned}\frac{\omega_{*e}}{N_i}\Bigg[\omega\left(1-\frac{2L_{ni}}{R}\right)+\left(\frac{L_{ni}}{L_{Ti}}-\frac{7}{3}+\frac{10}{3}\frac{L_{ni}}{R}\right)\omega_{Di}\\ -k_\theta^2\rho_s^2\left(\omega-\omega_{*iT}\right)\left(\frac{\omega}{\omega_{*e}}+\frac{10}{3}\frac{T_i}{T_e}\frac{L_{ni}}{R}\right)\Bigg]\\ =f_t\frac{\omega_{*e}}{N_e}\left[\omega\left(1-\frac{2L_{ne}}{R}\right)+\left(\frac{L_{ne}}{L_{Te}}-\frac{7}{3}+\frac{10}{3}\frac{L_{ne}}{R}\right)\right]+1-f_t\end{aligned} \tag{5.12}$$

In [56], the heat flux is split into two parts: diffusive and convective, in the form of Equation (5.11), in which the corresponding transport coefficients using mixing length estimates are also given,

$$q_e=-n_e\chi_{ee}\nabla T_e+T_e\chi_{en}\nabla n_e-V_e n_e T_e \tag{5.13}$$

$$\chi_{ee}=f_t\left[\frac{3}{2}+b_1(\hat{\omega})\right]\Gamma \tag{5.14}$$

$$\chi_{en}=-f_t\left[1+\frac{7b_1(\hat{\omega})}{3}-b_2(\hat{\omega})\right]\Gamma \tag{5.15}$$

$$V_e = -\frac{2f_t}{L_B}\left[\frac{5}{3}b_1(\hat{\omega}) - b_2(\hat{\omega})\right]\Gamma \tag{5.16}$$

where

$$b_1(\hat{\omega}) = \frac{9|\hat{\omega}|^2(2\hat{\omega}_r - 5) + 25}{9\left|\hat{\omega}^2 - \frac{10}{3}\hat{\omega} + \frac{5}{3}\right|^2} \tag{5.17}$$

$$b_2(\hat{\omega}) = \frac{|\hat{\omega}|^2\left(9|\hat{\omega}|^2 - 65\right) + 50}{9\left|\hat{\omega}^2 - \frac{10}{3}\hat{\omega} + \frac{5}{3}\right|^2} \tag{5.18}$$

$$\Gamma = \frac{\gamma^3 / k_x^2}{\left(\omega_r - \frac{5}{3}\omega_{De}\right)^2 + \gamma^2} \tag{5.19}$$

Here, the eigenvalues $\omega = \omega_r + i\gamma$, are calculated from the linearized equations using the strong ballooning approximation [57], and are normalized to the electron magnetic drift frequency ω_{De} ($\hat{\omega} = \omega / \omega_{De}$). The transport coefficients are summed over all unstable modes (here ITG and TEM) with $(k_\theta \rho_s)^2 = 0.1$ which corresponds to the fastest growing mode in the spectrum. In addition, isotropic turbulence at this scale is assumed, i.e. $k_r = k_\theta$. The reduced Weiland model is suitable for toroidal geometry and circular, concentric surfaces, as is the case for Tore Supra. Figure 5.17 shows the turbulence driven diffusivity (*a*) and convection velocity (*b*). Rather good agreement is found with the heat diffusivity profile determined by the power balance analysis. However, the magnitude of the pinch is smaller compared to that obtained from the Linear Pinch Model and the additional pinch with CGM. Moreover, the profile of the turbulence driven pinch is relatively stable despite the change of the temperature and density gradients during the ECRH modulation, which corresponds to a stationary pinch effect acting as a background.

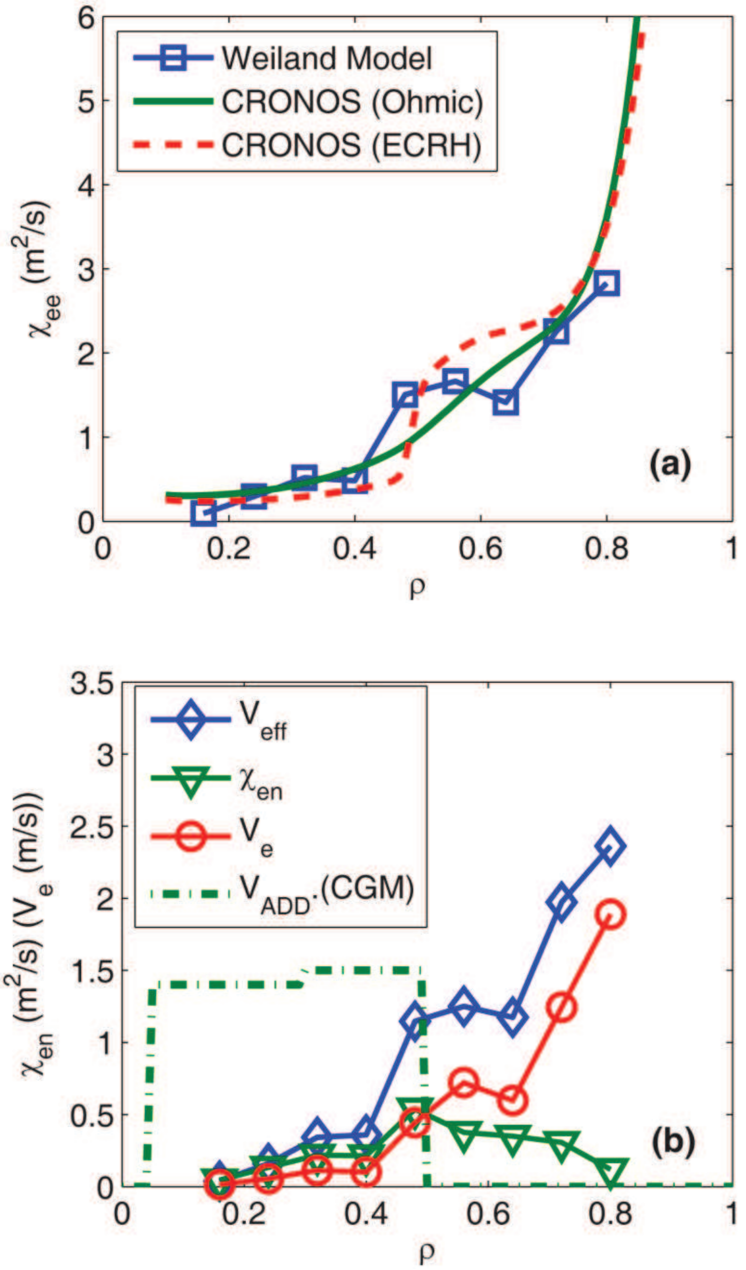

Figure 5.17 Diffusivity (*a*) and convection velocity profiles (*b*) predicted by the reduced Weiland Model (and Nordman method [56] for separation of heat pinch term) for shot TS#43234. In (*b*), $V_{\mathrm{eff}} = V_{\mathrm{e}} + \chi_{\mathrm{en}}/L_{\mathrm{ne}}$ is the effective pinch velocity, where $L_{\mathrm{ne}} = -ne/\nabla ne$.

5.6 Conclusion

Low frequency (1 Hz) ECRH modulation experiments have been carried out on the Tore Supra tokamak. These experiments show features that could correspond to inward heat transport, in particular in low density discharges. Two transport models, i.e., a simple diffusive/convective model with piecewise constant coefficients (LPM) and a purely diffusive non-linear model (CGM) have been applied in order to analyze the experimental behavior. Good agreement has been found for all harmonics between the experimental data and the simulation using the LPM, which includes time constant diffusivity and convection velocity profiles. It should be emphasized that the heat diffusivity, the heat convection velocity, and the damping time can be independently determined in LPM by using the sensitivity of the phase and amplitude of the modulated electron temperature relative to these three parameters. Conversely, using the purely diffusive CGM, good agreement has not been achieved: when the simulation is good for the amplitude profile, the phase profile does not agree with the experimental data, and vice versa. An additional heat pinch is needed for CGM in order to reproduce both experimental amplitude and phase. However, a picture in which this additional pinch is smaller and the pseudo-pinch is larger also inside $\rho = 0.3$ cannot be completely excluded. The additional pinch plus the pseudo-pinch obtained with the CGM is roughly equivalent to the pinch obtained with the LPM. The heat-pulse diffusivity χ^{HP} resulted from the CGM is qualitatively in agreement with the diffusivity obtained with the LPM in the core ($\rho < 0.6$). It is also found that the heat pinch feature is sensitive to the plasma density, since the heat pinch tends to increase for decreasing density.

Chapter 6 Density Pump-out experiments

Plasma fuelling is a critical issue for fusion. The fusion fuel, i.e. deuterium and tritium, has to be supplied as deep as possible into the plasma core. Since fusion power scales with the square of the density, obtaining high values of the central density in a reactor is of particular importance. Recent studies show that the cost of electricity produced by a fusion power plant is proportional to $\beta_N^{-0.4}(n/n_G)^{-0.3}$, where $\beta_N = \beta_T/(I_p/a/B_T)$ is an appropriately normalized thermal plasma pressure, with $\beta_T = 2\mu_0 \langle T \rangle / B_T^2$, B_T the toroidal magnetic field, I_p the plasma current and a the minor radius, while n/n_G is the ratio of the plasma density to the density limit, observed in tokamaks and calculated by means of the Greenwald empirical scaling.

Due to the merit of EC heating, an EC system has been specified to accomplish multiple functions in ITER: localized heating, localized current drive, real-time control of MHD instabilities, assisted breakdown, current ramp-up and wall conditioning via EC discharges [58]. As a result, particle transport under ECRH heating becomes an important issue. ECRH may strongly affect the plasma density profile, in particular at low densities. This effect, not yet completely understood, can be an interesting actuator for reducing impurity concentration, particularly for the removal of the α particles produced by fusion reactions in the fusion reactor, and also for the density peaking control to increase the β limit.

Density pump-out, namely the flattening of the density profile and the loss of particles during ECRH, has been observed in the HL-2A tokamak as well. In previous works, the profile analysis has often been used to investigate this phenomenon by calculating the stationary value of the density peaking before and after the application of the ECRH. The density peaking is directly linked to the ratio between the convective velocity V and the particle diffusivity D.

Taking the density continuity equation,

$$\frac{\partial n}{\partial t} + \nabla \cdot \left(- D \nabla n + V n \right) = S_p \tag{6.1}$$

For the stationary phase, the core of the plasma has no particle source, which means that the peaking factor of the density can be related to the ratio of V and D [59].

$$\frac{\nabla n}{n} = \frac{V}{D} \tag{6.2}$$

The convection velocity V is the sum of a neoclassical term V_{neo} and of an anomalous V_{an} one. V_{neo} includes the so-called Ware pinch (V_{ware}) proportional to the toroidal electric field E_φ, and the contributions of the main ion temperature T_i and impurity density gradients. For this approach, there is an unavoidable inconvenience: V and D are always associated, and the convection effect cannot be separated from the diffusion effect. In HL-2A perturbation transport experiments with the modulation of ECRH have been performed in order to investigate the density pump-out. The density modulation produced by ECRH modulation technique can be an effective way to determine separately the particle diffusivity and the particle convective velocity. In this dynamic approach, the transient phase of the density pump-out phenomenon is investigated effectively.

The existence of V_{an} is predicted by turbulent theories based on the ITG/TEM micro-instabilities, and has been evidenced in lower-hybrid driven and fully non inductive current plasmas in Tore Supra [72]. These theories predict two main turbulence mechanisms related to the profiles of the electron temperature and safety factor and are confirmed by several turbulence simulations as well as by analytical estimates. First, the turbulent thermodiffusion generates a pinch velocity, directed inwards or outwards, proportional to $\nabla T_e/T_e$. On the other hand, the turbulent equi-partition due to the curvature of the magnetic field lines drives an inward pinch proportional to $\nabla q/q$, called curvature pinch. The particle flux can hence be expressed as [60],

$$\Gamma = -D\left[\nabla n_e + \left(C_q \nabla q / q - C_T \nabla T_e / T_e\right) n_e\right] + V_{neo} n_e \tag{6.3}$$

6.1 Experimental setups on HL-2A

The HL-2A device is a tokamak with major radius R = 1.65 m, minor radius a = 0.40 m, on which the achieved operation parameters are the following: toroidal magnetic field B = 2.7 T, plasma current I_p = 450 kA, electron and ion temperatures T_e = 5 keV and T_i = 2.8 keV, line-averaged plasma density 5.5×10^{19} m^{-3}. The experiments are focused on the zonal flows physics, energetic particle driven instabilities, transport and confinement, MHD instabilities and more rencenly, the H mode physics with NBI [61].

In the density pump-put experiments considered here, the main plasma parameters are: major radius R = 1.65 m, minor radius a = 0.40 m, toroidal magnetic field B_T = 1.3 T, plasma current I_p = 160 kA. The plasma is circular with limiter or divertor configuration. The ECRH system in HL-2A has 3 Gyrotrons at 68 GHz with maximum output power of 1.5 MW and pulse duration of 1 s. The density profile is measured by a broadband O-mode reflectometer in the 26.5-40 GHz range [62], which covers a density domain of 0.8 to $2.0\times10^{19}m^{-3}$. The line-averaged density is measured by a HCN interferometer [63]. The electron temperature is measured by the 12-channel electron cyclotron emission diagnostic (ECE) [64], where the temporal and spatial resolutions are 4 ms and 3 cm respectively.

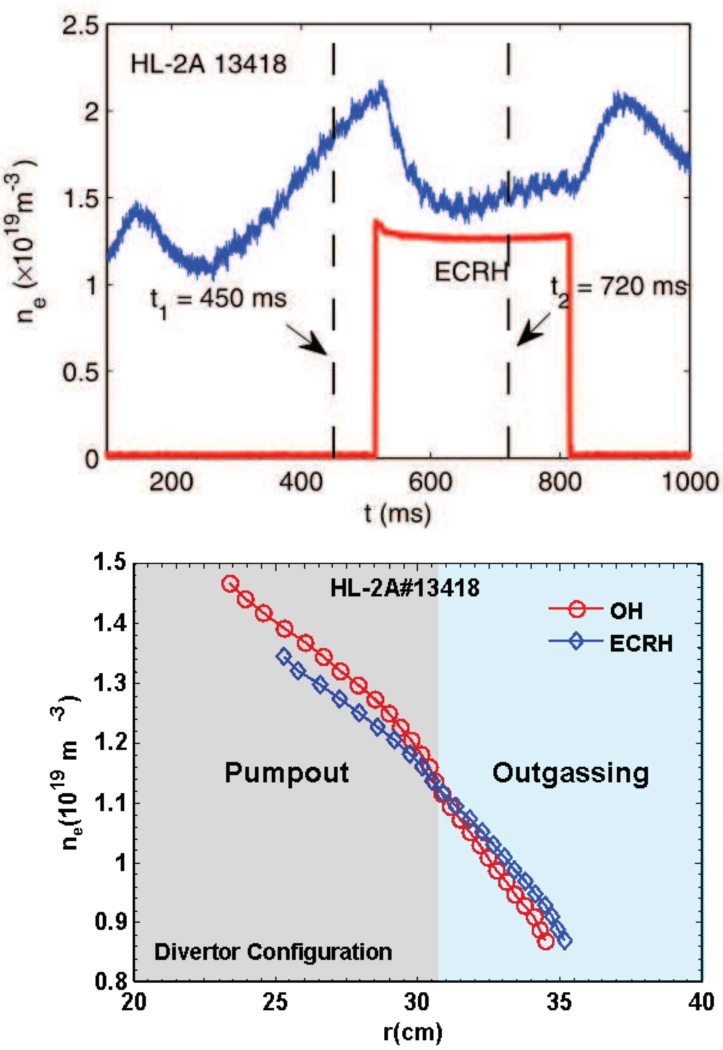

Figure 6.1 Upper panel: line-averaged density measured by interferometry; Lower panel: Density profile measured by the reflectometry in the Ohmic regime (red circles, t = 450 ms) and in the ECRH regime (blue diamonds, t = 720 ms) for shot HL-2A#13418.

Taking shot 13418 as an example, the line-averaged density shows classical pump-out phenomenon after ECRH is switched on, i.e., density decrease. However, if we consider the density profile, we can find that during the ECRH heating (t = 720 ms), the density level in the central region decreases compared to the Ohmic phase (t = 450 ms), while in the peripheral region it increases, as shown in Figure 6.1. The two regions on the two side of the crossing point is defined as out-gassing region (blue) and pump-out region (grey) respectively. To interpret this density perturbation after the switch-on of ECRH, a local outward particle flux has been invoked, directly driven by ECRH and with a radial width comparable with the ECRH deposition width [65]. The results of the simulation using the local outward flux seem to be satisfactory for the line-averaged density. This ECRH induced local outward particle flux could be explained by several mechanisms: a poloidal electric field induced by ECRH with an $\boldsymbol{E} \times \boldsymbol{B}$ drift [66]; an increase of the number of particles entering the loss cone in momentum space due to the enhancement of their perpendicular velocity by ECRH [67]; a local turbulent outward particle convection driven by the trapped electron modes (TEM) as suggested in [67]. However, in the model with local ECRH induced outward particle flux, the particle perturbation source as well as its inversion point are located at the ECRH deposition location, and the negative density perturbation should propagate from the ECRH deposition region to the plasma centre while the positive density perturbation should propagate in the opposite direction, i.e., from the ECRH deposition to the edge. These characteristics are not consistent with the experimental observations in HL-2A.

The drastic negative density perturbation in the central region represents the density pump-out. The edge density increase or positive perturbation is likely due to the out-gassing or inward particle flux caused by the ECRH. Generally the out-gassing effect (i.e., particles leaving the plasma facing components and entering the plasma) is much larger in limiter configuration than in divertor configuration, possibly due to the displacement of the limiter plasma contact point after the start of the ECRH pulse. The inversion point for the sign of the density perturbation in the present case is located around r = 30 cm or r/a = 0.75, i.e., much more peripheral than the ECRH deposition location (central). Of course, this inversion point can move according to the plasma configuration, more peripheral in divertor configuration than in limiter configuration, but in any case it is far from the ECRH deposition point. The spatial-temporal evolution of the density perturbation during the ECRH for divertor and limiter configurations is shown in Figure 6.2 and Figure 6.3, respectively. In divertor configuration, the dominant perturbation in the region probed by the O-mode reflectometry is negative because the out-gassing effect is reduced. In limiter configuration, the dominant perturbation in the region probed by the O-mode reflectometry is positive due to the out-gassing effect. The negative density perturbation propagates from the center to the edge, while the positive one propagates in the opposite direction, i.e., from the edge to the center. The pump-out propagation velocity from the center to the edge can be estimated to be roughly 5 m/s from Figure 6.2. The separation of different physical processes is a crucial point before using Fourier analysis.

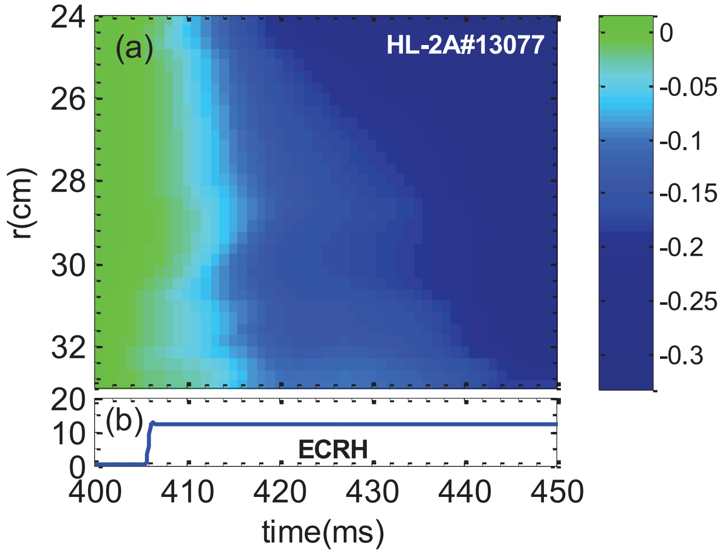

Figure 6.2 Spatial-temporal evolution of the negative density perturbation during ECRH with divertor configuration (*a*), and the ECRH signal (*b*).

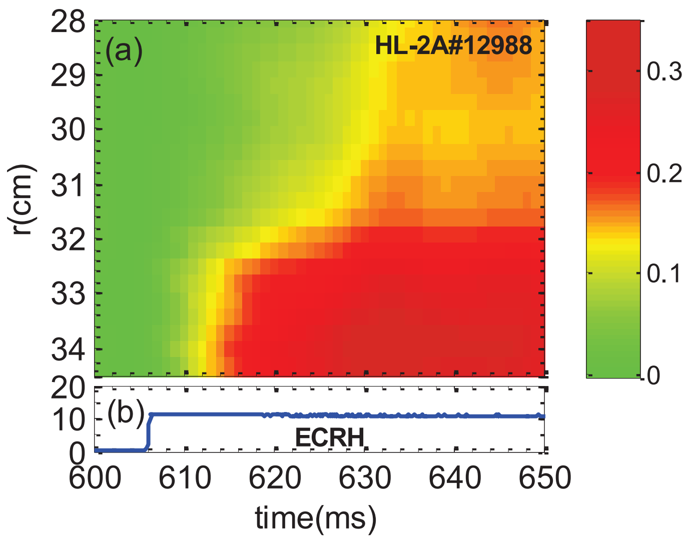

Figure 6.3 Spatial-temporal evolution the positive density perturbation during ECRH with limiter configuration (*a*) and the ECRH signal (*b*).

6.2 ECRH modulation analysis in limiter configuration

In the limiter configuration, as shown in Figure 6.3, the density perturbation is positive in the peripheral region, probed by the O-mode reflectometry. This positive perturbation propagates from the edge to the center, in opposite direction with respect to the density pump-out propagation. It corresponds to a particle inward flux at the plasma edge during the ECRH phase. Figure 6.4 shows the density modulation measured by the interferometer during the ECRH phase. The edge chord density (green) is in phase with ECRH, while the central chord density (blue) is in opposition of phase with respect to ECRH. Thus the central region is dominated by the density pump-out, while the peripheral region is dominated by the out-gassing. For the transport analysis, both density perturbations should be taken into account. Figure 6.5 displays the amplitude and the phase of the 1st harmonic of the Fourier transform of the density modulated by ECRH in limiter configuration. As the perturbation source is determined by the position of the minimum of the phase, thus the particle source for the positive density perturbation is located very close to the plasma edge (a = 37 cm). This confirms the observation in Figure 6.3, i.e., the positive density perturbation propagates from the edge to the center. Simulations have been done with an analytical linear diffusion/convection transport model [68] in order to fit the experimental data. In Figure 6.5 the solid lines represent the simulation with convection, and the dashed lines represent the simulation without convection (V = 0 m/s), in the region r = 28 ~ 34 cm. Figure 6.6 shows the diffusivity D and the particle convection velocity V used for the simulation of Figure 6.5 (solid lines). From Figure 6.5 we can see that the particle convection affects less the phase, but strongly the amplitude. Thus the phase is essentially determined by the diffusivity, while the amplitude depends on both diffusivity and convection. The simulation shows that the positive density perturbation propagates from the edge to the center, crossing two different areas: 1) core outward convection region (28.3 cm < r < 33.2 cm) with D_1 = 0.4 m^2/s, and V_1 = -4 m/s; 2) peripheral inward convection (pinch) region (33.2 cm < r < 37 cm) with D_2 = 0.8 m^2/s, V_2 = 15 m/s. In this case the out-gassing can be considered as a source of test particles for the transport. During the pump-out transient phase, the core particle convection can be directed outwards.

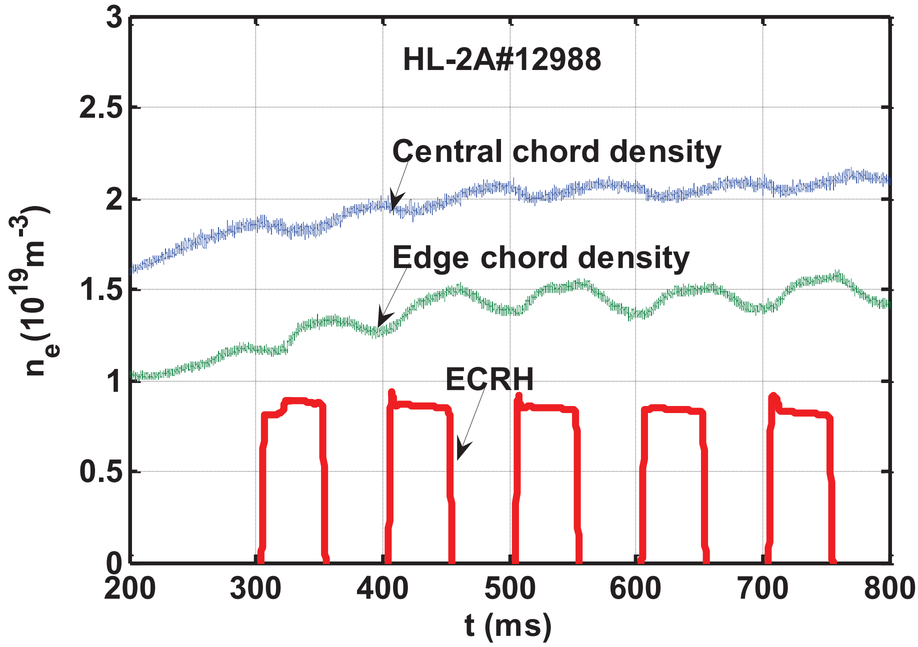

Figure 6.4 Temporal evolution of the edge (green) and central (blue) line averaged density n_e in the limiter configuration during ECRH modulation (red).

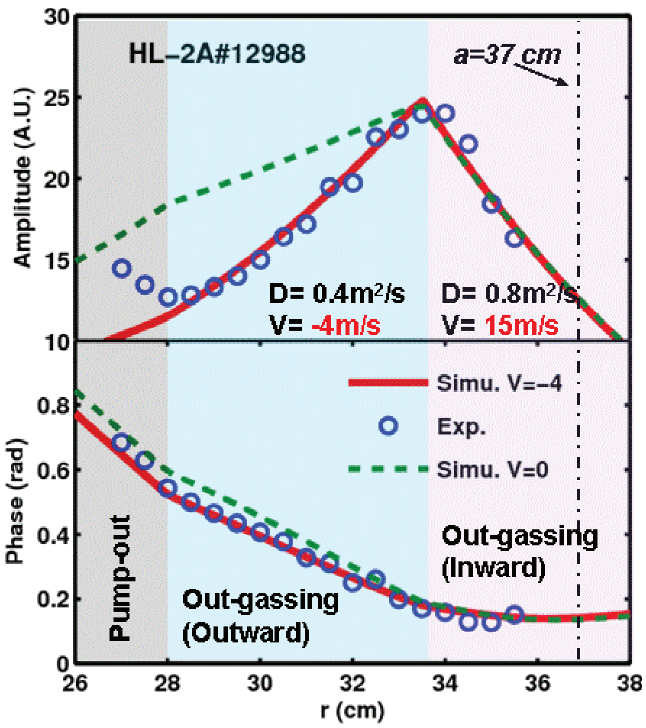

Figure 6.5 Amplitude and phase of the 1st harmonic of the Fourier transform of the density modulated by ECRH in limiter configuration (shot HL-2A#12988). Open circles are the experimental data; the solid lines represent the simulation with convection; the dashed lines represent the simulation without convection (V = 0 m/s) in the domain r = 28 ~ 34 cm. The vertical dash-dotted line shows the plasma minor radius (a = 37 cm).

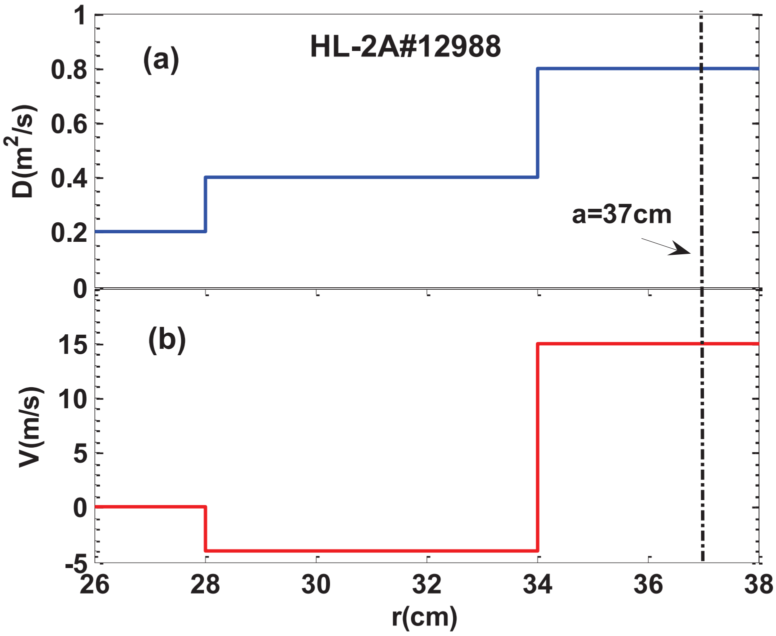

Figure 6.6 Parameters used for the simulation in Figure 6.5(solid line). Profile of the diffusivity D (a) and the particle convection velocity V (b). The vertical dash-and-dot line shows the plasma minor radius (a = 37 cm).

6.3 ECRH modulation analysis in divertor configuration

Figure 6.7 displays the edge and central chord density modulations driven by ECRH in the divertor configuration. In contrast with the limiter configuration (see Figure 6.4), now both edge and central chord densities are modulated in opposition of phase with respect to the ECRH pulse. These observations are corroborated by the density profile modulation measured by the reflectometry, shown in Figure 6.8 (temporal evolution of the density profile with ECRH modulation). It appears that the positive density perturbation (out-gassing) is strongly reduced in the divertor configuration when compared to the limiter configuration. In this case the density perturbation is largely dominated by the density pump-out. Furthermore, the density decrease is faster in the central chord than in the edge chord when the ECRH is applied. This confirms the observation in Figure 6.2, i.e., the negative density perturbation propagates from the center to the edge. The amplitude and the phase of the 1st harmonic of the Fourier transform of the density modulation are plotted in Figure 6.9. The minimum of the phase is now located toward the center, outside the region probed by O-mode reflectometry. This clearly indicates that the negative density perturbation (pump-out) source is located in the central region, and should be close to the ECRH deposition. As in the previous section, the experimental data have been fitted with an analytical linear transport model. The solid lines represent the simulation with convection term, and the dashed lines represent the simulation without convection term (V = 0 m/s). The diffusivity and the convective velocity are found to be D = 1.5 m^2/s, and V = -10 m/s (Figure 6.10) for the best fit.

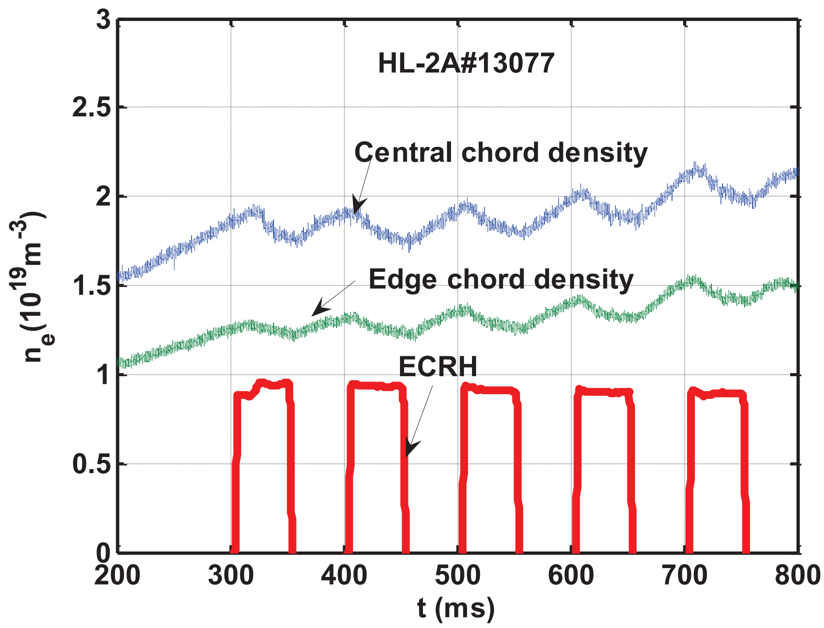

Figure 6.7 Temporal evolution the edge (green) and central (blue) line-averaged density n_e in the divertor configuration with ECRH modulation (red).

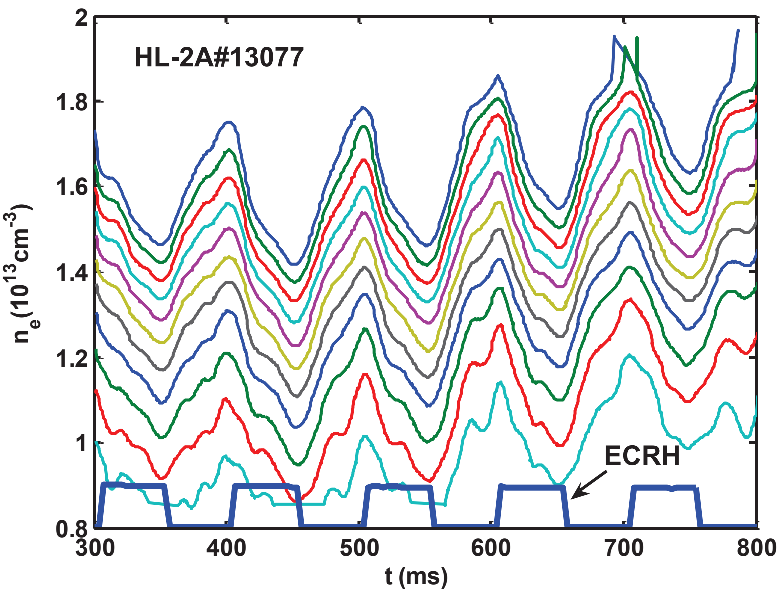

Figure 6.8 Temporal evolution of the density measured by reflectometry at different radii with ECRH modulation (blue). The innermost radius is r = 22 cm; and the outermost radius is r = 32cm.

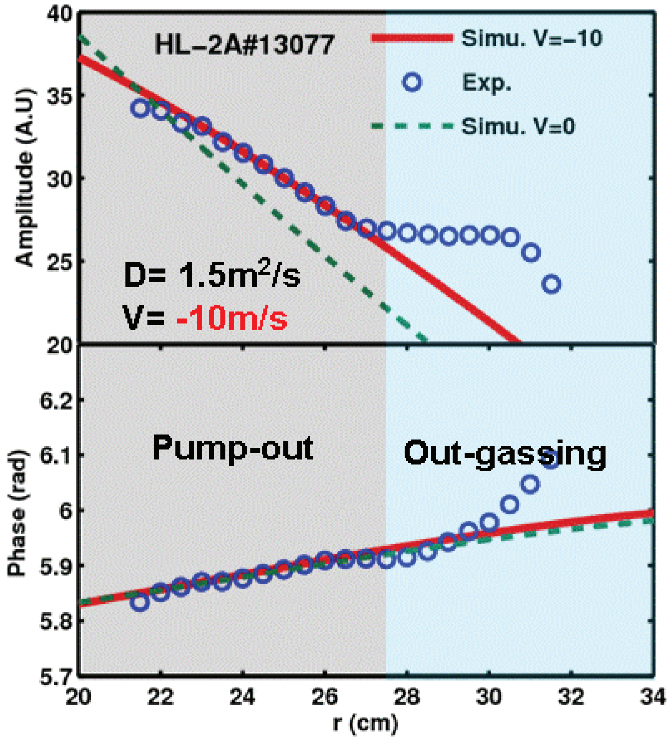

Figure 6.9 Amplitude and phase of the 1st harmonic of the Fourier transform of the density modulated by ECRH in divertor configuration. Open circles are the experimental data; the solid lines represent the simulation with convection; the dashed lines represent the simulation without convection (V = 0 m/s).

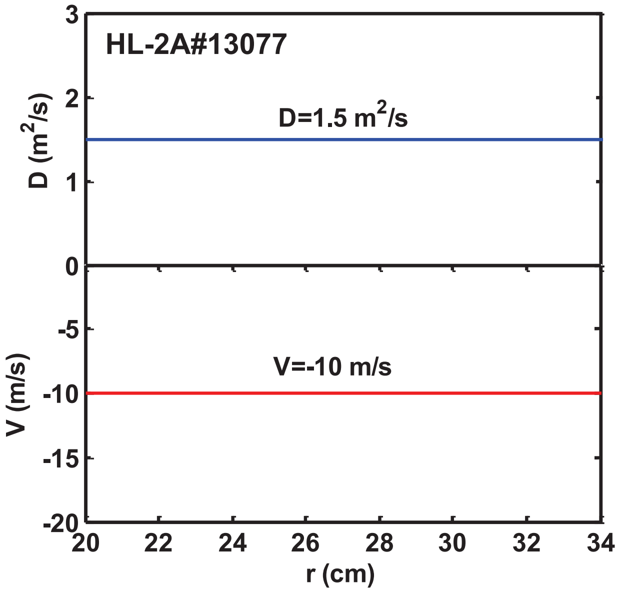

Figure 6.10 Parameters D (a) and V (b) used for the simulation in Figure 6.9 (solid line).

6.4 Discussion and Interpretation

As discussed in Sections 6.2 and 6.3, the values of the diffusivity D and the convective velocity V are much larger for the negative density perturbation than for the positive one, i.e., the negative density perturbation propagates much faster than the positive one. The strong asymmetry in D and V for the negative and positive density perturbations is very similar to that observed in cold and hot pulse heat propagation. By analogy, this difference can be explained by the fact that the positive density perturbation is due to particle propagation, while the negative density perturbation can be due to the turbulence spreading phenomenon [69-71]. The outward convection (negative velocity) has been observed only during the pump-out transient phase. It should be noted that the particle convection is always directed inwards in steady state before and after the pump-out phase. Experiments in tokamaks have shown the existence of the anomalous particle convection, likely driven by the turbulence [72]. Both the ion temperature driven mode (ITG) and the trapped electron mode (TEM) are believed to play a key role in the plasma core. It has been shown that the turbulence driven by the TEM can lead to an outward convection via thermo-diffusion [73]. Thus the previous observations can be a serious indication for the presence of TEM during the pump-out phase. Therefore, the density pump-out could result from the combination of two effects: a large particle outward convection (-4 m/s), probably driven by TEM, and, more important, a significant turbulence radial spreading with strong outward convection (-10 m/s).

To investigate the possible transition ITG/TEM during the density pump-out, an analytical model for the electrostatic drift turbulence, i.e., the Weiland model [56,57] has been used for the micro-instability analysis. In the calculation, the trapped particle fraction is assumed to be f_t = 0.5, the turbulence at this scale is assumed to be isotropic, i.e., $k_r = k_\theta$, where k_r, k_θ are respectively the radial and poloidal wavenumbers of the turbulence, and the fastest growing mode in the k-spectrum is assumed to be characterised by $(k_\theta \rho_s)^2 = 0.1$, where ρ_s is the Larmor radius. Figure 6.11 shows the time evolution of the normalized density gradient (red) and the normalized electron temperature gradient (blue) during the ECRH modulation. When the ECRH is applied, the normalized density gradient starts to decrease due to the pump-out, while the normalized electron temperature gradient increases at first for about 10 ms, then decreases. The stability diagram is represented by the plane of normalized gradient lengths of electron temperature and density, shown in Figure 6.12.

Now the experimental points at r/a = 0.6 have been plotted in the stability diagram for one ECRH modulation period within the time interval t = [400 455] ms. For this stability diagram it has been assumed that the electron and ion temperature ratio T_e/T_i is 1, the temperature and ion gradient length ratio L_{Te}/L_{Ti} equals 1, where $L_{Te} = -T_e/\nabla T_e$, $L_{Ti} = -T_i/\nabla T_i$. The red and blue square points correspond respectively to the ECRH and Ohmic phase. From this figure, it is found that both ECRH and Ohmic working points are situated close to the boundary separating the TEM area and the ITG/TEM co-existent area. Thus the ITG to TEM transition during the density pump-out cannot be excluded, and the outward particle convection obtained in the simulation can be likely explained by the TEM triggered by ECRH. However, as the error bars on the density and temperature gradients are rather large, Figure 6.12 does not constitute an irrefutable proof of the existence of TEM during the pump-out phase.

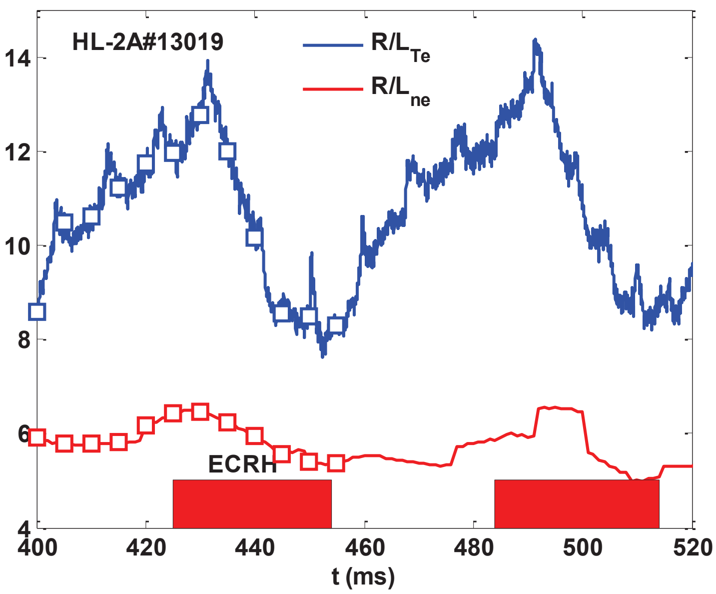

Figure 6.11 Temporal evolution of the normalized density gradient (R/L_{ne}) and temperature gradient (R/L_{Te}) with the ECRH modulation at r/a = 0.6. The square points correspond to those plotted in Figure 6.12.

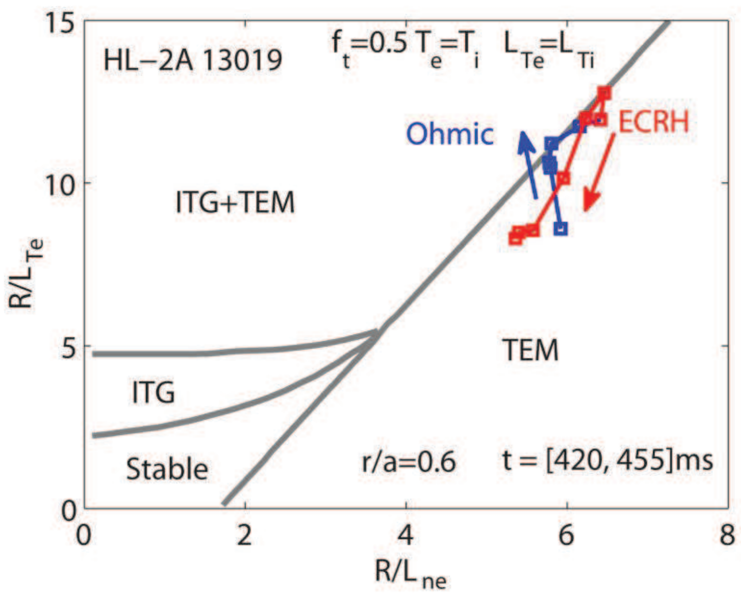

Figure 6.12 Stability diagram at r/a = 0.6. T_e/T_i = 1, L_{Te}/L_{Ti} = 1, f_t = 0.5 and $(k_\theta \rho_s)^2$ = 0.1. The red (blue) square points are during ECRH (Ohmic) phase. $L_{Te} = -T_e/\nabla T_e$, $L_{Ti} = -T_i/\nabla T_i$, $L_{ne} = -n_e/\nabla n_e$.

6.5 Conclusions

Experiments have been carried out in HL-2A with ECRH modulation to investigate the density pump-out phenomenon, characterized by a negative density perturbation in the central region. Positive density perturbation in the peripheral region has been simultaneously observed. This edge density increases is likely due to the out-gassing caused by ECRH. The out-gassing effect is much larger in limiter configuration than in divertor configuration. Strong correlation between the turbulence increase and the density pump-out has been found. Turbulence reduction has been observed during the pump-out/pinch transition. Different to the previous works, a dynamic approach using modulation technique has been performed for the investigation of the transient phase of the pump-out. Strong asymmetry for the negative and positive density perturbation has been observed. It can be explained by the fact that the positive density perturbation is due to the particle propagation, and the negative density perturbation is due to the turbulence spreading. The outward convection (negative velocity) has been observed during the density pump-out transient phase. This can be a serious indication for the presence of TEM during the pump-out. The density pump-out is not basically due to a direct increase of the outward particle flux, more likely to an indirect effect via the change of the turbulence.

Chapter 7 Non-local experiments

In the standard model for transport, local microinstabilities lead to local turbulence and hence local turbulent transport. Most experimental transient transport studies generally confirm this picture: they exhibit locally diffusive response to rapid, spatially localized perturbations of the plasma. However, several experiments have highlighted coexisting plasma responses that are ‘non-local’, i.e., long-range responses are observed in addition to diffusive effects. In some cases, the non-local response to edge cold pulses exhibit reversed polarity, with the core electron temperature increasing in response to edge cooling. These long-range, non-diffusive, and often reversed polarity responses challenge the standard local model or paradigm of turbulence and anomalous transport in toroidal, magnetically confined plasma. [74]. This provides a strong motivation to specific experimental studies of these effects, which has been carried out on Tore Supra.

7.1 Experimental setup on Tore Supra

An SMBI system based on the injection of a supersonic high density cloud of neutrals is installed on the Tore Supra tokamak. The SMBI is a plasma fuelling method that stands between gas puff and pellet injection. A small volume of gas at high pressure, containing about half a plasma content in particles (0.4 Pa.m^3), is expanded through a Laval nozzle into the plasma chamber within 1 ~ 2 ms. The injector located at the high field side benefits from a potential drift effect, which can improve fuelling efficiency. A second injector is located at the low field side, for the purpose of comparison. [75,76]

SMBI modulation pulses have been performed on Tore Supra plasmas. The supersonic pulses are injected from the high field side, with a Mach number of 4 and pulse duration of 2 ms [75]. A typical response of the plasma (shot 43248, I_p = 0.7 kA, B_t = 3.7 T, P_{ECRH} = 200 kW) is shown in Figure 7.1. An SMBI pulse is injected into the plasma every second. Steady ECRH power is injected into the plasma in order to investigate the effect of auxiliary heating. The ECRH phase starts from t = 3 s to t = 8 s, covers 5 SMBI pulses on which FT (Fourier Transform) method can be applied. In the Ohmic phase, a total of 9 SMBI pulses are injected. The ECRH power is deposited at ρ = 0.5. The density in the ECRH phase is clearly higher than that of the Ohmic phase, which is likely due to the out-gassing effect of ECRH power, as indicated in the previous chapter. At t = 13 s, a very short pulse of the neutral beam (NB) is applied for the measurement of the ion temperature by using charge exchange spectroscopy. Figure 7.1 shows the time traces of electron density at various radii. The electron density data comes from LFS reflectometry measurements. The increment of the density from ρ = 0.14 to the edge is evident. Figure 7.2 shows the contours of density before and after one SMBI pulse measured on the HFS. From this figure, we can appreciate the rapid response of the density to the SMBI pulse. The density contours with the level below $n_e = 0.6\times10^{19}$ m^{-3} expand outwards immediately at t = 10.045 s, and then contract inwards at around t = 10.054 s. The propagation velocity of the wave front (v_{fast}) and the propagation velocity of the peak (v_{slow}) are shown in the figure. The value of v_{fast} is about 50 m/s, while the value of v_{slow} is around 15 m/s.

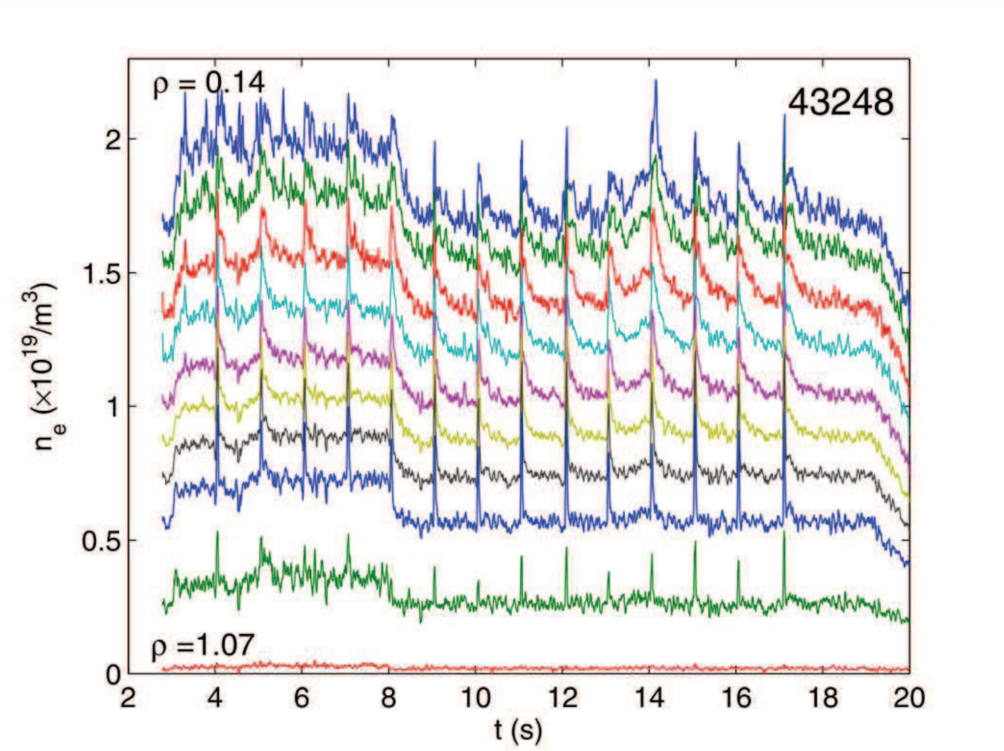

Figure 7.1 Time evolution of the electron density (measured by reflectometry) at various radii for shot 43248. The ECRH power is 200 kW, applied from 3 s to 8 s.

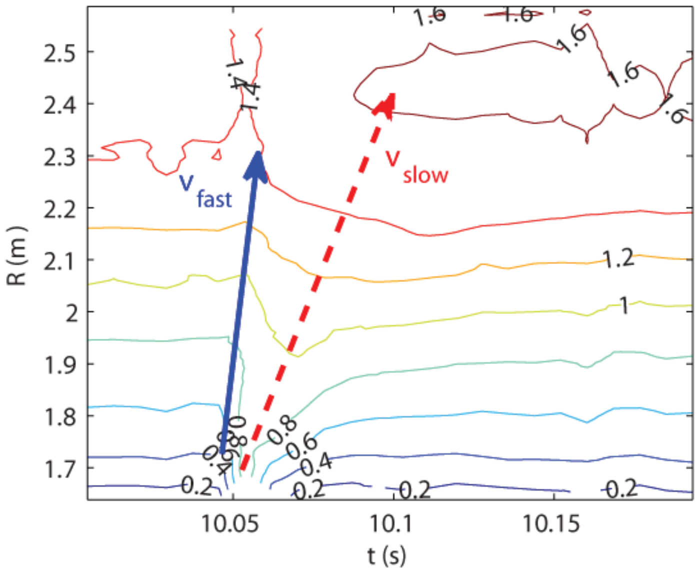

Figure 7.2 Electron density (reflectometry) contours before and after SMBI injection.

A typical phenomenon of non-local transport is illustrated by Figure 7.3, in which the time evolution of the electron temperature is shown. After the switch-off of the ECRH power, the temperature decreases, then increases again. The most attractive phenomenon observed is the double polarity change of the temperature triggered by SMBI, i.e., the temperature in the core region increases, while at the edge it decreases. This effect is generally attributed to the so-called '*non-local*' transport. For the sake of clarity, a zoomed version for the temperature in the Ohmic and ECRH phase during a single pulse is shown in Figure 7.4.

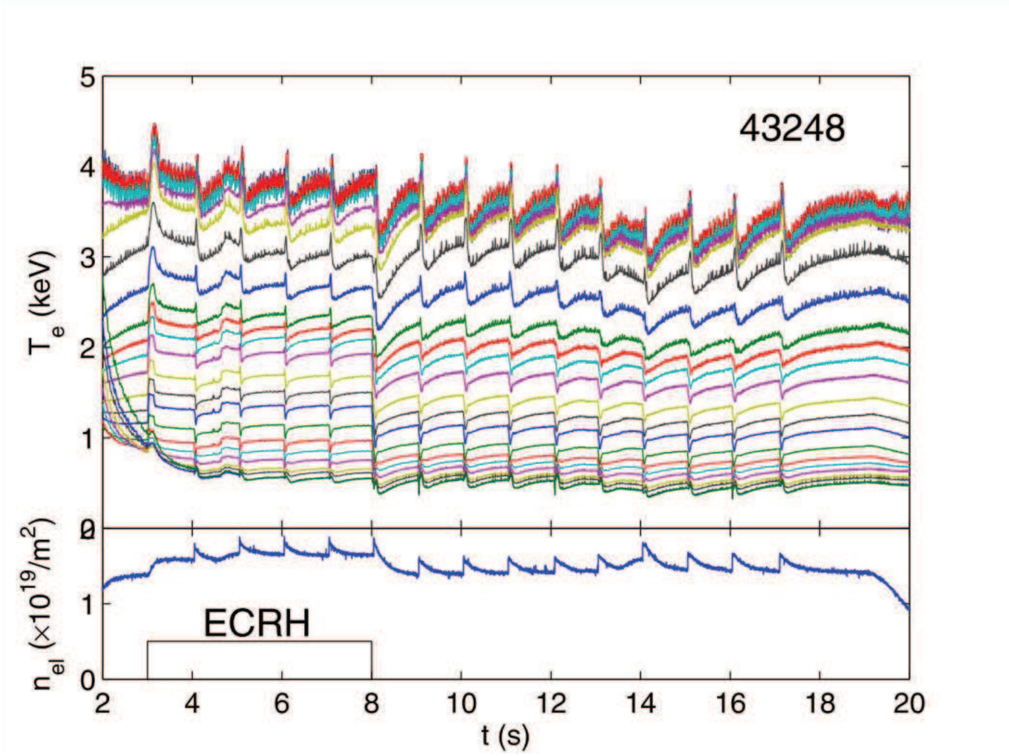

Figure 7.3 ECE electron temperature traces at various radii (upper panel) and line-integrated electron density (lower panel) for shot 43248. The ECRH power is 200 KW, applied from 3 s to 8 s.

The temperature in the core region is affected by small sawteeth, with a sawtooth inversion radius of about ρ = 0.15 in the Ohmic phase and ρ = 0.18 in the ECRH phase. The variation of the ρ_{inv} region is due to the heating effect of ECRH. In the expanded version of Figure 7.3, the detailed structure of the electron temperature evolution shows the following features: just after SMBI pulse, the temperature in the outer part of the plasma (ρ > 0.38 for ECRH phase and ρ > 0.26 for Ohmic phase) falls down rapidly and soon recovers partly; then it has a second rise followed by a second decrease, at last it grows up gradually. The short and rapid fall of the temperature in the outer region is due to ionization of the particle source delivered by SMBI. The time scale for this prompt temperature fall is consistent with the SMBI pulse length. The second and large temperature fall is probably due to the turbulence increase caused by SMBI. In the following analysis, this short perturbation will be omitted. Later in this section we will return to cover this issue.

As shown in the zoomed version of the temperature evolution around t = 7 s, the time delay of the central temperature increment is quite small, only about 1 ~ 2 ms for ρ = 0.14 compared to the temperature decrease at ρ = 0.85, which can be used as the injection time of the SMBI. Assuming the heat diffusivity χ to be 4 m^2/s, the time for the cold pulse to reach the center can be estimated by simulation, as about 5 ms. The hot pulse response is much faster than the typical local diffusive transport. This phenomenon is usually called non-local transport, where the denomination ‘non-local’ originally refers to spatial interactions between two distant points [77]. Another example can be found around t = 10 s: the sawteeth affect the observation at ρ = 0.14, but the time delay between ρ = 0.11 and ρ = 0.85 is also about 1 ~ 2 ms. Now the non-local transport is often explained with the turbulence spreading, which is not always sensitive to the local temperature gradient.

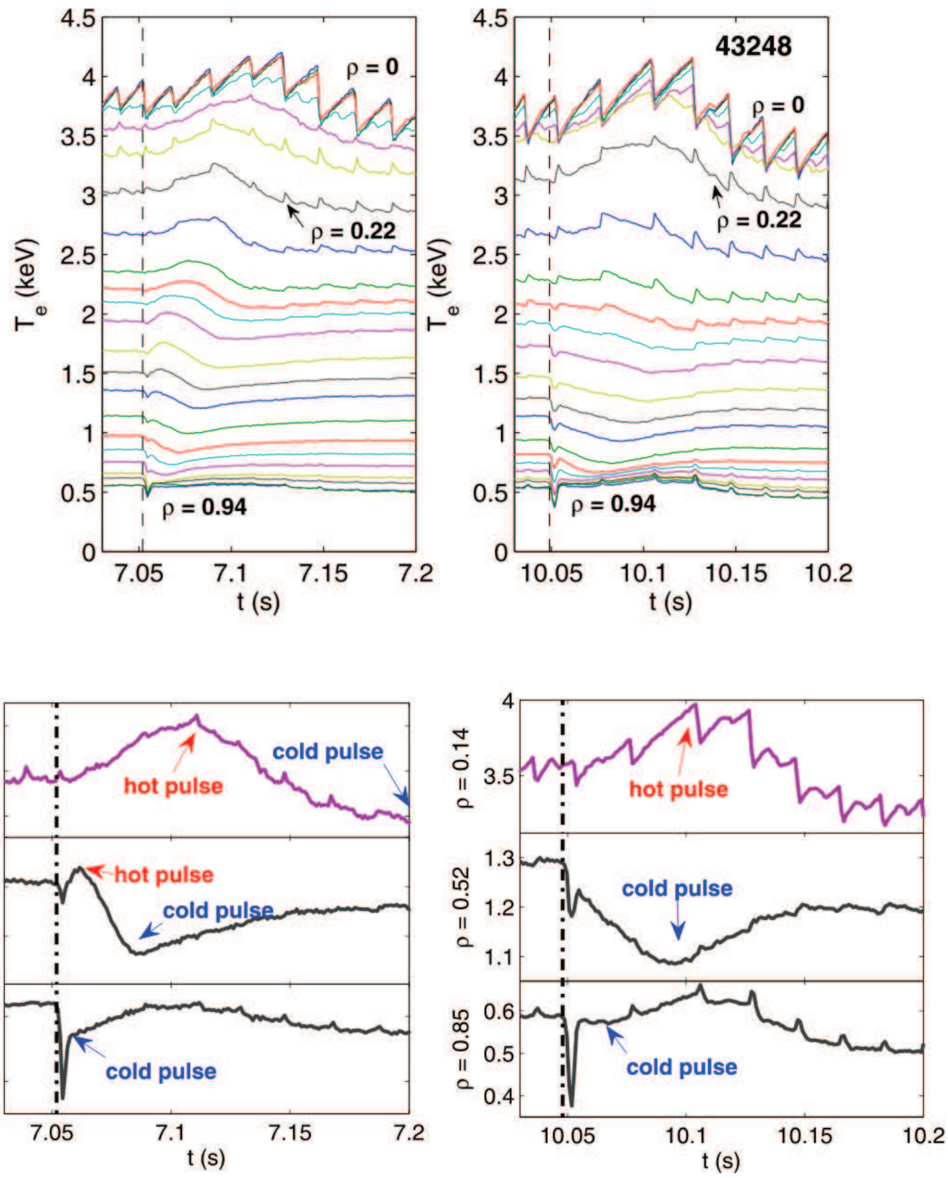

Figure 7.4 ECE electron temperature responses to the SMBI pulse at various radii. The top left panel is during the ECRH phase, and the top right one is during the Ohmic phase. The dashed and dash-dotted vertical lines show the injection time of SMBI; the bottom figures are time traces of the temperature at selected positions.

The hot pulse starts to emerge in the region $\rho = 0.3$ in the Ohmic phase, and at $\rho = 0.52$ in the ECRH phase. The extension of the hot pulse domain in the L regime compared to the Ohmic regime confirm that previously observed in Tore Supra with low-hybrid current drive [78]. The reason for this difference may come from the different density level. The statistical observation of the coexistence of both hot pulse and cold pulse is shown in Figure 7.5, using the line-integrated density and the central temperature as coordinates of the diagram. In the ECRH phase of the shots, all the pulses produce CHEC. From this figure we can observe that for the high density case, i.e., $n_{el} > 2.5\times10^{19}$ m^{-2}, only the cold pulse exists; for the low density case ($n_{el} < 1.6\times10^{19}$ m^{-2}), both edge cooling and central heating appear, whereas in the transition interval both are possible. As for the temperature dependence, below T_{e0} = 2.7 keV, only cold pulse exists; above T_{e0} = 3.5 keV, hot pulse appears; between the two values, both possibilities exist.

The limits for the observation of CHEC are $T_{e0} > 3$ keV and $n_{el} < 2.5\times10^{19}$ m^{-2}, which can be considered as the density and temperature thresholds.

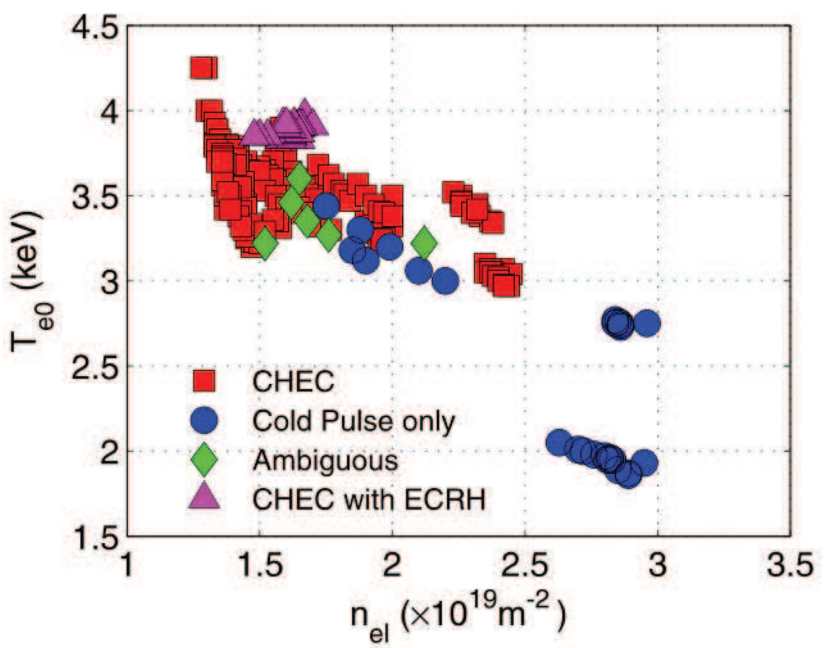

Figure 7.5 Diagram for the observation of Central Heating and Edge Cooling (CHEC); the blue circles stand for the cases where only cold pulse exists, the red squares stand for coexistence and green diamonds are for the ambiguous cases; in the ECRH phase, only CHEC cases appears, also shown in the figure by triangles.

An analogous diagram for the normalized gradients of temperature and density is also given in Figure 7.6. We only plot the pulses for which the density and temperature values are measured on the low field side. Compared to the CHEC with ECRH in

Figure 7.5, which is concentrated around $n_{el} = 1.5\times10^{19}$ m^{-2} and T_{e0} = 4 keV, the points scatter in the region 5 < R/L_{ne} < 10 and 8 < R/L_{ne} < 13. Note that the ECRH power is only 100 - 200 kW, while the Ohmic power is 500 kW. It seems that there is also a threshold on the normalized density gradient for the CHEC, i.e., $(R/L_{ne})_{crit} \sim 5$. For the normalized temperature gradient, the use of ECRH expands the observation sphere of CHEC from less than 9 to up to 13.

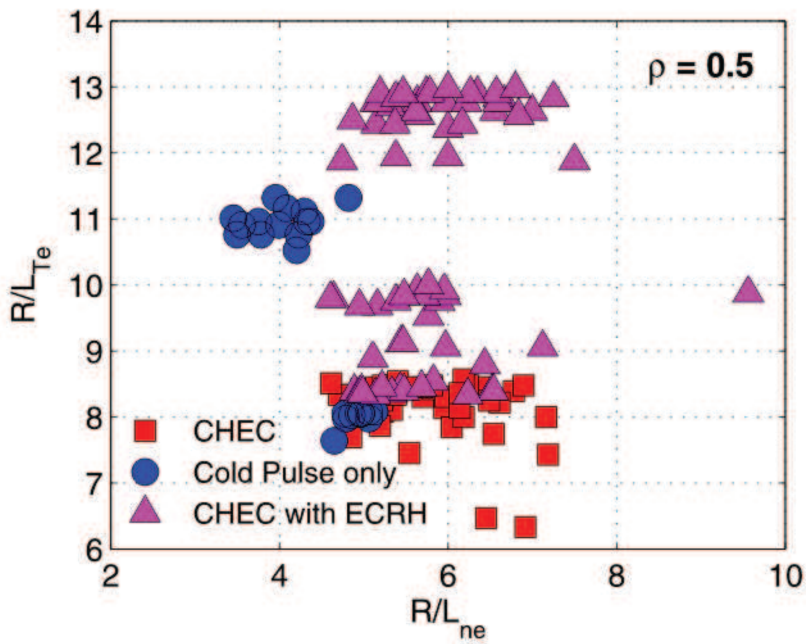

Figure 7.6 Diagram for the observation of Central Heating and Edge Cooling (CHEC); the blue circles stand for the cases when only cold pulse exists, the red squares stand for CHEC case in Ohmic phases, and the upper triangles represent the CHEC case in the ECRH phase.

Figure 7.7 shows an example of 6 SMB injections, which allows investigating the influence of density on the CHEC phenomenon. For shot 42509, the plasma parameters are: B_t = 3.21 T, I_p = 0.7 kA, R = 2.4 m, and a = 0.72 m. In this shot, the line-integrated density increases from 1.5 to 2.1×10^{19} m^{-2}, while the other parameters are kept invariant. In total, 6 SMBs and 4 pellets are injected into the plasma, and here we focus on the SMBI pulses. The first SMBI produces opposite polarity effect on the temperature, while the response to the following three pulses are ambiguous; for the fifth and sixth pulses, the polarity effect disappears and only cold pulses are observed. Different phenomena in different cases are shown in Figure 7.8. In Figure 7.8(a) (CHEC case), the temperature in the core region has a trend of increasing after SMBI, while the decreasing trends prevail after t = 4.15 s even in the core region. In Figure 7.8(b) (Ambiguous case), the temperature in the core region stays almost unchanged after SMBI, while it decreases after t = 5.14 s. In Figure 7.8(c) (Cold Pulse only case), the temperature at various radii, including the core region, starts to decrease immediately after the SMBI. The corresponding diagram of normalized density and temperature gradients is plotted in Figure 7.9.

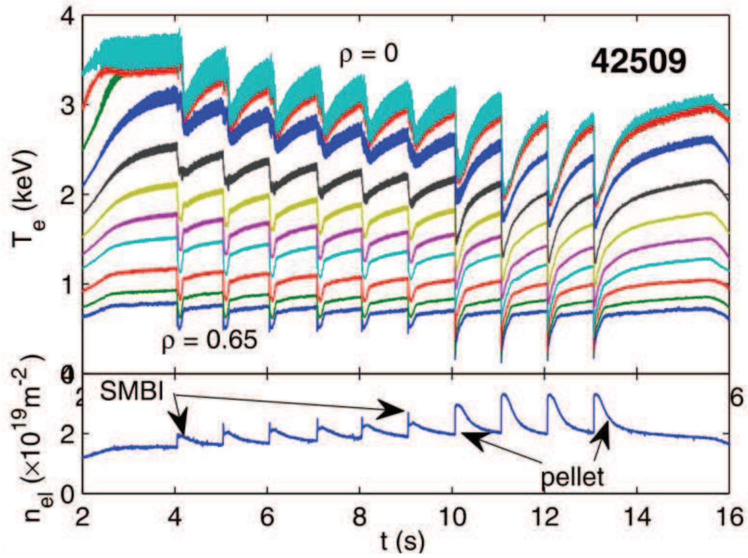

Figure 7.7 ECE electron temperature traces at various radii (top) and line-integrated electron density (bottom) for shot 42509.

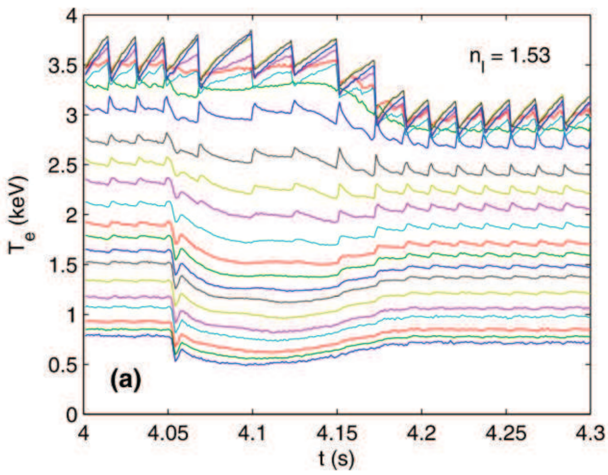

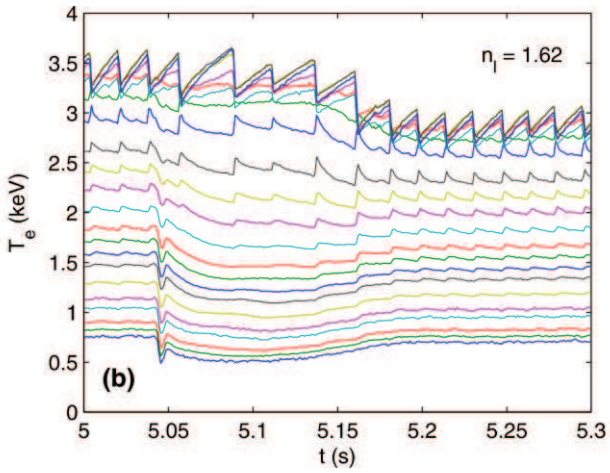

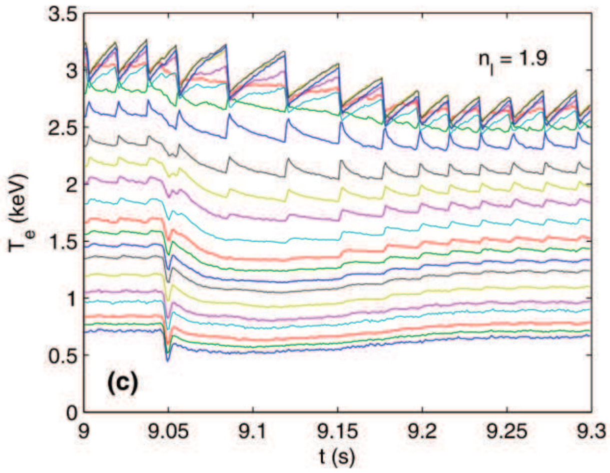

Figure 7.8 Electron temperature traces for the three cases, i.e., (*a*) CHEC, (*b*) ambiguous case and (*c*) cold pulse only. These figures are for shot 42509.

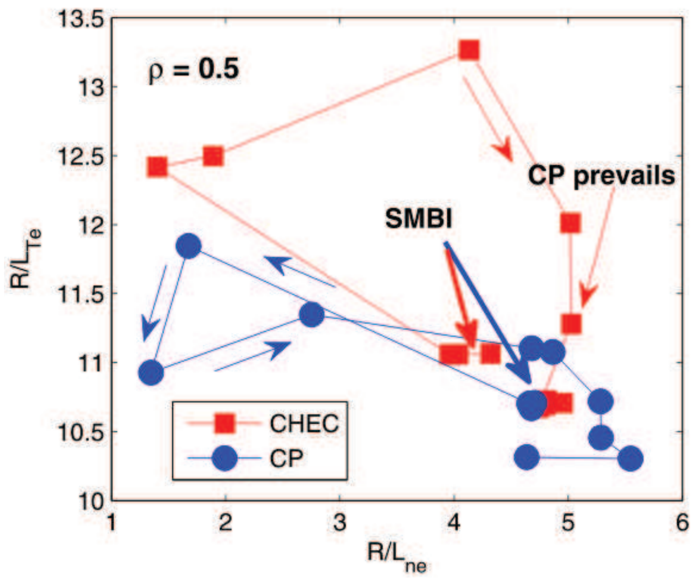

Figure 7.9 Diagram of the normalized temperature and density gradients at $\rho = 0.5$ during SMBI for shot 42509. The red squares stand for CHEC case, the blue circles stand for the cold pulse only case, which corresponds to the (*a*) and (*c*) panels of Figure 7.8.

It is interesting to observe that the two cases have different behaviors in the normalized gradient diagram. The rotation of the diagram points for CHEC case is clockwise, while for the Cold Pulse only case a counter-clockwise rotation starts to take effect. This can be easily explained by the temperature gradient steepness accompanying hot pulse and the flattening of the temperature gradient accompanying cold pulse at the considered radius. In the CHEC case, the time point corresponding to a prevailing cold pulse (i.e., the whole plasma is cooled down by the SMB) is shown in the diagram. At that time point, the two traces in the parametric diagram nearly finish a circle, which correspond to the phase after $t = 4.15$ s and 5.14 s respectively.

For the purpose of comparison, the time traces of temperature and the diagram for the pellet injection at $t = 10$ s are shown in Figure 7.10. It appears that the temperature decreases sharply after the injection of the pellet everywhere in the plasma. It is interesting to note that in the diagram the points are disposed in a similar way, but they rotate in the opposite direction compared to the Cold Pulse only case in SMBI pulses. This is due to the difference in the particle source deposition for SMBI and pellet.

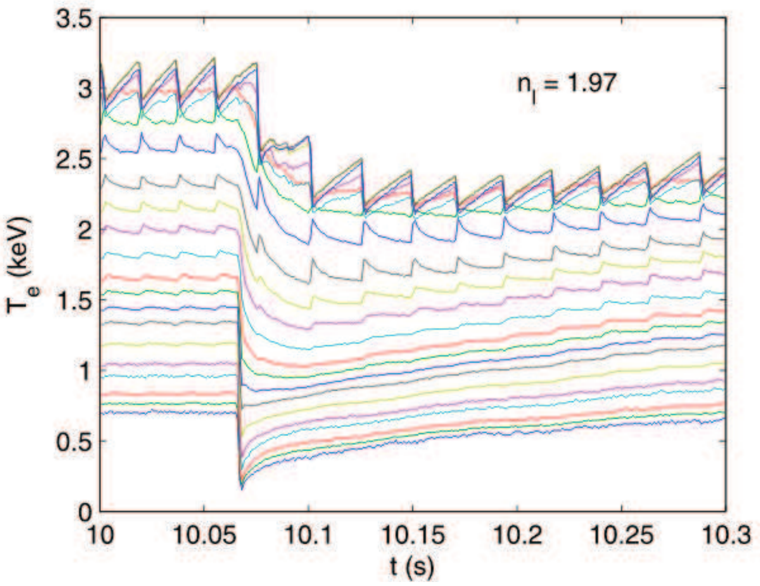

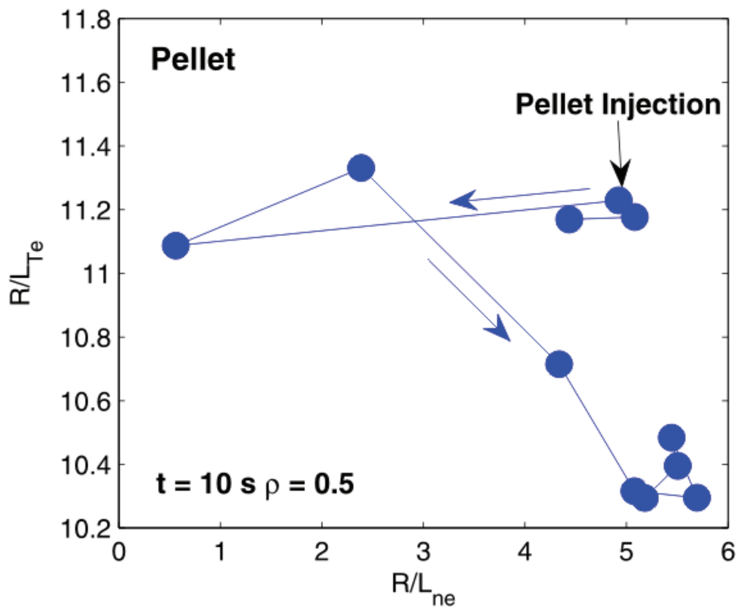

Figure 7.10 Time traces of electron temperature (upper panel) and diagram for the normalized density and temperature gradients (lower panel) during pellet injection for shot 42509. The density data come from low field side reflectometry measurements, while the temperature gradients are calculated from the high field side measurements.

Figure 7.11 shows the diagram for the CHEC case at different positions, $\rho = 0.3$, 0.4, 0.5 and 0.6. The rotation direction at different locations is the same, which suggests that the behavior of Figure 7.9 is a robust property of the experimental results.

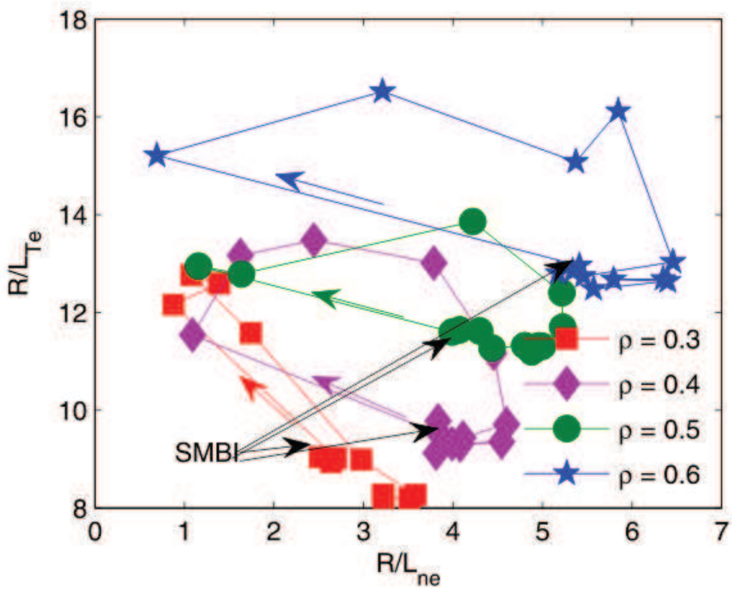

Figure 7.11 Diagram of the normalized density and temperature gradients at different positions for the CHEC case ($t = 4$ s) for shot 42509.

During the experiments, fast acquisition ECE measurements are carried out in order to investigate heat response to the SMBI. Figure 7.12 (top panel) shows the electron temperature perturbation measured by fast ECE during the ECRH phase at around t = 5 s for shot 43248. The perturbation shown in Figure 7.12 is the real-time temperature minus the time-averaged temperature before SMBI. In the central part, the vertical lines correspond to sawtooth crashes. Due to the duration of the sawtooth period, sawteeth play some role in the total increment of the temperature. It appears that the propagations of the hot pulse and of the cold pulse are almost parallel. The propagation velocity of the two heat pulses is about $v_{hot} \approx v_{cold} \approx 7$ m/s, which is much slower than the density pulse. The bottom panel shows the ECE temperature perturbation during the Ohmic phase at around t = 11 s. The CHEC is not as obvious as in the ECRH case, the hot pulse region only covers $R \in [2.2\ 2.7]$ m. The propagation velocity of the cold pulse is found to be $v_{cold} \approx 4$ m/s.

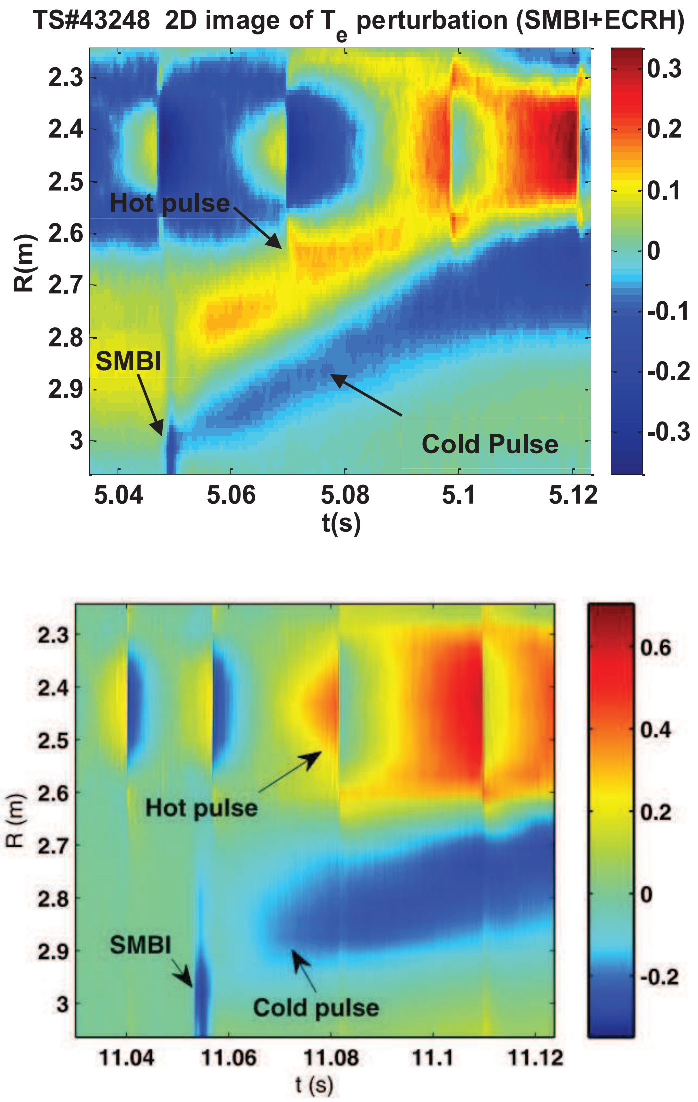

Figure 7.12 Time-space evolution of T_e perturbation during SMBI in the ECRH phase (upper panel) with CHEC and in the Ohmic phase (lower panel) with CHEC. Both figures are for shot 43248.

Figure 7.13 shows the diagram of normalized density and temperature gradients for the ECRH phase and for the Ohmic phase. In the ECRH phase, i.e., (*a*) and (*b*), the rotation of the cloud of points is clockwise for all the three positions, $\rho = 0.4$, 0.5 and 0.6. In the Ohmic phase, i.e., (*c*) and (*d*), the rotation at $\rho = 0.5$ is clearly clockwise for both LFS and HFS measurements. However, with HFS density data, the rotation of the dimensionless parameters at $\rho = 0.4$ is clockwise; while it is unclear for the LFS data. The rotation at $\rho = 0.6$ is clear for the LFS data, and ambiguous for the HFS data. This corresponds to the weakening of the CHEC compared to the ECRH phase, as seen in Figure 7.12.

To summarize, clockwise rotation appears to be one of the characteristics of the hot pulse; while the figure-eight shape is characteristic of the cold pulse.

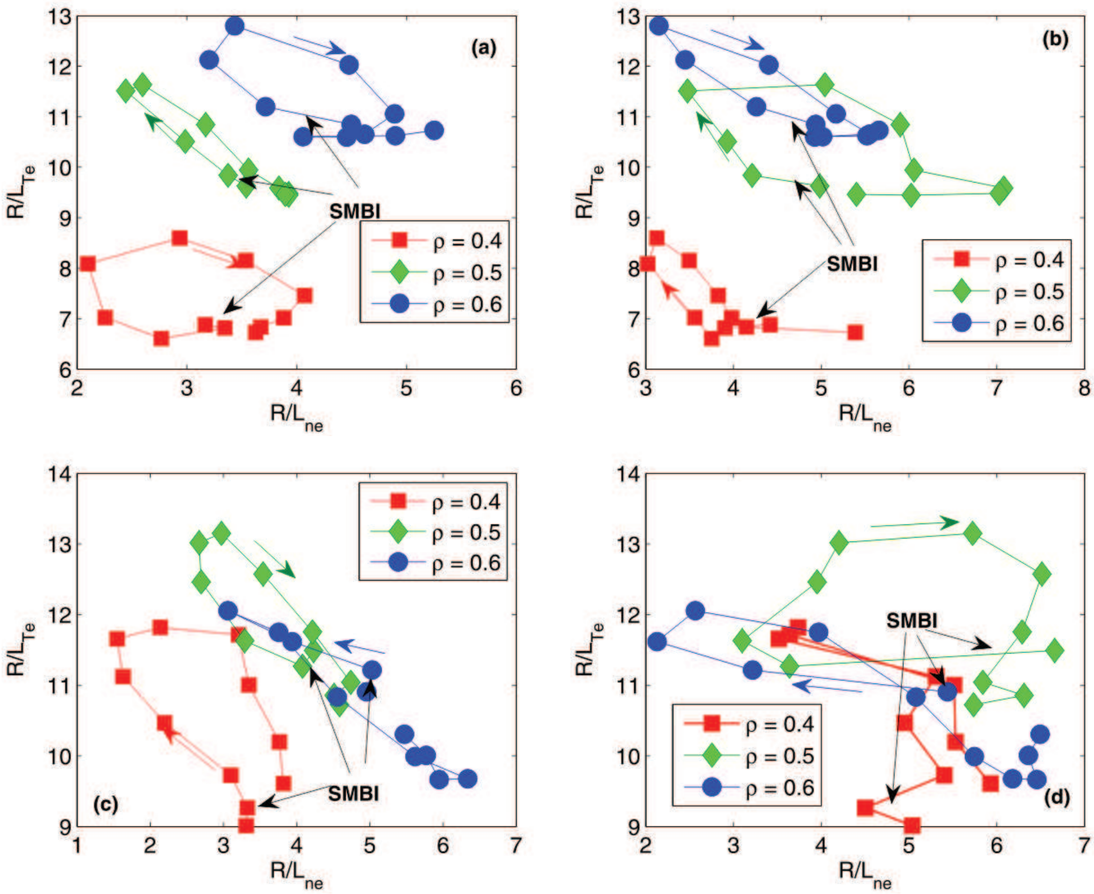

Figure 7.13 Diagrams of normalized electron density and temperature gradients at various radii and different time for shot 43248. (*a*) and (*b*) are for ECRH phase at around $t = 5$ s; (*c*) and (*d*) are for Ohmic phase at around $t = 11$ s. For (*a*) and (*c*), the density data are measured on the high field side; while (*b*) and (*d*) are from low field side. The electron temperatures are measured on the low field side.

For the Cold Pulse only case, we take shot 43253 as an example. Figure 7.14 shows the time traces of temperature and line-integrated density for shot 43253. For shot 42509, B_t = 3.7 T, I_p = 0.7 kA, R = 2.38 m, and a = 0.72 m. In total there are 14 SMB injected into the plasma. The pressure of each pulse is the same as for the previous shots. At t = 13 s, NBI is applied in order to measure the ion temperature. During the phase from t = 4 s to 8 s, the line-integrated density n_{el} increases from 2.6 to $2.8\times10^{19}m^{-2}$, and after t = 8 s, n_{el} is kept almost constant, which is favorable for FFT analysis. For all these 14 SMBs, only cold pulses are produced. The typical behavior is illustrated by Figure 7.15, which shows the response of the temperature due to the SMBI. The sawteeth inversion radius is at ρ = 0.15, which is the same as shot 43248. The main difference between the two shots lies in the different level of density. The electron density evolution is shown in Figure 7.16 and Figure 7.17, which corresponds to the LFS data and HFS data, respectively. The time sequence on the density is clearer for the HFS case: after the injection of SMB, the density perturbation starts to propagate from the edge to the center. However, in the LFS data, the transport process is less clear. The shape of the density pulse measured on the HFS varies from a sharp pulse at the edge to the smoothed bump in the core, which is a by-product of the transport process, as shown in the following sections.

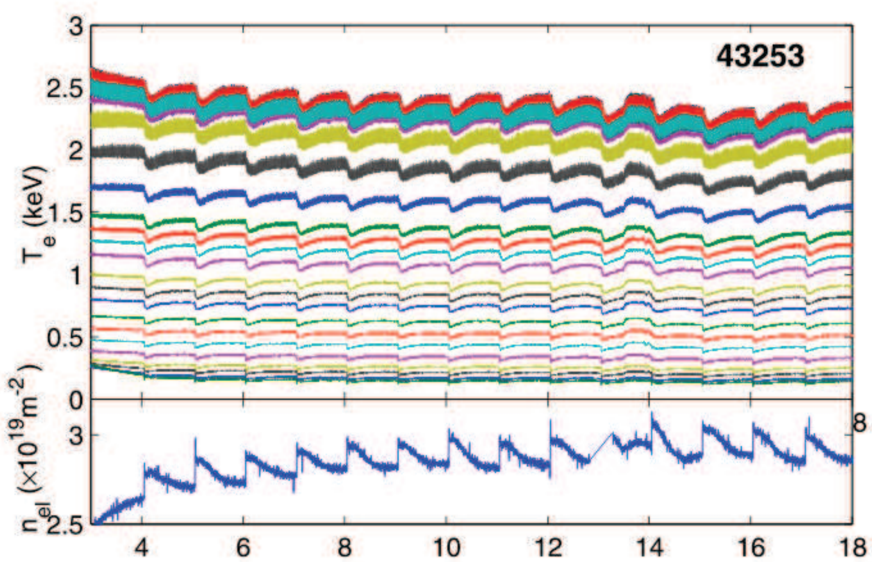

Figure 7.14 ECE electron temperature traces at various radii (up) and line-integrated electron density (down) for shot 43253. (Note: at around t = 13 s there is a discontinuity of density data.)

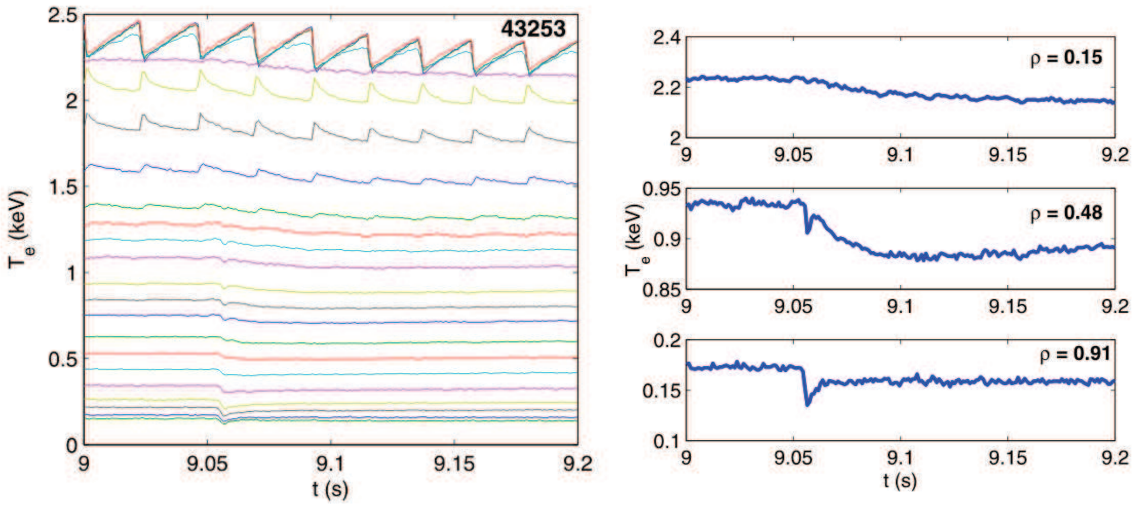

Figure 7.15 ECE temperature evolution during one SMB injection. The left panel shows the time traces of temperature at various radii; the right panel shows only three selected channels.

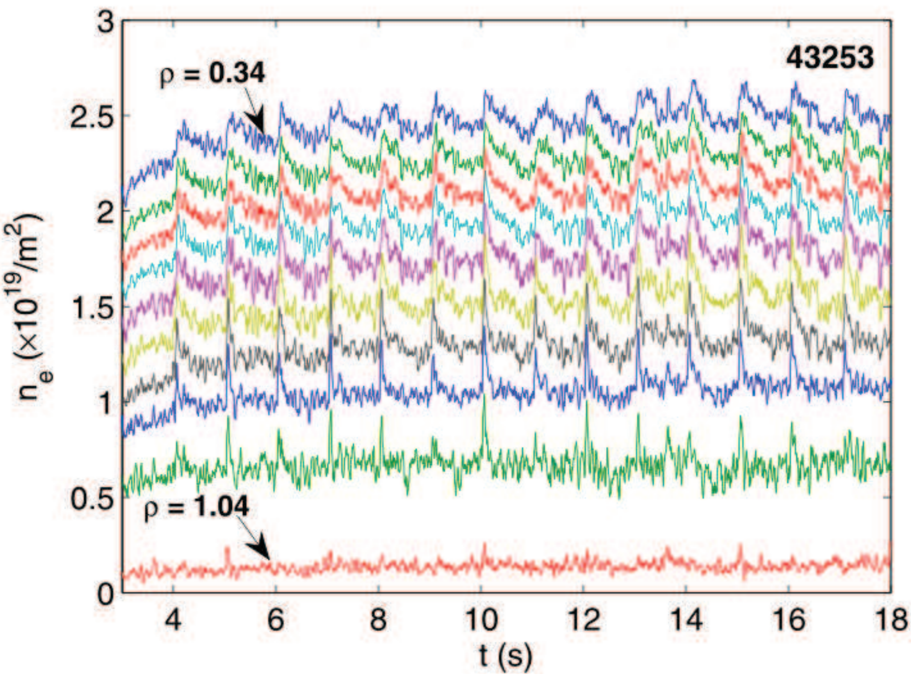

Figure 7.16 Time traces of electron density measured on the low field side for shot 43253.

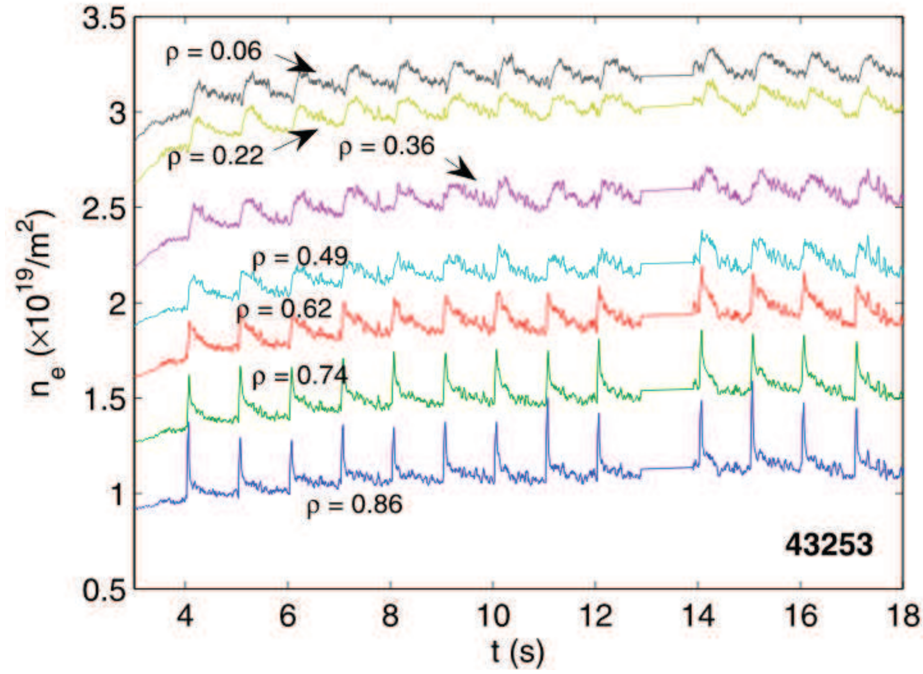

Figure 7.17 Time traces of electron density measured on the high field side for shot 43253. Note, there is a data gap at around $t = 13$ s.

The diagram of the normalized density and temperature gradients is shown in Figure 7.18. At various radii, $\rho = 0.4$, 0.5 and 0.6, the rotations of the clouds of points are all counterclockwise, which confirms the previous result. However, based on the ITG/TEM turbulent theory, the rotation is the effect rather than the cause. The initial position in the parameter diagram itself mainly determines the direction the rotation will follow. Further investigation by means of turbulence codes will be done in the future.

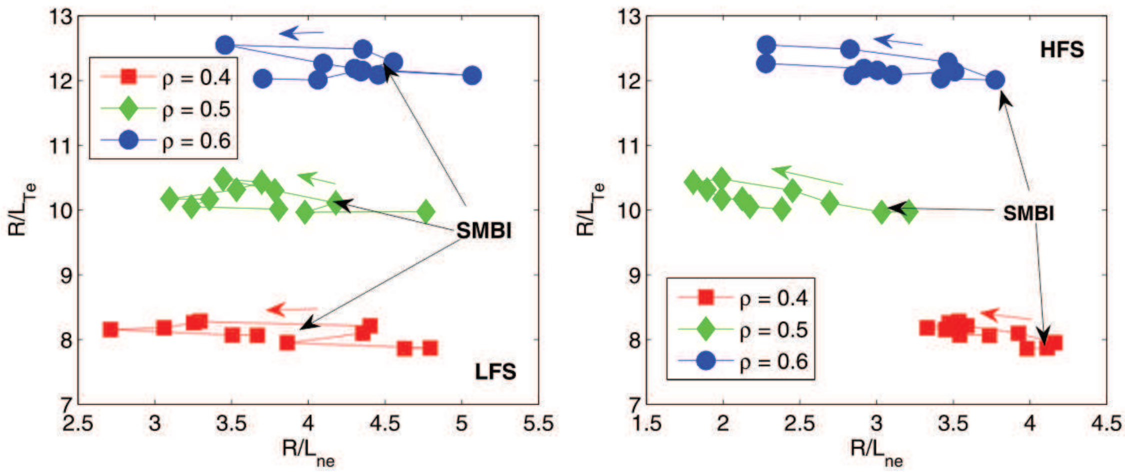

Figure 7.18 Diagrams of normalized density and temperature gradients at various radii around $t = 9$ s for shot 43253. The density in the left panel comes from LFS measurement, while the right panel comes from the HFS.

Figure 7.19 shows the electron temperature perturbation obtained by the measurement of fast ECE on the low field side. The hot part in the figure is only due to the sawteeth effect in the core, while the injection of SMB only produces a cold pulse, which covers the bottom-right area. The speed of propagation of the cold pulse can be estimated to be $v_{cold} \approx 6$ m/s.

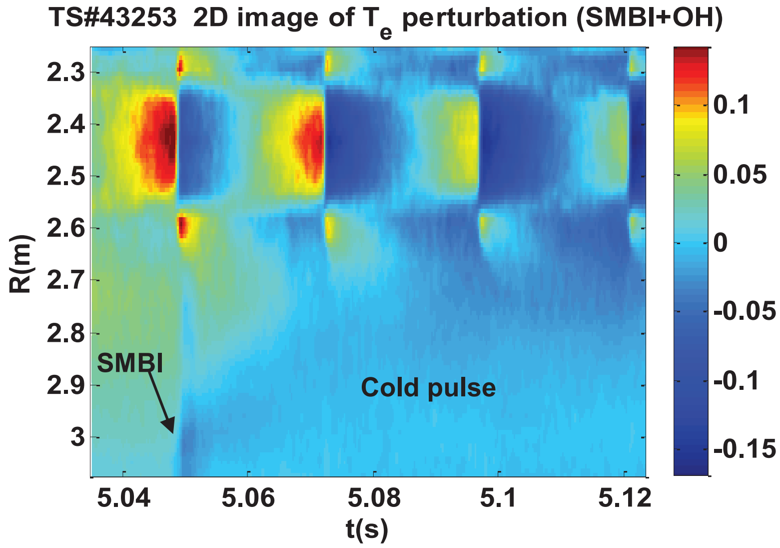

Figure 7.19 Time-space evolution of T_e perturbation during SMBI without CHEC for shot 43253 at around $t = 5$ s.

7.2 Fourier analysis

In the experiments, the SMBs are kept with the same backing pressure in order to project similar bundles of gas into the plasma. The modulation frequency varies from 1 Hz to 2 Hz. The typical FFT harmonics for the electron temperature are shown in Figure 7.20. As discussed in the previous section, shot 43253 is a Cold Pulse only case with modulation frequency of the SMBI $f = 1$ Hz. Since the duty factor of the modulation is less than 10%, the Fourier harmonics series not only contains odd harmonics but also the even ones, which is different from the 50% duty factor ECRH modulation experiments discussed in Chapter 4.

As the harmonic number increases, the amplitude and phase reflect the more rapid process involved. The fundamental harmonic ($f = 1$ Hz for this shot) is thought to contain the major information of the slow process. The phase profile characterizes the propagation velocity. The point with minimum value locates the center of the perturbation.

From the experimental harmonics we can get the following information:

(i) The minimum point on the phase shifts slightly outwards as the frequency increases;

(ii) The profile is flatter in the region $R \in [2.2\ 2.55]$ m compared to the region $R >$ 2.55 m, which may due to the contribution of sawteeth; for $f = 1$ Hz, it is $R =$ 2.9 m, while for $f = 2$, 3 Hz, it is $R = 3$ m.

(iii) The amplitude keeps increasing moving from the edge in the low field side to the center for the fundamental harmonic;

(iv) The amplitude decreases as the harmonic frequency increases, and it decreases faster in the center than at the edge, which reflects the diffusive character of the transport process.

By deleting the rapid drop (the technique of 'deleting' is linear interpolation of the data on the two sides of the rapid drop) shown in the zoomed version of Figure 7.4, almost no difference is found in the amplitude and phase profiles of the first three harmonics, which excludes a possible influence of the rapid drop on the position of minimum.

During the evolution, the cold pulse propagates into the plasma core. The cold pulse itself becomes wider and wider, as shown in Figure 7.17.

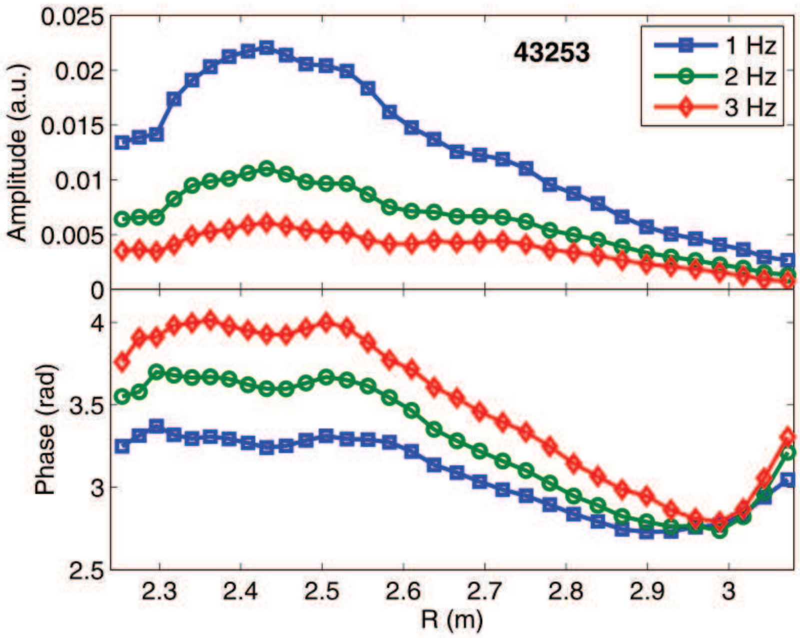

Figure 7.20 Amplitude and phase of the FFT harmonics of electron temperature perturbation for shot 43253. The FFT time window is set to be from $t = 5$ s to 12 s.

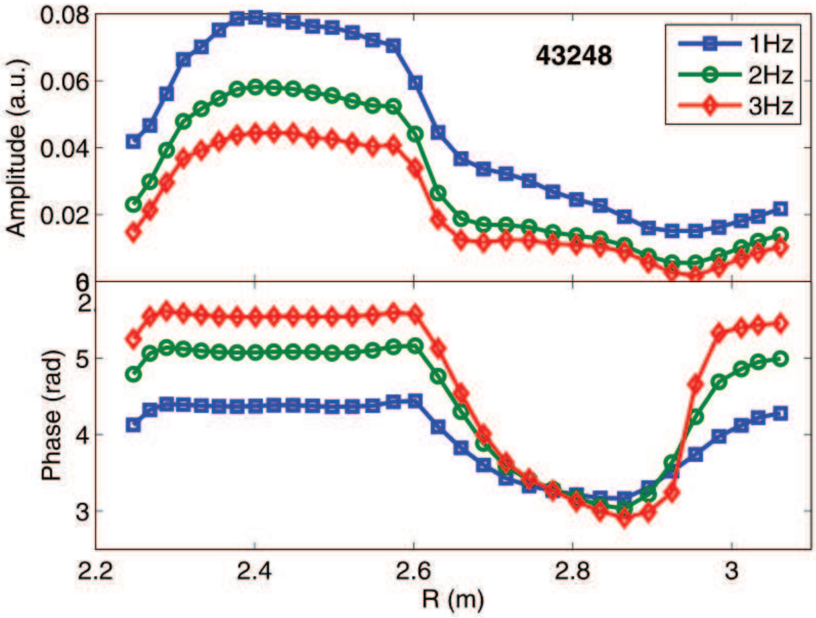

Figure 7.21 Amplitude and phase of the FFT harmonics of electron temperature perturbation for shot 43248. The FFT time window is set to be from $t = 9$ s to 13 s.

From the Equation (3.8) for a purely diffusive model, the heat diffusivity can be derived. For shot 43253, at R = 2.79 m (ρ = 0.5), the diffusivities derived from the three harmonics are χ_e^{HP} = 0.6, 0.93 and 1.18 m^2/s respectively (from fundamental harmonic to the 3rd harmonic). For shot 43248, at the same position, the respective diffusivities are χ_e^{HP} = 0.79, 0.95 and 1.01 m^2/s. Statistical analysis of the data shows that the diffusivity is the larger for the higher harmonic. It is interesting that in CGM regime, where the diffusivity is not constant but dependent on the temperature and its gradient, the resultant harmonics produce the same diffusivity.

Simulation of the FFT harmonic data is also carried out with the Linear Pinch Model described in Chapter 5. The simulation results and associated parameters are shown in Figure 7.22 and Figure 7.23, respectively. Good agreement has been obtained assuming a cold pulse injection at around ρ = 0.6 with a width w = 7 cm. The heat diffusivity displays a well-type feature in the region from ρ = 0.2 ~ 0.35, inside which the value of χ_e is as low as 0.1 m^2/s. This indicates the possible existence of a transport barrier. Transport barrier here is a possible explanation of the CHEC phenomenon. The convection velocity is oriented inwards inside ρ = 0.65, by which the slope of the amplitude at ρ = 0.2 ~ 0.35 is formed. Note here that the condition of this shot is similar to the low density case of the heat pinch experiments, i.e., the line-averaged density agrees with the *low* density definition in Chapter 4. From this point of view, the existence of heat pinch may also be demonstrated by modulated SMBI experiments.

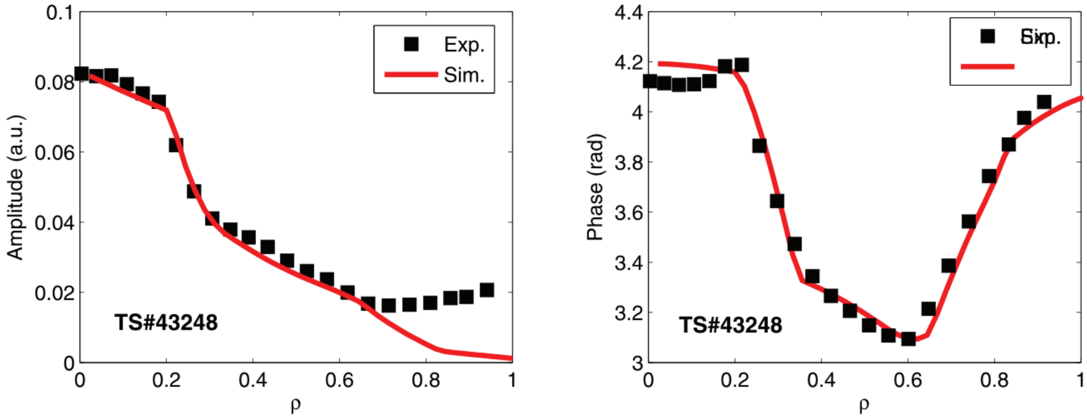

Figure 7.22 Simulation of the fundamental harmonic of SMBI experiments (shot TS#43248): left panel (amplitude) and right panel (phase). The squares stand for the experimental data, and the red curves stand for the simulation results.

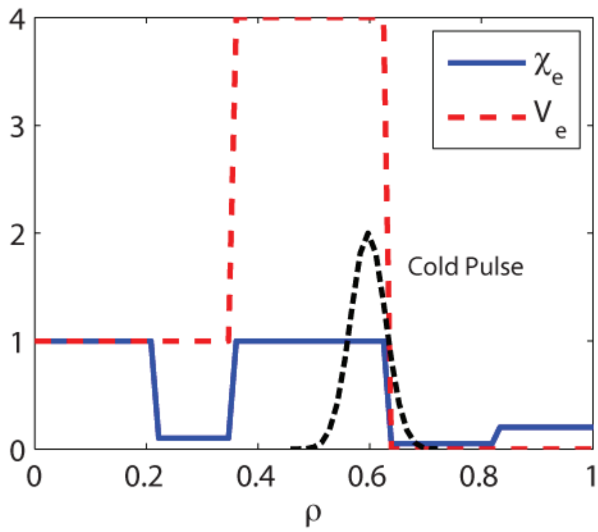

Figure 7.23 Profiles of χ_e and V_e (positive means inward) which correspond to the simulation curve of Figure 7.22. The black dashed curve represents the shape of the cold pulse.

7.3 Energy confinement and turbulence rotation

In the previous CHEC experiments, energy improvement has not been observed during the temperature perturbation. Figure 7.24 displays the time evolution of the energy confinement time during a pulse of SMBI with CHEC. It shows there is a significant improvement in this case. The energy improvement can transiently reach 30%. This value is very impressive for a small and local perturbation. On the other hand, Figure 7.25 displays the time evolution of the energy confinement time during a pulse of SMBI without CHEC. Here no improvement has been observed. Thus the strong improvement of global energy in CHEC case indicates the presence of an internal transport barrier (ITB). This is consistent with the results obtained in the previous section using Fourier analysis for the temperature and the density modulations.

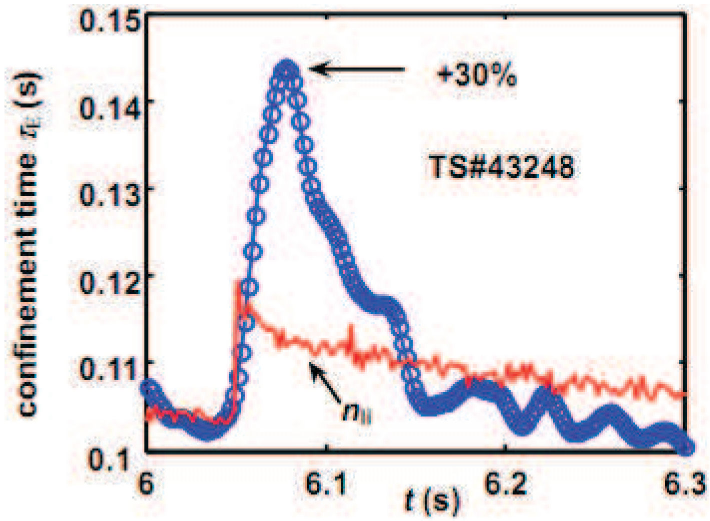

Figure 7.24 Confinement time during SMBI for the case with CHEC

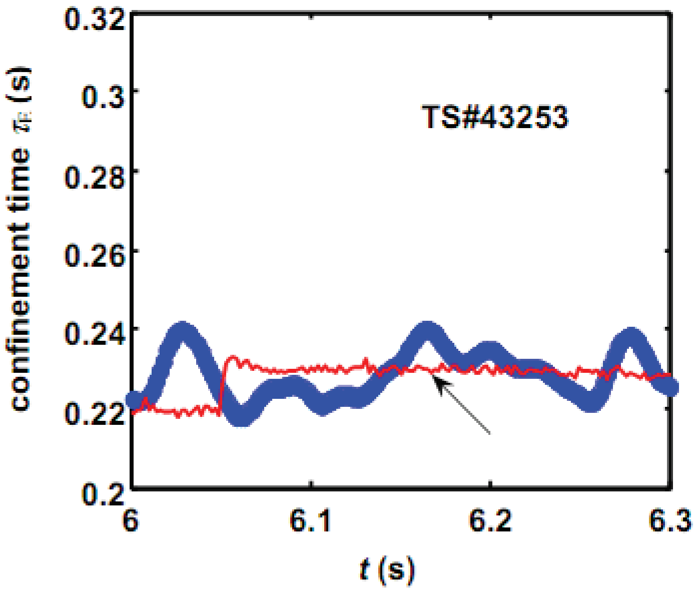

Figure 7.25 Confinement time during SMBI for the case without CHEC

Figure 7.26 displays the radial profile of the turbulence poloidal rotation velocity measured by Doppler reflectometry in the high density case without CHEC before and after SMBI. The time necessary for the construction of a profile is about 80 ms. Thus this time resolution is not enough for the investigation of the rotation propagation. From this figure, it is clear that the radial profile of the rotation velocity remain nearly unchanged after SMBI. On the other hand, as shown in Figure 7.27, the radial profile of the turbulence poloidal rotation velocity has undergone a significant change in the CHEC case after SMBI. This indicates a possible connection between the formation of ITB and the plasma rotation shear in the CHEC case.

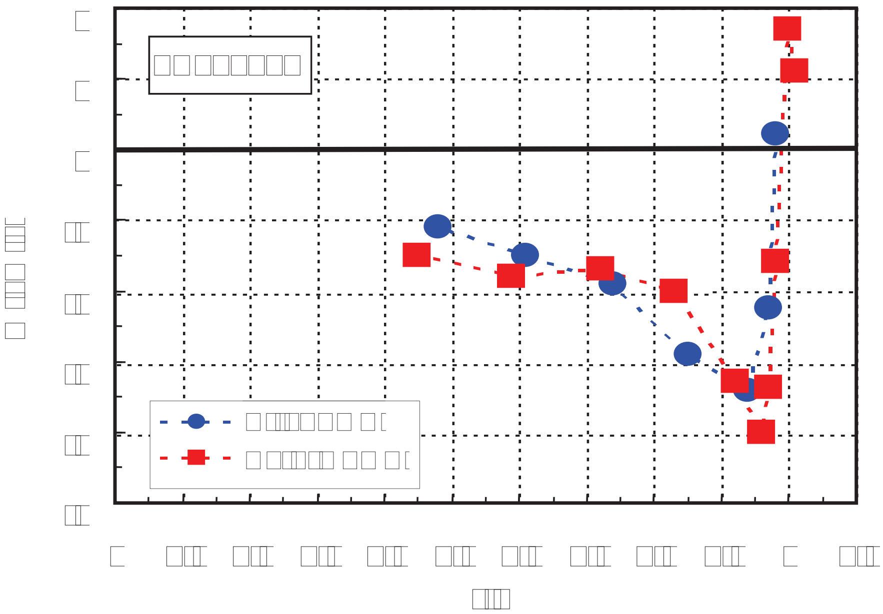

Figure 7.26 Poloidal rotation velocity measured by Doppler reflectometry. High density case without CHEC.

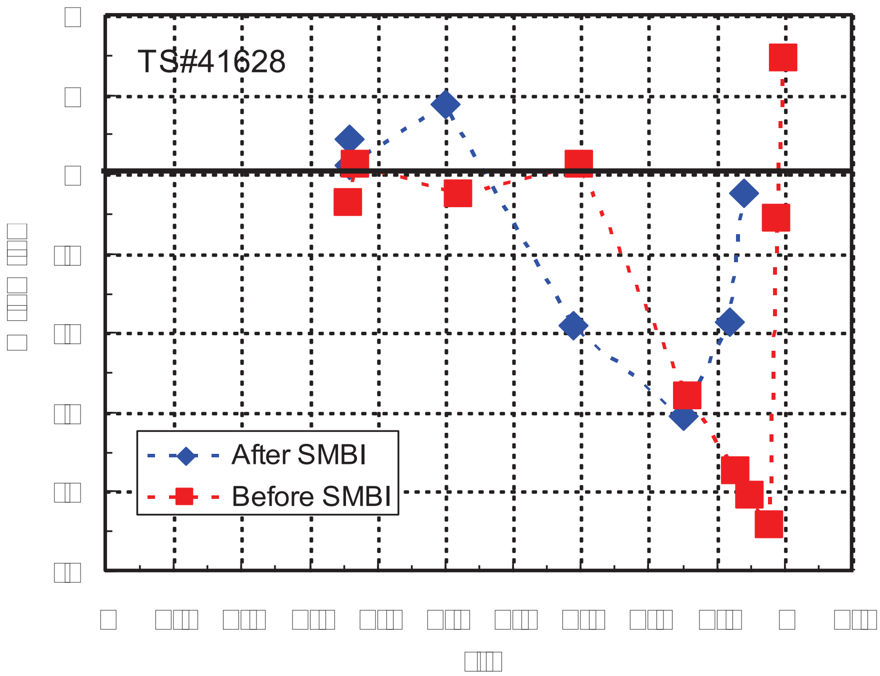

Figure 7.27 Poloidal rotation velocity measured by Doppler reflectometry. High density case without CHEC.

7.4 SMBI experiments on HL-2A

Non-local transport phenomena induced by supersonic molecular beam injection (SMBI) have been previously observed for the first time in the HL-2A tokamak in low density discharges [79,80]. Three fuelling methods, gas puffing (GP), pellet injection (PI) and supersonic molecular beam injection (SMBI) have been used on HL-2A. It should be noted that the SMBI was first successfully developed on the HL-1M tokamak, and later on it was applied to the HL-2A, Tore Supra and other tokamaks. The SMBI systems on HL-2A are installed on both LFS and HFS [81]. The valve in the LFS has been provided by Tore Supra. The backing pressure of the LFS could be as high as 60 bars, and the duration is longer than 0.5 ms. Normally each pulse corresponds to a number of 2×10^{17} deuterium molecular particles. The pulse duration of the HFS injection is about 2 ms, which is not adjustable due to the structure of the valve. The backing pressure is designed to be 1 ~ 10 bars, and the frequency is less than 10 Hz [82-86].

From tangential D_α measurement, the injection depth of the beam can be estimated. The signals from the tangential D_α array have shown that the SMBI from the low field side consists of a slow component (SC) and a fast component (FC) because of a small percentage of H_2 present in the D_2 reservoir. The FC can penetrate more deeply than the SC, e.g., 8.5 cm inside the last closed flux surface, while the SC is around 4 cm. The penetration depth of the SMBI is weakly dependent on plasma parameters before injection and on its backing pressure. [87]. Figure 7.28 shows a typical injection of SMBI and observations by tangential D_α measurements.

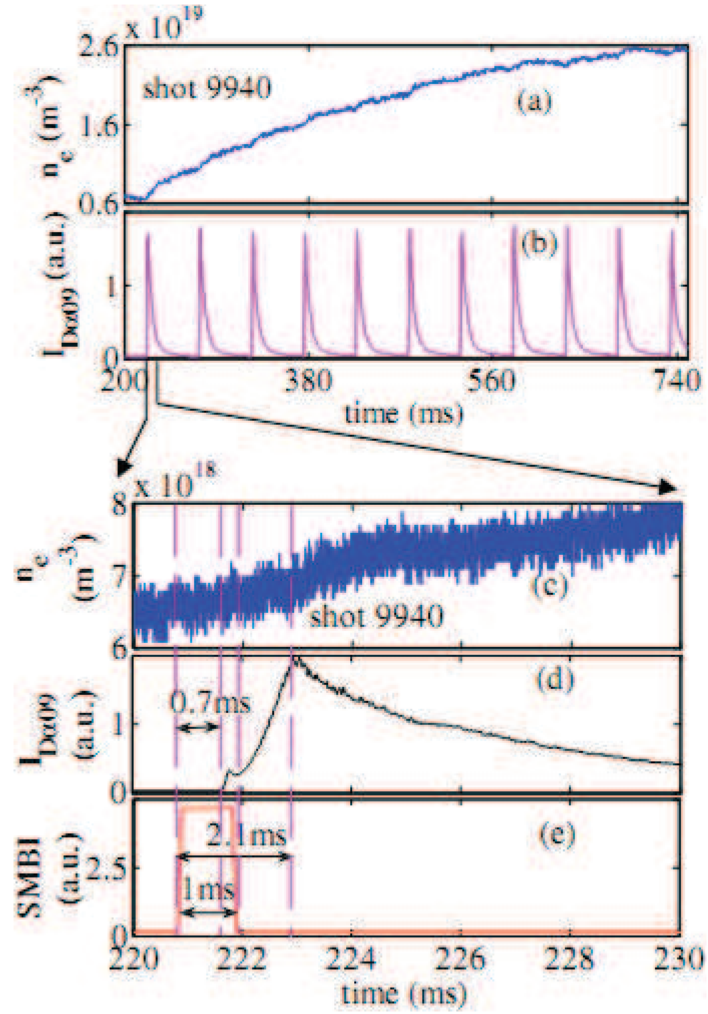

Figure 7.28 Characteristics of D_α emission monitored by the tangential array. Time traces from top to bottom are (*a*) line-averaged electron density, (*b*) D_α emission monitoring the molecular beam, (*c*) and (*d*) expanded views of (*a*) and (*b*), (*e*) SMBI controlling signal. The backing pressure is 1.7 MPa with a duration of 1 ms for shot 9940; the lifetime of the FC (the first peak) is about 0.3 ms; the rising time of the SC (the second peak) is close to the pulse duration, e.g., ~ 1 ms. (Adapted from [87])

The successive appearance of FC and SC is explained by the self-blocking effect in Ref [85]. The basic idea of the self-blocking effect is the following: the ionized electrons and ions accumulate and then block the subsequent penetration of SMBI. Since the local electron density in the main deposition region is at least an order of magnitude higher than that before the injection, the injection depth of the SMBI is only weakly dependent on the plasma parameters before the injection. Figure 7.29 shows the position of the maximum D_α intensity induced by FC and SC, from which we can conclude that the injection depth of the FC is deeper than that of the SC.

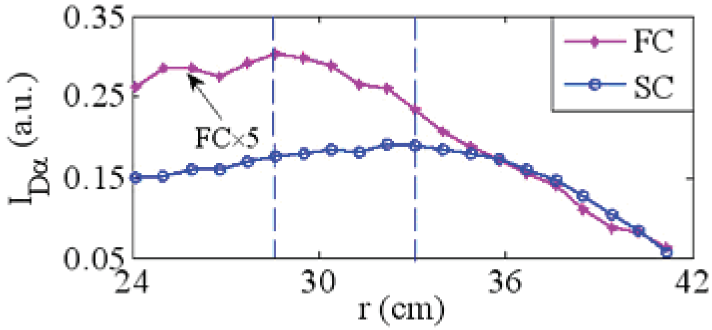

Figure 7.29 Profiles of maximum D_α emission along the minor radius for the FC and SC respectively. (Adapted from [87])

Figure 7.30 shows the time traces of the electron temperature during the modulated SMBI (shot 9898 is from the HL-2A 2009 experiment campaign). The regime which causes temperature oscillations at t = 700 ~ 900 ms is not clear yet. However, the typical opposite polarity phenomenon during the modulation phase is observed. During one beam injection, the increment in the central channels is even higher than the temperature decrement at the edge. During the modulation series, the line-averaged density increases gradually, which means that the particle loss is not large enough to keep a balance between the injected particles and the outward particle flux. Like sawteeth, the increment and decrement are separated by a channel, where the temperature varies little.

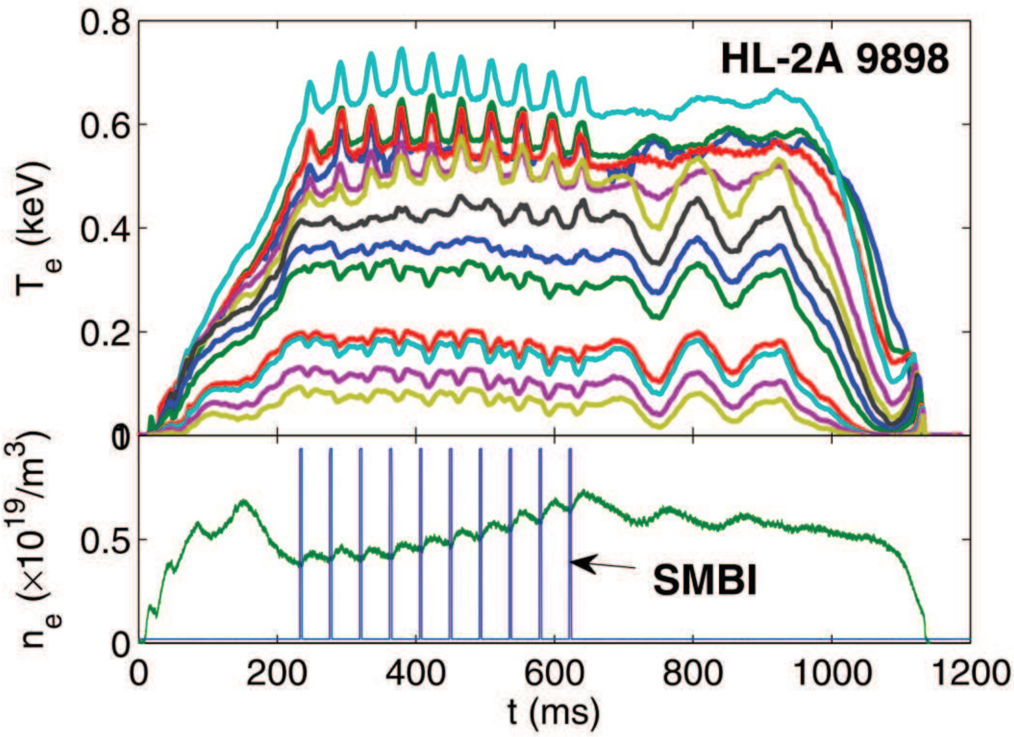

Figure 7.30 SMBI modulation with non-local phenomenon on T_e profiles.

Note that the ECE data are not absolutely calibrated; hence the profile of temperature is not used. In this case, the relative perturbation is used instead and the phase profile is well suited to show propagation of the perturbation. From the phase profile, one can get the incremental diffusivity, as shown below [88],

$$\chi_e^{\phi} = \frac{3\omega}{4\phi'^2} \tag{7.1}$$

Normally the value is larger than χ_e^{HP} expressed in the form of Equation (3.8). Figure 7.31 shows the relative amplitude profile and the phase profile of temperature responding to the SMBI. The whole plasma is divided into two regions, the hot pulse region and cold pulse region. The areas on the two sides of the dashed-dotted line in the figure have a phase difference of about π. The transition region is quite narrow, which is different from the case of Tore Supra, as shown in Figure 7.20 and Figure 7.21. On the amplitude profile, the difference between the two devices is more pronounced: on Tore Supra, the amplitude in the transition region is smooth and can be explained by the propagation of a single cold pulse at the edge; while on HL-2A, the amplitude shows two separate regions which cannot be reproduced by a single cold source. In the HL-2A case, the explanation is more likely related to the turbulence spreading rather than to the transport barrier.

The incremental diffusivity deduced from the phase profile at r = -26 cm is χ_e^{ϕ} = 19 m^2/s, while the derivation of convection velocity is difficult since the amplitude is a relative one.

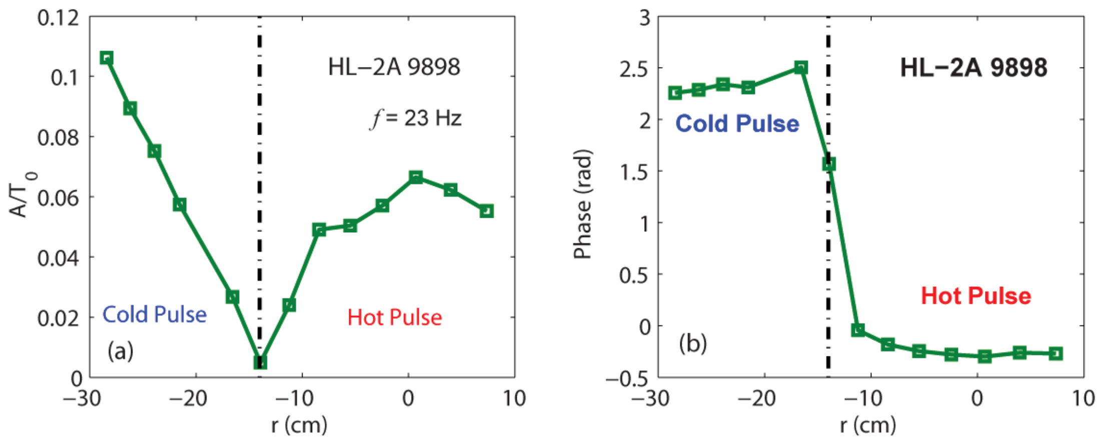

Figure 7.31 Amplitude (*a*) and phase profile (*b*) for shot HL-2A#9898. The amplitude profile is divided by the mean temperature. The FFT time window is from 278 ms to 664 ms.

7.5 Conclusions

The response of plasma to the localized cooling and cold pulse propagation have been observed in many experiments, with peculiar opposite polarity perturbation of the electron temperature, and with density and temperature variations much faster than in the normal transport process. These phenomena are usually denoted as the so called non-local effect. The concept of non-locality is not quite strict, since exact non-local effects would infringe causality. We prefer to consider the non-local effect as a phenomenon in which the diffusivity exceeds the gyro-Bohm value and hence it is rather Bohm like.

Perturbation transport experiments with both SMBI have been performed on Tore Supra and HL-2A to investigate the “non local” transport effect. For low density, the Central Heating driven by the Edge Cooling (CHEC), or opposite polarity on temperature perturbation, has been observed, with features similar to those previously observed with pellet injection. Simultaneously a strongly nonlinear and localized behaviour has been observed for the cold pulse propagation generated by SMBI, i.e., inward and ballistic convection. In addition, the hot pulse propagates inward, accompanying the cold pulse. Moreover, an improvement of the global energy confinement has been found for this regime. Fourier analysis of the temperature modulations due to SMBI confirms a strong reduction of the heat transport during SMBI with CHEC. A density transport barrier, characterized by a sharp decrease of the particle diffusivity, has been observed around the temperature inversion radius. Furthermore, a significant change of the plasma rotation is also observed during SMBI with CHEC. It has been found that simulations with positive and negative turbulence solitons, governed by zonal flow, are qualitatively able to reproduce the hot and cold pulse propagation phenomena.

The SMBI experiments are carried out on both the Tore Supra and HL-2A tokamaks. On Tore Supra sharp but small transient decrease is found on the ECE signal at the edge; whereas on the HL-2A tokamak, coexistence of fast and slow components on the D_α signal is reported in [87]. The plasma evolution has been discussed using diagrams of the normalized density and temperature gradients. Central Heating driven by Edge Cooling (CHEC) and pure Cold Pulse effect show different rotation rules on the points of the diagrams. The threshold of CHEC (or opposite polarity) has also been shown and discussed.

Chapter 8 Coupled heat and particle transport simulation

In the SMBI injection experiments and ECRH modulation experiments carried out on Tore Supra and described in the previous chapters, the density and temperature perturbations have similar magnitude. Therefore, the coupling between particle and heat transport equations has to be taken into account. In this Chapter, simulations of the pump-out and non-local transport experiments are performed, using coupled particle and heat transport equations. Conversely, coupling of other physical quantities, such as, current and momentum will be neglected for the moment.

There are some differences in pump-out and non-local transport experiments, especially in the way in which transport of particles and heat are coupled. In the pump-out experiments, the outer perturbation source is ECRH heating; particle transport is affected only through the variation of diffusivity and convection velocity, if we omit the density perturbation coming from the edge. However, in the non-local transport experiments, when the cold pulses are injected into the plasma, a perturbation source to both the heat and particle transport is present at the same time.

Section 8.1 will give a short description of the paradigm model, in which necessary formulas have been introduced; section 8.2 investigates the responses of electron temperature and density to the external induced particle source, for which comparison with non-local experiments are carried out; section 8.3 investigates the their responses to the external heat source, compared to the pump-out experiments; section 8.4 gives the simulation results with a fixed pure diffusive transport matrix, in which the responses of temperature and density to external particle and heat sources show qualitative agreement with the respective experiments; a short discussion and interpretation is given in section 8.5.

8.1 The paradigm model

The interaction of the density and temperature can be analysed using the general transport matrix described in reference [39]. The particle and heat transport can be expressed as follows:

$$\frac{\partial}{\partial t} n = -\nabla\Gamma + S_p \tag{8.1}$$

$$\frac{\partial}{\partial t}\left(\frac{3}{2}nT\right)=-\nabla q_e-\nabla\left(\frac{5}{2}T\Gamma\right)+\frac{1}{n}\Gamma\nabla(nT)+S_h \tag{8.2}$$

where n and T represent the electron density and temperature respectively, q_e and Γ represent the electron heat and particle flux respectively, S_h and S_p represent the heat and particle source/sink. Here we do not investigate the equilibrium state: the density and temperature profiles are treated as background data. We focus on the perturbation of density and temperature. After linearization, Equation (8.1) can be transformed into

$$\frac{\partial}{\partial t}\tilde{n}=-\nabla\tilde{\Gamma}+\tilde{S}_p \tag{8.3}$$

$$\frac{3}{2}n_0\frac{\partial}{\partial t}\tilde{T}=-\nabla\tilde{q}-\nabla\left(\frac{5}{2}T_0\tilde{\Gamma}\right)+\tilde{\Gamma}\left[\frac{1}{n}\nabla(nT)\right]_0-\frac{3}{2}T_0\frac{\partial}{\partial t}\tilde{n}+\tilde{S}_h \tag{8.4}$$

where the tilde denotes the perturbed quantities, the subscript 0 denotes the value in the equilibrium state. In the derivation process, the gradient lengths of the perturbed quantities are assumed to be much shorter than the static ones.

Defining $n_1\equiv\tilde{n}/n_0$ and $T_1\equiv\tilde{T}/T_0$, we get

$$\frac{\partial}{\partial t}n_1=-\nabla\frac{\tilde{\Gamma}}{n_0}+\frac{\tilde{S}_p}{n_0} \tag{8.5}$$

$$\frac{\partial}{\partial t}T_1=-\frac{2}{3}\nabla\left(\frac{\tilde{q}}{n_0T_0}+\frac{\tilde{\Gamma}}{n_0}\right)+\frac{2}{3}\frac{\tilde{S}_h}{n_0T_0}-\frac{\tilde{S}_p}{n_0} \tag{8.6}$$

Assuming the particle and heat flux Γ, q_e only depend on n, T, ∇n and ∇T, for the perturbed q_e and Γ, we have,

$$\tilde{\Gamma}=\frac{\partial\Gamma}{\partial\nabla n}\nabla\tilde{n}+\frac{\partial\Gamma}{\partial\nabla T}\nabla\tilde{T}+\frac{\partial\Gamma}{\partial n}\tilde{n}+\frac{\partial\Gamma}{\partial T}\tilde{T} \tag{8.7}$$

$$\tilde{q}=\frac{\partial q_e}{\partial\nabla n}\nabla\tilde{n}+\frac{\partial q_e}{\partial\nabla T}\nabla\tilde{T}+\frac{\partial q_e}{\partial n}\tilde{n}+\frac{\partial q_e}{\partial T}\tilde{T} \tag{8.8}$$

As a result,

$$\frac{\tilde{\Gamma}}{n_0}=\frac{\partial\Gamma}{\partial\nabla n}\nabla n_1+\frac{T_0}{n_0}\frac{\partial\Gamma}{\partial\nabla T}\nabla T_1+\frac{\partial\Gamma}{\partial n}n_1+\frac{T_0}{n_0}\frac{\partial\Gamma}{\partial T}T_1 \tag{8.9}$$

$$\frac{\tilde{q}}{n_0T_0}=\frac{1}{T_0}\frac{\partial q_e}{\partial\nabla n}\nabla n_1+\frac{1}{n_0}\frac{\partial q_e}{\partial\nabla T}\nabla T_1+\frac{1}{T_0}\frac{\partial q_e}{\partial n}n_1+\frac{1}{n_0}\frac{\partial q_e}{\partial T}T_1 \tag{8.10}$$

$$\frac{\tilde{q}}{n_0 T_0}+\frac{\tilde{\Gamma}}{n_0}=\left(\frac{\partial\Gamma}{\partial\nabla n}+\frac{1}{T_0}\frac{\partial q_e}{\partial\nabla n}\right)\nabla n_1+\left(\frac{T_0}{n_0}\frac{\partial\Gamma}{\partial\nabla T}+\frac{1}{n_0}\frac{\partial q_e}{\partial\nabla T}\right)\nabla T_1$$
$$+\left(\frac{\partial\Gamma}{\partial n}+\frac{1}{T_0}\frac{\partial q_e}{\partial n}\right)n_1+\left(\frac{T_0}{n_0}\frac{\partial\Gamma}{\partial T}+\frac{1}{n_0}\frac{\partial q_e}{\partial T}\right)T_1 \tag{8.11}$$

The heat source S_h includes energy exchange between ions and electrons, the Ohmic power, and also external contribution from ECRH and other heating systems. The radiation is omitted here. The perturbed heat source can be rewritten in the form of

$$\tilde{S}_h=\tilde{S}_{ie}+\tilde{S}_{\Omega}+\tilde{S}_{ext} \tag{8.12}$$

$$\tilde{S}_{ie}=\frac{\partial S_{ie}}{\partial n}\tilde{n}+\frac{\partial S_{ie}}{\partial T}\tilde{T}=3\frac{T_i-T_0}{\tau_{ie}}\tilde{n}-\frac{3}{4}\frac{3T_i-T_0}{\tau_{ie}T_0}\tilde{T} \tag{8.13}$$

$$\tilde{S}_{\Omega}=\frac{\partial S_{\Omega}}{\partial T}\tilde{T}=-\frac{3}{2}\frac{S_{\Omega}}{T_0}\tilde{T} \tag{8.14}$$

Therefore we have,

$$\frac{\tilde{S}_h}{n_0 T_0}=\frac{3}{\tau_{ie}}\frac{T_i-T_0}{T_0}n_1-\left(\frac{3}{4n_0\tau_{ie}}\frac{3T_i-T_0}{T_0}+\frac{3}{2}\frac{S_{\Omega}}{n_0 T_0}\right)T_1 \tag{8.15}$$

Defining $\mathbf{u}\equiv\begin{pmatrix}n_1\\T_1\end{pmatrix}$, the equation can be written in matrix form as,

$$\frac{\partial}{\partial t}\mathbf{u}=-\nabla(\mathbf{A}\nabla\mathbf{u}+\mathbf{B}\mathbf{u})+\mathbf{C}\mathbf{u}+\mathbf{S} \tag{8.16}$$

Where **A**, **B** and **C** are 2 × 2 matrices, **S** is a vector. **A** stands for the diffusive transport coefficients, **B** is convective contribution, **C** is the damping term, and **S** is the external source contribution. The elements of these matrices are expressed as follows,

$$A_{11}=\frac{\partial\Gamma}{\partial\nabla n} \qquad B_{11}=\frac{\partial\Gamma}{\partial n}$$

$$A_{12}=\frac{T_0}{n_0}\frac{\partial\Gamma}{\partial\nabla T} \qquad B_{12}=\frac{T_0}{n_0}\frac{\partial\Gamma}{\partial T}$$

$$A_{21}=\frac{2}{3}\left(\frac{\partial\Gamma}{\partial\nabla n}+\frac{1}{T_0}\frac{\partial q_e}{\partial\nabla n}\right) \qquad B_{21}=\frac{2}{3}\left(\frac{\partial\Gamma}{\partial n}+\frac{1}{T_0}\frac{\partial q_e}{\partial n}\right)$$

$$A_{22}=\frac{2}{3}\left(\frac{T_0}{n_0}\frac{\partial\Gamma}{\partial\nabla T}+\frac{1}{n_0}\frac{\partial q_e}{\partial\nabla T}\right) \qquad B_{22}=\frac{2}{3}\left(\frac{T_0}{n_0}\frac{\partial\Gamma}{\partial T}+\frac{1}{n_0}\frac{\partial q_e}{\partial T}\right)$$

$$C_{11} = 0 \qquad S_1 = \frac{\tilde{S}_p}{n_0}$$

$$C_{12} = 0$$

$$C_{21} = \frac{2}{\tau_{ie}} \frac{T_i - T_0}{T_0} \qquad S_2 = \frac{2}{3} \frac{\tilde{S}_{ext}}{n_0 T_0} - \frac{\tilde{S}_p}{n_0}$$

$$C_{22} = -\left(\frac{1}{2 n_0 \tau_{ie}} \frac{3T_i - T_0}{T_0} + \frac{S_\Omega}{n_0 T_0} \right)$$

The simplest form is a purely diffusive one, in which convective and damping terms are omitted, i.e., **B**, **C** = **0**, as in Equation (8.17).

$$\frac{\partial}{\partial t}\mathbf{u} = -\mathbf{A}\nabla^2\mathbf{u} + \mathbf{S} \tag{8.17}$$

This formulas implies that Γ and q_e only depend on ∇n and ∇T (since $\mathbf{B} = \mathbf{0}$).

8.2 Qualitative simulation for the non-local phenomenon

Below we investigate systematically how the opposite polarity phenomenon takes place, on the basis of this simplified formulation. Here we assume that all the elements of the **A** matrix are constant. For simplification, we also omit the thermal contribution of the injected particle pulse (e.g., SMBI) i.e. the direct cooling down effect due to the temperature difference between hot plasma and cold gas bundle. The boundary conditions are assumed to be

$$\frac{\partial}{\partial \rho}\begin{bmatrix} n_1 \\ T_1 \end{bmatrix}\Bigg|_{\rho=0} = 0, \text{ and} \begin{bmatrix} n_1 \\ T_1 \end{bmatrix}\Bigg|_{\rho=1} = 0.$$

The particle source is assumed to be Gaussian shaped, with a half width of 0.05 and located at $\rho = 0.9$. Matter is injected at $t = 1$ s and the duration is 0.01 s.

$$S_p \propto \exp\left[-\left(\frac{\rho - 0.9}{0.05} \right)^2 \right] \tag{8.18}$$

(i) $\mathbf{A} = -\begin{bmatrix} 1 & 0 \\ 0 & 1 \end{bmatrix}$, *the non-diagonal elements are assumed to be zero.*

Note that the diagonal elements are assumed to be negative (pay attention to the minus symbol in front of the matrix), which is in agreement with the diffusive processes. In the following simulation, the diagonal elements are kept unchanged, while only the non-diagonal elements vary.

The time traces of the normalized density and temperature perturbations are shown in Figure 8.1. The evolution of density and temperature show that the injection of particles at ρ = 0.9 induces positive perturbation of $\widetilde{S}_p / n_0$ for the particle transport, while it induces a negative perturbation of the same amount for the electron temperature, as shown by the matrix coefficients. However, after the injection and also outside the source region, the transfer of density and temperature are purely diffusive and not affected by each other. The perturbation propagates inwards (the region $\rho > 0.9$ is out of our consideration), along with the phase shift and amplitude decrease.

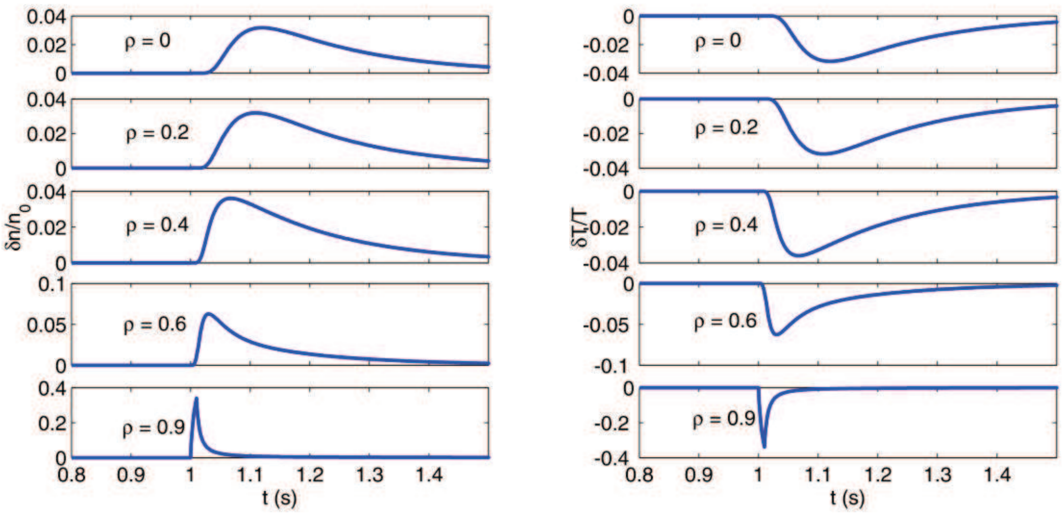

Figure 8.1 Time traces of the density (left panel) and temperature (right panel) perturbations at various radii. The external particle source is injected into the plasma at t = 1 s and ρ = 0.9. The diffusivity matrix is A = -[1 0; 0 1].

For the sake of clarity, we investigate the gradient and flux terms at ρ = 0.5, which is shown in Figure 8.2. The particle and energy fluxes have the form of

$$\frac{\widetilde{\Gamma}}{n_0} = A_{11}\nabla n_1 + A_{12}\nabla T_1 \tag{8.19}$$

$$\frac{\widetilde{Q}}{n_0 T_0} = A_{21}\nabla n_1 + A_{22}\nabla T_1 \tag{8.20}$$

For the zero non-diagonal case, $\widetilde{\Gamma}/n_0 = -\nabla n_1$ and $\widetilde{Q}/n_0 = -\nabla T_1$.

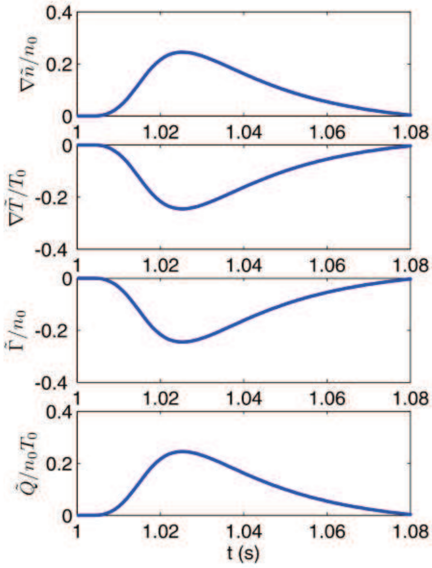

Figure 8.2 Time traces of the normalized gradients of the perturbed density and temperature, and also the particle and energy fluxes at $\rho = 0.5$. The diffusivity matrix is A = - [1 0; 0 1].

(ii) $\mathbf{A} = -\begin{bmatrix} 1 & 0 \\ 1 & 1 \end{bmatrix}$, *the upper non-diagonal element is assumed to be zero, while the lower one is set to be 1,* i.e., no influence of temperature gradient on density, while the density gradient affects the heat transport.

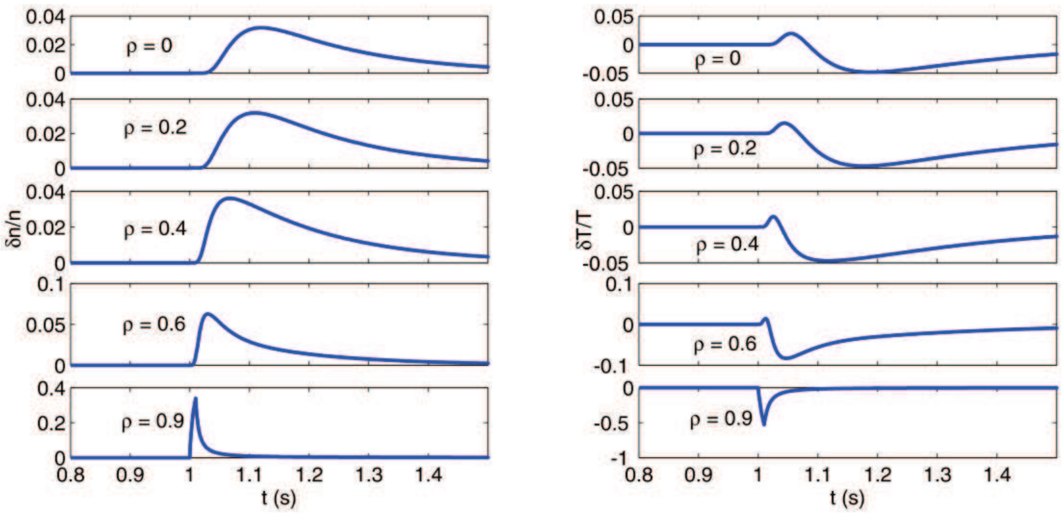

Figure 8.3 Time traces of the density (left panel) and temperature (right panel) perturbations at various radii. The external particle source is injected into the plasma at t = 1 s and ρ = 0.9. The diffusivity matrix is A = - [1 0; 1 1].

Figure 8.3 shows the time traces of density and temperature. It is clear that the density variation is the same as the first case. In fact, the density transport is independent of the heat counterpart. However, the temperature shows an opposite polarity phenomenon which is similar to the experimental one. This can be explained by the following derivation.

Substituting the given matrix **A** into Equation (8.17), we get,

$$\frac{\partial}{\partial t} n_1 = -\nabla^2 n_1 + \frac{\widetilde{S}_p}{n_0} \tag{8.21}$$

$$\frac{\partial}{\partial t} T_1 = -\nabla^2 n_1 - \nabla^2 T_1 - \frac{\widetilde{S}_p}{n_0} \tag{8.22}$$

Eliminating the second derivative of the density, we get,

$$\frac{\partial}{\partial t} T_1 = -\nabla^2 T_1 - 2\frac{\widetilde{S}_p}{n_0} + \frac{\partial}{\partial t} n_1 \tag{8.23}$$

For region $\rho < 0.8$, the sink term can be omitted, then

$$\frac{\partial}{\partial t} T_1 = -\nabla^2 T_1 + \frac{\partial}{\partial t} n_1 \tag{8.24}$$

For the heat transport, the variation of density becomes the source/sink term. Figure 8.4 shows the time traces of effective source terms for the heat transport. The correlation between the variation of density at various radii and that of the temperature at the corresponding radii is a clear proof of the causality between the particle variation and the positive bulk on temperature.

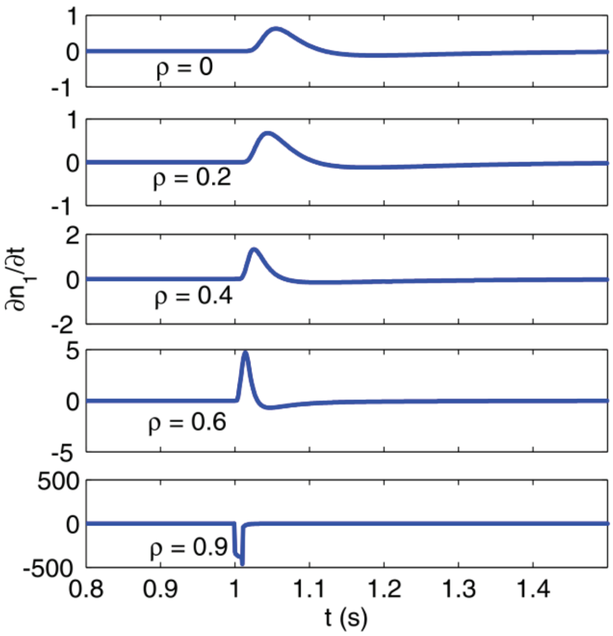

Figure 8.4 Time traces of the effective source/sink for heat transport. The diffusivity matrix is A = -[1 0; 1 1].

(iii) $\mathbf{A} = -\begin{bmatrix} 1 & 0 \\ -1 & 1 \end{bmatrix}$, *the upper non-diagonal element is assumed to be zero, while the lower one is set to be -1.*

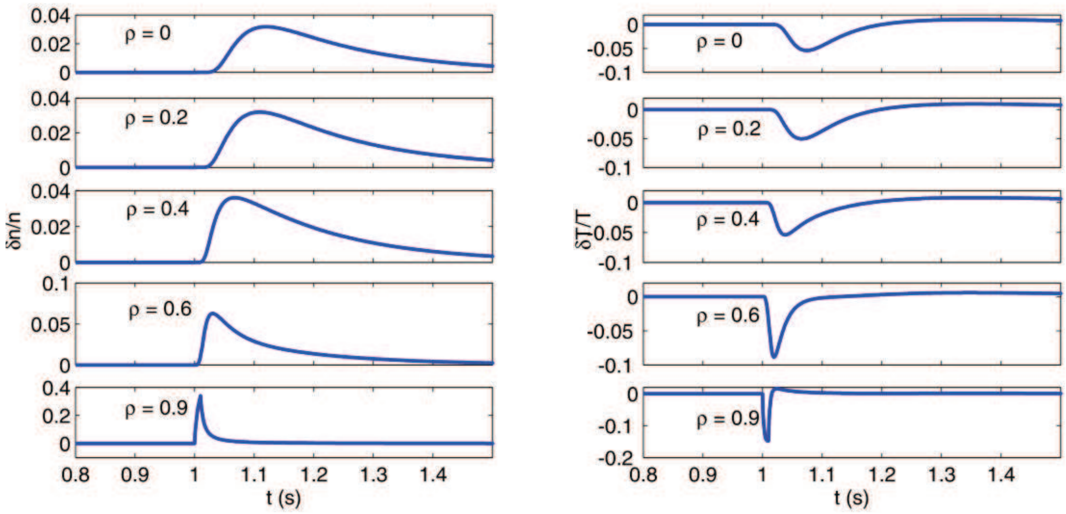

Figure 8.5 Time traces of the density (left panel) and temperature (right panel) perturbations at various radii. The external particle source is injected into the plasma at t = 1 s and ρ = 0.9. The diffusivity matrix is A = - [1 0;1 1].

Figure 8.5 shows the time traces of the density and temperature perturbation. This case is similar to the case (ii), only the non-diagonal element is changed to -1. The density is not affected compared to the purely diagonal case.

The temperature perturbation can be written as

$$\frac{\partial}{\partial t}T_1 = -\nabla^2 T_1 - \frac{\partial}{\partial t}n_1 \tag{8.25}$$

In this case, the particle source term is cancelled, while the density variation becomes the cooling source instead.

(iv) $\mathbf{A} = -\begin{bmatrix} 1 & 1 \\ 0 & 1 \end{bmatrix}$, *the lower non-diagonal element is assumed to be zero, while the upper one is set to be 1.*

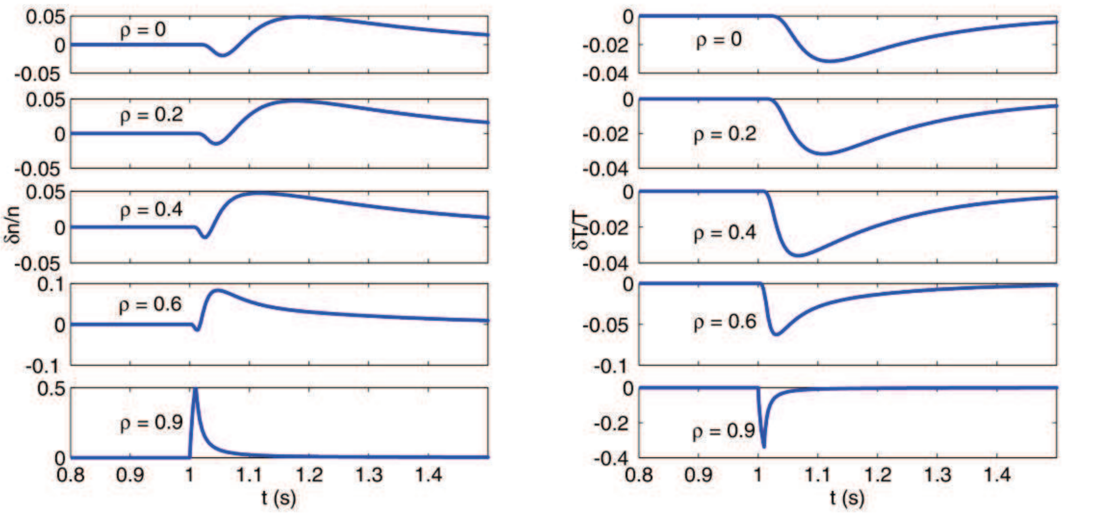

Figure 8.6 Time traces of the density (left panel) and temperature (right panel) perturbations at various radii. The external particle source is injected into the plasma at t = 1 s and ρ = 0.9. The diffusivity matrix is A = - [1 1;0 1].

In this case, the temperature variation becomes a source/sink to the particle transport. Similarly to the second case, we derive,

$$\frac{\partial}{\partial t}n_1 = -\nabla^2 n_1 + 2\frac{\widetilde{S}_p}{n_0} + \frac{\partial}{\partial t}T_1 \qquad (8.26)$$

On the particle transport, the opposite polarity phenomenon appears, i.e., the decrease of density in the core plasma after the injection of particle beam.

(v) $\mathbf{A} = -\begin{bmatrix} 1 & -1 \\ 0 & 1 \end{bmatrix}$, *the lower non-diagonal element is assumed to be zero, while the upper one is set to be -1.*

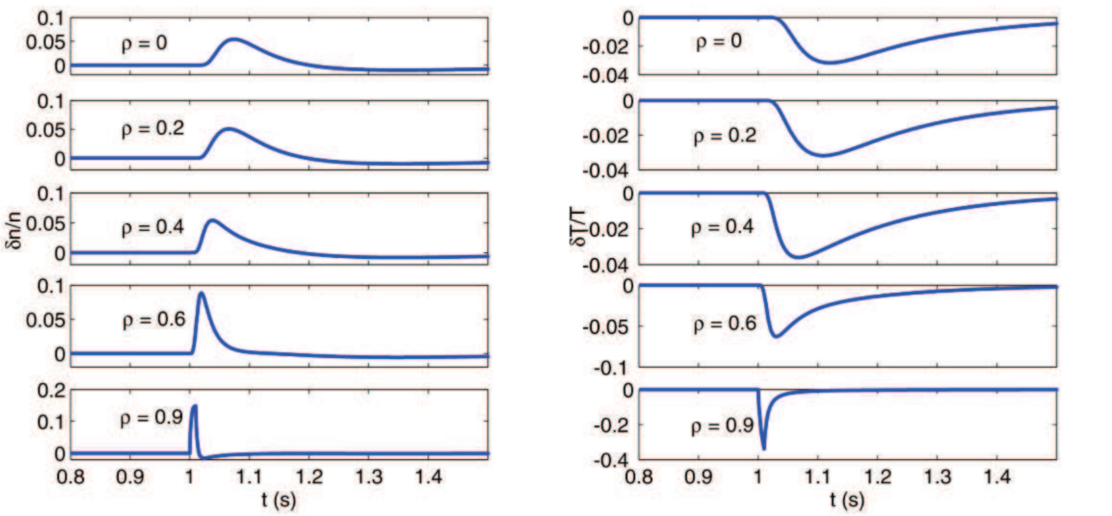

Figure 8.7 Time traces of the density (left panel) and temperature (right panel) perturbations at

various radii. The external particle source is injected into the plasma at t = 1 s and ρ = 0.9. The diffusivity matrix is A = - [1 -1;0 1].

The heat transport process is not affected by corresponding particle transport, while the heat transport influences positively the particle one.

$$\frac{\partial}{\partial t} n_1 = -\nabla^2 n_1 + 2\frac{\widetilde{S}_p}{n_0} + \frac{\partial}{\partial t} T_1 \tag{8.27}$$

To summarize, the previous three cases have a common point, i.e., one of the non-diagonal elements of the diffusivity matrix is zero. This property leads to unperturbed transport: for particle, the transport process is the diffusive transport of the positive external source; while for the heat, it is the diffusive transport of the negative external source. The coupling between the two is embedded in the fact that the variations of the unperturbed quantity (density or temperature) become the source or sink to the other one. In our case, the diffusion times of the non-coupled transport processes for both quantities are the same. Compared to that, the effective source variation time is shorter than the diffusive time; at least there is a shorter rise or decrease in the early stage, as shown in Figure 8.4. In the specific case, when the two elements on the same row in the transport matrix have the same sign, the transport embeds an opposite polarity phenomenon. Here we refer to this effect as negative feedback, while when the sign is opposite, the effect is positive feedback.

It is natural to think that the coupling of the two processes is mutual. Here we give an example:

(vi) $\mathbf{A} = -\begin{bmatrix} 1 & -1 \\ 1 & 1 \end{bmatrix}$, *the lower non-diagonal element is set to be 1, while the upper one is set to be -1.*

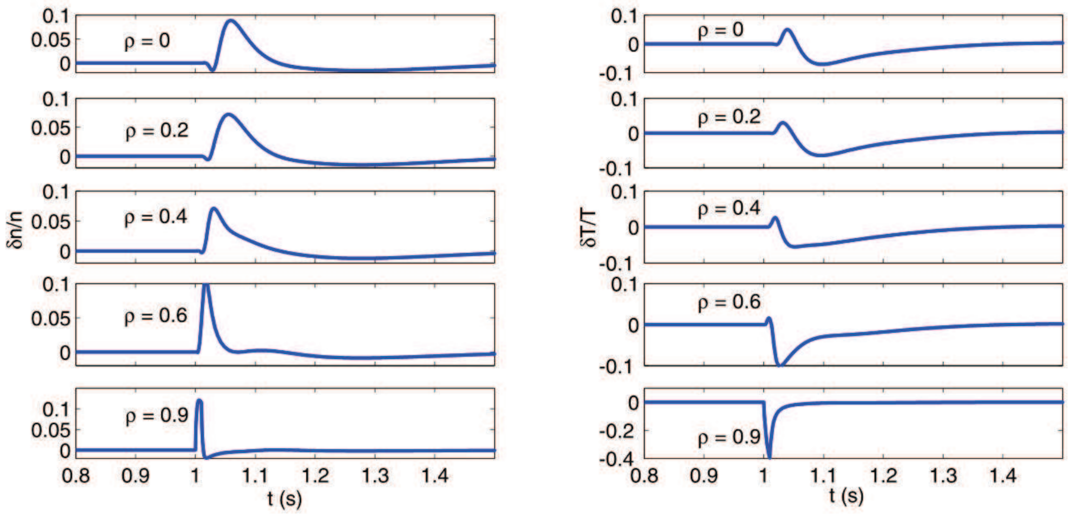

Figure 8.8 Time traces of the density (left panel) and temperature (right panel) perturbations at various radii. The external particle source is injected into the plasma at t = 1 s and ρ = 0.9. The diffusivity matrix is A = - [1 -1;1 1].

Figure 8.8 shows the time traces for this case. Through careful inspection, we can find that the variation rate of density is faster than the fourth case, where only temperature is coupled to density, while the temperature correspondent is faster than the second case, where only density is coupled to temperature.

In our investigation, the transport matrix method is only a qualitative method to show the reason why the opposite polarity appears in experiments, and also other possible phenomena. However, the quantitative investigation is more difficult to carry out. In Ref. [89], an eigenmode method is developed, however, in this reference, real eigenvalue is a prerequisite, which may be invalid in various cases. Nevertheless, quantitative methods remain to be developed in future work. The main difficulties lie in the following facts:

(i) The dependence of the matrices on the position may not be omitted;

(ii) The introduction of convection matrix and damping matrix and the determination of all the elements (there are at least eight unknown parameters, which determine the damping matrix, e.g., damping rate of Ohmic power and electron-ion exchange rate);

(iii) Different combination of the three matrices may explain the same phenomenon within experimental measurement precision;

(iv) The non-linearity of fluxes with respect to the gradients;

(v) The influence of the direct cooling effect induces an additional sink to the heat transport equation.

8.3 Qualitative simulation for the pump-out phenomenon

In this section we use the previously illustrated method to investigate the pump-out effect observed in the experiments. It is helpful to make a comparison between the opposite polarity and pump-out phenomenon. The main difference lies in the source term, i.e., cold pulse in opposite polarity while hot pulse in pump-out.

We also use the most simplified version of the coupled transport equation, Equation (8.17). Other definitions are kept the same as in the previous simulations, but the source term is a new one. Here we use a Gaussian-shaped heat pulse, with a half-width of 0.05 and located at $\rho = 0.5$ (other than $\rho = 0.9$). It is injected at $t = 0.3$ s and it has duration of 0.5 s. No external particle source is used in the simulation.

$$S_h \propto \exp\left[-\left(\frac{\rho - 0.5}{0.05}\right)^2\right] \tag{8.28}$$

We investigate from the simplest case to complex ones.

(i) $\mathbf{A} = -\begin{bmatrix} 1 & 0 \\ 0 & 1 \end{bmatrix}$, *the non-diagonal elements are assumed to be zero.*

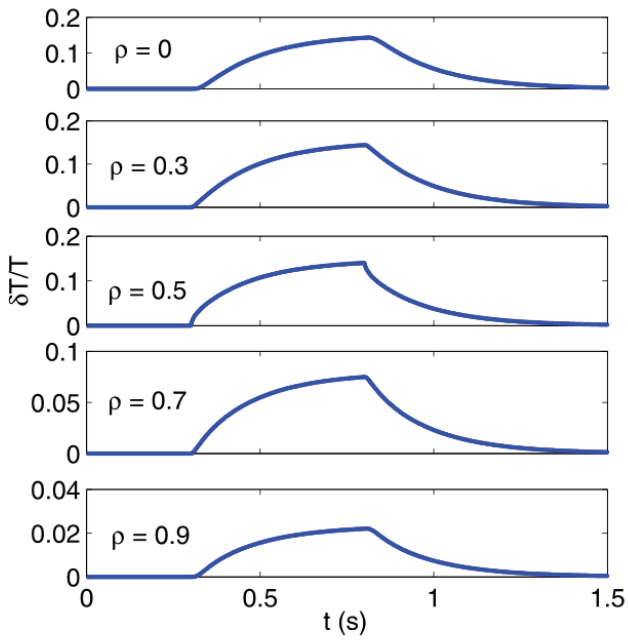

Figure 8.9 Time traces of the temperature perturbation at various radii. The external heat source is injected into the plasma at $\rho = 0.5$ and $t = 0.3$ s with a duration of 0.5 s. The diffusivity matrix is A = - [1 0;0 1].

The transport of particles and heat is independent. Since there is no particle source or effective source/sink, the density does not vary during the heat pulse. The temperature increment and decrement during and after the heat pulse are shown in Figure 8.9. The external power is deposited at ρ = 0.5, thus the increment rate after injection and decrement at the end of the pulse are the steepest.

(ii) $\mathbf{A} = -\begin{bmatrix} 1 & 1 \\ 0 & 1 \end{bmatrix}$, *the lower non-diagonal element is assumed to be zero, while the upper one is set to 1.*

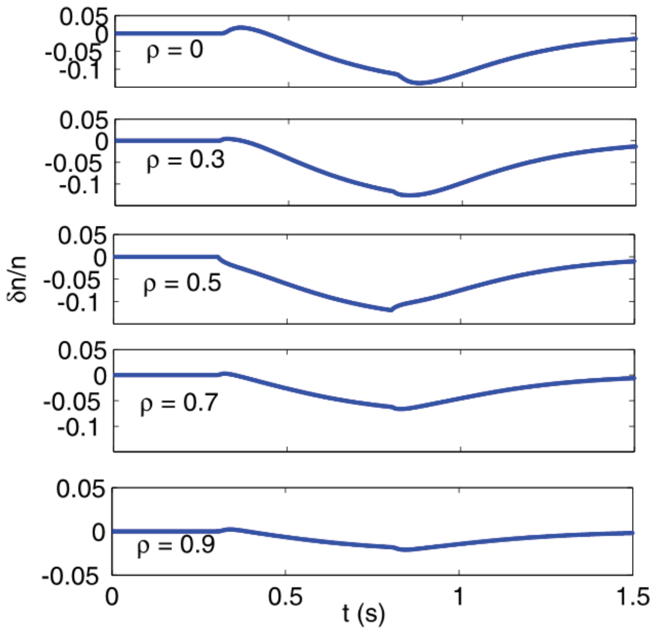

Figure 8.10 Time traces of the density perturbation at various radii. The external heat source is injected into the plasma at ρ = 0.5 and t = 0.3 s with a duration of 0.5 s. The diffusivity matrix is A = - [1 1;0 1].

The coupling effect from heat transport to its particle counterpart is shown in Figure 8.10. Here we can see the typical pump-out effect, i.e., as the heat pulse is injected, the density in the plasma core decreases; when the heat pulse ends, the density of the core plasma recovers. If we observe carefully we can find a slight increase before the pump-out, a small effect not seen in experiments.

Since there is no feedback to the heat transport, the perturbative temperature evolution is not shown, because it is the same as in the first case. The particle transport equation can be rewritten as,

$$\frac{\partial}{\partial t}n_1 = -\nabla^2 n_1 + \frac{\partial}{\partial t}T_1 - \frac{2}{3}\frac{\widetilde{S}_h}{n_0 T_0} \tag{8.29}$$

the heat source and temperature variation together become the source/sink of the particle transport. The effective source/sink is shown in Figure 8.11. The main trend of increase during hot pulse comes from the heat source with a minus sign, while the slight structures come from the temperature variation.

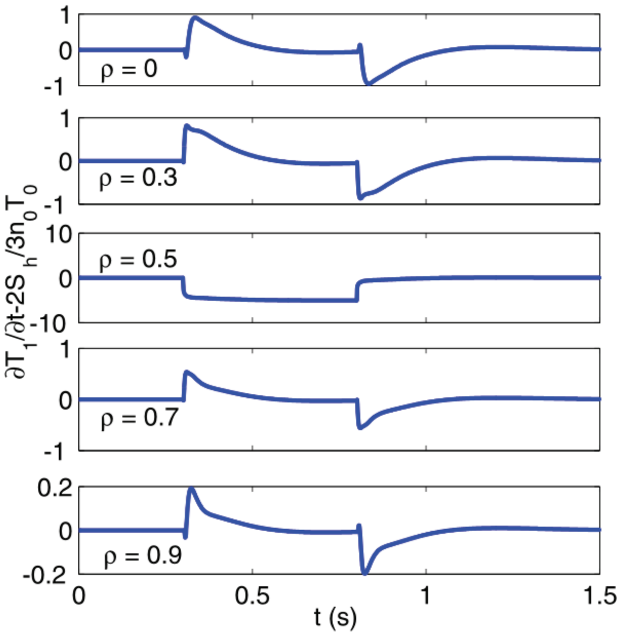

Figure 8.11 Time traces of the effective source/sink for the particle transport at various radii. The external heat source is injected into the plasma at $\rho = 0.5$ and $t = 0.3$ s with a duration of 0.5 s. The diffusivity matrix is A = - [1 1; 0 1].

(iii) $\mathbf{A} = -\begin{bmatrix} 1 & -1 \\ 0 & 1 \end{bmatrix}$, *the lower non-diagonal elements are assumed to be zero, while the upper one is set to be -1.*

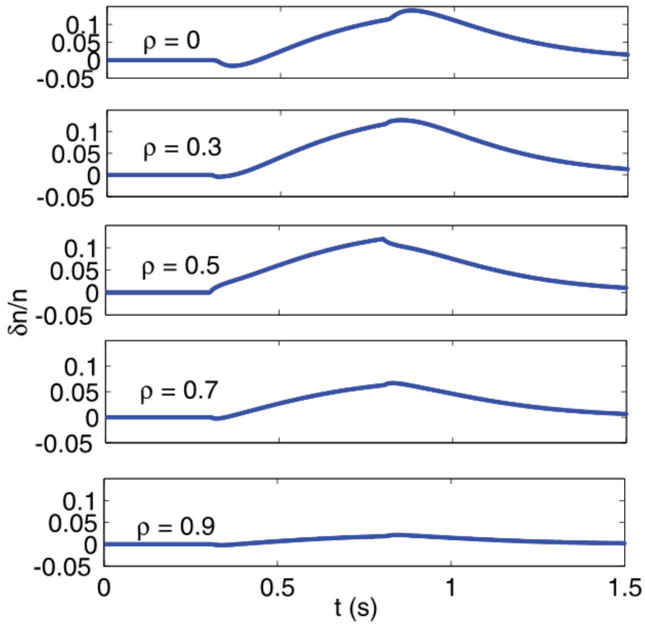

Figure 8.12 Time traces of the density perturbation at various radii. The external heat source is injected into the plasma at $\rho = 0.5$ and $t = 0.3$ s with a duration of 0.5 s. The diffusivity matrix is A = - [1 -1; 0 1].

The density variation at various radii is shown in Figure 8.12. In this case, the density increases when the heat pulse is injected, accompanied by a small but rapid decrease at both sides of the heat pulse location; this has been observed in experiments. The causality lies in the temperature coupling effect. The particle transport equation can be rewritten into,

$$\frac{\partial}{\partial t} n_1 = -\nabla^2 n_1 - \frac{\partial}{\partial t} T_1 + \frac{2}{3} \frac{\widetilde{S}_h}{n_0 T_0} \tag{8.30}$$

The heat pulse affects the density positively, while the temperature's time derivative produces the slight structures.

The interaction between density and temperature should be mutual. Here we investigate two other cases, in which particle transport also affects its heat counterpart.

(iii) $\mathbf{A} = -\begin{bmatrix} 1 & 1 \\ -1 & 1 \end{bmatrix}$, *the upper non-diagonal elements is set to be 1, while the lower is set to be -1.*

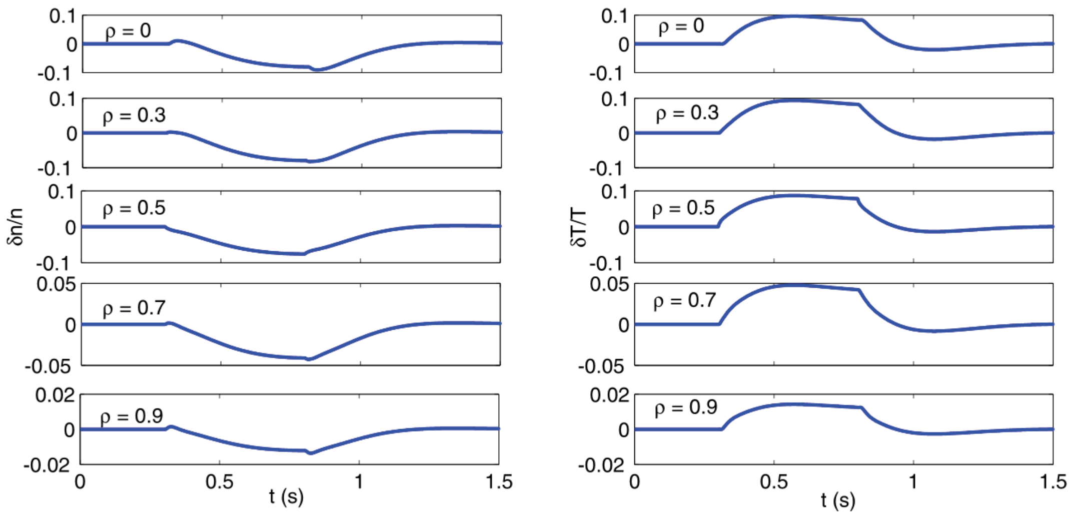

Figure 8.13 Time traces of the density (left panel) and temperature (right panel) perturbation at various radii. The external heat source is injected into the plasma at $\rho = 0.5$ and $t = 0.3$ s with a duration of 0.5 s. The diffusivity matrix is A = - [1 1; -1 1].

As shown in Figure 8.13, the pump-out effect is still present; the additional coupling increases the temperature rise rate before t = 0.4 s while it reduces the increase trend for 0.5 s < t < 0.8 s. Around t = 1 s the temperature perturbation becomes negative, i.e., the hot pulse can lead to cooling effect at a specific time. This phenomenon has been observed in ECRH modulation experiments. The two transport equations can be rewritten as,

$$\frac{\partial}{\partial t} n_1 = -2\nabla^2 n_1 - \frac{\partial}{\partial t} T_1 - \frac{2}{3} \frac{\widetilde{S}_h}{n_0 T_0} \tag{8.31}$$

$$\frac{\partial}{\partial t} T_1 = -2\nabla^2 T_1 - \frac{\partial}{\partial t} n_1 + \frac{2}{3} \frac{\widetilde{S}_h}{n_0 T_0} \tag{8.32}$$

We can find that the diffusivity increases from 1 to 2 for both particle and heat transport, which accelerates the variation rate of density and temperature.

(iv) $\mathbf{A} = -\begin{bmatrix} 1 & -1 \\ 1 & 1 \end{bmatrix}$, *the upper non-diagonal elements is set to be -1, while the lower is set to be 1.*

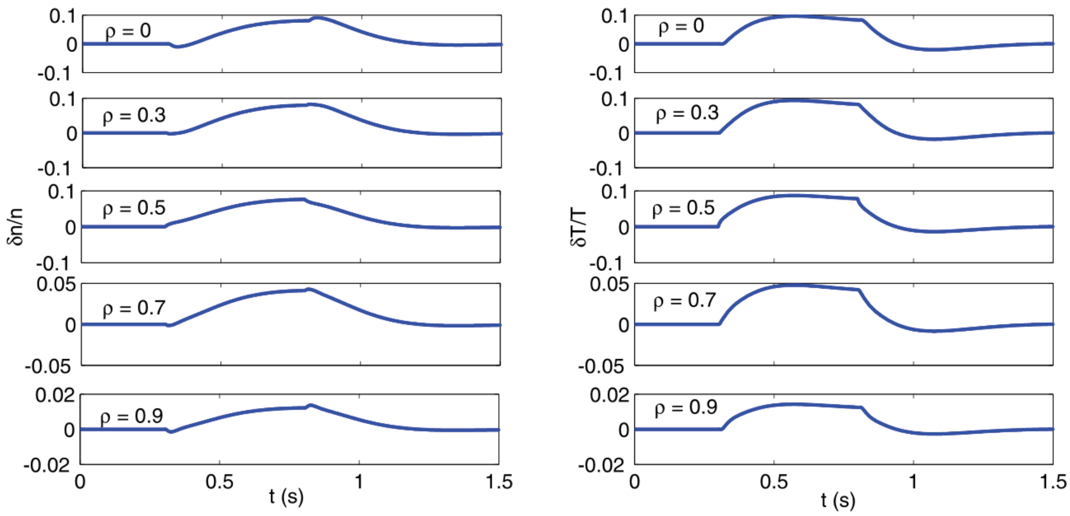

Figure 8.14 Time traces of the density (left panel) and temperature (right panel) perturbation at various radii. The external heat source is injected into the plasma at $\rho = 0.5$ and $t = 0.3$ s with a duration of 0.5 s. The diffusivity matrix is A = - [1 -1; 1 1].

From Figure 8.14, we can find that the temperature perturbation is totally the same between the former case and this one, while the density behaves in the opposite way. This tells us that to determine the transport matrix (if it is possible) we should not only check one physical quantity (i.e., n or T), but the two at the same time.

8.4 Comparison with experiments

The response of the density, temperature system to the modulated ECRH pulses is compared to the experimental data of shot 43234 in Figure 8.15, using for simplicity the diffusive matrix A = [1 -0.5; 2 2]. The agreement on the density perturbation is rather good, including the slight drop after the injection of ECRH power and the rapid increment after the switch-off of ECRH in the central channels. For the temperature part, the perturbation amplitude agrees well, but the increment after the switch-on of ECRH in the experimental data is faster in the simulation. The decrease of the temperature after the switch-off is also faster than that of the simulation results.

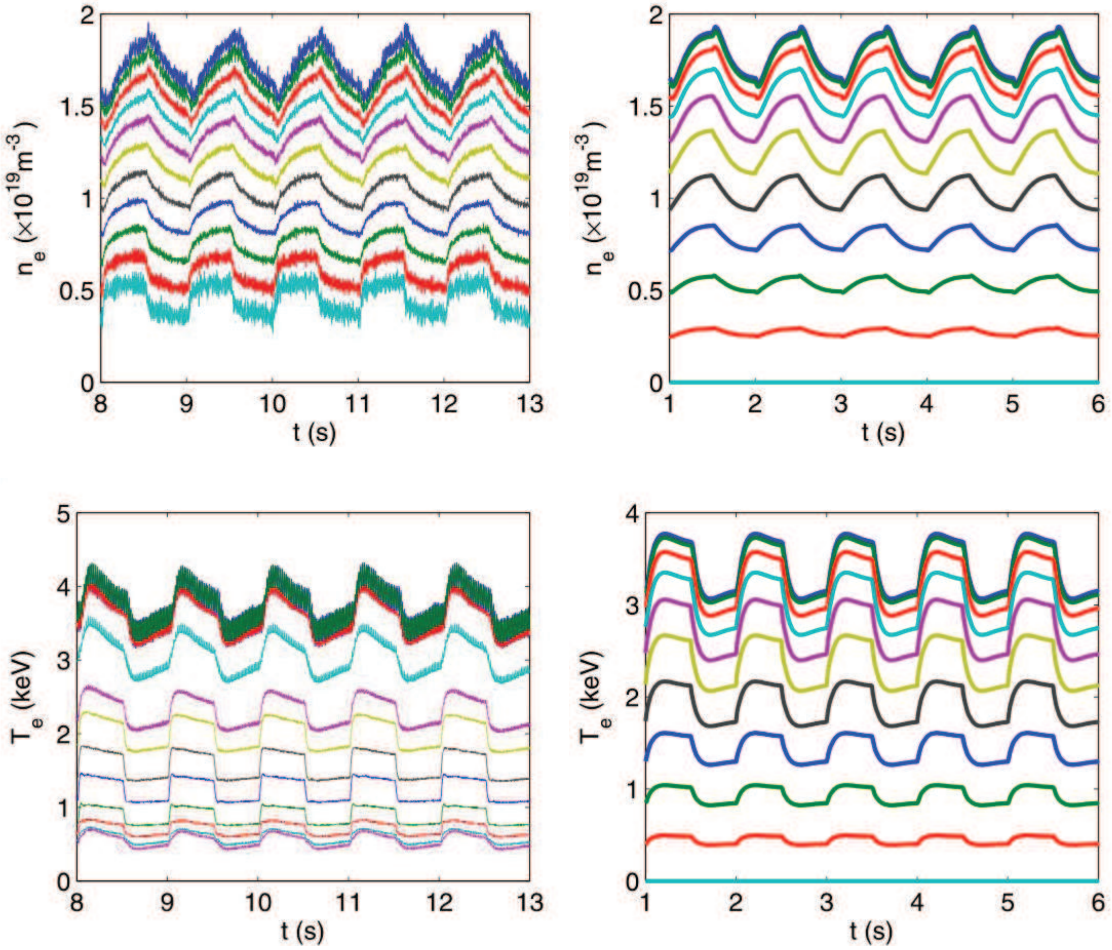

Figure 8.15 (Left panels) Experimental density and temperature oscillation in the ECRH experiments for shot TS#43234. (Right panels) Simulation results obtained using the diffusive matrix of A = [1 -0.5; 2 2;]; the ECRH power is located at $\rho = 0.5$.

The response to the SMBI at $\rho = 0.9$ with the same transport matrix is compared to the experimental data of shot 43248 in Figure 8.16, using the same transport matrix. Qualitative agreement has been found on the amplitude of density and temperature perturbations, while some differences are found in the propagation speeds. The transient response on the density and temperature are almost at the same time in experiment, while the simulation results show a slower change.

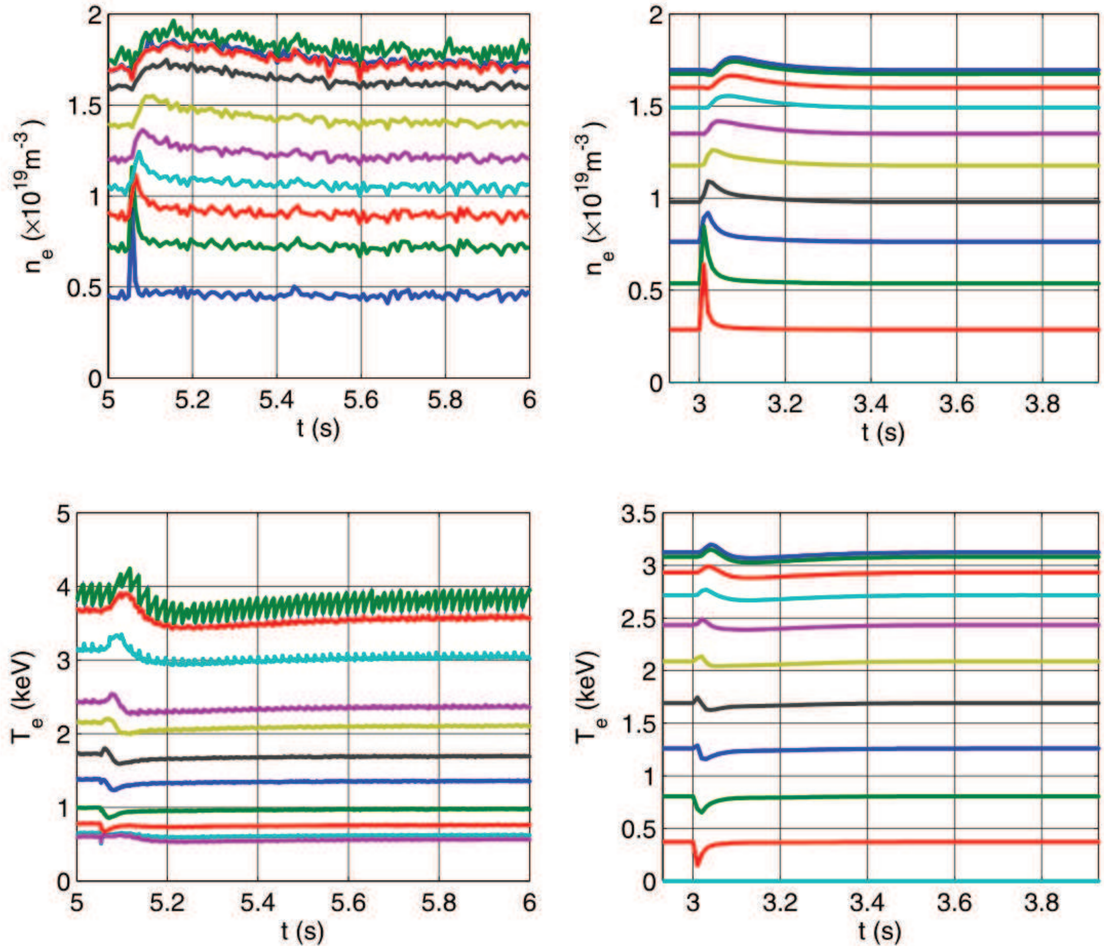

Figure 8.16 (Left panels) Experimental density and temperature oscillation in the SMBI experiments for shot TS#43248. (Right panels) Simulation results using the diffusive matrix of A = [1 -0.5; 2 2]; the SMBI pulse duration is 0.01 s and it is located at $\rho = 0.9$.

In order to improve the agreement between simulations and experiments, it is natural to consider including a nonlinear mechanism, which can induce much faster propagation than the diffusive process, into the transport equation. As a result, the initial response caused by the nonlinear effect can lead to the simultaneous variation on the coupled density and temperature system.

8.5 Discussion and interpretation

The opposite polarity and pump-out effect can be explained qualitatively by using a non-diagonal transport matrix. Still focusing on the purely diffusive transport process, if we use the usual definition of the transport coefficients, we have,

$$D_{inc} = -\partial\Gamma / \partial\nabla n = -A_{11} \tag{8.33}$$

$$\chi_{inc} = -\partial q_e / n_0 \partial \nabla T = -\frac{3}{2} A_{22} + A_{12} \tag{8.34}$$

The effective incremental convective velocities are

$$V_{inc} = \left(\widetilde{\Gamma} - \widetilde{\Gamma}_{diff}\right) / \widetilde{n} = A_{12} \frac{T_1}{n_1} \frac{\nabla \widetilde{T}}{\widetilde{T}} \tag{8.35}$$

$$U_{inc} = \left(\widetilde{q} - \widetilde{q}_{diff}\right) / n_0 \widetilde{T} = \left(\frac{3}{2} A_{21} - A_{11}\right) \frac{n_1}{T_1} \frac{\nabla \widetilde{n}}{\widetilde{n}} \tag{8.36}$$

where the V_{inc} and U_{inc} are the particle and heat convection velocities, respectively. From the formulas we can find that the values of the two velocities are not constant. Taking the particle pinch as an example, the velocity depends not only on the ratio between the relative temperature and density perturbation, but also on the normalized gradient of the temperature perturbation.

The transport matrix is a useful tool for the understanding of experimental phenomena. However, the physical background should be investigated. As known from experiments, the opposite polarity phenomenon has a density threshold, i.e., it has been observed only in low density cases. This may be explained by possible variation of the A_{21} term from negative to zero or even positive [12].

As shown in Equation (6.3) of Chapter 6, the particle flux can be divided into four parts, the diffusion part which is proportional to the density gradient, the turbulence equi-partition which is determined by the geometry factor, the thermo-diffusion part which is proportional to the normalized temperature gradient, and the Ware pinch part which is related to neoclassical collisional process. In fact, for the particle transport, the coupling between density and temperature is shown intuitively by the thermo-diffusion term. Correspondingly, the contribution of the density gradient could also be written in a form similar to that of the heat flux. This provides the theoretical basis of the transport matrix model for the coupled heat and particle transport.

Chapter 9 Conclusions

The transport of heat and particles in magnetically confined tokamak plasmas has a strong influence on the viability of the tokamak approach to harnessing fusion power and, in the context of the next step ITER device, this subject has recently been reviewed extensively [48,90].

The transport of macroscopic plasma quantities in tokamaks is generally considered to originate from two different types of phenomena: the first one is due to collisions in the peculiar magnetic structure of the tokamak device and is called neoclassical. The second one, called anomalous or turbulent transport, is due to electromagnetic turbulence. Both neoclassical and turbulent transport can be studied on the basis of computer simulations using a number of quite complex fluid or kinetic codes, which led to important discoveries. However, dedicated experiments, which provide source materials for theory and simulation, are also commonly employed to generate substantial progress in this area.

Perturbative transport studies are one of the two main experimental ways of investigation on transport. Many choices of the perturbative source have been used so far. They range from tokamak intrinsic sawteeth/ELMs/L-H transition, modulated heat source such as ECRH and ICRH, to the gas puffing, pellet/supersonic molecular beam/neutral beam injection and so on. A variety of experimental results have been acquired. However, due to the nonlinear dependence on the plasma parameters, the transport coefficients obtained from perturbative analysis differ from the ones from those of equilibrium (e.g., power balance) analysis. This thesis mainly focuses on the perturbative transport investigation methods utilizing modulated ECRH/SMBI/Pellet injection.

This thesis reports on experimental studies of heat and particles transport performed on two large tokamaks: Tore Supra (based at CEA/Cadarache, France) and HL-2A (based at the Southwestern Institute of Physics, Chengdu, China). Tore Supra is one of the largest tokamak in the world, and it is equipped with superconducting toroidal magnetic coils and actively cooled plasma facing components. Its long pulse capability has produced a wealth of information for the future ITER reactor. The main structure of HL-2A comes from the old ASDEX, on which the H-mode was firstly observed.

The steady-state characteristics of Tore Supra have been used to develop low frequency (f = 1 Hz) ECRH and SMBI modulation experiments. FFT technique and the low frequency modulation have been used together with the appropriate diagnostics, such as Electron Cyclotron Emission for electron temperature and Microwave Reflectometry for density, in order to provide high quality experimental data.

In the ECRH modulation experiments, evidence of inward heat convection has been observed. The inward heat transport is a phenomenon that would improve energy confinement. For the purpose of realizing fusion reactions, the main part of the plasma has to be confined to supply fusion fuel steadily, which demands a high energy confinement time. Inward energy convection weakens or decreases the outward energy loss. The inward convection, or heat pinch, has been observed in earlier experiments. In the Tore Supra experiments described in this thesis, the ECRH heating position was set at the middle of minor radius, i.e., $\rho = 0.5$. The heat pinch evidence was obtained through the simulation of the FFT harmonics. As well known, for the purely diffusive transport, the maximum point of the amplitude profile shares the same location with the minimum point of the phase profile, normally the two being located at the heating position. In experiments with high density case ($n_e \sim 3\sim5\times10^{19}$ m^{-3}), the amplitude and phase profile have the above mentioned character. However, in the low density case ($n_e \sim$ 1.5-1.8$\times10^{19}$ m^{-3}), the maximum point of the fundamental harmonic amplitude profile shifts inwards, about 10 cm inside the heating position. With the help of the ANALYTIQUE code, we have determined the value of the heat diffusivity and convection velocity by a trial-and-error method. The results shows that near the heating position ($0.4 < \rho < 0.6$), the diffusivity is higher than in other plasma regions, around 2 ~ 4 m^2/s; while the pinch velocity was necessary in order to reproduce the harmonic maximum shift, with a value around 8 m/s.

In our analysis, the high value of the diffusivities may well come from the nonlinear dependence on the temperature gradient. For comparison, we named the above mentioned analysis procedure as Linear Pinch Model (LPM). We have adopted a well-known empirical model trying to describe the pinch like character, which was first proposed in Ref.[31] and developed in Ref.[40]. The so-called Critical Gradient Model (CGM) is based on often referred marginal instabilities, in which a threshold is found in the temperature gradient for the two major turbulence regimes, i.e., Ion Temperature Gradient modes (ITG) and Trapped Electron Modes (TEM). Above the threshold the heat flux increases abruptly, while under it the heat flux will stay at a low level. The model bases itself on the gyro-Bohm diffusion assumption, and use a residual diffusivity to denote the diffusivity level under the threshold. We have tried to use this purely diffusive but non-linear model to reproduce the experimental results, and finally reached the conclusion that this model could not reproduce the shift of the amplitude profile maximum. The simulation results have contradictive behaviour on phase and amplitude profiles, namely, they cannot be reproduced simultaneously. However by using an additional pinch, good agreement was found. Under the CGM regime, this additional inward pinch is concentrated into the region $\rho < 0.3$ with the value of around 1.5 m/s.

Further investigation on micro-instabilities with the simplified Weiland Model (WM) was also carried out. The WM is based on a fluid description. It solves the dispersion equation to find the frequency and growth rate of the main instabilities, by which the transport coefficients can be derived using a mixing length estimate [56]. The results showed agreement between WM and other models (LPM, CGM, power balance analysis) on the diffusivity level; an inward convection velocity was also estimated, although its value is much lower than required to explain the experimental results. The evidence of inward pinch demands further investigation by quasi-linear models or even gyro-kinetic codes.

Two other types of experimental investigation focusing on the heat and particle transport were also carried out, i.e., the pump-out and non-local experiments. In the ITER tokamak, the ECRH system will play an important role as one of the main heating systems and plasma actuators. However, the injection of EC wave may lead to particle loss, as been observed in some experiments. During the modulated ECRH experiments (both on Tore Supra and HL-2A), and in particular conditions, we have also observed such a density reduction, also called the pump-out phenomenon. In fact, two different regions have been identified, a central one dominated by pump-out, and a peripheral one dominated by outgassing (i.e., density increase). By Fourier analysis, the behaviour of the two different regions has been analyzed according to the amplitude and phase profile character.

The so-called non-local transport phenomenon has been observed in different experimental configurations. The effect is an anomalously quick response to an outer stimulation, away from the position of the perturbation source. An important characteristic of this phenomenon is the opposite polarity, i.e., when a cold pulse is injected at the edge, the plasma core heats up at the same time. We have carried out modulated SMBI and pellet experiments on the two tokamaks, and this opposite polarity phenomenon has been observed under low density conditions (central electron density $n_e < 2.5 \times 10^{19}$ m^{-3}). Almost at the same time, the temperature increment in the core region and decrement in the outer region appear. Fourier analysis has been used to determine the transport coefficients. An attempt to explain these phenomena by using a non-diagonal transport matrix has been carried out with qualitatively good results.

The question of whether the transport is diagonal or non-diagonal has been discussed for many years [39]. A systematic study of the coupled density and temperature transport equations has been carried out, using a very simple, purely diffusive but non-diagonal transport matrix. In this way, it was possible to reproduce both the pump-out and the non-local effect, at least qualitatively. In order to obtain a more quantitative description, the transport of particles and heat should be treated as the combination of non-linear and non-diagonal effects, with additional convective terms. A large amount of theoretical and experimental work is still needed in order to combine these experimentally developed concepts with the first principle theory of transport phenomena.

Publications and conferences

Publications

S.D. Song, X.L. Zou, G. Giruzzi, W.W. Xiao, X.T. Ding, B.J. Ding, J.L. Ségui, D. Elbeze, F. Clairet, C. Fenzi, T. Aniel, J.F. Artaud, V. Basiuk, F. Bouquey, R. Magne, E. Corbel and the Tore Supra Team, *Analysis of modulated heat transport with off-axis ECRH in Tore Supra*, *Nucl. Fusion*, to be published (2012)

W.W. Xiao, X.L. Zou, X.T. Ding, L.H. Yao, **S.D. Song**, Z.T. Liu, Y.D. Gao, B.B. Feng, X.M. Song, Q.W. Yang, L.W. Yan, Yi Liu, X.R. Duan, C.H. Pan and Yong Liu, *A method of particle transport study using supersonic molecular beam injection and microwave reflectometry on HL-2A tokamak* 2010 *Rev. Sci. Instrum.* **81** 013506

W.W. Xiao, X.L. Zou, X.T. Ding, J.Q. Dong, Z.T. Liu, **S.D. Song**, Y.D. Gao, L.H. Yao, B.B. Feng, X.M. Song, C.Y. Chen, H.J. Sun, Y.G. Li, Q.W. Yang, L.W. Yan, Yi Liu, X.R. Duan, C.H. Pan and Yong Liu, *Observation of $E\times B$ flow velocity profile change using Doppler reflectometry in HL-2A* 2009 *Chin. Phys. Lett.* **26** 035201

W.W. Xiao, X.L. Zou, X.T. Ding, L.H. Yao, B.B. Feng, X.M. Song, **S.D. Song**, Y. Zhou, Z.T. Liu, B.S. Yuan, H.J. Sun, X.Q. Ji, Y.D. Gao, Y.G. Li, L.W. Yan, Q.W. Yang, Yi Liu, J.Q. Dong, X.R. Duan, Yong Liu, C.H. Pan and HL-2A Team, *Observation of a spontaneous particle-transport barrier in the HL-2A tokamak* 2010 *Phys. Rev. Lett.* **104** 215001

M. Lennholm, L-G. Eriksson, F. Turco, F. Bouquey, C. Darbos, R. Dumont, G. Giruzzi, M. Jung, R. Lambert, R. Magne, D. Molina, P. Moreau, F. Rimini, J-L. Segui, **S. Song** and E. Traisnel, *Demonstration of effective control of Fast-Ion-Stabilized sawteeth by electron-cyclotron current drive* 2009 *Phys. Rev. Lett.* **102** 115004

M. Lennholm, L-G. Eriksson, F. Turco, F. Bouquey, C. Darbos, R. Dumont, G. Giruzzi, M. Jung, R. Lambert, R. Magne, D. Molina, P. Moreau, F. Rimini, J-L. Segui, **S. Song** and E. Traisnel, *Closed loop sawtooth period control using variable ECCD injection angles on Tore Supra* 2008 *Fusion Sci. Tech.* **55** 45

Conferences

Investigation of the heat pinch by low frequency ECRH modulation experiments in Tore Supra, *European Physical Society Conference* on Plasma (Crete, 2008)

Heat and particle transport experiments in Tore Supra and HL-2A with ECRH and SMBI, *European Physical Society Conference* on Plasma (Sofia, 2009)

Heat and particle transport experiments in Tore Supra and HL-2A with ECRH and SMBI, *Journées de l'Ecole Doctorale*, (Marseille, 2010)

Analysis of inward heat transport with off-axis ECRH in Tore Supra, EFDA *Transport Topical Group* (Córdoba, 2010)

Bibliography

[1] V. Erckmann and U. Gasparino 1994 *Plasma Phys. Controlled Fusion* **36** 1869

[2] V. V. Alikaev 1976 *Fiz. Plasmy* **2** 390 [1976 *Sov. J. Plamsa Phys.* **2** 212]

[3] H. Weisen and I. Furno 2001 *Nucl. Fusion* **41** 1227

[4] L. M. Kovrizhnykh 1984 *Nucl. Fusion* **24** 851

[5] L. Spitzer 1958 *Phys. Fluids* **1** 253

[6] M. Greenwald 1999 *Fusion Plasmas* (New York: John Wiley & Sons)

[7] R. Hawryluk 1998 *Rev. Mod. Phys.* **70** 537

[8] Summary of the ITER Final Design Report 2001 *ITER EDA Documentation Series* No 22 (Vienna: IAEA)

[9] B J Green and ITER International Team and Participant Teams 2003 *Plasma Phys. Control. Fusion* **45** 687

[10] M. Valovic *et al* 2004 Proc. 20th IAEA Fusion Energy Conference, Vilamoura, Portugal.

[11] C. Nguyen *Magneto-HydroDynamic activity and energetic particles*, Ph.D thesis, Ecole Polytechnique, 2009

[12] E.J. Doyle *et al* 2000 *Fusion Energy 2000: Proc. 18th Int. Conf.* (*Sorrento, 2000*) (Vienna: IAEA) Ex6/2

[13] F. Ryter *et al* 2010 *Plasma Phys. Control. Fusion* **52** 124043

[14] M. R. de Baar Electron transport barriers in tokamak plasmas, Ph.D thesis, Eindhoven University of Technology, 1999

[15] S. Ejima *et al* 1974 *Phys. Rev. Lett.* **32** 872

[16] J.D. Callen *et al* 1977 *Phys. Rev. Lett.* **38** 491

[17] B.J.D. Tubbing *et al* 1987 *Nucl. Fusion* **27** 1843

[18] E.D. Fredrickson *et al* 1990 *Phys. Rev. Lett.* **65** 2869

[19] F. Ryter *et al* 1999 *Proc. 26th EPS Conf. on Controlled Fusion and Plasma Physics* (*Maastricht, The Netherlands, 1999*) vol 23J (ECA), ed C Bastian et al

(Geneva : EPS) pp 1433-6 (CD-ROM)

[20] A. Bruschi *et al* 1990 in *Controlled Fusion and Plasma Heating*, Proceedings of the 17th European Conference, Amsterdam, Netherlands (E.P.S., Petit-Lancy, Switzerland, 1990), Vol. 1, p. 170

[21] A. Jacchia *et al* 1991 *Phys. Fluids B* **3** 3033

[22] V. Basiuk *et al* 2003 *Nucl. Fusion* **43** 822

[23] J.F. Artaud *et al* 2010 *Nucl. Fusion* **50** 043001

[24] V. Krivenski *et al* 1985 *Nucl. Fusion* **25** 127

[25] Y.R. Lin-Liu *et al* 2003 *Phys. Plasmas* **10** 4065

[26] T.C. Luce, C.C. Petty and J.C.M. de Haas 1992 *Phys. Rev. Lett.* **68** 52

[27] P. Mantica, G. Gorini, G.M.D. Hogeweij, N.J. Lopes Cardozo and A.M. R. Schilham 2000 *Phys. Rev. Lett.* **85** 4534

[28] C.C. Petty, T.C. Luce 1994 *Nucl. Fusion* **34** 121

[29] P. Mantica *et al* 2005 *Phys. Rev. Lett.* **95** 185002

[30] P. Mantica *et al* 2006 *Plasma Phys. Control. Fusion* **48** 385

[31] F. Imbeaux *et al* 2001 *Plasma Phys. Control. Fusion* **43** 1503

[32] M. Lennholm *et al* 2003 *Nucl. Fusion* **43** 1458

[33] J.L. Ségui *et al* 2005 *Rev. Sci. Instrum.* **76** 123501

[34] C. Gil *et al* 2009 *Fus. Sci. Techn.* **56** 1219

[35] F. Clairet *et al* 2001 *Rev. Sci. Instrum.* **72** 340

[36] R. Sabot *et al* 2006 *Nucl. Fusion* **46** S685

[37] F. Porcelli *et al* 1996 *Plasma Phys. Control. Fusion* **38** 2163

[38] B.B. Kadomtsev 1987 *Rep. Prog. Phys.* **50** 115

[39] N.J. Lopes Cardozo *et al* 1997 *Plasma Phys. Control. Fusion* **39** B303-B316

[40] X. Garbet *et al* 2004 *Plasma Phys. Control. Fusion* **46** B557

[41] F. Ryter *et al* 2001 *Phys. Rev. Lett.* **86** 2325

[42] P.H. Rebut, P.P. Lallia and M.L. Watkins 1989 *Proc. 12th Int. Conf. on Plasma Physics and Controlled Nuclear Fusion Research* (*Nice, 1988*) vol II (Vienna: IAEA) p 191

[43] M. Kotschenreuther *et al* 1995 *Phys. Plasmas* **2** 2381

[44] R.E. Waltz *et al* 1997 *Phys. Plasma* **4** 2482

[45] M. Ottaviani, W. Horton and M. Erba 1997 *Plasma Phys. Control. Fusion* **39** 1461

[46] P. Zhu *et al* 2000 *Phys. Plasma* **7** 2898

[47] Weiland J 2000 *Collective Modes in Inhomogeneous Plasma* (Bristol: Institute of Physics Publishing)

[48] ITER Expert Groups on Confinement and Transport and Confinement Modelling Database 1999 *Nucl. Fusion* **39** 2175

[49] F. Ryter *et al* 2003 *Nucl. Fusion* **43** 1396

[50] F. Ryter *et al* 2005 *Phys. Rev. Lett.* **95** 085001

[51] J.C. DeBoo *et al* 2005 *Nucl. Fusion* **45** 494

[52] P. Mantica *et al* 2008 *Fusion Sci. Technol.* **53** 1152

[53] A. Jacchia *et al* 2002 *Nucl. Fusion* **42** 1116

[54] F. Ryter *et al* 2006 *Plasma Phys. Control. Fusion* **48** B453

[55] E. Asp, J. Weiland, X. Garbet, V. Parail, P. Straud and the JET EFDA contributors 2007 *Plasma Phys. Control. Fusion* **49** 1221-1243

[56] H. Nordman *et al* 2001 *Plasma Phys. Control. Fusion* **43** 1765

[57] E. Asp *et al* 2007 *Plasma Phys. Control. Fusion* **49** 1221

[58] J. Jacquinot *et al* 2009 *Fusion Eng. and Des.* **84** 125-130

[59] G.T. Hoang *et al* 2006 *Nucl. Fusion* **46** 306

[60] C. Angioni *et al* 2004 *Nucl. Fusion* **44** 827

[61] X.R. Duan *et al* 2010 *Nucl. Fusion* **50** 095011

[62] W.W. Xiao, Z.T. Liu, X.T. Ding *et al* 2006 *Plasma Sci. Technol.* **8** 133

[63] Y. Zhou *et al* 2009 *Plasma Sci. Technol.* **11** 413

[64] Z.B. Shi *et al* 2005 *Plasma Phys. Control. Fusion* **47** 2019–2028

[65] K. Nagashima *et al* 1995 *Nucl. Fusion* **35** 994

[66] J.Y. Hsu *et al* 1984 *Phys. Rev. Lett.* **53** 564

[67] F. Castejón *et al* 2008 *Phys. Plasmas* **15** 012504

[68] S.P. Eury, E. Harauchamps, X.L. Zou *et al* 2005 *Phys. Plasmas* **12** 102511

[69] P.H. Diamond, T.S. Hahm 1995 *Phys. Plasma* **2** 3640

[70] O.D. Gurcan, P.H. Diamond, T.S. Hahm 2006 *Phys. Rev. Lett*. **97** 024502

[71] X. Garbet, Y. Sarazin, F. Imbeaux *et al* 2007 *Phys.Plasmas* **14** 122305

[72] G.T. Hoang, C. Bourdelle, X. Garbet *et al* 2003 *Phys. Rev. Lett*. **90** 155002

[73] X. Garbet, L. Garzoti, P. Mantica *et al*. 2003 *Phys. Rev. Lett*. **91** 035001

[74] J.D. Callen and M. W. Kissick 1997 *Plasma Phys. Control. Fusion* **39** B173–B188

[75] J. Bucalossi *et al* 2002 19th IAEA Fusion Energy Conference EX/P4-04

[76] B. Pégourié *et al* 2003 J. Nucl. Mater. **313-316** 539-642

[77] N. Tamura *et al* 2010 *Contrib. Plasma Phys.* **50** No.6-7 514-519

[78] X.L. Zou *et al* 2002 *Plasma Phys. Control. Fusion* **42** 1067

[79] H.J. Sun, X.T. Ding, L.H. Yao *et al* 2009 *Chin. Phys. Lett.* **26** 035202

[80] H.J. Sun, X.T. Ding, L.H. Yao *et al* 2010 *Plasma Phys. Control. Fusion* **52** 045003

[81] L.H. Yao *et al* 2010 *Plasma Sci. Technol.* **12** 529

[82] C.Y. Chen *et al* 2010 *J. Plasma Fusion Res.* **9** 35-42

[83] L.H. Yan *et al* 1998 *Nucl. Fusion* □□ 631

[84] L.H. Yao *et al* 2001 *Nucl. Fusion* **41** 817

[85] L.H. Yao *et al* 2004 *Nucl. Fusion* **44** 420

[86] L.H. Yao *et al* 2007 *Nucl. Fusion* **47** 1399

[87] D.L. Yu *et al* 2010 *Nucl. Fusion* **50** 035009

[88] F. Ryter *Etude expérimentale du transport electronique de la chaleur dans les tokamaks*, 2006 Thèse d'habiliation a diriger des recherches a l'Université de Provence Aix-Marseille I

[89] J.C.M. de Haas, J. O'Rourke, A.C.C. Sips, N.J. Lopes Cardozo 1991 *Nucl. Fusion* **31** 1261

[90] C.M. Roach *et al* 2008 *Nucl. Fusion* **48** 125001